



AL-TR-89-084

AD:

AD-A222 504

Final Report
for the period
1 September 1988 to
1 September 1989

FLOW INDUCED NUTATION INSTABILITY IN SPINNING SOLID PROPELLANT ROCKETS

April 1990

Authors:
G. A. Flandro
M. Leloudis
R. Roach

Wasatch Research & Engineering, Inc.
375 N. Virginia Street
Salt Lake City UT 84103

F04611-88-C-0014

DTIC
ELECTE
MAY 30 1990
S B D

Approved for Public Release

Distribution is unlimited. The AL Technical Services Office has reviewed this report, and it is releasable to the National Technical Information Service, where it will be available to the general public, including foreign nationals.

Prepared for the:

Aeronautics Laboratory (AFSC)
Air Force Space Technology Center
Space Systems Division
Air Force Systems Command
Edwards AFB CA 93523-5000

059

NOTICE

When U.S. Government drawings, specifications, or other data are used for any purpose other than a definitely related Government procurement operation, the fact that the Government may have formulated, furnished, or in any way supplied the said drawings, specifications, or other data, is not to be regarded by implication or otherwise, or in any way licensing the holder or any person or corporation, or conveying any rights or permission to manufacture, use, or sell any patented invention that may be regarded thereto.

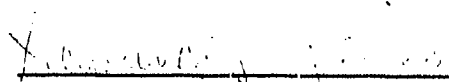
FOREWORD

This final report was submitted by Wasatch Research and Engineering, Inc., Salt Lake City UT on completion of Task 2 of contract F04611-88-C-0014 with the Astronautics Laboratory (AFSC), Edwards Air Force Base, CA. AL Project Manager was Gary L. Vogt.

This report has been reviewed and is approved for release and distribution in accordance with the distribution statement on the cover and on the DD Form 1473.



GARY L. VOGT
Project Manager



LAWRENCE P. QUINN
Chief, Aerothermochemistry Branch

FOR THE DIRECTOR



ROBERT C. CORLEY
Director, Astronautical Sciences Division

REPORT DOCUMENTATION PAGE

Form Approved
OMB No. 0704-0188

1a. REPORT SECURITY CLASSIFICATION UNCLASSIFIED		1b. RESTRICTIVE MARKINGS	
2a. SECURITY CLASSIFICATION AUTHORITY		3. DISTRIBUTION/AVAILABILITY OF REPORT Approved for Public Release. Distribution is Unlimited.	
2b. DECLASSIFICATION/DOWNGRADING SCHEDULE			
4. PERFORMING ORGANIZATION REPORT NUMBER(S)		5. MONITORING ORGANIZATION REPORT NUMBER(S) AL-TR-89-084	
6a. NAME OF PERFORMING ORGANIZATION Wasatch Research & Engineering, Inc.	6b. OFFICE SYMBOL (If Applicable)	7a. NAME OF MONITORING ORGANIZATION Astronautics Laboratory (AFSC)	
6c. ADDRESS (City, State, and Zip Code) 375 N. Virginia Street Salt Lake City, UT 84103		7b. ADDRESS (City, State, and Zip Code) AIJLSCF Edwards Air Force Base, CA 93523-5000	
8a. NAME OF FUNDING/SPONSORING ORGANIZATION	8b. OFFICE SYMBOL (If Applicable)	9. PROCUREMENT INSTRUMENT IDENTIFICATION NUMBER F04611-88-C-0014	
8c. ADDRESS (City, State, and Zip Code)		10. SOURCE OF FUNDING NUMBERS	
		PROGRAM ELEMENT NO. 62302F	PROJECT NO. 5730
		TASK NO. 00	WORK UNIT ACCESSION NO. 8U
11. TITLE (Include Security Classification) FLOW INDUCED NUTATION INSTABILITY IN SPINNING SOLID PROPELLANT ROCKETS			
12. PERSONAL AUTHOR(S) Flandro, G. A., Leloudis, M., and Roach, R.			
13a. TYPE OF REPORT Final	13b. TIME COVERED FROM 88/9/1 TO 89/9/1	14. DATE OF REPORT (Year, Month, Day) 04/90	15. PAGE COUNT 190
16. SUPPLEMENTARY NOTATION Wasatch Research & Engineering performed this work as subcontractor to Science Applications International Corporation, 21151 Western Avenue, Torrance, CA 90501			
17. COSATI CODES		18. SUBJECT TERMS (Continue on reverse if necessary and identify by block number)	
FIELD	GROUP	SUB-GROUP	
21	08	2	
		Spinning Rockets, Spin Stabilized, Internal Ballistics, Jet Damping, Gasdynamic Driving, Jet Gain, Navier-Stokes Solver	
19. ABSTRACT (Continue on reverse if necessary and identify by block number.) <p>This work is a continuation of earlier studies by the same authors aimed at clarifying the role of rocket motor internal ballistics on the observed coning instability of large, spinning, orbit raising propulsion stages. This phenomenon first appeared in the PAM-D (STAR 48) vehicles. Unexpected coning appeared near the end of motor burn with final cone angles of the order of 15 degrees. Earlier vehicles of similar design were not afflicted by this problem.</p> <p>Although no PAM missions were lost as a result of coning, it is conceivable that lighter vehicles using the same propulsion concept and spin stabilization could be seriously jeopardized.</p>			
20. DISTRIBUTION/AVAILABILITY OF ABSTRACT <input checked="" type="checkbox"/> UNCLASSIFIED/UNLIMITED <input type="checkbox"/> SAME AS RPT. <input type="checkbox"/> DTIC USERS		21. ABSTRACT SECURITY CLASSIFICATION UNCLASSIFIED	
22a. NAME OF RESPONSIBLE INDIVIDUAL Gary L. Vogt		22b. TELEPHONE (Include Area Code) (805) 275-5268	22c. OFFICE SYMBOL LSCF

It is imperative that the exact cause of the instability be illuminated so that future systems can be corrected at the design stage. On a short-term basis, better understanding of the problem is needed in order that attitude control systems can be designed on a rational basis. Capability to estimate likely nutation amplitudes is also needed in many system design decisions. These needs are met in the present program in the form of rational scaling laws that allow extension of the available experimental data to new motor/spacecraft configurations.

Numerous physical mechanisms have been proposed to explain the origin of the PAM-D disturbing torque. Most of these have been eliminated by their failure to comply to key features of the telemetry data. Two mechanisms still remain to be more fully evaluated. The first is the "slag sloshing" hypothesis, which links the instability to sloshing of accumulations of aluminum oxide slag within the aft closure of the rocket motor combustion chamber. This mechanism is preferred by some investigators because it is similar to the familiar liquid-sloshing nutation source. In this case, the driving mechanism is linked to the mass center offset caused by the relative motion of the assumed pool of liquid material. However, this interpretation predicts a sensitivity to vehicle acceleration that does not appear in the data. A much more massive vehicle, the SGS-II first stage, also employing the STAR 48 exhibits a torque gain factor that does not reflect acceleration sensitivity. (2.2)C

Our study of the PAM-D coning problem has focused on forces and torques caused by interaction of the motor internal gas flow with the wobbling motions of the spacecraft. The mechanism is closely related to the well-known jet damping effect. During the early part of the STAR 48 motor burn, the standard jet damping estimates apply fairly well. However, as burning proceeds the damping gradually changes into a driving influence as if the damping force switches direction. The magnitude of the disturbing torque remains in a range typical of jet damping. We refer to this situation as the *jet gain* or gas dynamic driving effect.

Jet damping calculations assume the motor flow is uniform with respect to the chamber despite the nutation wobbling. A careful analysis shows that jet damping theory does not apply for spinning motor chambers when a critical size is exceeded. Wobbling induces an unsymmetrical traveling vorticity wave that drastically alters the internal pressure distribution and a destabilizing effect arises when the waves are in resonant coincidence with the vehicle precession frequency. The gas motion is analogous to a sloshing liquid in the more familiar liquid-induced coning. However, instead of free-surface waves, elastoid-inertia vorticity waves are involved. Coriolis forces provide the "spring constant" that allows oscillatory response in the effectively incompressible behavior of the relatively slow moving gases within the motor chamber. The wave system exhibits numerous natural frequencies in close proximity to the wobbling frequency. Predicted resonant points coincide with peaks in nutation growth rate appearing in flight telemetry data.

We have verified this "jet gain" model of nutation instability using cold flow simulations. The angular velocity environment characteristic of a spinning, nutation rocket chamber is reproduced in the laboratory by spinning the test chamber simultaneously about two axes with a properly chosen angular separation. Induced wave motion in the chamber is made visible by a suspension of fine particles or by dye filaments. Data is recorded on a video camera that rotates with the chamber. The observed vorticity waves closely follow the pattern predicted by the analytical results.

A full three-dimensional Navier-Stokes numerical algorithm for study of the induced wave motions has also been developed. In order that this tool can be used in practical situations, special attention was devoted to design of a grid generation method appropriate to the motor chamber geometries typical of spinning space motors. The code was tested extensively by comparing results to known solutions for chamber flow. In its current state of development, it verifies many of the physical features of the jet gain mechanism displayed in the theory.

Methods for measuring the nutation interaction gain factors have been developed using laboratory scale spinning rocket motors. Although the nutation interaction torques generated in these small motors (two-inch outside diameter propellant grains) are very small, useful experience in designing and carrying out such tests was gained. The techniques are readily scaled for full-size motor characterization. To acquire useful quantitative data with small motor tests (say two-inch motors), the spin rates about both axes with an angular separation of about 20° must be over 2000 rpm in order to achieve dynamic similarity and sufficient torque resolution.

The jet gain model provides the basis for scaling laws for propulsion driven nutation instability. Unlike other proposed mechanisms, this allows the instability to be described in terms of known system parameters such as motor mass flow rate, chamber size, vehicle moments of inertia, and propellant burning rate. It is not necessary to introduce unknown parameters such as fictitious pendulum lengths or spring constants. These scaling laws make it possible to extend available PAM-D experimental data in making reliable estimates of expected coning in new spacecraft system configurations.

CONTENTS

	Page
PREFACE	i
GUIDE TO READING THIS REPORT	ii
EXECUTIVE SUMMARY	iii
INTRODUCTION	1
Description of the Research Program	2
Status of the PAM Coning Problem	3
The Need for Scaling Rules	4
The Need for New Experimental Techniques	5
The Need for a Complete Numerical Analysis	5
Plan of the Report	6
DESCRIPTION OF THE PAM-D PHENOMENON	9
Overview	9
History	9
Relationship to Classical Jet Damping	13
Summary of Main Features of PAM-D Telemetry Data	14
Self-Excited Oscillations	16
The Evidence for Resonance	20
Effect of Nutation Disturbance on Wobbling Frequency	20
Requirements for a Satisfactory Mechanism	23
Proposed Nutation Mechanisms	23
Flow Interaction Models	24
Slag Models	24
Modified Slag Models	25
MECHANICS OF NUTATION INSTABILITY	27
Overview	27
Equations of Motion	27
Application of Reynolds Transport Theorem	30
Definition of System Mass Properties	31
Treatment of Internally Generated Interaction Forces and Torques	33
Comparison to Equations in Lagrangian Form	34
Alternate Control Volume Definitions	34
Effect of Internally Generated Moments on Spacecraft Motion	35
Stability Calculations	38
MODELING OF GAS FLOW IN A NUTATING ROCKET	41
Overview	41
Formulation of Flow Equations for a Spinning, Nutating Rocket Chamber	43
Governing Equations and Dimensionless Variables	44
Similarity Parameters	45
Flow Regimes	46
Flow in the Main Chamber	47

Equations in Vorticity Transport Form	48
Simple Flow Interactions: Jet Damping	50
Origins of Classical Jet Damping Concepts	51
The Classical Jet Damping Effect: Angular Momentum Approach	52
The Classical Jet Damping Effect: Fluid Dynamics Approach	54
Effects of Spin on Flow Interactions	60
Simplifying Assumptions	61
Mean Flow Analysis	63
Perturbation Analysis	63
Unsteady Flow Computations	65
Pressure Waves in Spinning Flows	66
Unperturbed Inertial Waves: Poincare' Problem	66
Solution of the Poincare' Equation	70
Summary	73
Nozzle Effects	74
Lateral Torques and Sideforces Produced in the Nozzle Flow	74
The Nozzle Boundary Condition	74
Forced Motion of the Combustion Chamber Gas Flow	78
Overview	78
Forced Oscillations	78
Using Rossby Number as a Small Parameter	79
Derivation of the Forced Wave Equation for the Pressure	80
Solution for the Pressure Wave	86
Solution for the Unsteady Velocity Field	86
Calculation of Nutation Interaction Torques	90
Pressure Torque	90
Momentum Torque	92
Torque Gain Factors	93
Sample Stability Computations	95
Overview	95
Determination of Rgain for Actual Vehicle Configurations	95
 NAVIER STOKES SOLUTIONS OF SPINNING ROCKET FLOW	 99
Overview	99
Numerical Procedure	99
Initial Conditions	102
Boundary Conditions	103
Computational Grid	104
Results	108
SRB Motor Results	108
STAR 48/PAM-D Results	111
Future Work	111
 EXPERIMENTAL METHODS IN FLOW DRIVEN NUTATION	 117
INSTABILITY	
Overview	117
Scaling Laws for Propulsion Induced Nutation	118
Features of Jet Gain Nutation Instability Theory	118

Scaling Laws for the Jet Gain Model	123
Dimensional Analysis of the Jet Gain Coning Mechanism	123
Application of Nutation Scaling Rules	124
Application to Design of Nutation Experiments	126
Summary	126
Experimental Techniques	127
The Two-Spin Axis Nutation Simulation Techniques	127
Design of Laboratory Scale Test Techniques	130
Results	134
Cold Flow Nutation Simulations	137
Results	138
CONCLUSIONS	139
APPENDICES	143
REFERENCES	152



Accession For	
NTIS GRA&I	<input checked="" type="checkbox"/>
DTIC TAB	<input type="checkbox"/>
Unannounced	<input type="checkbox"/>
Justification	
By _____	
Distribution/	
Availability Codes	
Dist	Avail and/or Special
A-1	

LIST OF FIGURES

Figure		Page
1	Development of Coning Instability During Motor Burn	iii
2	Differences Between the Two Nutation Mechanisms	vi
3	Comparison of Predicted (Jet Damping) and Actual Interaction Moment	ix
4	Origin of the Jet Damping Torque	x
5	Some Effects of Coriolis Forces in (a) Spinning and (b) Nutating Chambers	xii
6	Induced Flow in a Closed Spinning, Nutating Cylinder (Vaughn et al)	xlii
7	Induced Flow in Spinning, Nutating Cylinder (Vaughn, et al)	xiv
8	Computational Grid for STAR 48 Motor at 50 Seconds After Ignition	xv
9	Streamlines in STAR 48 Motor, Navier-Stokes Solution	xvi
10	Cold Flow Nutation Simulation Using Two Spin-Axis Method	xviii
11	Test Chamber Showing Submerged Nozzle Entrance	xix
12	Two-Spin Axis Method Measurement of Interaction Torque	xix
13	Froude Pendulum Nutation Instability Simulation	xx
14	Two-inch Rocket Motor and Propellant Grains	xx
15	Froude Pendulum Pivot and Spin Motor	xxi
16	Linear Relationship between Nutation Rate and Apparent Torque	xxvii
17	Rgain vs Time for WESTAR V (PAM-D)	xxvii
18	Rgain vs Time from Jet Gain Analytical Model	xxiv
19	Variation of Rossby Number with Time for Typical Spinning Stages	xxv
20	Launch of PAM-D Spin Stabilized Upper Stage	10
21	Internal Configuration of STAR 48, PAM-D Rocket Motor	11
22	Body-Fixed Pitch Angular Rate vs Time for Typical PAM-D	15
23	Evidence for Self-Excited Nutation Instability	17
24	Rgain vs Time from WESTAR Telemetry	18
25	Rgain vs Time from SGSII (Flight 4) Telemetry	19
26	Nutation Growth Rate for Typical PAM-D	21
27	Apparent Lateral Disturbing Torque	21
28	Effect of Perturbation Torque on Coning Frequency	22
29	Coordinate System and Basic Control Volume	28
30	Alternate Control Volume	36
31	Nonuniform Pressure Distribution Induced by Wobbling	58
32	Simplified Motor Geometry for Analytical Solutions	62
33	Variation of Inertial Wave Frequencies with Slenderness Ratio, b	72
34	Predicted Torque Gain Factor, Rgain, vs Time	96
35	Resonant Coincidence of Spacecraft and Wave Frequencies	97
36	Finite Difference Grid for Generic Rocket Motor	105
37	Finite Difference Grid for STAR 48 Motor Type	106
38	Burnback Profiles for STAR 48 Motor Type	107
39	Comparison of Experimental and Computed Axial Velocity Profiles	109
40	Comparison of Experimental and Computed Radial Velocity Profiles	109
41	Contours of Dependent Variables for Generic Motor	110
42	Particle Trace Diagrams for Spinning Generic Rocket	112
43	Development of Circumferential Velocity	113
44	Oblique View of Particle Trace for the STAR 48 Type Motor	114

Figure		Page
45	Mach Number Contours for STAR 48 Type Motor	115
46	Circumferential Velocity Contours for STAR 48 Motor Type	115
47	Comparison of Predicted and Actual Interaction Moments	119
48	Two Views of the Origin of Jet Damping	121
49	Simulation of Nutation Angular Velocities by Two-Axis Spin Method	128
50	Two-Axis Spin Lab-Scale Motor Test Device	131
51	Schematic of Laboratory-Scale Nutation Experiment	132
52	Two-Inch Leloudis Rocket Firing During Froude Pendulum Nutation Test	133
53	Drive Motor and Gimbal Arrangement in Froude Pendulum Test	133
54	Motor Components Showing Typical Grain and Aft Closure	135
55	Assembled Motor Showing Pressure Relief System	135
56	Slip Ring Assembly in Froude Pendulum Test Device	136
57	Slag Deposition (Motor on Left was Fired Without Spin)	136
58	Cold Flow Test Arrangement	137

LIST OF TABLES

Table		Page
1	Governing Equations for Chamber Flow	44
2	Dimensionless Variables	45
3	Similarity Parameters	45
4	Forcing Functions for Case 1	84
5	Forcing Functions for Case 2	84
6	Forcing Functions for Case 3	85
7	Solution of Fourier Ccoefficients for Case 1	88
8	Solution of Fourier Coefficients for Case 3	89

PREFACE

This document is the final report for Task 02, Vortex Interaction Study, of the Research Applications Scientific and Engineering Technical Assistance (SETA) contract, F04611-88-C-0014. This contract provides support to the Air Force Astronautics Laboratory (AL). Dr. Lawrence Quinn, AL/LSC, is the Air Force Project Manager for this contract. Science Applications International Corporation (SAIC) is the contractor and Dr. Robert Long, Jr. is the SAIC Program Manager. The duration of the technical effort was 1 September 1988 to 31 August 1989.

The Air Force Task Manager for this program was Gary Vogt, AL/LSCF. The Principal Investigator was Dr. Gary Flandro[†] of Wasatch Research and Engineering, Inc. Co-Investigators included Dr. Robert Roach of Georgia Institute of Technology who developed the Navier-Stokes numerical solutions, Dr. Richard Shorthill of the University of Utah who helped in performing the cold flow laboratory simulations of gas flow in a nutating rocket, and Mr. Mark Leloudis of Wasatch Research who played a major role in the design, construction, and operation of the laboratory-scale nutation instability rocket tests. Brett Hussey of the Wasatch Division of Thiokol Corporation aided us in the acquisition of STAR 48 propellant grains for use in the two-inch rocket motor used in these tests.

The authors wish to express their sincere thanks to Dr. Robert Long, Mr. William Haynes, and Mr. Stephen Duntley of SAIC who aided us immeasurably in the efficient operation of the study. We are also grateful to Dr. Lawrence Quinn, Dr. R. C. Corley, and Dr. Phillip Kessel of the Astronautics Laboratory for the benefit of numerous discussions and for many excellent ideas. Gary Vogt of the Astronautics Laboratory deserves special thanks for his continuous interest in the details of the work. We also wish to thank him for his diligent work in checking numerical solutions and his application of nutation instability predictive computer programs developed in the course of this study.

[†] President and CEO. Also Professor of Aerospace Engineering, Georgia Institute of Technology (on leave of absence 1988-1989 academic year) and Research Professor of Mechanical Engineering, University of Utah.

GUIDE TO READING THIS REPORT

This report deals with a complex phenomenon, the PAM-D coning problem, that is still under intensive study by several research groups. In order to make the findings readily accessible both to experienced nutation instability investigators and to interested newcomers, it is organized to facilitate reading and reference. Each key topic is identified verbally, and each is preceded by an overview so that the reader can determine easily whether to read the complete discussion or to move to parts of greater interest.

An executive summary is provided immediately following this guide for those concerned only with the main findings of the study. It is completely self-contained and includes a brief description of the PAM-D coning effect and its history. Emphasis is on the physical interpretations of interactions between the internal combustion gas motion and spinning vehicle dynamics.

Introductory material of a more detailed type in the form of overviews is included in each chapter of the main body of the report to enable those new to the problem to understand the motivations for each of the program tasks and the methods used in their execution. This material is easily identified and can be skipped by those familiar with the nutation problem.

All main elements of the gas flow theory for nutation instability are introduced initially by means of the simplest possible example problems and formulations. All assumptions are carefully described and justified as required. For some readers this will be a sufficient level of study to grasp the main essence of the analytical findings. For others, the detailed mathematical analysis is of greatest significance.

Since understanding of the results depends heavily on a thorough understanding of the physics and its mathematical basis, a very complete derivation of all major elements of the theory is included. Pivotal algebraic steps are included in all developments in which there is any possibility of misinterpretation. Recent literature makes it clear that there is widespread misunderstanding of many of the concepts on which flow-induced nutation instability model depends. We hope by this means to provide aid to those who require an in-depth understanding of the influence of the motor internal ballistics on the dynamics of spinning rocket propelled vehicles.

A very extensive bibliography is included that will enable any interested reader to access the vast literature that provides the basis for the work reported.

EXECUTIVE SUMMARY

Coning (also known as nutation or wobbling) degrades performance of modern, spin-stabilized solid rocket motors used to raise payloads to synchronous orbit. Figure 1 describes the key features of the phenomenon showing that it occurs during the perigee motor burn and is linked in some way to motor operation.

The unexpected wobbling motion threatens several aspects of the orbital injection process, and has resisted correction based on current models of the behavior of rotating vehicles. Conventional analysis has failed to solve this potentially costly problem. Therefore designers have resorted to inefficient and expensive corrective measures. These are in conflict with the basic principals of spinning solid propellant upper-stage design, which are founded on the inherent simplicity and

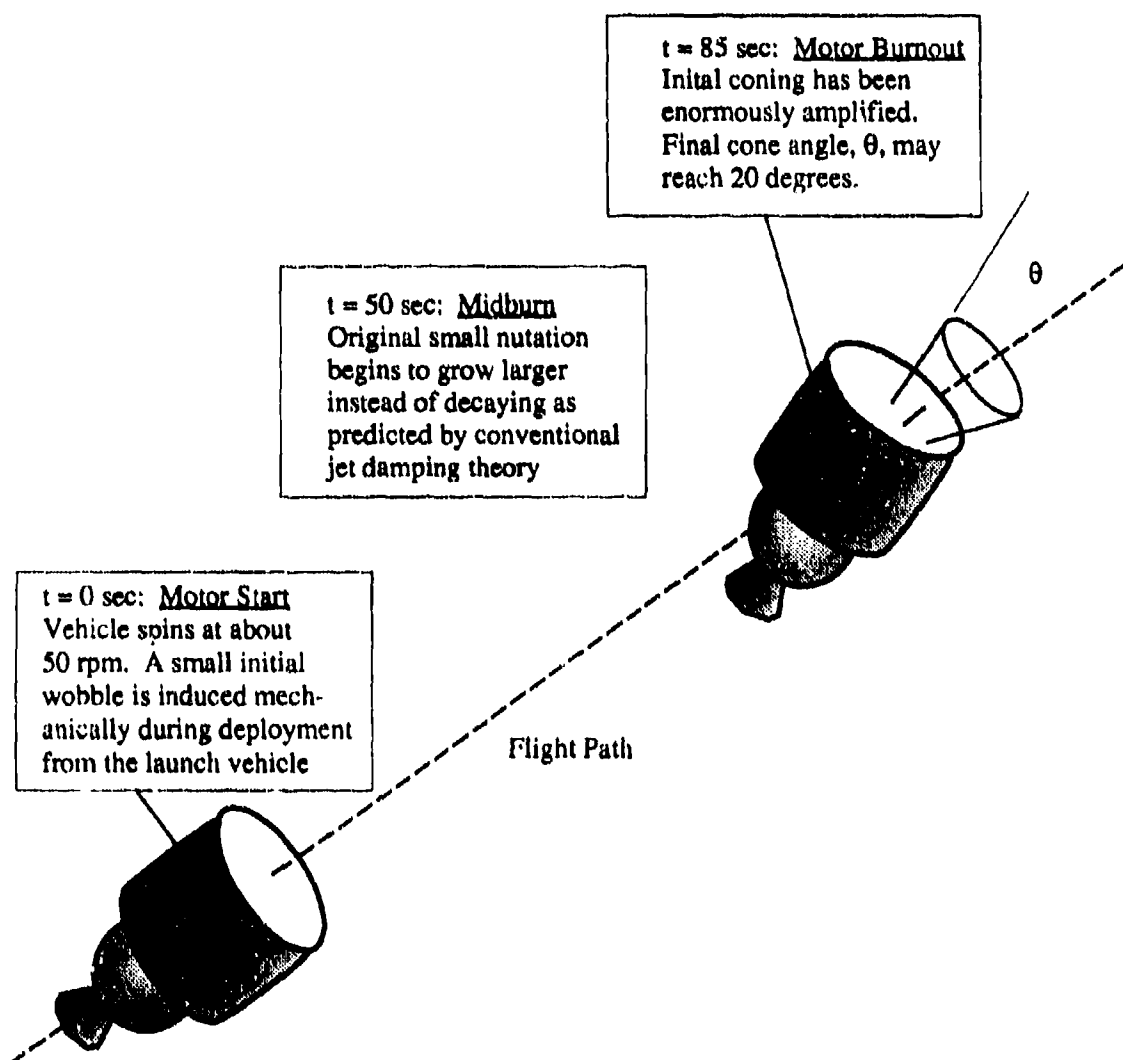


Figure 1. Development of Coning Instability During Motor Burn (PAM-D, STAR 48)

relatively low cost of such systems. The most common approach has been the application of a strap-on attitude control system to counteract the disturbing torques created within the system. This adds system complexity and cost as well as decreasing reliability.

This report describes a program to provide improved understanding of the physics of nutation instability with the goal of identifying approaches for avoiding it in the design of new upper-stage vehicles so that the advantages of spin stabilization and solid rocket propulsion can be restored.

Program Objectives

This research and development program explored the origins of coning instability by application of three tools:

- Mathematical analysis of internal ballistics of a spinning, nutating rocket motor
- Numerical simulation of interactions between spin, nutation, and motor gas flow
- Laboratory scale experimentation using both cold flow and small spinning motors

Program objectives included:

- Clarification of the role played by combustion gas flow in driving coning
- Development of methods for laboratory experimentation on coning mechanisms
- Development of scaling rules for use in upper stage design to avoid coning
- Development of comprehensive analytical understanding of coning
- Exploration of numerical procedures for accurately determining flow effects
- Formulation of corrective design procedures

A much improved physical understanding of the nutation phenomenon has resulted from a careful analysis of the motor internal ballistics. Although our contract specified that only the initial steps be taken in developing comprehensive numerical tools, a complete three-dimensional, Navier-Stokes model of flow in a spinning motor was brought to a highly developed form before the end of the study. The experimental studies demonstrated that both small-scale and full size nutation instability tests can be successfully undertaken.

Features of the Nutation Phenomenon

Several features of the PAM-D observations must be emphasized. These allow us to eliminate many potential disturbing mechanisms. The features of most importance are:

- PAM-D coning originates within the rocket motor (its growth either ceases or abruptly decreases at end of burn).
- The disturbing torque vector moves relative to the vehicle and rotates in a lateral plane in the retrograde direction at the precession frequency. Its phase angle with respect to the wobble angular velocity changes dramatically during the motor burn.

- The driving torque is proportional to the magnitude of the lateral perturbation angular velocity indicating a closed loop, self-excited oscillation. The factor of proportionality (called Rgain) varies tremendously throughout motor burn. Its largest value occurs about midburn.
- Coning growth is not a smooth, sustained process. It occurs in a series of spurts with the largest growth usually appearing about the middle of the motor burn. These spurts and the associated shifts in frequency follow a pattern suggesting a resonant interaction with the disturbing mechanism.
- The pitch/yaw rate amplitude growth is accompanied by shifts of wobble frequency that are strongly correlated with the Rgain factor.
- Rgain is not sensitive to the acceleration of the vehicle.
- Rgain is sensitive to the vehicle mass properties suggesting that modification of the wobbling frequency by differences in lateral moments of inertia may be important.
- Periods of growth can occur early in motor operation when jet damping is expected to dominate the motor spacecraft interaction.

Many proposed mechanisms have been eliminated because of their lack of agreement with one or more of these features. In particular, effects related to thrust offsets or nonuniform combustion of the propellant do not fit the experimental data.

The nutation is strikingly similar to that frequently related to sloshing of liquid stores or vibration of structural components. This brings with it the opportunity for a resonant interaction. Resonance may allow what might ordinarily be an insignificant disturbance to interact strongly with the vehicle motion. Thus, we are led to expect a transient phenomenon like sloshing. Clearly anything in the motor that can slosh or vibrate must be examined with care. Two such effects have survived a careful assessment of an originally long list of candidate mechanisms.

Search for the Disturbing Torque

The mechanism at the heart of the nutation disturbance must be identified because such knowledge is essential in determining corrective procedures. It is very possible that rather small changes in motor design geometry or propellant configuration could minimize or eliminate the coning growth. The spacecraft system designer now needs a new set of rules in selecting spin rates and mass center tolerances. Design rules that worked effectively in smaller spin stabilized systems are clearly not working when applied to the larger systems such as the PAM-D and its derivatives.

Knowledge of the mechanism is also required in order that a predictive capability can be developed. One must have easily applied scaling laws available if estimates of attitude control needs or estimates of expected coning growth are to be available prior to flight testing. The economics of commercial and military space operations demands that phenomena such as the PAM coning effect are totally understood in order that costly failures can be avoided.

Two theories have evolved that attempt to provide physical understanding of the origins of the disturbing forces that drive the unexpected wobbling motion. These are compared in Figure 2. They are what remain of an originally long list of twenty-two potential mechanisms. Most of the mechanisms proved unable to fit one or more key features of the experimental data collected in

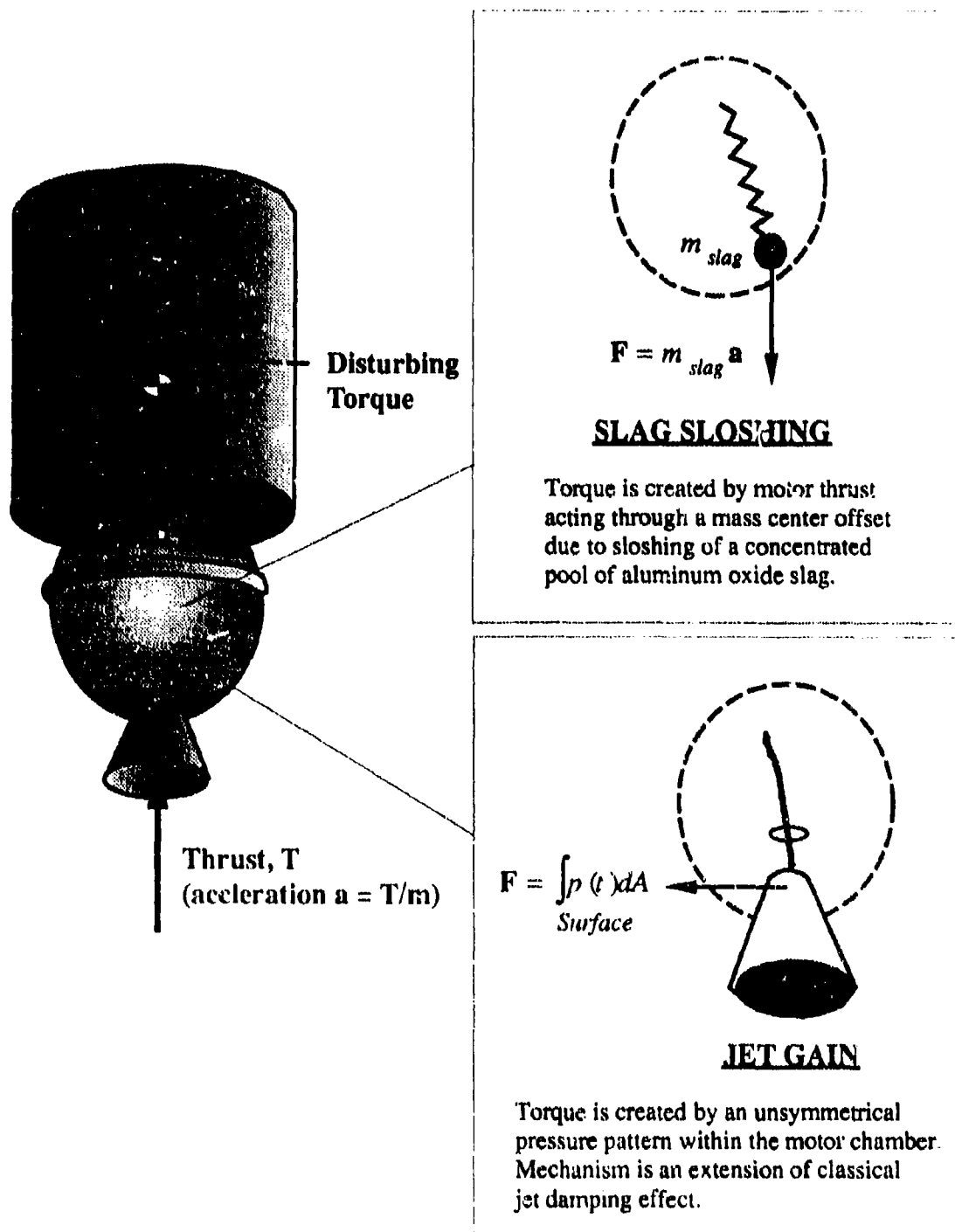


Figure 2. Differences Between the Two Nutation Mechanisms

about twenty flights of the PAM-D, SGS-II, and PAM-DII vehicles.¹

Some investigators prefer the "slag" theory², which assumes that aluminum oxide slag produced in the combustion process accumulates in a liquid pool within the motor chamber and sloshes in response to the wobbling spacecraft. Under certain conditions, this hypothetical slag pool moves in resonance with the wobble and a torque is produced on the vehicle because of the center of mass offset relative to the thrust line. Therefore, the torque should be proportional to the vehicle acceleration. This expected sensitivity to thrust (or acceleration) does not appear in the flight data. Laboratory experiments, numerical simulation, and flight tests of small spinning rockets containing a simulated slag pool do not appear to support the slag accumulation nutation instability theory. The theoretical results are unsatisfactory because they introduce physical variables such as spring constants or pendulum lengths that cannot be determined from the motor or spacecraft characteristics. Thus, one can make the theory fit the data by adjustment of the variable parameters.

The second mechanism, which is the subject of the present study, links the instability to nonuniform pressure forces induced within the internal motor gas flow by the vehicle motions.¹ This interaction has its origin in the same physical processes that produce the well-known jet damping effect. If a rocket rotates about a lateral axis, internal pressure forces are generated that usually tend to stabilize the motion. However, as this report shows, classical jet damping theory is not applicable when

- The motor combustion chamber exceeds a critical size
- The system rotation exceeds a critical spin rate

Inclusion of the effects of motor geometry and size coupled with spin effects on the internal gas flow lead to an interaction with the spacecraft dynamics that may cause nutation *growth* instead of the *decay* predicted by classical jet damping theory.

The Inadequacy of Classical Jet Damping Theory

The analytical tasks have led to greatly improved understanding of the complex flow effects that occur in a spinning rocket combustion chamber. An important finding is that conventional jet damping ideas do not apply in large, spinning motors of the type now in use in satellite orbit raising missions.

The classical theory of jet damping³⁻¹⁰ appears to be reliable for smaller systems and has been correctly applied in previous situations. However, when the motor chamber exceeds a critical size, the internal flow of combustion products becomes increasingly sensitive to the external motions of the vehicle.

Even when the system is not spinning, the flow field simplifications usually assumed to be adequate in jet damping calculations do not apply. The gas motion is greatly affected by spin, which leads to an array of flow phenomena in the chamber that are not addressed by jet damping. In particular, the assumptions that the flow is steady and uniform are incorrect.

Nevertheless, jet damping theory yields an interaction torque with a *magnitude* very similar to the nutation disturbing moment observed in flight. We will show in this report that, when time-dependent gas motions are properly accounted for, the interaction force between the chamber and the flow is altered mainly in its *direction* relative to the angular motions of the spacecraft. A destabilizing, rather than a stabilizing, interaction may result under certain conditions.

The Significance of Jet Damping

Figure 3 compares the expected flow interaction moment based on accepted jet damping theory to the disturbing moment actually present during flight. The conditions shown correspond to a typical PAM-D near the end of its motor run. Several crucial observations are summarized in the figure. They are:

- Jet damping shows that gas flow interaction forces are significant
- The predicted jet damping moment is nearly equal to the actual nutation moment
- The actual moment has a component in the same direction as the nutation rate rather than opposite to it as predicted by jet damping theory

The theory of the dynamics of rotating bodies shows that it is necessary that the applied moment have a component in the wobble direction in order that nutation is amplified. The other component, the one perpendicular to the nutation angular rate vector, causes the wobbling frequency to change. In effect, if we can find the reasons for the change of direction of the jet damping moment then we have, in all likelihood, found the source of PAM-D wobble.

As Fig. 3 emphasizes, the jet damping torque is created by the nonuniform pressure distribution in the combustion chamber. The conditions that lead to a purely damping flow interaction must be examined. This will give us useful guidance regarding conditions needed to rotate the pressure distribution into the driving configuration shown in Fig. 3(b).

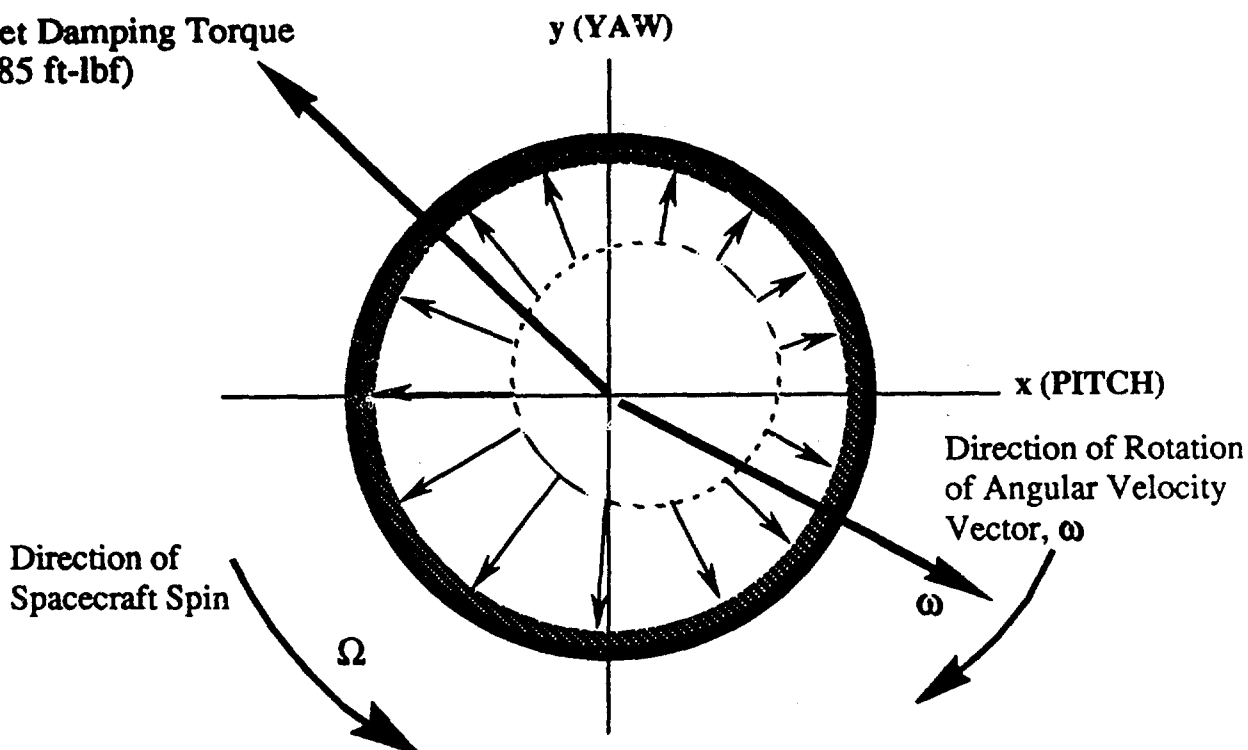
The Fluid Dynamics of Jet Damping

Figure 4 illustrates the physical content of the jet damping concept. A portion of the chamber wall and the nearby gas stream is shown. The figure shows how the direction of the stream must change in response to the rotation of the chamber. In jet damping, it is assumed that the flow stream changes in direction only, *without being affected in any other way*. This is equivalent to assuming that the gas acts as a rigid body. Clearly this is not a realistic description of the fluid mechanics.

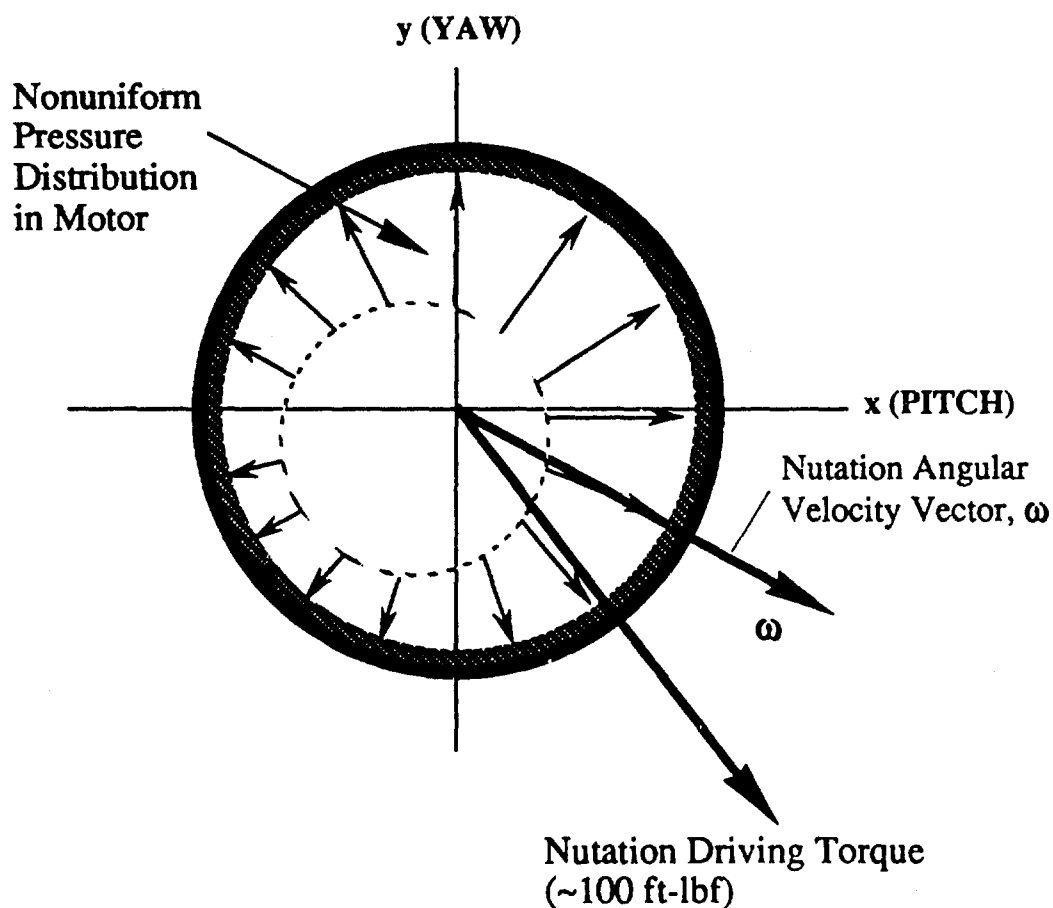
The flow is *assumed* to be completely uniform and more importantly to stay that way even though it is acted upon by a very complex set of internal stresses created by the lateral wobble of the system coupled with the relative gas motion and spin. The Coriolis and angular acceleration stresses are assumed in jet damping theory to be balanced by a nonuniform pressure. This pressure distribution creates the damping moment as the figure shows.

This is a realistic picture only if the gas moves through the chamber and out of the nozzle very rapidly. In small rockets this condition is met, but in large ones like the STAR 48, the gases move very slowly over very large distances. For example, a gas particle leaving the propellant grain travels through the chamber at an average speed of about 3 m/s (10 ft/sec). It must travel a distance of about 1.2 m (4 ft) to reach the nozzle entrance where it rapidly accelerates to high speed and compressibility effects then dominate its motion. Thus, the particles remain within the influence of the chamber boundaries for about a half-second, a significant length of time. In this time the spacecraft has rotated about 2 full revolutions. Clearly the effects of spin are likely to be more important when the gases remain in the chamber for multiple revolutions. The gas stay-time in the STAR 48 is typically ten times longer than in earlier, smaller spin stabilized rockets. We must determine if the assumption of uniform flow relative to the chamber is appropriate under these conditions.

Jet Damping Torque
(85 ft-lbf)



(a) Force System Predicted by Jet Damping Theory



(b) Force System Observed in Flight Telemetry

Figure 3. Comparison of Predicted (Jet Damping) Flow Interaction to the Observed Moment

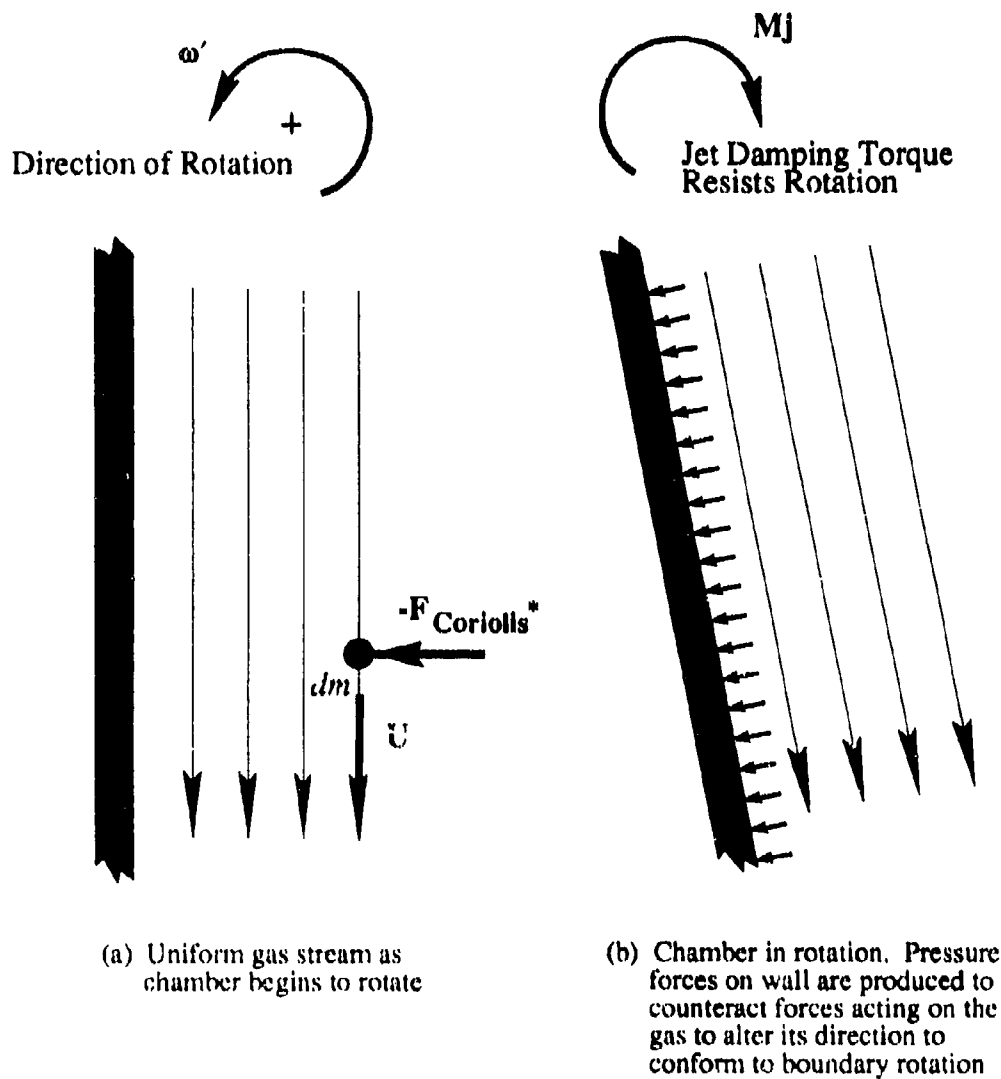


Figure 4. Origin of the Jet Damping Torque

* Coriolis Force is one of the effects of rotation on the apparent motion of particles as observed in a coordinate system fixed to the rocket. The Coriolis force on a particle of mass dm is

$$F_{\text{Coriolis}} = (2\omega' \times U)dm$$

This apparent force acts perpendicular to the plane of the relative velocity, U , and the angular velocity, ω' . In jet damping theory, the Coriolis force is assumed to be balanced by pressure forces (hence the negative sign in the figure). The particle motion is assumed to be unaffected by the Coriolis effect. Under these assumptions, the reaction torque is "damping," that is, it acts to resist the rotation.

The nature of the force system acting on fluid particles is described in Figure 5. This shows the system from the point of view of an observer moving with the rocket motor combustion chamber. This is the point of view that must be used to properly determine forces acting on the walls of the chamber.

The angular velocity is separated into two parts in the figure. Figure 5(a) illustrates the effect of Coriolis acceleration due to the chamber rotation about its symmetry axis. The gas particles pick up an azimuthal velocity component as they move through the chamber producing a vortex flow. The azimuthal velocity increases enormously as the particles move through the nozzle due to conservation of angular momentum.

Figure 5(b) shows the Coriolis force produced because of the nutation wobble. Diametrically opposite particles are illustrated to show that the force system is not symmetrical. If the gas is not allowed to move in response to this force (as jet damping theory assumes) then this is of no consequence. However, we must question this assumption. What would happen if the gas were free (as we know it is) to move in response to the Coriolis force? It appears by analogy with the effect of axial spin that the gas must acquire a lateral velocity. Since the angular velocity perturbation ω' rotates with respect to the chamber (see Figure 3) the velocity pattern it produces must also rotate in the retrograde direction.

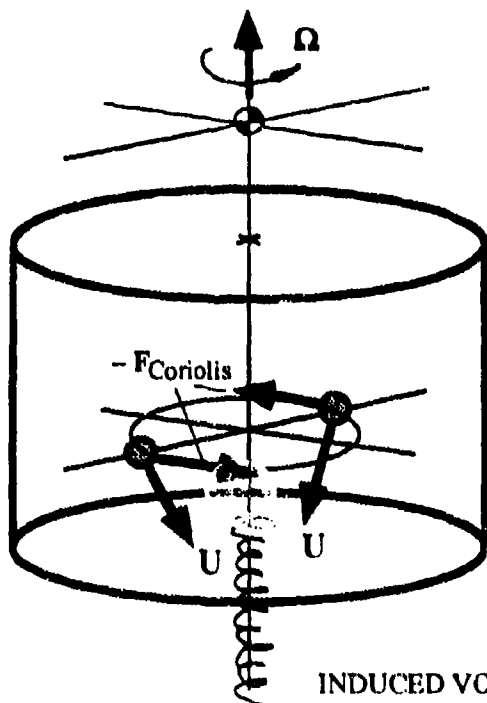
It is useful to attempt to visualize the resulting flow by means of simple geometrical arguments. The lateral Coriolis-induced flow can be taken to be a small perturbation superimposed on a uniform mean flow. Obviously the sideward motion must be balanced by an axial mass flux in order that continuity is satisfied, so the axial velocity on one side of the chamber is higher than on the other. A circulatory flow perturbation is created by the Coriolis acceleration. Since this entire pattern revolves around the chamber as ω' rotates, it exhibits wave-like behavior. We will describe this as a traveling vorticity wave or inertial wave as it is called in the literature.¹¹⁻¹⁷ Such waves are a familiar topic in the study of rotating fluids.¹¹ They play a central role in the jet gain theory of nutation instability.

We have now demonstrated that complex waves should be expected in spinning rockets. Their importance in the behavior of the motor depends on the relative size of the Coriolis forces. These forces play an increasingly important role in the gas motion as the chamber size increases as we have been careful to point out. If one accepts that a uniform axial flow is not a realistic description of the flow under the conditions described, then one must also accept that the associated pressure distribution is modified. That is, the expected jet damping pressure distribution that leads to the usual damping influence is highly suspect.

It remains to be shown that the pressure distribution is modified in such a way that the integrated pressure force acting on the chamber is no longer pointing in the direction indicated by jet damping theory. Much of the analytical material in Chapter 4 of this report is devoted to establishing that the result is a pressure pattern much like that illustrated in Figure 3(b). That is, *jet damping becomes jet gain*.

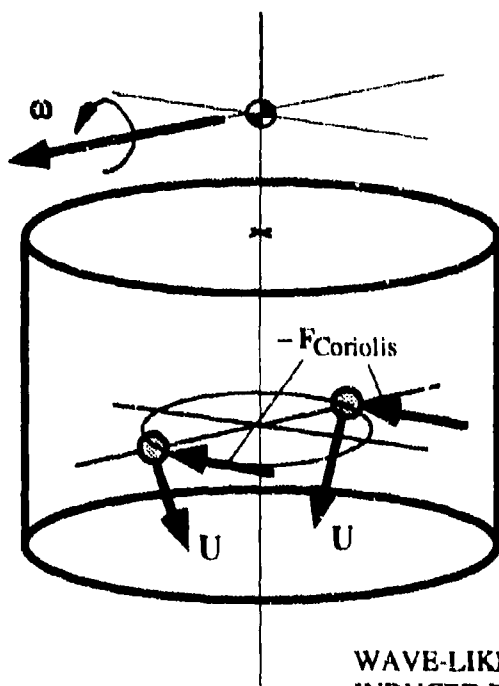
Wavelike Behavior of Chamber Gas Flow

It is well-known that when a rotating fluid or gas is disturbed, the disturbance propagates like a wave¹¹⁻¹². In the last subsection we demonstrated the origin of such "inertial" waves by a simple interpretation of the Coriolis acceleration acting on the gas particles. They are called inertial waves because the restoring force that leads to oscillatory behavior is the Coriolis force, one of the inertial correction terms in the equations of motion written in rotating coordinates. It is important not to confuse them with free surface waves or waves of compressibility (acoustic waves). These waves owe their existence solely to the Coriolis inertial force.



(a) Effect of Coriolis Force due to Axial Spin. If particle velocity U has a radially inward component, as shown, then Coriolis force acts to induce an axial vortex flow in the gas. Two diametrically opposite particles are shown.

INDUCED VORTEX FLOW



(b) Effect of Coriolis Force due to Nutation Wobble. Lateral component of angular velocity induces an unsymmetrical gas motion. Flow pattern rotates about the chamber axis as ω precesses in the retrograde direction.

WAVE-LIKE TIME-DEPENDENT
INDUCED FLOW PATTERN

Figure 5. Some Effects of Coriolis Forces in (a) Spinning and (b) Nutating Chambers

These waves have been studied extensively, mainly in the context of meteorology.^{11, 16} Unfortunately, many engineers trained in this country are not introduced to this concept so it is difficult to convey to them the significance of inertial waves in the PAM-D coning problem.

Inertial oscillations were first studied experimentally by Lord Kelvin¹³. The theory of inertial waves was developed by Poincare¹⁴ and Cartan¹⁵. Later, it was elegantly demonstrated in experiments by Fultz¹⁶ and Aldridge.¹⁷ Their methods for exciting inertial waves were adopted in some of the cold flow experiments carried out in the present program to aid in visualization of the complex gas motions in a spinning rocket.

An example of the importance of inertial internal flow interactions can be found in the extensive work done on spinning, liquid-filled, artillery projectiles.¹⁸⁻²⁵ In this case, there is no net mass flow through the system. However, the problem is analogous to the PAM coning phenomenon in many respects. Wobbling instability is introduced because inertial waves are induced by small initial nutation. This case was recently studied by numerical means by Vaughn, et al.²⁶, Navier-Stokes finite-difference methods were used. Several of their plots are shown here to illustrate the type of wave motion induced by wobbling. The reader should study the flow patterns with the discussion of the last subsection in mind. It will be clear that the numerical results are precisely what we would expect on the basis of the influence of the Coriolis forces.

Figure 6 shows induced velocity vectors in the closed cylindrical chamber studied by Vaughn. The flow resembles a recirculation pattern. However, to an observer at rest in the rotating frame attached to the cylinder, the motion is oscillatory, and would be described as wave-like.

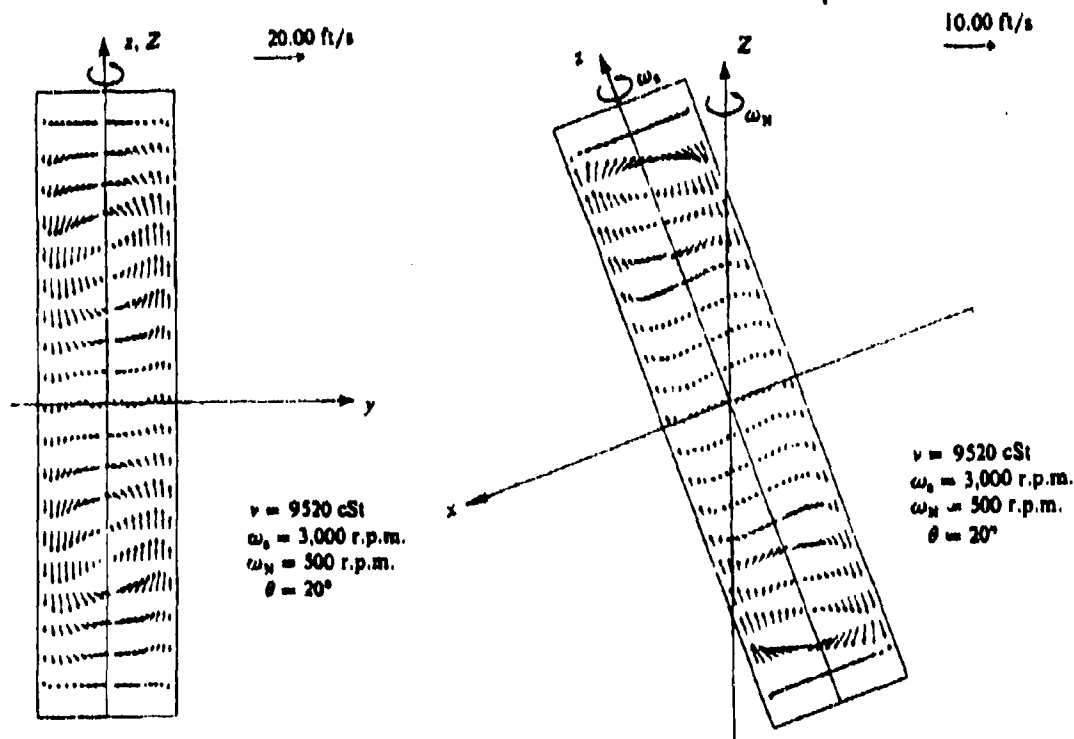


Figure 6. Induced Flow in a Closed Spinning, Nutating Cylinder (Vaughn et al. Ref. 26)

Figure 7 shows the induced flow pattern in cross sections near the chamber ends. The motion could be described as a "sloshing" of fluid particles back and forth across the chamber. Notice that the oscillations are out of phase at the ends with a nodal plane at the center of the chamber. The unsymmetrical flow pattern is accompanied by shear and pressure forces at the walls of the cylinder that yield a net lateral torque. The disturbing torque was determined from the integrated-computations to be destabilizing.²⁶ This is in full agreement with flight test observation of spinning liquid-filled projectiles.¹⁸⁻²⁵

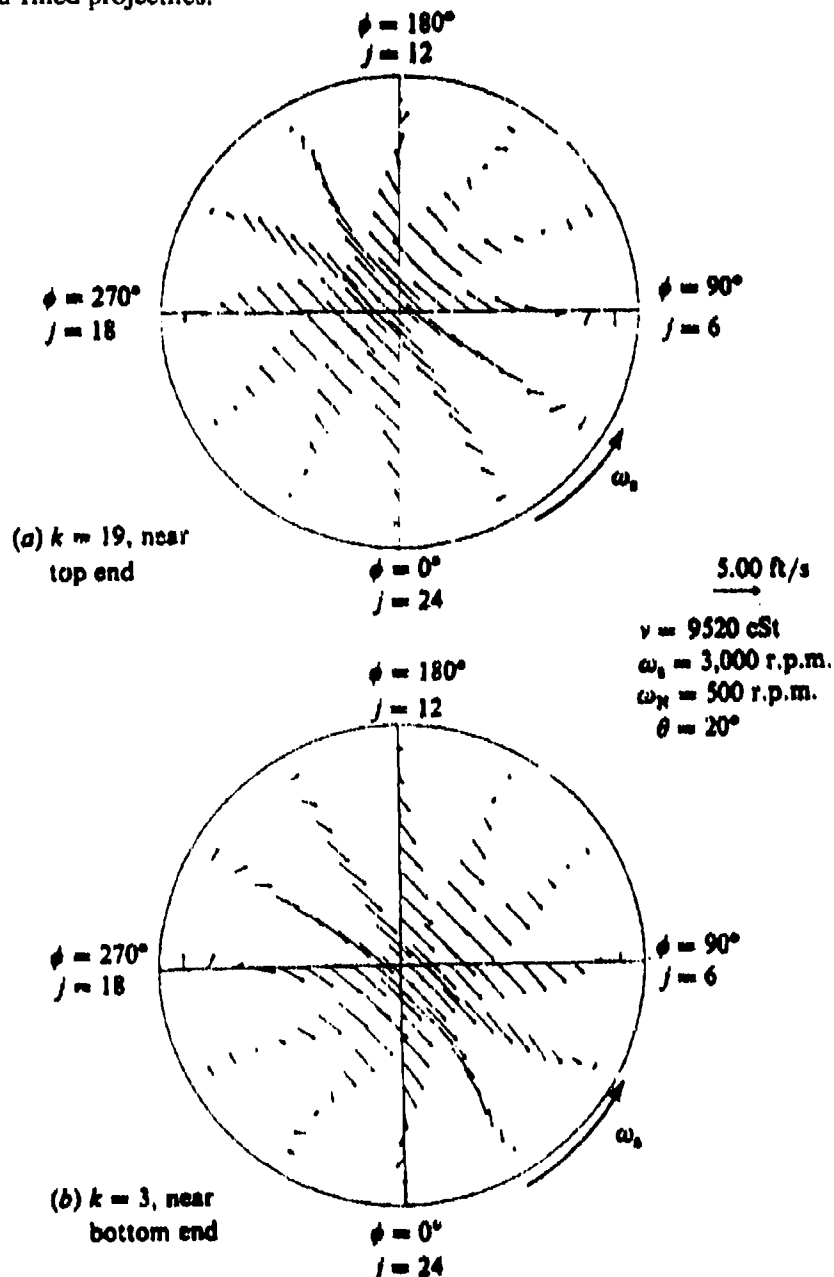


Figure 7. Induced Flow in Spinning, Nutating Cylinder (Vaughn, et al. Ref. 26)

Numerical Verification of Theoretical Results

The program of research was aimed at exploring all facets of the proposed jet gain nutation mechanism by application of every available tool. Considerable progress was made in developing numerical solutions simulating all of the physical and geometrical details of the flow in a spinning nutating rocket.

Although the program (Task 4, Planning of a Complete Numerical Model) was intended only to determine the best means to produce these tools, we made significant progress in development of a full three-dimensional Navier-Stokes computational algorithm that solves the entire time-dependent flow throughout the chamber and nozzle. The code was completed at the end of the one-year program, but has not been fully exercised in pursuit of the solutions we seek. However, it has been used to verify many of the assumptions used in the analytical work. It is discussed in detail in the body of the report.

Unlike the method used by Vaughn,²⁶ our algorithm is not limited to small a Reynolds number. It solves the full flow field with conditions that match all geometrical and physical features of an actual large rocket motor. A full three-dimensional grid generation package was also developed to simulate actual motor nozzle and grain burnback geometry. Figure 8 shows the grid, and Figure 9 shows calculated streamlines in a STAR 48 motor at 50 seconds after ignition. Notice that the solution extends throughout the entire chamber and the nozzle.

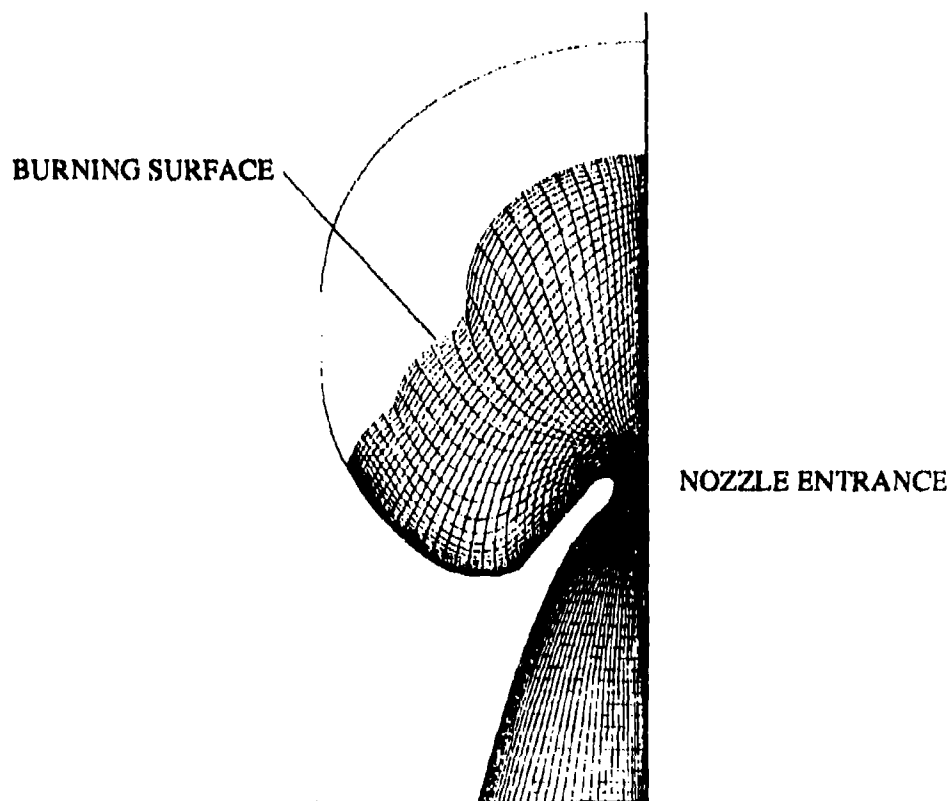


Figure 8. Computational Grid For STAR 48 Space Motor Flow

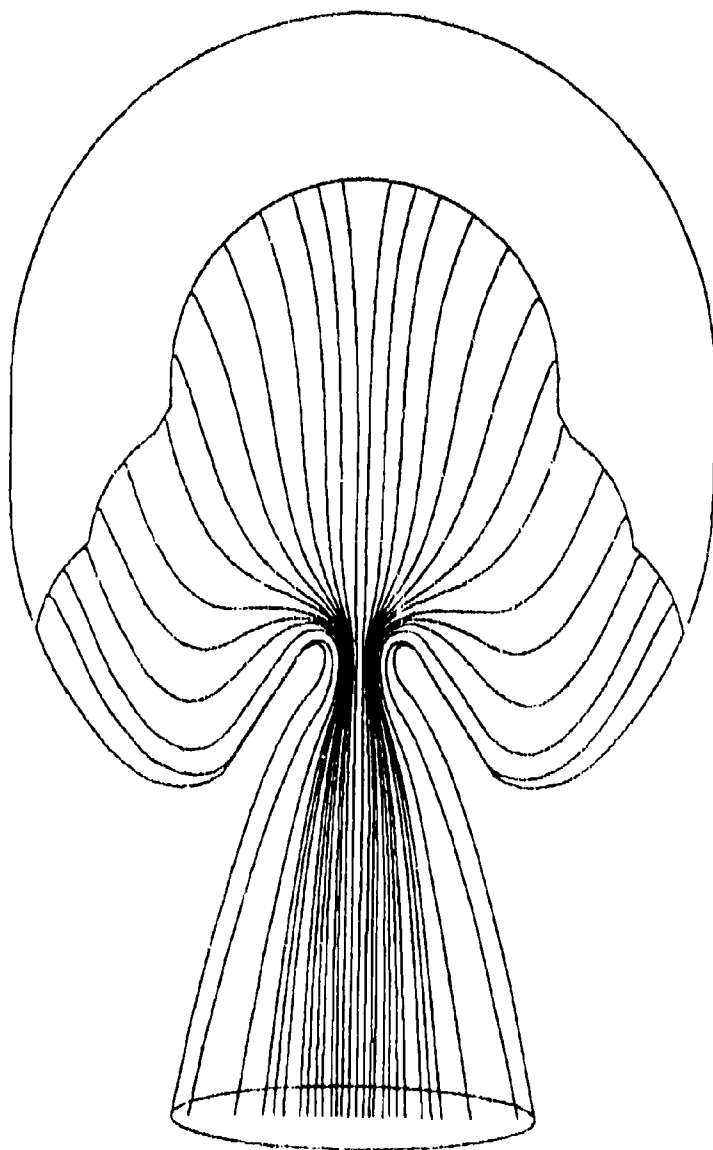


Figure 9. Streamlines in Spinning STAR 48 Motor. Navier-Stokes Solution

Experimental Verification of Theoretical Results: Cold Flow Tests

The program also supported two experimental tasks. The first was a cold flow study intended to verify the theoretical work by giving flow visualization of the fluid motion in a spinning, nutating chamber.

Figure 10 shows the experimental arrangement. Figure 11 shows one of the transparent test chambers with submerged nozzle. The inertial wave mechanism was activated by means of the two-axis spin method that is described in detail in the body of the report. It allows precise simulation of the angular velocity environment experienced by the gases in a spinning, nutating chamber. Two rotating platforms are used with their rotation axes offset at an appropriate angle. This produces an angular velocity environment in the test chamber that is identical to that experienced in a spinning, nutating rocket motor combustion chamber.

A video camera is used to record the induced-flow effects. A suspension of fine aluminum particles or dye filaments injected into the fluid make the flow oscillations visible. Some of the flow visualization recordings are presented in the video summary of the program included as part of the final report package.

A sensitive pressure transducer was also used to measure the fluctuating pressure signal associated with the wave motion. All observations support the theoretical model for the jet gain mechanism. A retrograde traveling inertial wave formed in response to the two-axis spin excitation. The waveform was not sensitive to the presence of the submerged nozzle entrance.

Experimental Verification of Theoretical Results: Hot Motor Tests

A method is needed to test chamber geometry, propellant, and nozzle modifications on the nutation jet gain factor. We developed two methods to accomplish this by means of laboratory-scale motor firings. Figure 12 shows an implementation of the first method by United Technologies (Chemical Systems Division). This device utilizes the two-axis spin method. It is arranged to measure the interaction torque directly by means of a four-component torque transducer fixed in laboratory coordinates. Testing of this hardware had not begun at the time of writing.

A second method is based on the Froude pendulum concept as shown in Figure 13. The rocket motor and an electric spin motor are suspended as a physical pendulum in a double gimbal arrangement. At the beginning of a test the pendulum motion is initiated with a known amplitude. The subsequent motion is recorded during motor burn and the nutation interactions can be deduced from this data. In order that the small nutation interactions are measurable the spin rate must be high. A direct drive was selected that produced a spin rate of approximately 1700 rpm. This required use of a large electric motor producing a power output of one Hp. The large mass of the spin motor results in a small pendulum frequency, which is undesirable in terms of resolution of the forcing effects as discussed later.

The rocket motor utilizes cylindrical propellant grains cast from actual STAR 48 propellant mixes. The grains are two inches in outside diameter and have a web thickness of 0.5 inches as shown in Figure 14. Three grain lengths (2.5, 3.0 and 3.5 inches) are used to deduce effects of chamber length/diameter ratio. The motor is equipped with a replaceable graphite submerged nozzle.

Figure 15 shows the Froude pendulum universal joint and drive motor. The nutation torques induced in the system are very small. This makes them very difficult to measure accurately. However, test data indicates that there is a definite nutation growth during the burn. The effect is small, but appears to confirm the theoretical findings of the study. Improvements in the test facility and method of data analysis are planned. These are discussed in detail in the report and are aimed at direct measurement of the nutation interaction torque.



Figure 10. Cold Flow Nutation Simulation Using Two Spin-Axis Method

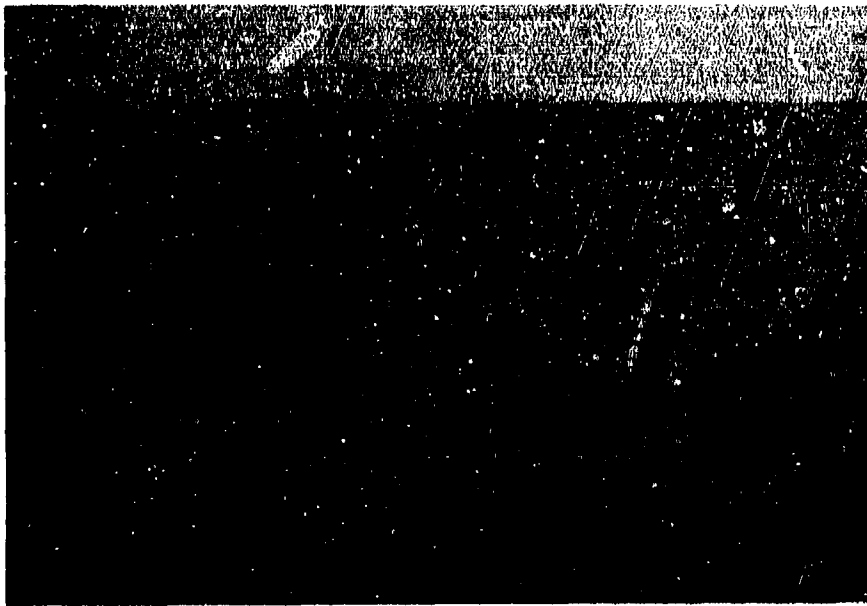


Figure 11. Test Chamber Showing Submerged Nozzle Entrance

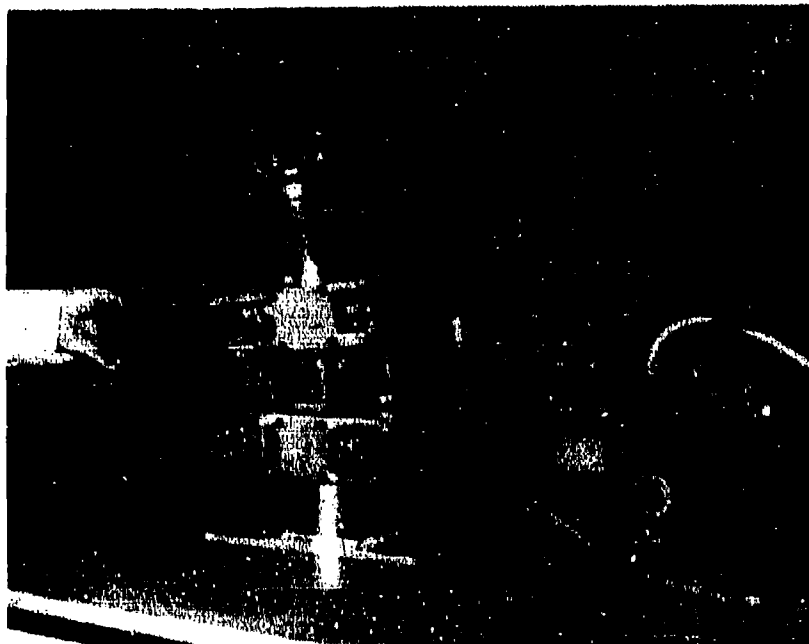


Figure 12. Two Spin-Axis Measurement of Interaction Torque (CSD, R. S. Brown)

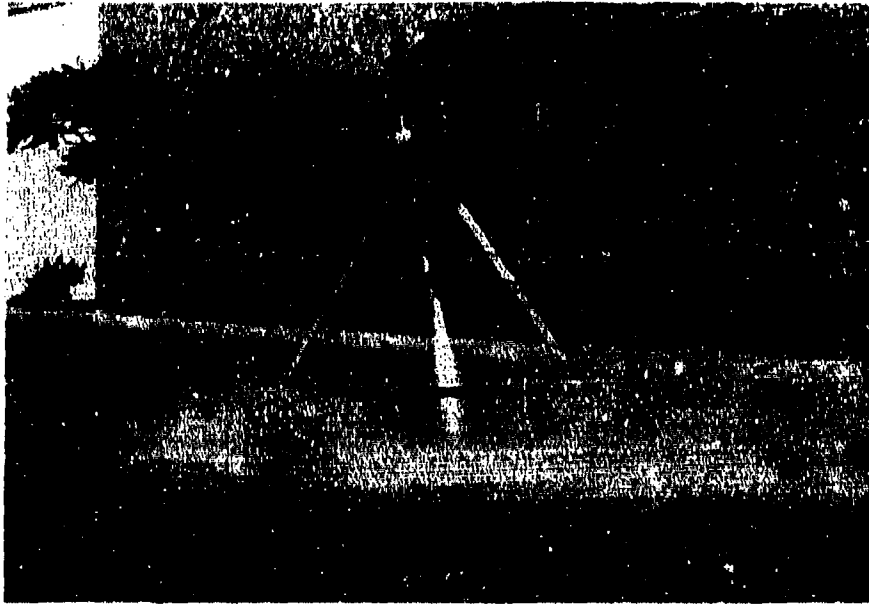


Figure 13. Froude Pendulum Nutation Instability Simulation

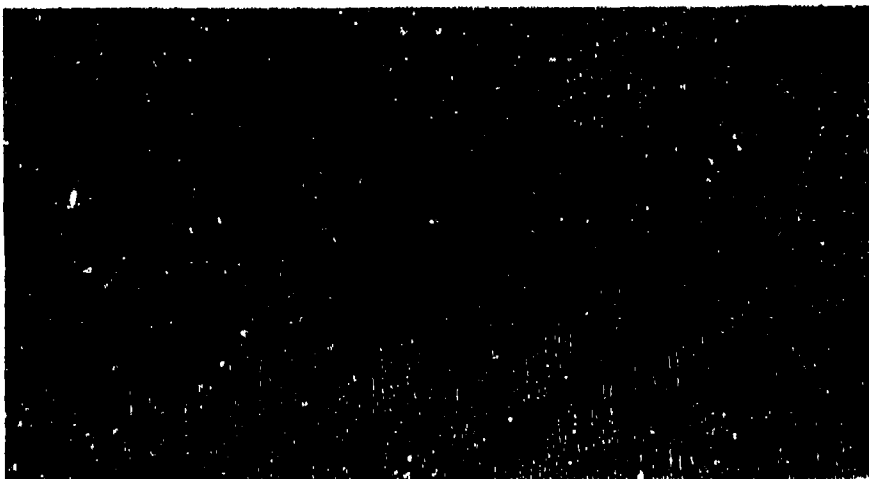


Figure 14. Two-Inch Rocket Motor and Propellant Grains

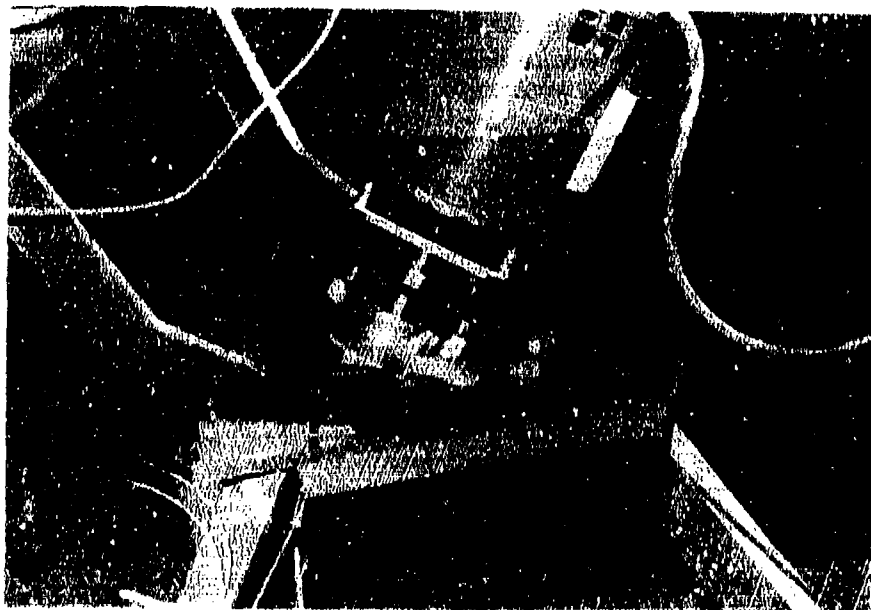


Figure 15. Froude Pendulum Pivot and Spin Motor

The Jet Gain Mechanism

The jet gain mechanism for nutation instability is defined here to be an extension of the classical jet damping effect with corrections that account for the size and shape of the motor combustion chamber. It is also necessary to introduce corrections for nozzle effects that have not been treated correctly in previous analyses. The high-speed compressible flow in the nozzle greatly modifies the gas interactions with chamber wobbling in that part of the flow field.

The proposed mechanism is consistent with every major feature of the PAM-D phenomenon discussed earlier. It is useful to summarize the points of agreement between the jet gain model and the experimental data:

- The gas motion responds to the chamber wobble in a nearly linear way. The amplitude of the induced velocity and associated pressure perturbations are directly proportional to the magnitude of the wobble angular velocity.
- The pressure forces acting at the internal surfaces of the combustion chamber are the source of the destabilizing torque. The torque has a component parallel to and with the same sense as the wobble angular velocity. Under certain conditions this torque produces a strong growth of nutation.
- The torque also has a large component normal to the wobble angular velocity. This produces a significant shift of nutation frequency similar to that observed in telemetry data.

- Since the gas motion in a spinning chamber exhibits wave-like behavior, it is enhanced when resonant conditions exist. *It is of the greatest significance that the wobbling frequency is in resonant coincidence with low-order inertial modes of oscillation at just those times in motor burn when large shifts in frequency and large changes in nutation growth or decay appear.*
- The gas dynamic mechanism is insensitive to vehicle acceleration because it is not dependent on center of mass offsets as is the slug slosh mechanism. This agrees with telemetry data showing that the nutation torque gain factor is not dependent on acceleration.

These findings lead us to the conclusion that the interaction of vehicle nutation with the combustion chamber gas flow produces destabilizing torques in the proper range to explain the observed PAM-D phenomenon. Furthermore, the timing of all key events such as multiple periods of coning growth and decay are well represented even using simple analytical representations of the jet gain effect. Numerical and experimental tasks carried out in this program support the analytical results in considerable detail.

It is also appropriate to compare the predictions of the jet gain model to data from flight tests. A parameter which best characterizes the nutation disturbing torque is the factor of proportionality between the torque and the nutation angular velocity. This has been called *Rgain* by designers of nutation attitude control systems, and we will adopt this nomenclature. Figure 16 shows the correlation for PAM-D flight vehicles at two times near the end of burn. It is clear that a straight line relationship of the form

$$\text{Nutation Torque} = R_{\text{gain}} \times \text{Nutation Angular Rate}$$

is a good representation of the correlation. The average value of *Rgain* for PAM-D vehicles is approximately 5. However, at several times during burn *Rgain* reaches much higher values as though the system passes through resonance.

Figure 17 is a plot showing the variation of *Rgain* with time through the flight of WESTAR V, a typical PAM-D vehicle. Please note the strong evidence of resonance at several times. There is a large peak at about 55 seconds that marks the beginning of the nutation growth. Lesser peaks are also present near ignition at about thirty seconds. Figure 18 is the theoretical prediction based on a simplified motor geometry that closely approximates the actual motor configuration. Although one would not expect close agreement, there is ample evidence that the theoretical model provides an amazingly good estimate of what actually occurs.

Scaling Rules for Nutation Instability

An important program task was to deduce scaling laws based on the jet gain theory for use in sizing nutation attitude control systems and for estimating possible nutation effects in new spacecraft designs. It is noteworthy that such rules are readily found for the gas flow interaction model without the need to introduce auxiliary parameters such as spring constants, damping factors, pendulum lengths, or amounts of slug accumulation that can only be determined by fitting experimental data. All parameters appearing in the gasdynamic model are real physical quantities that can be readily estimated for any system configuration.

It happens that the *form* of final scaling rules are effectively the same regardless of which of the two coning mechanisms is chosen. However, the similarity parameters involved are quite different. The torque depends on the same main system parameters. For example, motor thrust is

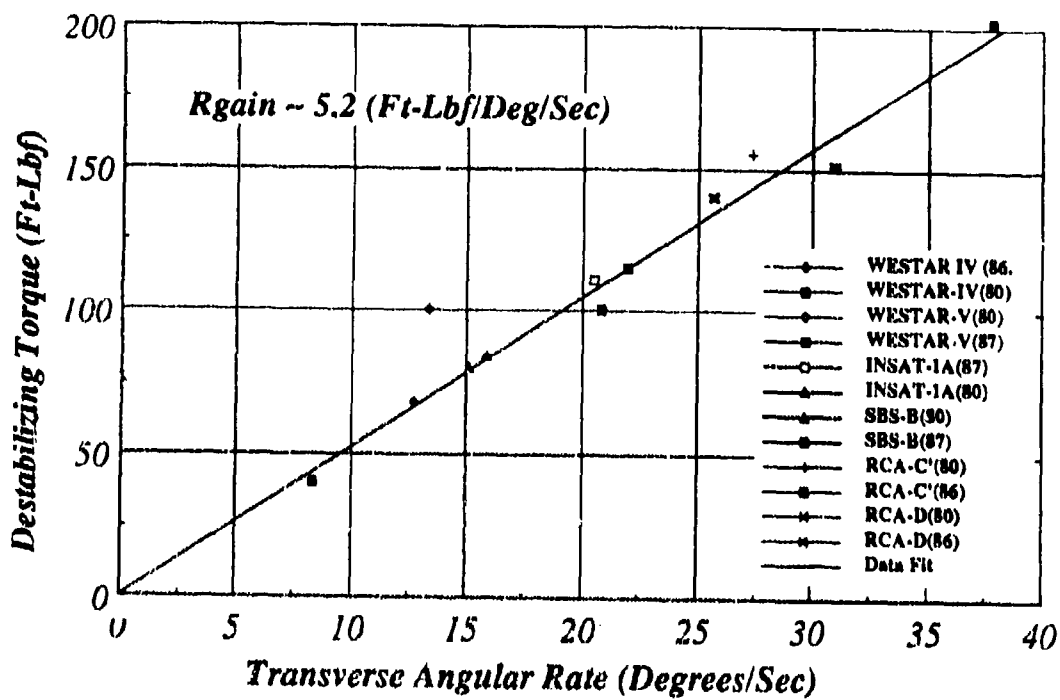


Figure 16. Linear Relationship Between Nutation Rate and Apparent Torque

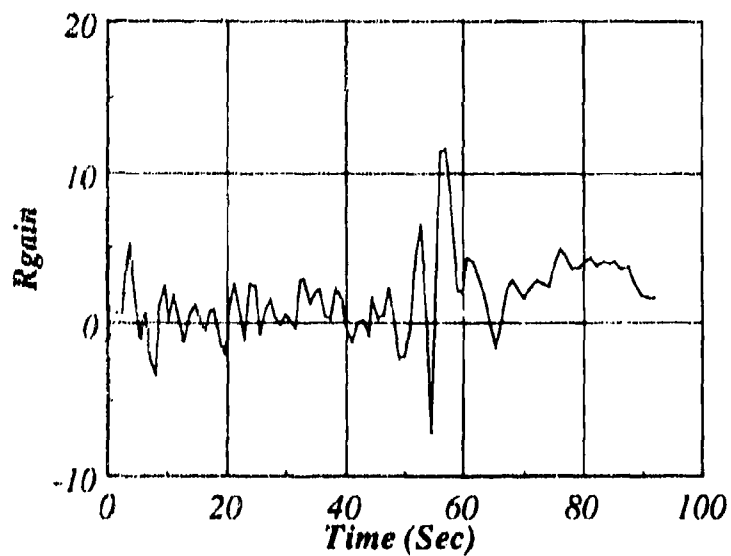


Figure 17. Rgain vs Time for Typical PAM-D (WESTAR V)

clearly important in the slag model; mass flow rate of combustion products is crucial in the gasdynamic model. Since thrust and mass flow rate are proportional, then they are represented identically in the scaling laws. The basic length variable involved in either mechanism is the motor radius. In the slag mechanism, this limits the lateral offset of the sloshing pool of liquid slag; in the gasdynamic mechanism it determines the moment arm of the unbalanced pressure forces.

Using simple dimensional analysis, and using the parameter set for the jet gain model, one finds the the disturbing moment is of the form

$$M_{flow} = R_{gain} \omega = \left\{ \dot{m} L_{cg}^2 C_T \right\} \omega$$

where ω is the amplitude of the nutation wobble angular velocity perturbation. The main parameters are the mass flow rate and the center of mass position relative to the motor exit plane. The numerical coefficient C_T depends on a set of dimensionless parameters including the spin rate and the Rossby number

$$Ro \equiv \frac{v_b}{R\Omega}$$

where v_b is the gas flow speed at the burning surface, R is the motor chamber radius, and Ω is the spin rate. The Rossby number is a measure of the relative importance of Coriolis forces in shaping the internal flow field. A small value indicates that Coriolis effects play a strong role in the

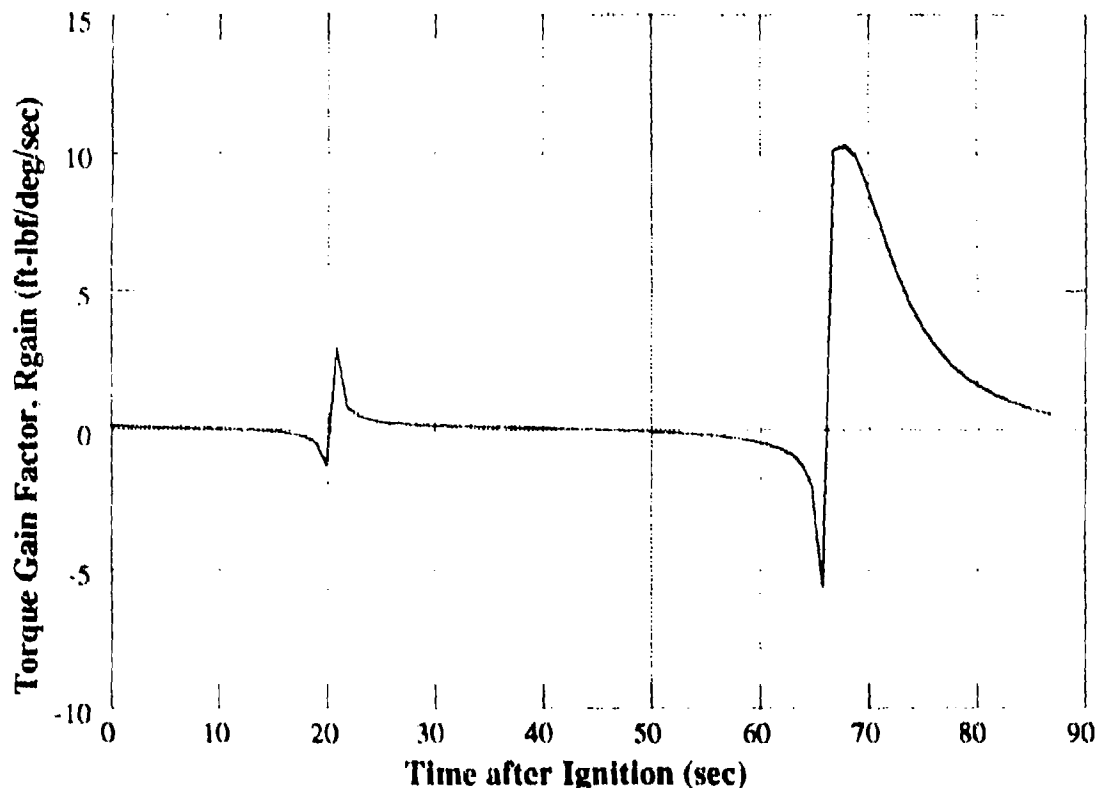


Figure 18. Rgain vs Time from Jet Gain Analytical Model

sensitivity of the flow field to nutation wobbles. It is significant that in the PAM-D and DII vehicles the Rossby number was much smaller than in earlier system that did not cone. Figure 19 illustrates the variation of Rossby number with time for PAM D (STAR 48), DII (STAR 63) and the smaller STAR 37E propelled vehicles. The latter did not experience significant coning despite the similarity of their design to the larger PAM vehicles.

The scaling relationships correlate the experimental data in a completely satisfactory way. This establishes their validity as a reliable interim means for estimating disturbing torques in new spacecraft designs.

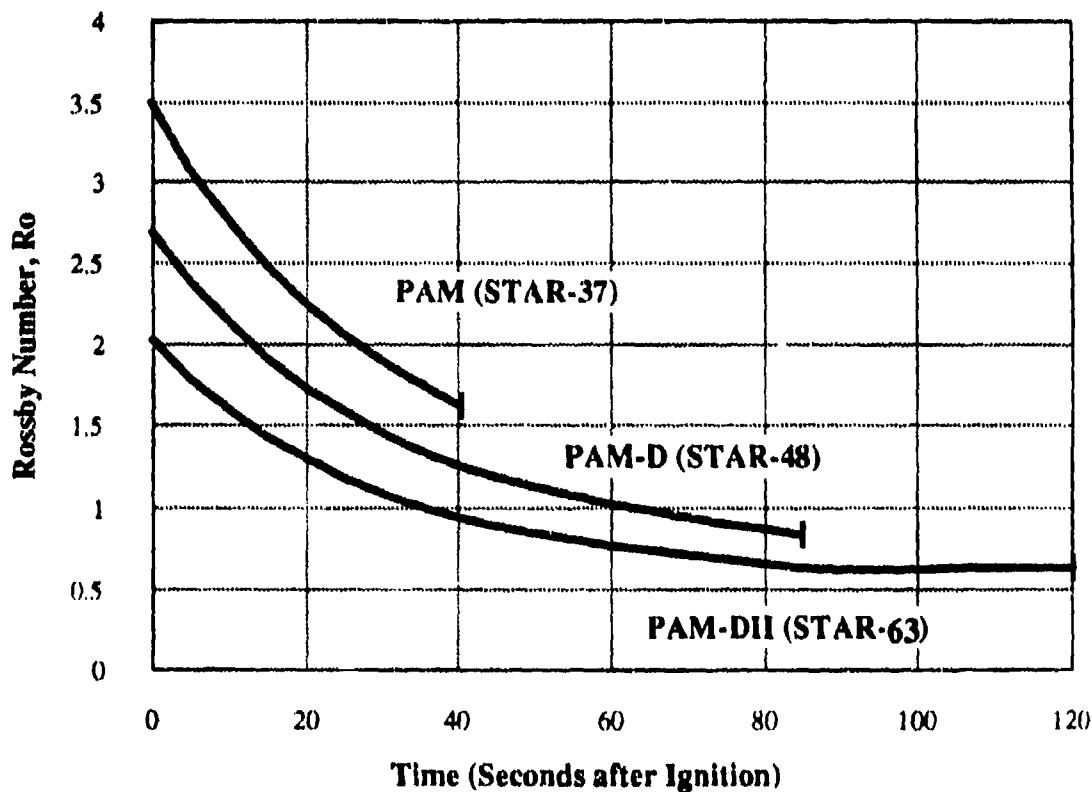


Figure 19. Variation of Rossby Number with Time for Typical Spinning Stages

Conclusions

This program of research was motivated by a need to understand, in detail, the mechanics of interaction of an internal flow in a rocket motor with the spin dynamics of a nutating vehicle. Proposed mechanisms have not been successful either in predicting coning effects in new vehicles or in suggesting corrective procedures. The problem is currently handled in the industry by use of strapon nutation attitude control systems (NCS). These are sized by means of extrapolations of earlier coning experimental data that do not take account of the physical characteristics of the nutation mechanism. This often results in NCS devices that are overdesigned, and therefore expensive in terms of both cost and loss of useful payload capability. In other cases, (for example, light-weight spinning vehicles such as the Ulysses spacecraft due to be launched in 1990) uncertainties in the coning mechanism characteristics lead to the possibility of mission failure, since in such systems there is very limited mass available for control systems that were not anticipated during the design process.

The use of an NCS system is in direct conflict with the basic design concept of spin-stabilized solid propellant upper stages. Their value is based on their simplicity and relatively low cost. The use of strapon control systems adds measurably to the cost, decreases the payload capability, and increases the possibility for failure because of increased complexity. Thus, it is imperative that the source of the nutation instability be determined, and that means for dealing with it at its source be formulated. This program has been carried out with these two needs as its primary focus.

We have found that

- There are strong resonant, wavelike interactions between the flow of combustion gases in the motor chamber and the angular motion of a wobbling spacecraft.
- These interactions have been previously accounted for by a simple theory, the classical jet damping model, that is based on an overly simplified description of the internal flow, namely that the relative motion of gases passing through the motor chamber and nozzle are unaffected by the wobbling of the vehicle.
- The magnitude of the jet damping torque predicted by the classical theory follows a time-history and exhibits similar magnitude to the torque that drives the coning instability. However, the direction of the torque vector predicted by this model is always such that it decreases the amplitude of nutation wobbles.
- If proper account is taken of the details of the time-dependent internal flow effects, then the flow interaction torque vector changes direction. Nutation growth may then occur.
- Jet damping theory applies only in small rocket systems. In large spinning space motors (such as those in used in the PAM-D and DII series), jet damping results are no longer applicable if typically high rates of spin (~ 60 rpm) are used.
- Although it is possible that slag accumulation mechanisms affect nutation characteristics, *the gas dynamic effects alone are sufficient to explain the observed nutation instability.*

- All effects predicted in detailed theoretical treatments of the problem are borne out in simple cold flow experiments. The basic wavelike nature of the internal flow response to vehicle wobbling is clearly present in flow-visualization experiments.
- It is possible to simulate the nutation effects in small-scale rocket motor firings. However, in order that measureable interaction torques are produced, it is necessary to spin the motor at very high angular rates. Also, the torque varies approximately as the fourth power of the average diameter of the combustion chamber, so motors of the order of six inches in diameter may be needed to make laboratory scale experiments useful. Tests run with two-inch motors in this program were inconclusive.
- Scaling rules have been devised that show that the nutation torque generated by the gas flow is proportional to the mass flow rate of combustion products and to the square of the distance from the motor chamber to the vehicle center of mass. The torque depends on several similarity parameters, the most important of which is the Rossby number.
- The theoretical results show that changes in internal configuration of the motor chamber, placement of the motor relative to the vehicle mass center, and axial spin rate can be used to control the tendency for nutation growth in a given system.

We have developed means for detailed modeling of the gas flow in a nutating rocket motor chamber. This method is based on advanced CFD techniques, and in its final form will allow simultaneous consideration of both the gas dynamic effects and two-phase motions of entrapped aluminum oxide slag particles. We recommend that this approach be the primary focus of future research efforts.

Experimental studies should also continue. Small scale motors using both aluminized and nonaluminized propellants will be used in continued development of the laboratory scale nutation simulation technique. However, we have concluded that the most fruitful experiments would involve full-scale motors. The simplest and most revealing flight test that could be performed at the present time would be a full-scale PAM launch with a much reduced spin rate. We feel on the basis of the work reported here that reduction of the spin rate to about half the value used currently would effectively eliminate the nutation instability problem.

INTRODUCTION

It has been known from the earliest days of modern rocketry that the flow of combustion gases through the motor chamber and nozzle interact significantly with the lateral dynamics (such as yawing or pitching deviations) of the vehicle. This has come to be known as the *jet damping* or *thrust damping* effect because under normal conditions it leads to a decay of any wobbling caused by an angular perturbation of the vehicle axis of symmetry from the flight path. However, flight data from large spinning rockets indicate that the jet damping mechanism does not always operate as expected and significant angular deviations (called *nutation* or "coning") may develop. That is, jet *damping* may become jet *driving*. The purpose of the research described in this report is to determine why simple jet damping theory seems to become less applicable as motor size increases. Interactions between the motor internal flow and the vehicle dynamics are described in detail using analytical, numerical, and experimental tools.

The propulsion driven nutation phenomenon, often called the *PAM-D coning anomaly*, was first observed about ten years ago. Nutation is a wobbling motion of spin-stabilized spacecraft that grows to an undesirable degree during the perigee propulsion maneuver. Its source is evidently related to operation of the rocket motor, since coning growth ceases abruptly at the end of motor burn. Such instability was not observed in earlier systems utilizing smaller but otherwise similar solid rocket motors and spacecraft configurations. Its late appearance is evidently related to increasing motor size as the payload mass carried in orbit-raising missions has increased. Other basic system design features have changed very little. The PAM-DII system employing a larger version of the motor (STAR-63) used in the PAM-D flights also experienced coning instability; earlier PAMs based on the smaller STAR 37 motors did not experience significant coning. There is considerable evidence that it appears only in spinning vehicles since there have been numerous flights of large solid propelled vehicles with three-axis attitude control systems in which no unusual wobbling tendencies have been detected during motor operation.

No orbit raising operations are known to have failed as a result of the PAM-D nutation effect alone. Nevertheless, the observed wobbling is at the threshold of posing a serious performance problem. Systems that carry liquid stores present a special risk due to the tendency for sloshing in partially filled tanks. The sloshing is triggered by the propulsion driven coning effect and may cause additional coning growth after motor burnout. This occurred in several PAM-D flights and led to severe coning. Also, lightweight, high-performance vehicles such as the Ulysses spacecraft to be launched in 1990 are at risk because large coning amplitudes will arise due to the low lateral moments of inertia for such vehicles.

It is clear that a complete understanding of the physical conditions and design features that promote propulsion driven coning is mandatory. Design rules that work for smaller spin stabilized vehicles appear to become inadequate as motor size increases. A major difficulty is the lack of an acceptable analytical model revealing the details of the coning mechanism. The search for such models is hampered by the difficulty of acquiring detailed data describing motor operation under spinning spaceflight conditions. All acceptable mechanisms, thus far proposed, involve some feature of the internal flow field or associated feature such as slag accumulation that are difficult to handle experimentally. Motor ground tests conducted in existing fixed-axis spin facilities using traditional testing methods cannot excite the disturbing mechanism.

Nutation is apparently triggered in flight by small residual wobbling induced during ejection from the spin platform or during the pre-ignition coast phase. The motion interacts with some feature of motor operation such that it is amplified instead of damped as conventional jet damping theory predicts. The available flight data consist mainly of rate gyroscope and accelerometer information describing the growth of the instability in body-fixed coordinates. The data are not sufficiently complete to serve as a statistical basis for critical design decisions. Hence, developers of vehicles requiring yet larger upper-stage motors are faced with difficulty in selecting spin rates, attitude control system configurations, and allowable launch tipoff wobble.

A multitude of physical mechanisms has been proposed to explain the observations. Most of these have been systematically eliminated by testing them against the flight data. The two that have not been eliminated at the present time are:

- **Slag Sloshing** - a mechanism closely akin to the liquid sloshing effects that have appeared frequently in spaceflight operations in which particulate material formed in the combustion process acts to produce a center of mass offset and a corresponding disturbing torque.
- **Gas Flow Interactions** - a variation of the jet damping effect in which unsymmetrical internal pressure forces produce an unbalanced torque with a phase relative to the vehicle wobble that leads to amplification instead of damping.

The aim of this research program is to focus on the second mechanism with the object of either eliminating it or providing support for its role as the primary source of nutation instability. It will be referred to in this report as the *jet driving* mechanism to emphasize its close relationship to jet damping.

Description of the Research Program

This work was motivated by the need to understand the origins of the PAM-D nutation instability phenomenon and to establish methods for minimizing or eliminating such instabilities. The purpose of the study is to provide quantitative evidence of the influence of the flow of combustion gases within a spinning rocket motor on the nutation dynamics of the vehicle. Emphasis was on development of experimental methods for the study of interactions of the gas flow with vehicle spin dynamics. However, analytical and numerical tools were also developed to enhance the interpretation of experimental data acquired in this and in subsequent investigations. An important feature of the program is the interactive use of the available tools. An important task was development of scaling rules to serve as an interim tool in sizing nutation attitude control systems in new vehicle designs. Another was to take the first steps toward a comprehensive numerical treatment of the gas flow interactions that can eventually be used for testing design changes.

Specific program tasks were designed to establish:

- Validity of the flow-induced nutation mechanism (*jet driving*)
- Improved description of the jet damping flow interaction

- Scaling rules for use in design of nutation control systems
- Methods for cold-flow simulation of motions in a spinning rocket chamber
- Methods for small-scale experimentation with the nutation phenomenon
- Methods for full-scale and flight test nutation experiments
- Analytical techniques for characterizing flow-induced nutation instability
- Numerical approaches for study of internal flow nutation interactions

The resulting analyses, cold flow simulations and experimental data strongly support gas flow interactions as a completely acceptable model for the observed nutation instability phenomenon. The failure of classical jet damping theory is shown to be a direct result of the size of the motor chamber coupled with the relatively slow burning rate of the solid propellants used in current space motor designs. This conclusion is applicable for the prolate mass distributions usually employed in spinning stages and for spin rates dictated by standard stability algorithms.

Status of the PAM Coning Mechanism Search

Rate gyroscope and accelerometer data from about thirty flight vehicles establish beyond any reasonable doubt that the PAM coning instability results from a dynamical interaction with some feature of the burning solid propellant rocket motor. A set of about twenty proposed mechanisms has been systematically reduced to the two described schematically in Figure 2. These mechanisms represent two totally different ways in which the spacecraft dynamics can interact with the propulsion system.

Of these, the one favored by several analysts is the *slag sloshing* model, which assumes that aluminum oxide slag produced in the combustion process accumulates during motor burn in a liquid pool and sloshes in response to the wobbling spacecraft. This proposed mechanism has found much support because it is similar to familiar instabilities observed in previous flight experience. Nutation driven by sloshing of liquid stores or by mechanical vibration of elastic structures has been a common problem in spin-stabilized satellites. It is natural to attempt to extend this experience from coasting flight into the PAM-D problem which afflicts the powered phase of flight. In effect, the slag sloshing as applied to powered flight generates an offset in the mass center with resulting thrust-induced torques as shown in Figure 1. If the offset has the correct phase relative to the angular velocity vector representing the lateral motion, the system may be unstable to small angular disturbances present in the vehicle before ignition. In modeling slag sloshing, it is necessary to incorporate some form of restoring force and damping. Several analyses have been completed using various combinations of pendula and spring-dashpot models.^{1,2} Such models can be made to fit the experimental data by proper selection of the adjustable parameters. Some very sophisticated experimentation including simulated slag motion in a nutating chamber and scale model flight testing has been carried out to verify this mechanism, but the results are inconclusive. They have yet to be published in the open literature.

It is quite difficult to construct rational fluid-dynamical models describing the slag motion because of the complex geometry, unknown physical properties of the material as it occurs in a burning rocket, and amounts of slag accumulation. Data from ground-based spin motor tests are not a reliable indication of slag accumulation because the effect of axial acceleration is missing. Characteristics of the material in its mobile state during burn must be deduced by examination of solidified fragments remaining in the motor case after the test. Some useful information may come from real-time X-ray cinematography.

The second remaining mechanism, the *jet gain*, *jet driving*, or *gasdynamic* coning effect, is related to interactions between the vehicle dynamics and the motor internal gas flow. Again, a kind of sloshing motion in response to vehicle angular motion is the basis for the mechanism and development of an asymmetrical flow field must be considered. This produces, in effect, a small deviation in the direction of the exhaust flow and an associated unbalanced side force. It is the unsymmetrical pressure distributions produced in the combustion chamber and nozzle, especially around the submerged nozzle entrance, that create the disturbing torques in the jet gain mechanism. Unfortunately, development of a quantitative mathematical description requires solution of a very complex problem in gas dynamics that involves several elements not studied previously. An Air Force sponsored study¹ led to some progress in generation of the necessary solutions. A destabilizing effect was identified that agreed qualitatively with experimental data without arbitrary adjustment of the physical parameters. Other work on flow interactions^{34, 35} based on less complete representations of the system fluid mechanics did not lead to a source of nutation driving associated with the internal flow.

The present work is intended to aid in resolving the mechanisms issue so that further progress can be made in eliminating coning at its source. Emphasis is on development of experimental methods that can be used for studying a variety of driving effects. However, only a limited number of tests could actually be accomplished in the course of the one-year program. Thus, considerable attention was paid to development of interim methods for the practical treatment of the problem. One such task led to a set of scaling laws that can be used in estimating coning behavior of new spacecraft configurations.

The Need for Scaling Rules

In order to establish an organizing framework within which one can deduce the nutation instability scaling laws, it is necessary to choose a set of parameters associated with a definite physical model. The latter of the two models just described, the gasdynamic model, is chosen as the basis for the scaling system described in this paper. A compelling reason for this choice is that it is not necessary to introduce auxiliary parameters such as spring constants, damping factors, pendulum lengths, or amounts of slag accumulation that can only be determined by fitting the experimental data. All parameters appearing in the gasdynamic model are real physical quantities that can be readily estimated for any system configuration.

It happens that the structure of the final scaling rules is the same regardless of which of the two coning mechanisms is chosen. Ultimately, the same basic parameters appear in each of these in slightly different form. For example, motor thrust is clearly important in the slag model; mass flow rate of combustion products is crucial in the gasdynamic model. Since thrust and mass flow rate are proportional, then they are represented identically in the scaling laws. The basic length variable involved in either mechanism is the motor radius. In the slag mechanism, this limits the lateral offset of the sloshing pool; in the gasdynamic mechanism it determines the moment arm of the unbalanced pressure forces.

The scaling relationships will be shown to properly represent the parametric relationships implied in the experimental data set. This establishes their validity as a reliable interim means for estimating disturbing torques in new spacecraft designs. It does not constitute proof of the validity of any particular mathematical model. There are surely other phenomena not yet investigated that could give rise to similar disturbing torques. Unfortunately, the mechanism controversy can be resolved only if an experimental program is devised that can adequately simulate the spinning propulsion maneuver. A strong motivation for the analysis given here is the need to establish guidelines for the rational configuring of such experiments. Any testing with full-scale space motors is a costly endeavor, and must be approached with the best possible understanding of the dependence of the nutation torque on the physical variables.

The Need for New Experimental Techniques

In a situation as complex as that encountered in the nutation instability effect, analytical models for quantitative assessments, for data interpretation, or for design purposes may not be reliable. It is vital that experimental techniques be developed both for verification of models and for characterizing a new system quantitatively.

Questions regarding the use of small-scale experiments must be addressed. Full-scale system tests are exceedingly costly. There are many other reasons equally compelling. It is notoriously difficult to secure detailed information concerning the internal workings of a full-scale solid rocket motor. It is difficult or impossible to implement appropriate instrumentation. Most information is deduced from measurements made external to the motor chamber. Full-scale tests of satellite spin motors are performed in facilities that do not provide the correct physical environment for simulation of nutation effects on the internal flow. Tests conducted in fixed-axis spin test facilities do not produce data of direct use in the nutation problem. It is necessary to simulate the angular velocity environment experienced during wobbling flight to activate the feedback mechanism that produces coning.

An important task in this study was to establish useful procedures for securing the needed data from scale motor testing and from flow visualization experiments. It is also anticipated that full-scale verification will be needed in the future, therefore test procedures to yield the necessary information were studied.

The Need for a Complete Numerical Analysis

In order to fully understand how the gas flow interacts with the vehicle motion, it is necessary to treat a very complex geometry containing a compressible viscous gas. Although our analytical models give invaluable insight into the workings of this flow, it is necessary to utilize numerical methods if a truly complete and quantitative result is required.

The effort devoted in this program to the development of a comprehensive numerical tool for analysis of the interactive flow field in a spinning solid propellant rocket combustion chamber was considerably beyond that originally planned. We did this because we found that such analytical capability does not presently exist. The full Navier-Stokes treatment of a realistic spin motor internal ballistics problem gives us the ability to determine, in detail, the nature of the flow when it is perturbed by motion of a spinning, nutating spacecraft. This, in turn, provides a method for accurately determining the reaction forces on the spacecraft and the resultant driving or damping of nutation wobbling. The program accommodates the complex flow conduit geometry typical in an upper-stage space motor. It has been designed to work in a realistic range of Reynolds numbers and represents the full flow field continuously from the

propellant burning surface, through the burning port, into the nozzle entrance region, and through the supersonic part of the nozzle expansion cone. The only physical effects not represented are turbulence and detailed multiphase near-surface chemical reactions, which we do not feel play an essential role in the coning problem. Eventually, an appropriate turbulence model will be added to verify this assumption.

Plan of the Report

The report is intended for use by individuals with a very wide spectrum of backgrounds. Since it is expected that the most interested readers will be spacecraft dynamicists and designers with little or no background in fluid dynamics, considerable detail is provided in the sections on the modeling of motor internal flow effects. In order that the findings of the study can be easily accessible to those interested in the physical descriptions, rather than the detailed mathematical developments and descriptions of experimental facilities and data reduction methods, an executive summary is provided at the beginning of the report. A video presentation describing the nutation instability problem, the experimental results, and the origins of the jet driving mechanism in animated form is also available as part of the final report package.

The report consists of a comprehensive description of the coning phenomenon and its analysis from the viewpoint of internal flow field interactions. The experimental characteristics of the nutation problem as represented by telemetry data from about twenty flights are reviewed briefly to emphasize certain important features. There is much guidance in the flight data in our search for the source of the nutation driving torque.

Since the nutation problem is mainly one of spinning body dynamics, a complete section is devoted to a careful analysis of the motion including effects of contained flowing gases. This clearly establishes the manner in which interactions between the internal flow of combustion products and the vehicle motion take place. This provides guidance for the analyses to follow by indicating the parts of the system that must be adequately modeled. It shows in detail how motion of the gas is affected by wobbling and spinning of the vehicle and how the perturbed flow affects the growth or damping of the nutation disturbances.

Analytical and numerical methods for resolving the details of this complex flow environment are developed in detail. A very detailed discussion of the jet damping phenomenon is presented since it yields valuable clues regarding flow interactions. Furthermore, it clearly establishes the range of applicability of current jet damping models. Of great importance is the demonstration that jet damping theory does not apply in large spinning vehicles such as the PAM-D class spacecraft.

Much of the fluid dynamics chapter is devoted to providing a correct understanding of the jet damping gas flow model. The jet damping model used previously to represent flow interactions is shown to be a completely inadequate representation and does not properly reflect spin and motor geometry effects. Improved understanding is built by systematically analyzing the flow field dynamics by means of increasingly more complete models. These provide valuable insight into the complex time-dependent gas response to vehicle wobbling. The results are then interpreted in terms of the effects on vehicle dynamics and a comprehensive instability mechanism emerges. The origins of the jet driving effect can be found in the omissions and constraints built in to the classical jet damping model.

As one attempts to produce a complete representation of the three-dimensional, time-dependent, compressible viscous flow in the wobbling motor chamber, it becomes obvious that conventional analytical methods cannot be used to generate quantitative design information. Thus, considerable work was done on a numerical approach to solving the complete problem.

A program task was aimed at setting out the criteria for a complete numerical description. Since we believe that this is a vital part of the problem, we devoted much more effort on it than originally intended, and the result is a full three-dimensional Navier-Stokes finite difference algorithm and grid system for realistically representing the flow in a spinning, nutating rocket. The numerical approach and some of the initial findings are discussed. Obviously this represents a major departure from conventional methods for treating rocket flows, especially spinning ones. We expect to continue development of this extremely promising approach in future programs.

An important problem is the practical one of application of the results of the study in making spacecraft system design decisions. Simple scaling rules are developed that do not require extensive computations. These are intended to serve as a useful tool for determining nutation attitude control system requirements and for estimating expected nutation characteristics of new vehicle/propulsion system configurations.

Finally the results of the cold flow and laboratory scale nutation instability experiments are described. A new method for studying flow interactions using inexpensive solid propellant motors of convenient size is demonstrated. These experiments permit testing of both the scaling rules and the analytical results. Weaknesses are exposed and areas in which further work is required are identified. Methods for full-scale tests are proposed. Ultimately, full-scale verification will be required using either appropriately instrumented flight tests or ground tests in modified spin facilities.

The last section consists of brief interpretations of the results of the entire study and a set of practical guidelines for their application in the spacecraft design process. The need for continued development of experimental and numerical techniques is emphasized.

(Blank Page)

DESCRIPTION OF THE PAM-D PHENOMENON

Overview

In this section, we present a comprehensive discussion of information contained in the telemetry data from about twenty flight articles of the PAM-D, SGS-II and PAM-DII spacecraft types. Emphasis is on the features of the data indicating a consistent and repeatable phenomenon. Each feature is carefully assessed in order to extract all information that gives us hints regarding the origin of the nutation instability phenomenon. On the basis of this information, we construct a set of requirements that must be met by any proposed nutation instability mechanism. Later in the report we will test the gas dynamic interaction mechanism to see if it meets the criteria established by these requirements. It will also be useful to examine other proposed mechanisms in this regard to aid the reader in his search for a viable nutation mechanism.

History

For the benefit of readers not familiar with coning, this section begins with a short history of the PAM-D problem. PAM is the acronym for the McDonnell Douglas *Payload Assist Module*. The system consists of a solid propellant rocket motor, a payload attachment structure, and a spin table/separation module. It is designed to accept a wide variety of communication satellite payloads, and is used for ascent to geosynchronous altitude. The solid rocket space motor, FLEX PAM-D, STAR 48 is manufactured by Morton Thiokol, Elkton Division, and is designed for ready off-loading of propellant by machining the propellant grain. Figure 20 shows a typical PAM-D emerging from the space shuttle payload bay. Figure 21 is a cutaway illustrating the propellant grain configuration and submerged nozzle geometry.

The motor design increases payload by elimination of a gimbaled nozzle actuated by a complex and expensive attitude control system for trajectory control. Instead, spin stabilization is used to minimize dispersion during orbital transfer. A spin platform rotates the vehicle at a preselected rate before it is ejected from the carrier stage by a set of springs mounted in the separation module. Angular rates have ranged from 40 rpm to over 80 rpm. The vehicle coasts away from the Space Shuttle (or other carrier stage), and the motor is ignited when the proper separation distance is reached.

This technique has been used for many years on a variety of upper-stage solid rocket propelled spacecraft without any apparent difficulty. However, an unexpected problem appeared in the first PAM-D flight and has recurred with varying severity in all PAM-D operations and more recently in the larger PAM-DII spacecraft utilizing a larger version (63-inch diameter instead of 48 inches) of the STAR 48 solid rocket used to propel the PAM-D missions.

Another STAR 48 propelled system was the tandem SGS-II satellite launchers. This vehicle employed a nutation control system to suppress coning. Of great interest is data from the first-stage burn in which coning growth was too small to activate the nutation attitude control device. These data show the effect of a much more massive spacecraft with larger lateral moments of inertia (about four times larger than a typical PAM-D). The characteristics of the coning growth were nearly identical to the PAM-D in terms of the torque gain factor. This demonstrates insensitivity to vehicle acceleration and also to the wobbling frequency (precession frequency) that characterizes the coning motion.

Spin stabilization of these unguided stages is employed mainly to minimize the effects of mechanical energy dissipation on the flight stability during ascent. Such dissipation tends to



Figure 20. Launch of PAM-D Spin Stabilized Upper Stage

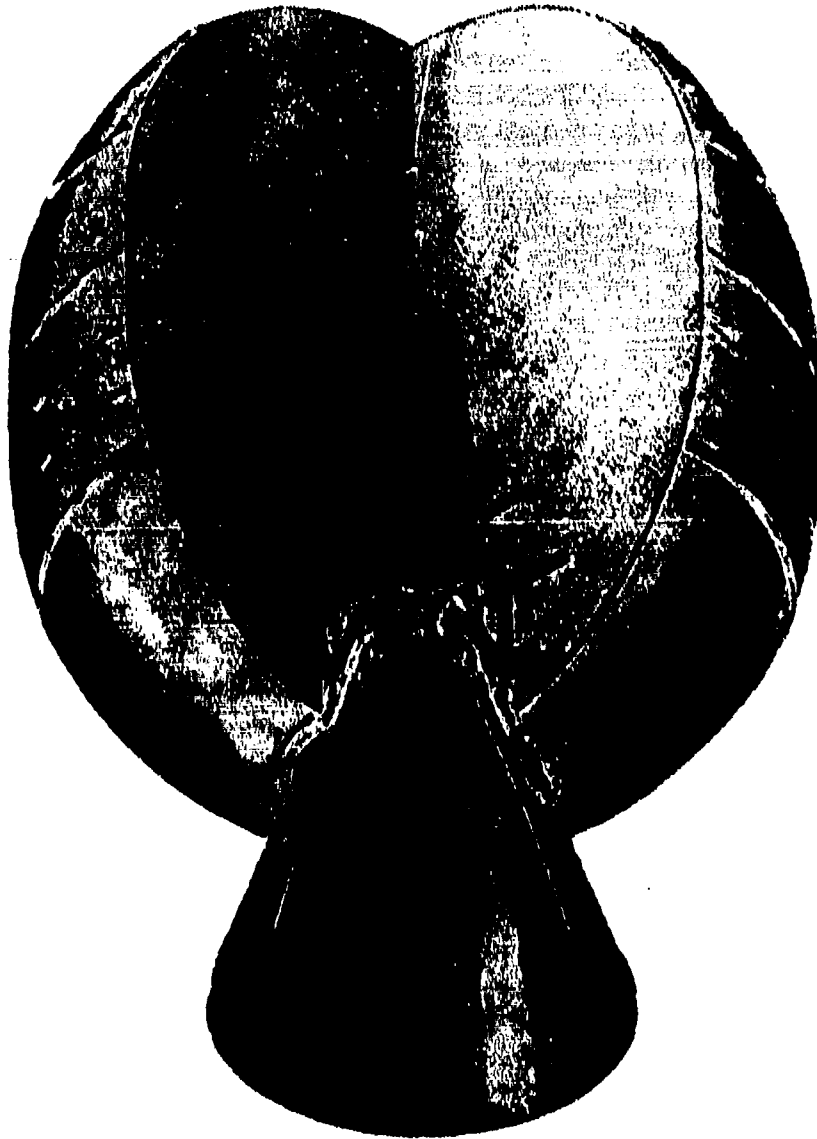


Figure 21. Internal Configuration of STAR 48 PAM-D Rocket Motor

induce tumbling of prolate (elongated) spinning bodies. Spin also is relied upon to reduce dispersion due to misalignment of the rocket motor subassemblies. Nevertheless, the nutation instability phenomenon occurs during operation of the solid rocket propulsion system then abruptly stops growing at the end of the motor burn. This was surprising because interaction between the coning and the gas stream was believed to create only a *decay* of wobbling: the "jet damping" effect.

The slight wobble imparted to the spacecraft before motor ignition by the separation system is at first partially damped out and then enormously amplified during the last ten seconds of the rocket motor burn. This wobbling motion is often referred to as "coning" instability, since to an observer fixed in space it would appear as a rotating angular deviation of the spacecraft and thrust axis from the flight path direction.

To visualize the motion, the reader might consider the precession of a spinning top or gyroscope, or the flight of a wobbling football. However, the PAM spacecraft wobbling is not caused by the same physical mechanism that drives the forced precession of a gyroscope. In other words, it is not a simple forced (or free) precession, even though the natural wobbling frequency seen in the flight data is very nearly the free precession frequency. The latter is a function of the spacecraft mass distribution. The correct technical term is "nutation instability" because the nutation angle increases with time. The words "coning," "wobbling," and "nutation" are used interchangeably in referring to this phenomenon throughout this report.

Figure 1 describes the type of motion that is observed. The final value of the nutation angle θ , the "cone angle" (actually the cone *half*-angle), can become almost 20° at the end of motor firing in some missions. Coning degrades performance by:

- Wasting motor impulse as the vehicle flies in a helical path
- Overtaxing the post-burn attitude control system
- Requiring use of a nutation control system that should be unnecessary since spin stabilization is employed

Note that coning can afflict *any* spinning propulsion system. The severity of the problem depends on a number of factors related to geometry, spacecraft mass properties, and burn time. Clearly we must understand precisely the dependence of coning on design and environment if we are to avoid catastrophic mission failures in future systems.

The coning behavior burdens the post-propulsion attitude control system with suppression of residual wobble as already mentioned. Further, coning degrades performance of the rocket motor. For example, a cone angle growing exponentially to 20° during the final 30 seconds of the motor run dissipates about 1% of the delivered impulse because of the pinwheel effect. Since great effort and expenditures are made in rocket motor development to *gain* a 1% increase in impulse (say about 2.5 seconds of specific impulse), this waste is intolerable. At present the problem is countered by use of strap-on attitude control devices (Nutation Control System)²⁸. This is an expensive and inefficient approach and is contrary to the principles of upper stage propulsion design. Modern design emphasizes reduced weight, simplicity, reliability, and relatively low cost. The physical origins of coning must be understood in detail so that it can be avoided in the design of future spacecraft systems. This is especially important because PAM-D or similar flexible launch vehicles must accommodate a wide variety of

spacecraft configurations. Sensitivity of coning to variations of system mass properties and geometry must be established.

Relationship to Classical Jet Damping

The use of spin to stabilize a rocket vehicle is a familiar stratagem. Possibly the first such application was in the Hale rocket developed by the American designer William Hale as described in the 1862 U. S. Ordnance Manual. These missiles used canted nozzles to impart spin. Some bombardment rockets used (mainly by the Germans) in the Second World War used a similar system. These devices used "fast spin" for the same reason it is used in rifle projectiles to produce gyroscopic stability. Slow spin is also frequently useful in unguided rockets since it tends to cancel the effects of misalignments of the nozzle exit cone or the propellant burning surfaces, etc. The spin rate for the PAMs is selected to minimize instability of the prolate spacecraft caused by mechanical energy dissipation within the structure. The latter can be caused by relative motion of loose parts (such as the whip antennae in the Explorer I vehicle) or by sloshing of liquid stores. The jet damping effect was expected to stabilize the craft during the rocket motor burn. However, as the flight data show, this design principle must be in error for these missions since jet damping either does not work in the expected way or is always overwhelmed by the coning source mechanism.

The propulsion system is the prime suspect as the source of the energy which drives the nutation instability. The growth of the disturbance either ceases abruptly or changes radically at burnout. This seems contrary to prior experience with spinning rockets. It has always been thought that the flow of combustion gases damps vehicle wobbles by the familiar jet damping mechanism, and there is an impressive body of data to back this belief.

Of great significance is that the interaction torques predicted by jet damping are of the same magnitude as those that drive the coning. That is, if the direction of the jet damping moment is changed, the result is almost equivalent to what is actually observed. This proves that flow interactions are sufficiently large to create the instability. Therefore, jet damping will be subjected to careful scrutiny in this report. Experimental methods were developed to study the jet damping mechanism and associated flow driving effects.

Most current models of jet damping are adaptations of some rather straightforward calculations made, apparently, before World War II. All are based on a very simplistic picture of gas flow in the combustion chamber. Much of the jet damping tradition comes from the trajectory analysis of small tactical rockets. It was always considered one of the less important effects to be accounted for in trajectory optimization, and hence was never seriously analyzed. Some of the words of the investigators in this regard are quite revealing:

"... the system is essentially all rotating at the same rate of rotation as the metal parts. There may be some variation from this due to the flow of gas inside the rocket motor. However, one cannot take account of this without a knowledge of the flow conditions inside the motor, which are *likely to be very complicated* (emphasis ours). In any case, it is doubtful if such internal flow contributes more than a very minor variation of the simple picture."³

These words accurately describe the expectations of those responsible for the jet damping calculations in current mission analysis. The expectations concerning the complexity of the flow are also correct, as will be discussed later. Perhaps the difficult fluid dynamics problem thus posed has discouraged prior study since the simpler jet damping model seemed adequate,

and indeed it has been for some vehicles. We will see that jet damping theory as when applied to spinning motors especially when a critical chamber size is exceeded.

The main assumption in simple estimates of the sort used today in jet damping analysis is that the flow is *steady*; it is also often assumed that the flow inside the motor is one dimensional and axial.^{3,9} These simplifications may be appropriate in the tactical rocket situation, but doubt about their applicability to the large, nearly spherical spinning rocket motors used in modern orbit-raising maneuvers is what motivated the work presented here.

Careful study of flight data taken many years ago in spinning vehicles makes it clear that nutation instability may have occurred then, but in a mild way. Flight data from early Scout missions are interesting. An example is discussed in the paper by Thomson and Reiter⁵ describing an analysis of the Explorer VI launch. It is clear that there was evidence of some trouble with the simple jet damping model. Note is made of a "... *transient observed at the end of burning* ..." (that) is not predicted by the theory." Since the burning time for this spinning motor (The ABL X-248 A4) was relatively short, it is clear that interactions that depend on the duration of the disturbance might not produce striking effects. It is possible that the more troublesome PAM disturbances are caused by the same mechanism responsible for the Explorer VI transient. This mechanism is enhanced by the relatively longer burn time of the STAR 48 motor.

The first to suspect the possibility of fluid dynamic interactions were analysts at NASA Goddard Spaceflight Center. The writer recently noticed that J. F. McGarvey³⁰ anticipated, conceptually, much of what has finally come forth in detailed fashion in this study. An impressive list of other candidate destabilizing mechanisms have also been posed and subjected to intense study. Progress in the fluid mechanics modeling has been slow because several new aspects of rocket motor gas dynamics required detailed exploration.

Summary of Main Features of PAM-D Telemetry Data

The observed instability is characterized by the development of a wobbling motion of the spinning spacecraft during the latter part of the motor burn, usually during the last 10-15 seconds. The final nutation angle θ (see Figure 1), between the original spin axis direction and the longitudinal axis of the spacecraft grows during the final third of the motor run.

The initial wobbling is a classical free precession excited during the tipoff process from the spin platform. The spacecraft is ejected by springs and always emerges with a small lateral wobble (usually less than 1 degree/second). The nutation continues throughout the pre-burn coast phase with nearly constant amplitude. Growth or decay during coast may occur in spacecraft carrying liquids or parts that can slosh or vibrate, respectively, relative to the structure. The characteristics of the wobbling change noticeably at ignition of the rocket motor. During the early phases of the burn, the nutation is damped, as expected, by the jet damping mechanism, although the decay rate is not as high as that anticipated on the basis of standard jet damping theory. About midway through the motor burn, the effectiveness of the jet damping appears to diminish rapidly, although the theory indicates that the decay rate should markedly *increase* as the vehicle center of mass moves forward and the combustion chamber length increases during the latter half of the burn.

During the last 10 - 15 seconds of the motor run, the nutation perturbations grow rapidly. The motion can be described as a growing oscillation of the pitch and yaw angular rates as shown in Figure 22. To an observer rotating with the spacecraft, the angular velocity perturbation would appear to be a disturbance moving relative to the vehicle in a direction *opposite* (retrograde) to the axial spin. Figure 22 is typical rate gyroscope telemetry data showing this

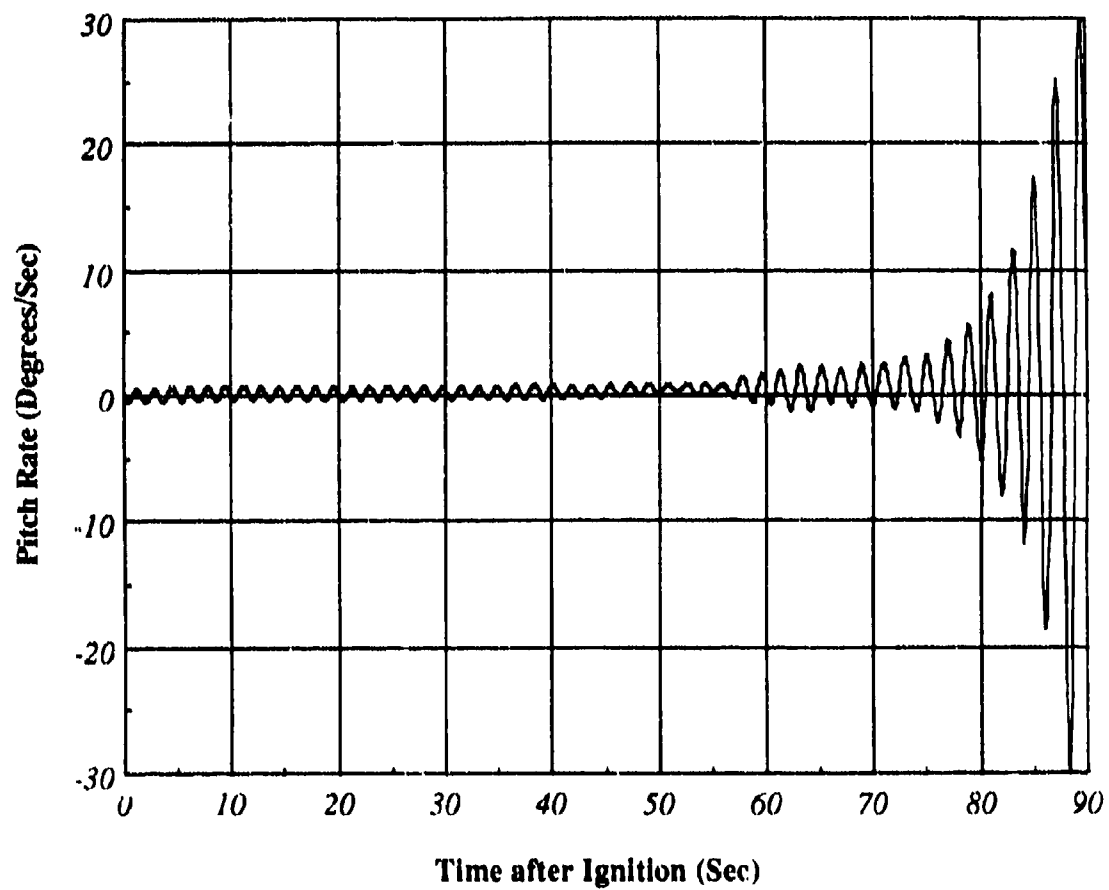


Figure 22. Body-Fixed Pitch Angular Rate vs Time for Typical PAM-D

motion. The apparent retrograde direction of rotation of the signal (the yaw signal always leads the pitch by almost exactly 90°) is clearly evident. This feature severely limits the array of possible coning sources. Mechanisms related to thrust misalignments, non-uniform burning of the propellant, or offsets of the center of mass cannot generate the observed motion.

Self-Excited Oscillations

Analysis of the flight data shows that the apparent destabilizing moment is proportional to the transverse component (the projection of the angular velocity on a plane perpendicular to the axis of symmetry) of the angular velocity vector. This clearly shows that the disturbance is created by a closed-loop driving mechanism in which the feedback of the spacecraft motion activates the instability in the manner of a self-excited oscillator. Figure 23 shows the proportionality of the driving torque to the wobble amplitude. The slope of this curve is a measure of the strength of the feedback. We will refer to this as the disturbing torque gain factor, often called *Rgain* in the coning literature. *Rgain* is defined to be the ratio of the component of the apparent disturbing torque, *M*, parallel to the nutation angular velocity perturbation to the magnitude of the nutation perturbation, ω' . Thus,

$$Rgain = \frac{M \cdot \omega'}{|\omega'|^2} \quad (1)$$

For the PAM-D vehicles this factor is of the order of 5 during the most rapid growth at the end of burn. A positive *Rgain* corresponds to a growing nutation disturbance. A negative value indicates nutation decay. The peak value of *Rgain* may be much larger as examination of the data will show. Also, the maximum does not occur during the prominent nutation growth near burnout, but rather much earlier. This is at about midburn for a typical PAM-D vehicle. The peak magnitude may be many times larger than the average found by averaging the sustained growth data. Any viable theory must predict a linear feedback gain with a magnitude in this range. Furthermore, it must be consistent with the observed large changes in sign and amplitude.

Figure 24 shows the typical variation of *Rgain* as a function of time during motor burn. The time of greatest feedback gain is near the midpoint of the burn rather than at the end of burn as is often assumed. This suggests that a resonance interaction mechanism may characterize the disturbance; several peaks and valleys in spacecraft response suggest that the disturbing entity is tuned in some way to the angular rate perturbations.

Notice that disturbances are present from the beginning of the motor run. This is evidence that the nutation instability is not caused by accumulation of particulate material, since a sufficiently large sloshing slag pool would not be expected until late in the motor burn when the aft end of the chamber can accommodate it and when the increasing vehicle acceleration promotes more a rapid buildup.

Figure 25 is the *Rgain* variation measured in an SGS-II first stage flight. This vehicle is about four times more massive than the PAM-D (WESTAR V) whose *Rgain* is shown in Figure 24. It is important to notice that the *Rgain* patterns are quite similar. The event times are altered, but the magnitudes of the torque gain are quite similar. Amplitudes are typically twice as large as the PAM values during the final seconds of motor operation. This observation is difficult to reconcile with the slag sloshing nutation instability model because the latter predicts that the torque should be sensitive to acceleration. If the acceleration is lower, so should the torque gain be significantly lower.

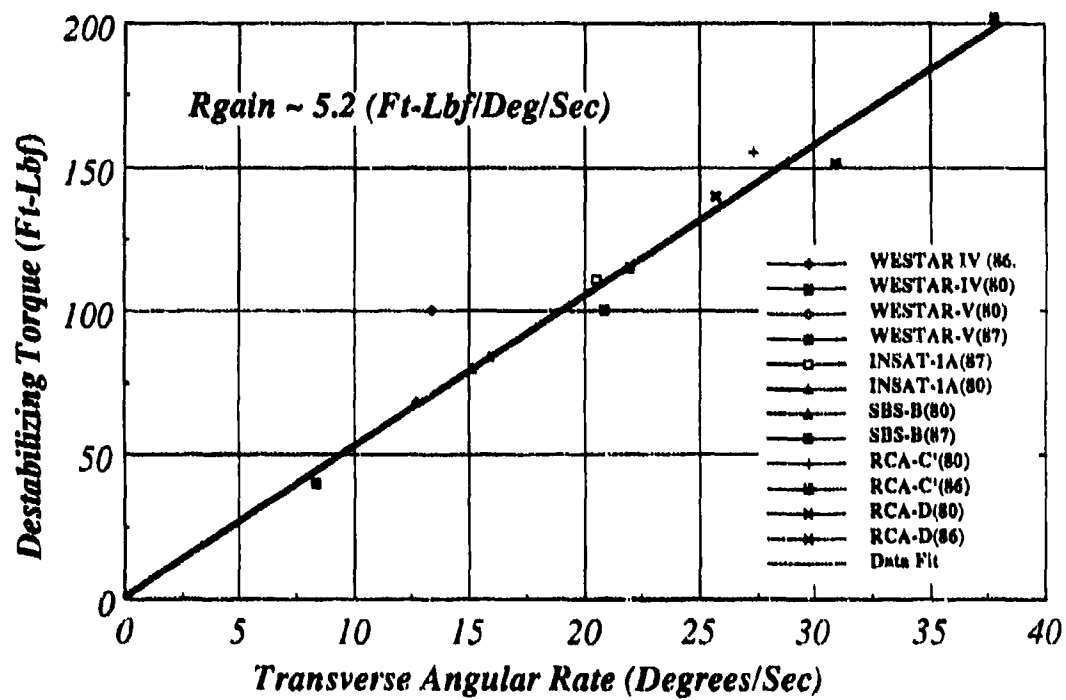


Figure 23. Evidence for Self-Excited Nutation Instability

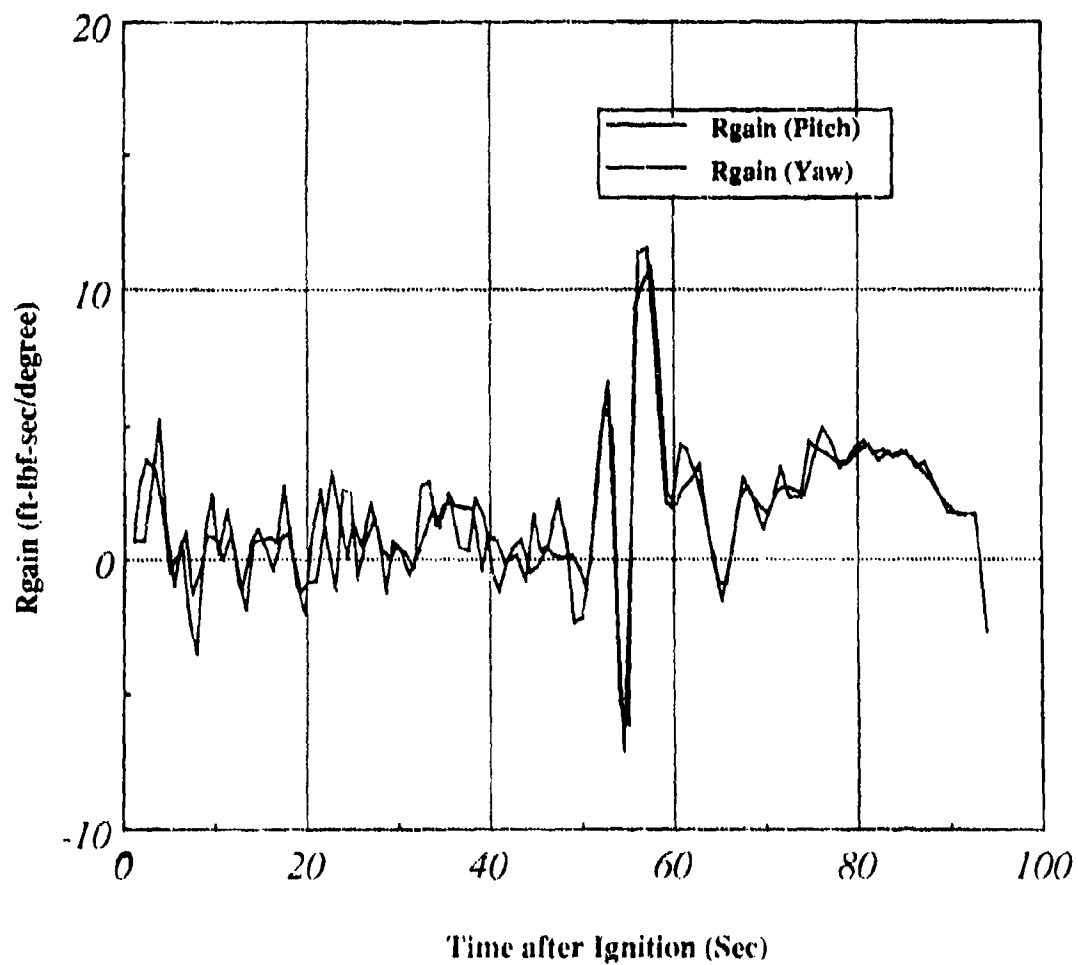


Figure 24. Rgain vs Time from WESTAR V Telemetry

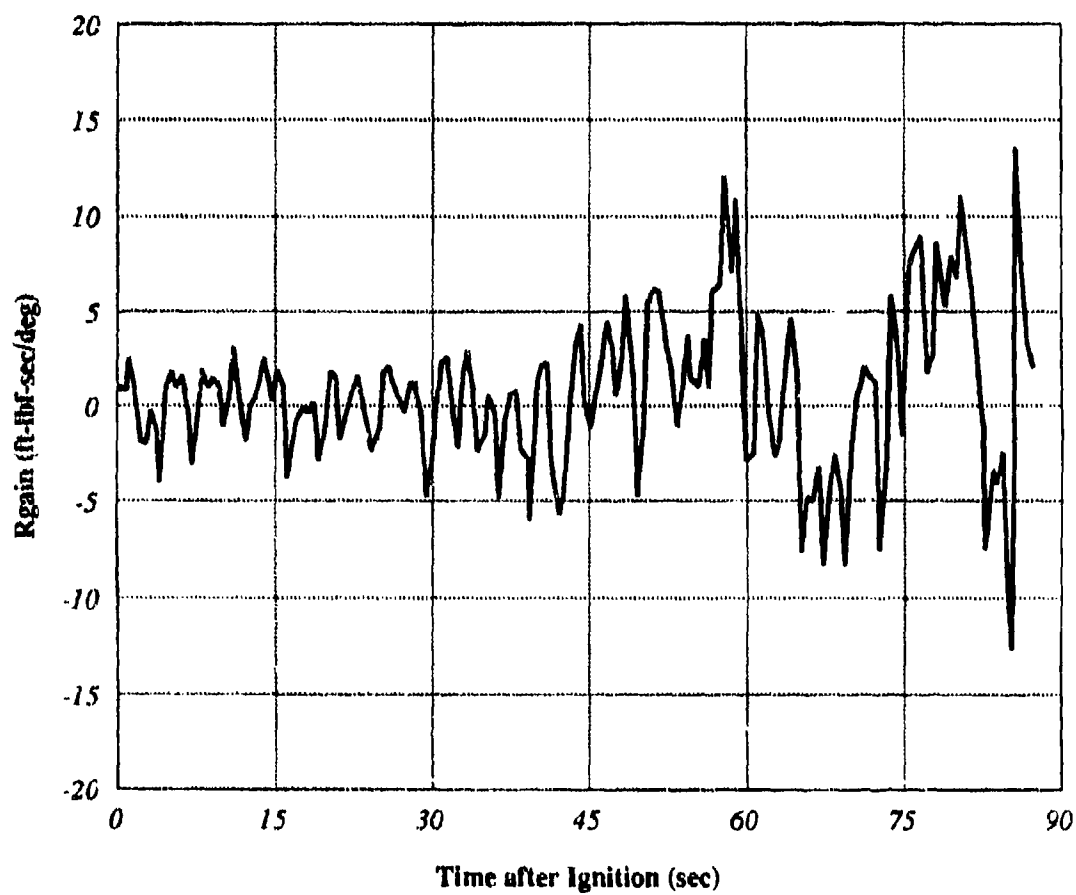


Figure 25. Rgain vs Time from SGSII (Flight 4) Telemetry

The largest growth and the largest disturbing torque, as shown in Figures 26 and 27, appear in the last few seconds not because the gain factor is growing rapidly, but because the moments of inertia are rapidly decreasing. Any useful analytical model must account for these features of the observations.

Not displayed in the plots shown here is evidence that the coning phenomenon is sensitive to the spin rate. Large upper stages employing nonspinning motors similar to the STAR series show no tendency for nutation growth. Limited testing was conducted during the PAM-D program that suggested the dependence on spin rate is approximately linear. Spin rates are currently determined by algorithms that do not include a representation of the PAM-D nutation growth mechanism. They are aimed at minimizing perturbations caused by vibration of the structure and internal stores. There is a pressing need to upgrade this design process as the propulsion impulse requirements (and the likelihood of nutation problems) grow with increasing payload mass. Clearly, since spin rate definitely influences the coning growth rate, continued use of traditional stability analyses to set rate of rotation is inappropriate.

Since coning is a self-excited phenomenon, the final amplitude of the disturbance is directly dependent on the initial wobble introduced during deployment from the spin platform or other spinup device. Outgassing, deployment of shrouds or other paraphernalia can also evidently modify the initial conditions at motor ignition. Again, detailed knowledge of the characteristics of the disturbing entity is required if constraints are to be placed on allowable initial wobble.

The Evidence for Resonance

The behavior of the gain factor (Figures 24 and 25) strongly suggests that a resonant interaction is responsible for the growth in coning. Resonance is an important ingredient in all known forms of nutation instability. For example, in systems susceptible to liquid slosh effects, significant coning growth only occurs when a natural sloshing frequency is in resonant coincidence with the wobbling frequency of the vehicle.

The rapid excursions in gain amplitude in Figure 24 and 25 are quite typical of a resonant phenomenon. The large transient at midburn is especially noteworthy. In fact, this feature is largely responsible for the later coning buildup because it introduces a rapid change in lateral rate even though the accompanying cone angle buildup is much smaller than that appearing at the end of burn. Remember that the nutation torque is proportional to lateral angular rate as illustrated in Figure 23. Thus, the midburn impulse triggers the events that follow. The later buildup in cone angle is very sensitive to the amplitude of the angular rate disturbance produced in the midburn event.

It should be emphasized that the identification of a resonance effect has many practical implications. It suggests that if the source of the coning disturbance can be isolated then it might be possible by means of minor changes in system geometry or other physical parameters to detune the system enough to prevent significant coning growth. Simulations of the motion show that if the midburn disturbance can be reduced by 50%, then the later nutation divergence will be practically eliminated.

Effect of Nutation Disturbance on Wobbling Frequency

Since the disturbing torque is not necessarily aligned with the wobble angular velocity vector, it can modify the frequency of nutation wobbling. This frequency is sometimes called the free precession frequency. Assuming the spacecraft is essentially a rigid axisymmetric

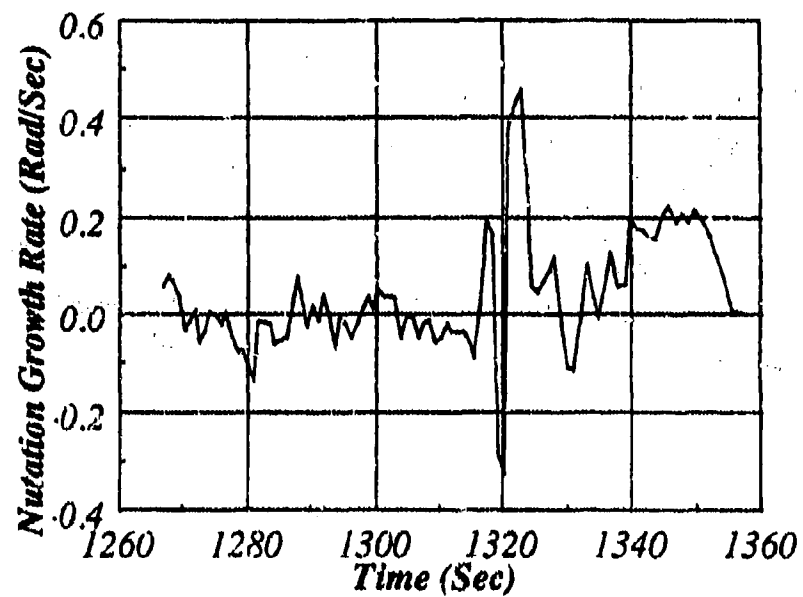


Figure 26. Nutation Growth Rate for Typical PAM-D (WESTAR V Spacecraft)

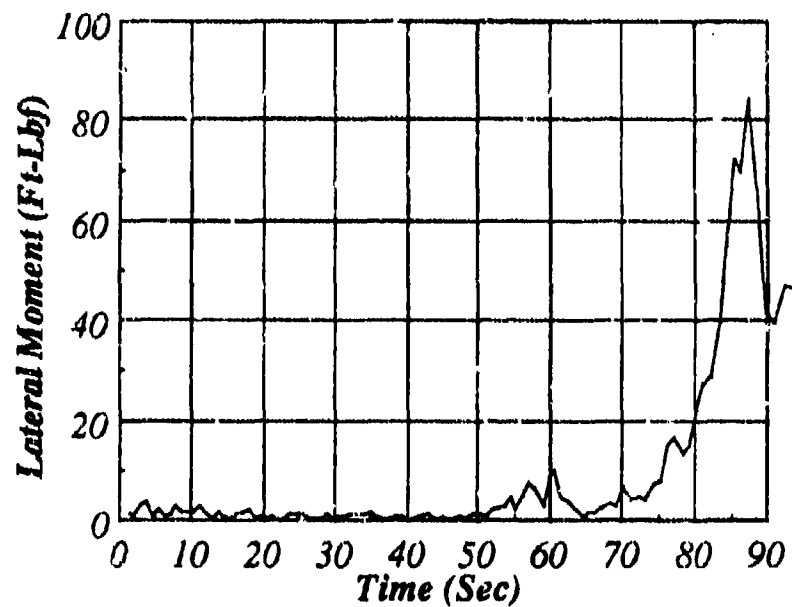


Figure 27. Apparent Lateral Disturbing Torque (WESTAR V)

body, the frequency is given by

$$\lambda = \Omega \left(1 - \frac{I_0}{I_1} \right) \quad (2)$$

where I_0 and I_1 are the axial and lateral moments of inertia, and Ω is the rate of axial spin.

The solid curve in Figure 28 is the calculated frequency for a typical PAM-D (WESTAR V). The downward trend reflects the relative changes in the moments of inertia as propellant is consumed. Superimposed on this plot are measured frequency data. Please note the major departure of the actual wobbling motion from the rigid body calculation. This is evidence that the force system acting on the vehicle is extremely energetic. The frequency shifts appear exactly at the same points as the peaks in the Rgain curve and represent just another manifestation of the same disturbing mechanism.

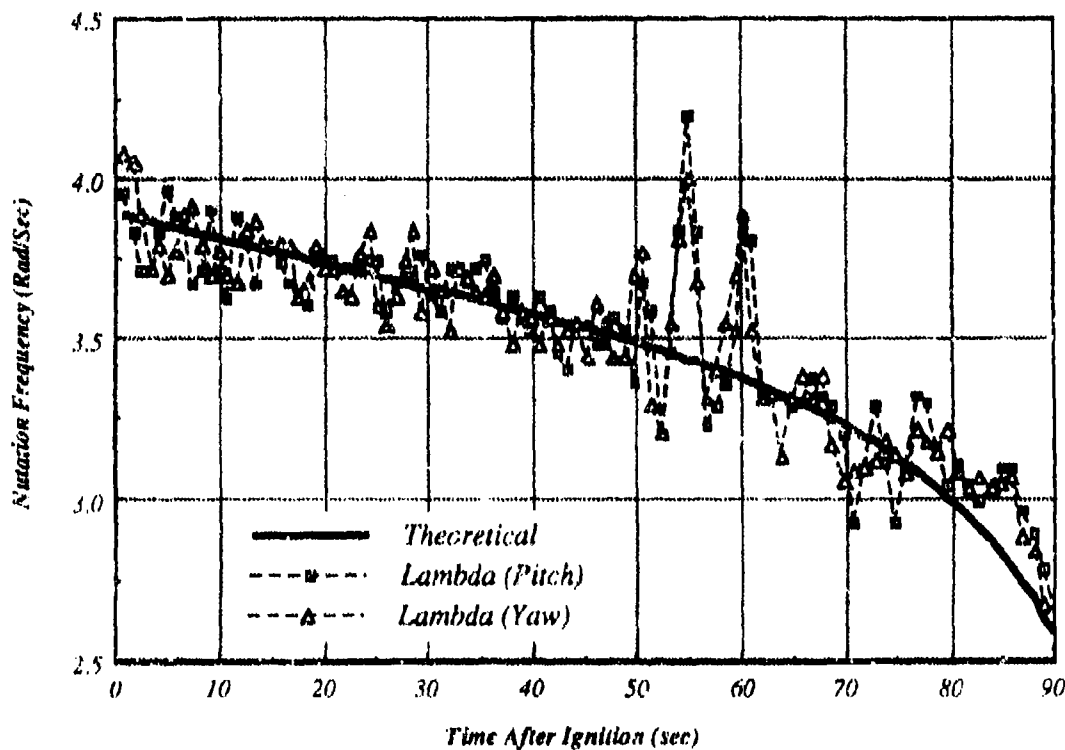


Figure 28. Effect of Perturbation Torque on Copping Frequency

Requirements for a Satisfactory Mechanism

On the basis of the key experimental data we have described, it is possible to identify the main features that must be present in any satisfactory coning model. To be acceptable, a coning mechanism must fit the following pattern:

- Disturbing torque must be linked to the wobbling angular velocity indicating a closed-loop, self-excited system. It must move relative to the vehicle in the same manner as the angular velocity perturbation.
- Magnitude of disturbing torque must be proportional to the lateral angular velocity.
- Torque gain factor (factor of proportionality with angular velocity) must have frequency dependence and associated resonance characteristics.
- Mechanism must be capable of generating a maximum interaction torque of the order of 100 ft-lbf.

The first requirement eliminates many mechanism proposed in earlier studies because they were based on unbalanced forces related to misalignment or nonuniformities in propellant geometry and so on that produce body-fixed torques. It is interesting that except for its sense, the jet damping torque fits all of the requirements. This is an important clue that led us to the mechanism studied in this report.

Proposed Nutation Mechanisms

In searching for potential coning mechanisms, a set of candidates was assembled by the McDonnell Douglas Company along with a number of PAM user companies and support organizations. Over a period of several years each separate mechanism has been studied carefully and eliminated from the list only when it became clear that it was inconsistent with the flight data. To our knowledge, the McDonnell Douglas list of suspects has now been pared down to the following :

- Sloshing of aluminum oxide slag that collects inside the rocket motor
- Interaction of combustion chamber gas flow
- A combination of these two possibly involving a two-phase flow of gases and oxide particles

The experimental evidence makes it clear that the disturbing entity must be free to move relative to the vehicle. The nearly exponential growth of the disturbance strongly suggests a closed-loop mechanism involving relative motion of part of the spacecraft or motor. Such instabilities are quite common. For example, the first American satellite, the Explorer I (a small instrument package attached to a spinning, scaled-down Sergeant solid rocket fourth stage), exhibited tumbling instability caused by relative motion of four whip antennas and attendant frictional energy dissipation. Spinning spacecraft carrying liquids often suffer nutation instability due to propellant sloshing. The coning instability of liquid-filled projectiles is

also well-known. Unfortunately, it has not been possible to link the PAM coning with any similar mechanical feature. Sloshing of liquid propellants affected the nutation amplitudes in some of the spacecraft, but it is clearly not the main cause of the problem. A recent Ariane upper-stage (using a spinning STAR 48 motor) failure has been attributed to liquid sloshing, but it is quite likely that the sloshing was initiated by the same propulsion-induced coning mechanism observed in the PAM-D flights. That is, without the triggering events during motor burn, the sloshing mechanism may not have been activated. Such phenomena are often highly amplitude dependent, and it is possible that system stability would not have been affected in the absence of the PAM-D effect.

The flight data strongly implicate the propulsion system as the source of the coning energy, since the growth of instability changes abruptly at the end of the motor burn. A major goal of this work was the careful evaluation of the interaction gas dynamics involving the propulsion system internal ballistics. We discovered that the most probable origin of the observed nutation instability is the unsteady counterpart of the well-known jet damping effect. Inclusion of the unsteady gas response to the motion of the spinning motor and nozzle boundaries gives rise to modified interaction moments that can, under certain combinations of flow parameters and geometry, decrease the net jet damping effectiveness or even cause growth of coning.

Flow Interaction Models

Although it might seem complex upon first examination, the basic instability mechanism is actually quite simple. To be successful in understanding it, one must learn to visualize the effects of spin on the flow of a gas stream. Let us state the flow interaction mechanism succinctly at this point. We will carefully amplify the details in later sections using simple physical examples and analogies. These will then be backed up by very complete analyses and numerical solutions.

Lateral angular momentum is imparted to the motor gas flow by the motions of the chamber boundaries. The initial triggering impetus is the wobble introduced in injection from the spin platform. The gases react to this excitation in a complex way that is controlled by the rate of angular gas motion due to spin relative to the convective flow speed of the combustion products. If the chamber throughflow is slow compared to the spin, then major changes in the streamline pattern and pressure distributions are produced.

This gas response produces a circumferentially traveling pressure wave because of the spin. This is like the jet damping pressure wave, but its orientation relative to the chamber is modified. Because of this wave-like behavior, energy can be stored in the motor chamber if there is *resonance* between the gas response and the vehicle wobbling. The rate of growth depends mainly on the closeness to a resonance at any particular instant. The lateral torque vector representing the integrated effect of the unsymmetrical pressure distribution rotates relative to the rocket motor at the spacecraft precession frequency in the retrograde (opposite to the axial spin) direction. If the phase of the moving torque vector is such that it has a component in the *same direction as the spacecraft angular velocity perturbation*, then the wobbling grows.

Slag Models

Mechanisms based on the possible influence of aluminum oxide slag accumulation in the rocket motor are still being studied. As mentioned earlier, the one favored by many analysts is the slag sloshing concept. Because the propellant is highly aluminized, aluminum oxide slag

particles are trapped within the motor because of the submerged nozzle in combination with axial acceleration and spin. The amount of slag that collects in the system is very sensitive to acceleration. The slag model is based on the idea that a pool of slag forms and sloshes in response to the vehicle wobbling.

Various pendulum models of the slag motion have been proposed to account for its motion relative to the chamber. These have the unfortunate feature of introducing physical parameters that are unrelated to the actual vehicle and motor configuration. That is, they must be determined by fitting the analysis to flight data. Given enough built-in flexibility, the models can be made to fit flight data quite well. Thus, there are many adherents to the slag hypothesis. Perhaps this is because it resembles familiar nutation mechanisms encountered in earlier flight experience. The slag mechanism is quite similar to other liquid slosh effects that have been encountered since the earliest days of spaceflight.

On the basis of the obvious potential of the slag idea, there have been several very interesting experimental studies that attempt to verify its role in the PAM-D problem. The first of these was conducted by McDonnell Douglas and led to the conclusion that it did not fit the observations. More recent experiments have involved flight testing of small spinning vehicles containing a simulated slag pool. The results have not been reported in the open literature.

Modified Slag Models

It has been proposed that a closer description of the real environment in a spinning rocket would involve a combination of gas flow effects and slag motions. The authors concur with this view. However, we believe that the slag material interacts with the system in the manner of a two-phase flow. Slag certainly tends to collect during motor operation in the aft end of the chamber, but we believe it would take the form of stratification layers whose motion is controlled more strongly by gas phase effects than by free surface sloshing effects. This is a major difference of opinion. Virtually all slag models that have been proposed either invoke some kind of a sloshing liquid pool or a clump of material that is taken to act as a concentrated mass at the end of a pendulum.

Very little is known of the physical characteristics of slag material in a burning rocket motor. Most information comes from inspection of the interior of rocket cases after the material has solidified. X-ray cinematography used in some recent studies at the Arnold Engineering Development Center (AEDC) suggests that the slag material moves more like a gas or low-density froth than a liquid. Until more is known of actual slag behavior and its physical makeup, it will be difficult to represent its effect on vehicle dynamics.

We have prepared for study of possible combined gas/slag interactions by developing a numerical algorithm that can readily incorporate two-phase flow effects and density stratification. However, we wish to emphasize that the interaction torques we predict on the basis of gas flow effects alone are in close agreement with those observed in flight both in magnitude and in timing of the appearance of resonant peaks. The gas dynamics effects alone satisfy all requirements for a viable nutation instability mechanism.

(Blank Page)

MECHANICS OF NUTATION INSTABILITY

Overview

In this section we will carefully analyze the motion of spinning vehicles with interacting internal motion of a contained fluid or gas. This is a familiar problem to spacecraft dynamicists who have had to deal with sloshing liquid stores in spin-stabilized satellites. However, the version of the problem that we must solve involves additional complications resulting from expulsion of mass, linear and angular momentum, and energy from the system with the combustion gas flow from the motor. This gives rise to a number of new interaction phenomena that have not been considered in earlier work on sloshing. For the most part, the disturbing mechanism created during propulsion, for instance by sloshing propellants, is due to the center of gravity offset relative to the motor thrust line. We emphasize at the outset that this is *not* the mechanism we want to describe. Instead, we will be more interested in the effects of nonuniform pressure distributions and resulting unbalanced moments on the vehicle caused by gas flow response to the angular motion of the vehicle.

The analysis provides the link between the spacecraft motion and the internal motions of the contained combustion gases. It therefore provides the necessary tools for assessing the influence of any such internal flow effects in producing vehicle disturbances of the type described in the last section. Since this is such an important part of the nutation problem, we devote this entire section to a careful analysis. This material follows the approach used by the authors of earlier works,⁵ but includes a much more thorough interpretation of the dynamics. It is intended to aid the reader to understand the implications in more depth by means of examples and analogies with more familiar cases of spinning and nonspinning dynamics.

Equations of Motion

What is required in assessing the interactions between a spinning, nutating body with the generation and expulsion of combustion gases is a dynamic analysis of a multi-phase system as depicted in Figure 29. We will carefully derive the equations of motion starting from first principles. Newton's second law is the starting point, and the rates of change of linear and angular momentum are related to the externally applied force system and moments (\vec{F} and \vec{M}) by

$$\left\{ \begin{array}{l} \vec{F} = \frac{d\vec{P}}{dt} = \frac{d}{dt} \int_m \vec{v}_{abs} dm \end{array} \right. \quad (3)$$

$$\left\{ \begin{array}{l} \vec{M} = \frac{d\vec{H}}{dt} = \frac{d}{dt} \int_m \vec{R} \times \vec{v}_{abs} dm \end{array} \right. \quad (4)$$

where \vec{P} and \vec{H} are the linear and angular momentum of the system. We have written these vectors in continuum form to set the problem up for best handling of the gas phase of the system. A mass element of any part of the system is denoted dm and its absolute position is

$$\vec{R} = \vec{R}_o + \vec{r} \quad (5)$$

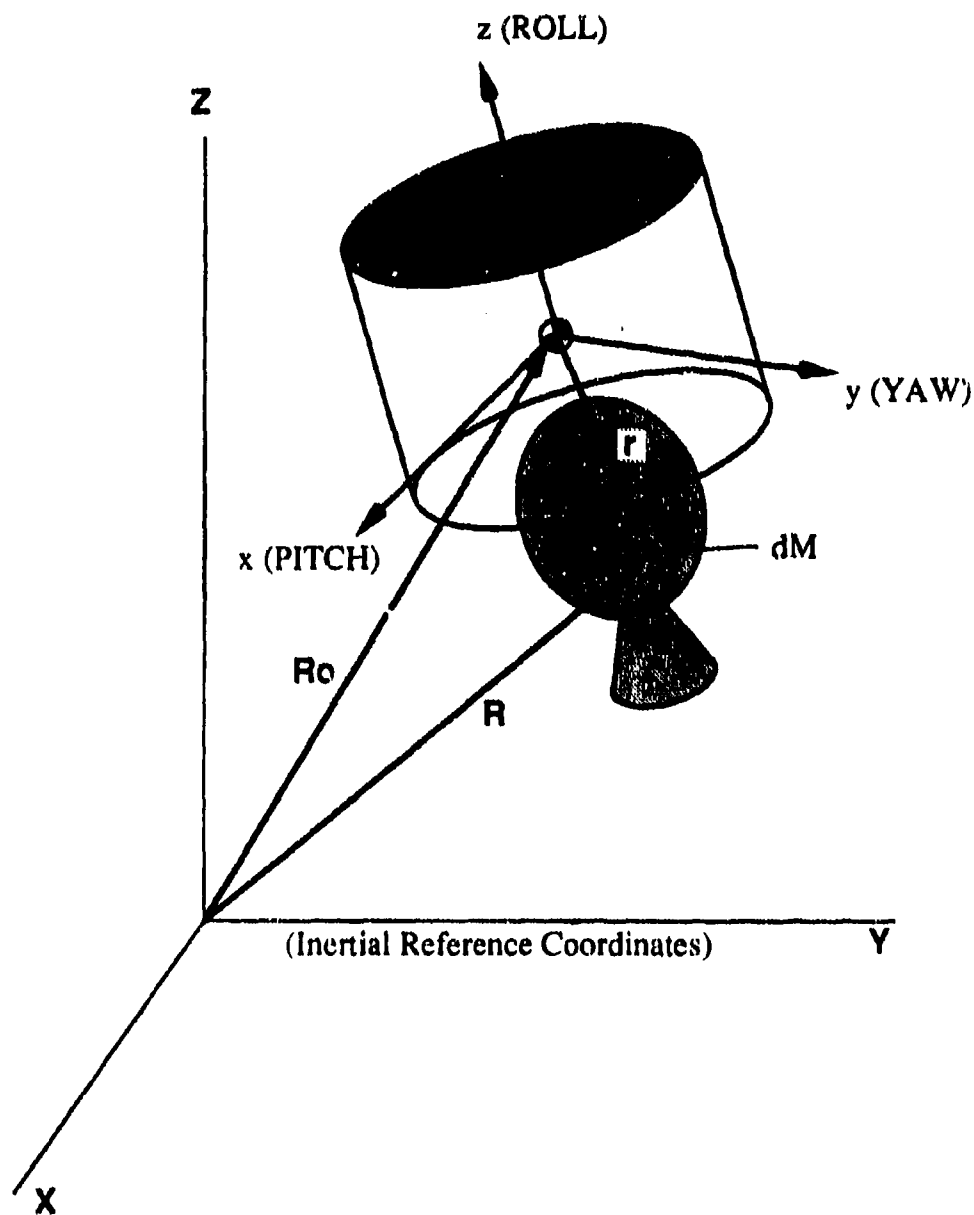


Figure 29. Coordinate System and Basic Control Volume

The absolute velocity and acceleration of the mass element are

$$\mathbf{v}_{abs} = \frac{d\mathbf{R}}{dt} = \mathbf{v}_o + \mathbf{v}_{rel} + \boldsymbol{\omega} \times \mathbf{r} \quad (6)$$

$$\mathbf{a}_{abs} = \frac{d\mathbf{v}_{abs}}{dt} = \mathbf{a}_o + \mathbf{a}_{rel} + \boldsymbol{\omega} \times \boldsymbol{\omega} \times \mathbf{r} + 2\boldsymbol{\omega} \times \mathbf{v}_{rel} + \boldsymbol{\alpha} \times \mathbf{r} \quad (7)$$

where \mathbf{v}_o and \mathbf{a}_o are the velocity and acceleration of the reference point o (we will find it convenient to locate this point at the instantaneous center of mass of the system). The angular velocity and angular acceleration of the coordinates fixed to the vehicle will be denoted as $\boldsymbol{\omega}$ and $\boldsymbol{\alpha}$, respectively. Since relative motion of gas particles or other entities is of prime interest, this motion is described by the relative velocity \mathbf{v}_{rel} . Note that vectors are indicated by bold-faced type.

With these definitions in place, the system motion can be described by

$$\left\{ \begin{aligned} \mathbf{F} &= \int_m \frac{d}{dt} \mathbf{v}_{abs} dm = \int_m \mathbf{a}_{abs} dm \end{aligned} \right. \quad (8)$$

$$\left\{ \begin{aligned} \mathbf{M} &= \int_m \frac{d}{dt} [\mathbf{R} \times \mathbf{v}_{abs}] dm = \int_m \mathbf{R} \times \mathbf{a}_{abs} dm \end{aligned} \right. \quad (9)$$

Solving for the terms involving the relative acceleration, we write

$$\int_m \mathbf{a}_{rel} dm = \mathbf{F} - \int_m (\mathbf{a}_o + \boldsymbol{\omega} \times \boldsymbol{\omega} \times \mathbf{r} + 2\boldsymbol{\omega} \times \mathbf{v}_{rel} + \boldsymbol{\alpha} \times \mathbf{r}) dm \quad (10)$$

$$\int_m \mathbf{R} \times \mathbf{a}_{rel} dm = \mathbf{M} - \int_m \mathbf{R} \times (\mathbf{a}_o + \boldsymbol{\omega} \times \boldsymbol{\omega} \times \mathbf{r} + 2\boldsymbol{\omega} \times \mathbf{v}_{rel} + \boldsymbol{\alpha} \times \mathbf{r}) dm \quad (11)$$

Now, without loss of generality, we can place the inertial origin at the instantaneous position of the center of mass so that

$$\mathbf{R}_o \rightarrow 0 \quad (12)$$

The integral terms containing the relative acceleration can be reinterpreted as statements of the time rates of change of linear and angular momentum as viewed relative to the moving coordinates as

$$\int_m \mathbf{a}_{rel} dm = \int_m \frac{d\mathbf{v}_{rel}}{dt} dm = \frac{d}{dt} \int_m \mathbf{v}_{rel} dm = \left(\frac{d\mathbf{P}}{dt} \right)_{rel} \quad (13)$$

$$\int_m \mathbf{r} \times \mathbf{a}_{rel} dm = \int_m \mathbf{r} \times \frac{d\mathbf{v}_{rel}}{dt} dm = \frac{d}{dt} \int_m \mathbf{r} \times \mathbf{v}_{rel} dm = \left(\frac{d\mathbf{H}}{dt} \right)_{rel} \quad (14)$$

This part of the analysis must be treated with great care because the choices we make will affect the ease with which interactions between the vehicle and gas motions can be analyzed.

We will eventually need to use the tools of fluid dynamics in treating the gas flow, so proper choices made now will help in later accommodation of these tools.

Application of the Reynolds Transport Theorem

Up to this point, the analysis follows standard practice and differs only in notation from earlier ones. For example, the equations we have written are identical to those developed by Thomson⁵ in their general study of jet damping. Unless details of the gas flow must be incorporated, one can continue to treat the gas and solid components as collections of discrete particles. To take this approach greatly limits the resolution that can be attained in describing the gas phase motions.

Instead of treating the system in the Lagrangian sense as a system of discrete particles, we pass to the Eulerian description by means of the Reynolds Transport Theorem. This is a key step because it allows us to bring to bear the powerful tools of continuum fluid mechanics in later vital parts of the analysis. This is accomplished by application of the Reynolds transport theorem, which can be written in general form for application to some property N of the gas as:

$$\left(\frac{dN}{dt} \right)_{\text{system}} = \frac{\partial}{\partial t} \int_V \eta \rho dV + \int_S \eta (\mathbf{u} \cdot \mathbf{n}) \rho dS \quad (15)$$

This allows us to pass from a description of the motion of the system of particles to a continuum description for a control volume V bounded by a surface S . Then η becomes the specific property associated with N . For example, if N is the relative linear momentum, then

$$\begin{cases} N = P_{rel} = \int_m \mathbf{v}_{rel} dm = \int_m \mathbf{u} dm \\ \eta = \mathbf{v}_{rel} = \mathbf{u} \end{cases} \quad (16)$$

and similarly if N is the relative angular momentum, we define

$$\begin{cases} N = H_{rel} = \int_m \mathbf{r} \times \mathbf{v}_{rel} dm = \int_m \mathbf{r} \times \mathbf{u} dm \\ \eta = \mathbf{r} \times \mathbf{v}_{rel} = \mathbf{r} \times \mathbf{u} \end{cases} \quad (17)$$

For later convenience we have passed from the conventional dynamics notation for the relative particle motion to the standard notation for gas velocity vectors, \mathbf{u} . Thus, we can convert from a system description of the individual motion of all particles comprising the solid part of the vehicle, motor and propellants and the gas particles produced by combustion flowing through the motor chamber out the nozzle and into to plume behind the vehicle. We convert to a force balance involving only convenient parts of the system. A useful choice of control volumes is one which encompasses all of the solid parts of the system and the the gas particles contained within the motor chamber and nozzle. Then the control surface encloses all of these elements and allows passage of mass, momentum, and energy across the nozzle exit.

Writing the equations in conventional form, we solve for the external force F and moment M and find:

$$\left\{ \begin{aligned} F - \int_V (\mathbf{a}_0 + \boldsymbol{\omega} \times \boldsymbol{\omega} \times \mathbf{r} + 2\boldsymbol{\omega} \times \mathbf{u} + \boldsymbol{\alpha} \times \mathbf{r}) \rho dV &= \frac{\partial}{\partial t} \int_V \mathbf{u} \rho dV + \int_S \mathbf{u}(\mathbf{u} \cdot \mathbf{n}) \rho dS \end{aligned} \right. \quad (18)$$

$$\left\{ \begin{aligned} M - \int_V \mathbf{r} \times (\mathbf{a}_0 + \boldsymbol{\omega} \times \boldsymbol{\omega} \times \mathbf{r} + 2\boldsymbol{\omega} \times \mathbf{u} + \boldsymbol{\alpha} \times \mathbf{r}) \rho dV &= \frac{\partial}{\partial t} \int_V \mathbf{r} \times \mathbf{u} \rho dV + \int_S \mathbf{r} \times \mathbf{u}(\mathbf{u} \cdot \mathbf{n}) \rho dS \end{aligned} \right. \quad (19)$$

Definition of System Mass Properties

For later use we define at this convenient point the mass properties to be used in describing the system. Since important parts of the system are to be described in continuum form, it is appropriate to define the system mass as

$$m = \int_V \rho dV \quad (20)$$

where ρ is the density and dV the volume element at any location. The equations of motion then become

$$\left\{ \begin{aligned} m \mathbf{a}_0 &= F - (\boldsymbol{\omega} \times \boldsymbol{\omega} \times \boldsymbol{\alpha} \times) \int_V \mathbf{r} \rho dV - \int_V (2\boldsymbol{\omega} \times \mathbf{u}) \rho dV - \frac{\partial}{\partial t} \int_V \mathbf{u} \rho dV - \\ &\quad - \int_S \mathbf{u}(\mathbf{u} \cdot \mathbf{n}) \rho dS \end{aligned} \right. \quad (21)$$

$$\left\{ \begin{aligned} \mathbf{I} \cdot \boldsymbol{\alpha} + \boldsymbol{\omega} \times \mathbf{I} \cdot \boldsymbol{\omega} &= M + \mathbf{a}_0 \times \int_V \mathbf{r} \rho dV - \int_V \mathbf{r} \times (2\boldsymbol{\omega} \times \mathbf{u}) \rho dV - \frac{\partial}{\partial t} \int_V \mathbf{r} \times \mathbf{u} \rho dV - \\ &\quad - \int_S \mathbf{r} \times \mathbf{u}(\mathbf{u} \cdot \mathbf{n}) \rho dS \end{aligned} \right. \quad (22)$$

In dealing with the angular motion, the inertia tensor will arise naturally. It is defined as

$$\mathbf{I} = \begin{bmatrix} I_{xx} & I_{xy} & I_{xz} \\ I_{yx} & I_{yy} & I_{yz} \\ I_{zx} & I_{zy} & I_{zz} \end{bmatrix} \quad (23)$$

where

$$\begin{aligned} I_{xx} &= \int_V (y^2 + z^2) \rho dV, \quad I_{yy} = \int_V (x^2 + z^2) \rho dV, \quad I_{zz} = \int_V (x^2 + y^2) \rho dV \\ I_{xy} &= I_{yx} = - \int_V xy \rho dV, \quad I_{xz} = I_{zx} = - \int_V xz \rho dV, \quad I_{yz} = I_{zy} = - \int_V yz \rho dV \end{aligned} \quad (24)$$

Please notice that since the volume integrals encompass all parts of the system, then the total mass and moments of inertia represent the inertia of the contained gas as well as the solid parts of the system. Effects of the relative gas motion are handled separately as described in the following subsection. Since in most later applications of the theory we be treating axisymmetric spacecraft configurations, the inertia tensor will reduce to

$$\mathbf{I} = \begin{bmatrix} I_1 & 0 & 0 \\ 0 & I_1 & 0 \\ 0 & 0 & I_0 \end{bmatrix} \quad (25)$$

where the products of inertia are all zero and the two lateral moments of inertia will be defined as

$$I_1 = I_{xx} = \int_V (y^2 + z^2) \rho dV, \quad I_1 = I_{yy} = \int_V (x^2 + z^2) \rho dV \quad (26)$$

and the moment of inertia about the axis of symmetry will be denoted as

$$I_0 = I_{zz} = \int_V (x^2 + y^2) \rho dV \quad (27)$$

For the remainder of this section we will treat the problem only in the completely general form. Reduction for specific applications will be accomplished later. Writing the equations in terms of the general mass property definitions yields

$$\left\{ \begin{aligned} m \mathbf{a}_O &= \mathbf{F} - (\boldsymbol{\omega} \times \boldsymbol{\omega} \times \mathbf{r}) \int_V \rho dV - \int_V (2\boldsymbol{\omega} \times \mathbf{u}) \rho dV - \\ &\quad - \frac{\partial}{\partial t} \int_V \mathbf{u} \rho dV - \int_S \mathbf{u} (\mathbf{u} \cdot \mathbf{n}) \rho dS \\ \mathbf{I} \cdot \boldsymbol{\alpha} + \boldsymbol{\omega} \times \mathbf{I} \cdot \boldsymbol{\omega} &= \mathbf{M} + \mathbf{a}_O \times \int_V \mathbf{r} \rho dV - \int_V \mathbf{r} \times (2\boldsymbol{\omega} \times \mathbf{u}) \rho dV - \\ &\quad - \frac{\partial}{\partial t} \int_V \mathbf{r} \times \mathbf{u} \rho dV - \int_S \mathbf{r} \times \mathbf{u} (\mathbf{u} \cdot \mathbf{n}) \rho dS \end{aligned} \right. \quad (28)$$

in standard Newton's law form.

In some applications, the location of the system center of mass plays an important role in determining the interaction forces. Hence, let us identify the center of mass position as it arises in the equations. By definition, the vector position of the mass center relative to the spacecraft fixed coordinate system is

$$\bar{\mathbf{r}} = \frac{1}{m} \int_V \mathbf{r} \rho dV \quad (30)$$

where m is the total mass contained within the control volume. Rewriting the equations by means of this definition yield

$$\left\{ \begin{aligned} m \mathbf{a}_0 &= \mathbf{F} - m(\boldsymbol{\omega} \times \boldsymbol{\omega} \times \bar{\mathbf{r}} + \boldsymbol{\alpha} \times \bar{\mathbf{r}}) - \int_V (2\boldsymbol{\omega} \times \mathbf{u}) \rho dV - \frac{\partial}{\partial t} \int_V \mathbf{u} \rho dV - \\ &\quad - \int_S \mathbf{u} (\mathbf{u} \cdot \mathbf{n}) \rho dS \end{aligned} \right. \quad (31)$$

$$\left\{ \begin{aligned} \mathbf{I} \cdot \boldsymbol{\alpha} + \boldsymbol{\omega} \times \mathbf{I} \cdot \boldsymbol{\omega} &= \mathbf{M} + m \mathbf{a}_0 \times \bar{\mathbf{r}} - \int_V \mathbf{r} \times (2\boldsymbol{\omega} \times \mathbf{u}) \rho dV - \frac{\partial}{\partial t} \int_V \mathbf{r} \times \mathbf{u} \rho dV - \\ &\quad - \int_S \mathbf{r} \times \mathbf{u} (\mathbf{u} \cdot \mathbf{n}) \rho dS \end{aligned} \right. \quad (32)$$

and we are now in a position to identify potential sources of internally generated disturbing forces and moments.

Treatment of Internally Generated Interaction Forces and Moments

The equations in their general form (equations 21-22) can be further manipulated to emphasize the effects of interactions between the solid parts and the internal gas flow. The form of equations 31-33 suggests that the unevaluated volume and surface integrals involving relative motion of the combustion gas flow can be interpreted as disturbing forces. Put

$$\left\{ \begin{aligned} m \mathbf{a}_0 &= \mathbf{F}_{\text{ext}} + \mathbf{F}_{\text{offset}} + \mathbf{F}_{\text{flow}} \end{aligned} \right. \quad (33)$$

$$\left\{ \begin{aligned} \mathbf{I} \cdot \boldsymbol{\alpha} + \boldsymbol{\omega} \times \mathbf{I} \cdot \boldsymbol{\omega} &= \mathbf{M}_{\text{ext}} + \mathbf{M}_{\text{offset}} + \mathbf{M}_{\text{flow}} \end{aligned} \right. \quad (34)$$

where we have now added a subscript to the external force and moment

$$\mathbf{F} = \mathbf{F}_{\text{ext}}, \quad \mathbf{M} = \mathbf{M}_{\text{ext}} \quad (35)$$

to keep their identity separated from internally generated forces. The latter are conveniently separated into two types. Those associated with effects of center of mass offset from the origin of the coordinate axes we denote as *offset* forces and moments defined as

$$\mathbf{F}_{\text{offset}} = -m(\boldsymbol{\omega} \times \boldsymbol{\omega} \times \bar{\mathbf{r}} + \boldsymbol{\alpha} \times \bar{\mathbf{r}}) \quad (36)$$

$$\mathbf{M}_{\text{offset}} = m \mathbf{a}_0 \times \bar{\mathbf{r}} \quad (37)$$

These allow handling of situations wherein the mass center departs from the thrust line of propulsion system for cases where the motor thrust vector passes through the reference point O . These effects vanish of course if the system is completely symmetrical with $\bar{\mathbf{r}}$ equal to zero.

The remaining interactions are related to relative motion of materials contained within the control volume. They can be used to represent either sloshing liquids or gas motions. It is the latter case that is of central interest here, so we denote these as flow related interactions defined

as

$$\mathbf{F}_{flow} = - \int_V (2\boldsymbol{\omega} \times \mathbf{u}) \rho dV - \frac{\partial}{\partial t} \int_V \mathbf{u} \rho dV - \int_S \mathbf{u} (\mathbf{u} \cdot \mathbf{n}) \rho dS \quad (38)$$

$$\mathbf{M}_{flow} = - \int_V \mathbf{r} \times (2\boldsymbol{\omega} \times \mathbf{u}) \rho dV - \frac{\partial}{\partial t} \int_V \mathbf{r} \times \mathbf{u} \rho dV - \int_S \mathbf{r} \times \mathbf{u} (\mathbf{u} \cdot \mathbf{n}) \rho dS \quad (39)$$

Each of these consists of two volume integrals involving Coriolis acceleration and effects of relative acceleration due to internal motion of the gas particles. They also incorporate surface integrals that account for transfer of momentum or angular momentum, respectively, across the control surface at the nozzle exit. These can indeed be potent forces if one remembers that

$$\text{Thrust} = - \int_S \mathbf{u} (\mathbf{u} \cdot \mathbf{n}) \rho dS \quad (40)$$

represents the motor momentum thrust. A review of the basic effects of momentum flux from the control volume will provide useful guidance in our search for the origins of nutation instabilities.

Comparison to Equations in Lagrangian Form

In order to verify the results presented, it is useful to compare them to equations of motion derived by others in Lagrangian form. In the latter approach, the gases are treated as discrete particles whose individual motions must be known or assumed in order to evaluate the interaction effects. This is the method that has been employed in most analyses of jet damping as we shall see in later sections. For example, the analysis of jet damping by Thompson and Reiter⁵ is based on the equations of motion

$$\begin{cases} m\ddot{\mathbf{R}}_0 = \mathbf{F} + \mathbf{T} - m(\boldsymbol{\omega} \times \boldsymbol{\omega} \times \bar{\mathbf{r}} + \boldsymbol{\alpha} \times \bar{\mathbf{r}}) - 2m\boldsymbol{\omega} \times [\dot{\bar{\mathbf{r}}}] - m\ddot{\bar{\mathbf{r}}} \\ \mathbf{I} \cdot \boldsymbol{\alpha} + \boldsymbol{\omega} \times \mathbf{I} \cdot \boldsymbol{\omega} = \mathbf{M} + \mathbf{M}_T + \ddot{\mathbf{R}} \times m\bar{\mathbf{r}} - \sum_i \mathbf{r}_i \times m_i[\ddot{\mathbf{r}}_i] - 2 \sum_i \mathbf{r}_i \times (\boldsymbol{\omega} \times m_i[\dot{\mathbf{r}}_i]) \end{cases} \quad (41)$$

$$(42)$$

which have been rewritten here in the notation used in earlier subsections for direct comparison. Notice that in place of the volume and surface integrals are summations over the individual particles. They are readily seen to be completely equivalent to the equations written in Eulerian form. However, in order to evaluate them, it is necessary to make rather sweeping assumptions about the gas motion. The usual one is that the flow relative to the motor chamber consists of a steady, uniform, one-dimensional flow. If this is done, the equations are easily evaluated and the classical jet damping theory emerges. We will have cause to check these assumptions in detail. In accounting for the actual gas motions, we will find the origins of the forces that drive nutation instability.

Alternate Control Volume Definitions

We have chosen to present the basic analysis in terms of a control volume completely surrounding the spacecraft and rocket motor. Mass crosses the surface of this volume through the nozzle exit plane. This is a convenient definition for general purposes, but to evaluate the gas dynamic interactions may require information that is difficult to secure. For example, we

would need to know in detail the time-dependent velocity distribution across the nozzle exit to arrive at a valid estimate of the disturbing torque. Thus, any chamber processes we have modeled are modified by complex interactions in the nozzle where the flow is dominated by compressibility. In our earlier study we followed this approach. The results were very promising, and showed the presence of destabilizing moments found on the basis of estimates of the angular momentum flux across the nozzle boundaries. The uncertainties of the nozzle influence made these results difficult to accept by most analysts.

Thus, it may be more convenient and more acceptable to determine the interaction torques with a modified control volume. Figure 30 shows a useful alternate definition. In this case we separate the solid parts of the system from the gas at the boundary of the control volume. Mass crosses this boundary at the propellant burning surfaces. This introduces what might at first appear to be an unsurmountable problem in that we are now compelled to add knowledge of the pressure distributions and possibly shear stress distributions at all interfaces between the solid body and the gas flow. This was not necessary in the basic control volume because the external pressures can be taken to be zero for a fully expanded nozzle flow.

It will become apparent in the next section that in spite of the additional information required, this represents a superior approach in estimating the interaction torques. Our knowledge of the flow field inside the chamber must be complete in order to understand the origins of all flow interactions. This includes the classical jet damping interaction as well as modifications that introduce nutation driving. We will show that it is largely the nonuniform pressure distributions within the chamber and nozzle that drive the nutation instability. Detailed information concerning the pressure distributions will be available as part of the solution of the time-dependent internal flow problem.

When we evaluate the interaction torques we will use the control volume of Figure 30. The same analysis used in the basic approach is adequate. However, we must now account for a nonuniform pressure distribution. Since the control volume consists of just the solid part of the system, no volume integrals are needed in the calculation. Therefore, we find for the gasdynamic disturbing moment:

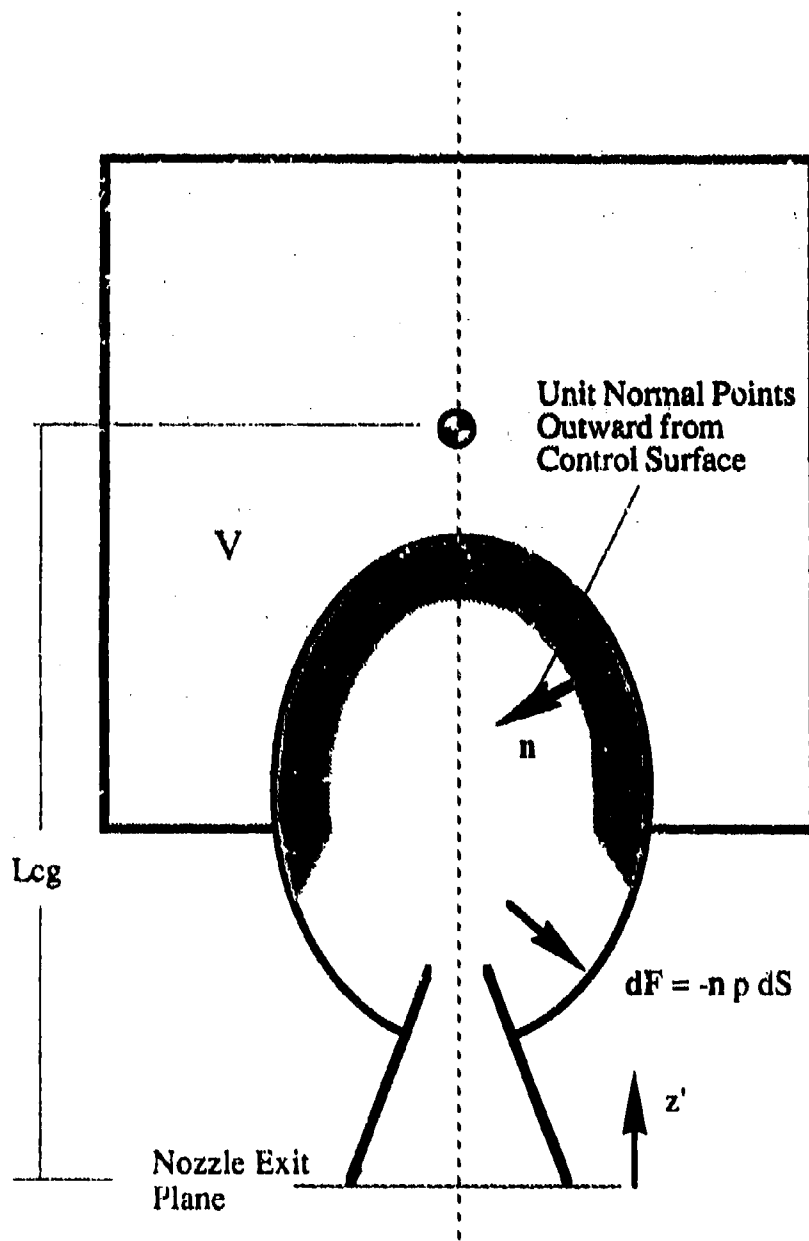
$$M_{flow} = - \int_S \mathbf{r} \times (p \mathbf{n}) dS - \int_S \mathbf{r} \times \mathbf{u} (\mathbf{u} \cdot \mathbf{n}) \rho dS \quad (43)$$

where the effects of the internal pressure distribution have been accounted for. Since a detailed description of the gas flow will evolve, it will be quite easy to determine the angular momentum flux term represented by the surface integral over the propellant burning surface.

We will use this approach in the next section to estimate the gas-generated nutation torques. It will also give us much guidance in understanding jet damping. It will be especially useful as an aid in focusing on the shortcomings of the jet damping model for flow interactions.

Effect of Internally Generated Moments on Spacecraft Motion

The equations we have derived for the angular motion are readily seen to be in familiar Euler equation form if we interpret the gas flow interactions as applied perturbing forces. It is useful, at this point, to describe simple solutions of the dynamical motion in order that characteristics of the forces and moments needed in explaining nutation instability can be identified. We will show that, for small lateral angular perturbations, what is needed is a set of linear coefficients that characterize the interaction moments. These represent the factors of propor-



Control surface S is at the interface between gas and solid parts
Control volume V encloses all solid elements

Figure 30. Alternate Control Volume

tionality between the vehicle motion and the interaction moments thus excited. Figure 16 showing the linear nature of the variation of the apparent disturbing moment in terms of vehicle motion is of fundamental importance in the following discussion. The bulk of this report will be devoted to explaining how the gain factors depend on the parameters of the vehicle and motor system and how they may arise in the nonuniform pressure distributions excited within the rocket by vehicle wobbling.

Assuming that the solid elements of the spacecraft constitute a rigid body, equation 34 may be written in component form as

$$\begin{cases} I_1 \frac{d\omega_x}{dt} = \Omega(I_1 - I_0)\omega_y + M_x \end{cases} \quad (44)$$

$$\begin{cases} I_1 \frac{d\omega_y}{dt} = -\Omega(I_1 - I_0)\omega_x + M_y \end{cases} \quad (45)$$

where we have assumed an axisymmetric vehicle for simplicity. These will be recognized as the Euler equations written for body-fixed axes. I_0 and I_1 are the moments of inertia about the spin and lateral axes respectively. In this discussion we will assume that $I_1 > I_0$ as in a typical prolate spacecraft layout of the PAM-D type.

The perturbation moment is also written in component form as

$$M_{flow} = M_x i + M_y j \quad (46)$$

where we are neglecting any axial torque due to gas interaction effects. The latter disturbing torque does exist and causes the spin rate to increase during burn. It is readily shown that this spinup is not due simply to decreasing roll moment of inertia. It appears to be due mainly to roll torques associated with interaction of a rapidly spinning vortex flow passing through the nozzle. These are very likely viscous interactions. For the present discussion, we will focus on lateral interaction torques only.

Both theoretical considerations (to be discussed at length in the next chapter) and the experimental data strongly indicate that the lateral torque components can be written as linear functions of the angular velocity

$$\begin{cases} M_x = K_1 \omega_x + K_2 \omega_y \end{cases} \quad (47)$$

$$\begin{cases} M_y = K_1 \omega_y - K_2 \omega_x \end{cases} \quad (48)$$

where K_1 and K_2 are proportionality factors that can be estimated from the experimental data or, hopefully, computed once a sufficiently complete model for the flow interactions has been devised.

The factor K_1 represents the part of the moment that is proportional to the component of lateral angular velocity corresponding to the same axis. This is the factor often related to jet damping, in which case it is a negative number. We choose not to separate jet damping from other interactions generated internally by gas motions. In fact, we will prove that in motors of the STAR 48 class and larger, jet damping simply does not work in the classical way and a more complete description of the gas motion is needed.

We will also show that nutation growth requires that K_1 is a positive quantity. This factor is often called Rgain in the recent literature on nutation instability (see discussions in Section 2). Its determination is one of the main objectives of analyses to follow.

Inserting the assumed form of the disturbing moments, we find

$$\begin{cases} I_1 \frac{d\omega_x}{dt} = [\Omega(I_1 - I_0) + K_2]\omega_y + K_1\omega_x \\ I_1 \frac{d\omega_y}{dt} = -[\Omega(I_1 - I_0) + K_2]\omega_x + K_1\omega_y \end{cases} \quad (49)$$

The gas dynamic interaction moment may have components both parallel to and normal to the nutation angular velocity vector. Factor K_2 represents the part of the torque perpendicular to the angular velocity vector. As we shall now show, this part affects the nutation frequency while the parallel part K_1 controls the decay or growth of the nutation.

Stability Calculations

Equations 49 and 50 are readily solved approximately if the mass properties, spin rate, and moment gain factors are treated as slowly changing functions of time. Numerical solutions are required if precise results are needed that include effects of changing moments of inertia and disturbing moments. For the present discussion, we are only interested in the general characteristics of the motion at a given instant of time. That is, we wish to determine the *stability* of the system. The pair of equations can be easily solved simultaneously with the result

$$\omega' = (\omega_x i + \omega_y j) = \omega_0 e^{\alpha t} [i \cos \lambda_s t - j \sin \lambda_s t] \quad (51)$$

where λ_s is the wobbling frequency (see discussion of experimental data and equation 2 in the last section)

$$\lambda_s = \Omega \left[1 - \frac{I_0}{I_1} \right] \quad (52)$$

Notice that this is the oscillatory motion described earlier. For a prolate vehicle it can be interpreted as a perturbation angular velocity vector rotating in the x-y plane in the retrograde direction just as the experimental data indicate. The amplitude of the wobble is controlled by the growth rate, α .

Clearly this theoretical model exactly fits the experimental data (over short intervals of time) as represented, for example, by Figure 22. As discussed in the last section, the observed wobbling frequency closely follows the theoretical value unless there is significant nutation driving present. That is, if K_2 is negligible, then the frequency is the free precession frequency.

The effect of the part of the torque parallel to the angular velocity vector is represented by the exponential growth rate

$$\alpha = \frac{K_1}{I_1} \quad (53)$$

where, again, we have not distinguished between different types of flow interactions. That is, we have not separated jet damping from other gas flow interactions. Notice that the growth rate depends on both the size of the gain constant K_1 and on the lateral moment of inertia of the vehicle. This explains why rapid growth occurs at the end of burn when I_1 approaches its smallest value while K_1 is not necessarily at its maximum during this period.

Some investigators prefer to describe the stability in terms of the inverse of the growth rate, the time constant, τ :

$$\tau = \frac{1}{\alpha} = \frac{I_1}{K_1} \quad (54)$$

In order that the system is unstable, it is necessary that α (or τ) be positive. If the flow interaction consists only of the classical jet damping effect, then α is negative indicating a decaying wobble.

The effect of the interaction torque on the wobbling frequency can be written as a correction to λ_s :

$$\Delta\lambda_s = \frac{K_2}{I_1} \quad (55)$$

Armed with these simple relationships, we can proceed to evaluate the effects of any potential interaction torques from the standpoint of system stability. If more detailed information regarding the actual spacecraft motion is required, we will need to know K_1 and K_2 as functions of time throughout the motor burn. Then, the equations of motion can be solved numerically, and all effects such as variable mass properties can be included.

To make further progress we must carry out an explicit determination of the gain factors. Unfortunately, this cannot be accomplished until we have acquired much more information concerning the time-dependent flow within the rocket combustion chamber and nozzle. This we will deal with in the next section

(Blank Page)

MODELING OF GAS FLOW IN A NUTATING ROCKET

Overview

In this section, we develop and solve the equations that represent the motion of combustion gases in a spinning, nutating solid propellant motor. This is an important part of the nutation instability problem for several reasons. First, it affords us the opportunity to reexamine the *jet damping* effect in the light of a complete representation of all important gas dynamic effects. In particular, it allows us to introduce corrections for rotation of the gas flow, both in the sense of spin of the motor chamber and the rotational flow effects related to vorticity transport. We will concentrate on production of vorticity by the body forces due to angular motion of the spacecraft. In the present case, vorticity created because of viscous effects plays a much less important role for reasons that will be made clear as the analysis unfolds.

Jet damping theory as it is now applied in making decisions on spin rates and other design features for spin stabilized systems is subjected to intense scrutiny. This is motivated by the great similarity in magnitude and general characteristics of the jet torque to the nutation disturbance. Thus, we are led to suspect that they may not be two separate phenomena, but on the contrary, that the nutation torque is a modified jet damping or "jet gain." That is, the jet damping interaction becomes a nutation driver as a result of certain physical features of the system. We will show that gradual increases in spin motor size and mass flow rate as payload requirements and resulting increased propulsion performance requirements have dictated are the main feature leading to the transition from spin stabilization to spin destabilization in solid propellant rocket upper stages.

The equations for the chamber internal ballistics are carefully developed and every key assumption is discussed. These are then reduced to the form that yields the classical jet damping result in order to emphasize the nature of the assumptions on which it is based. These assumptions are systematically examined and then modified to better represent the reality of the flow situation in a spinning rocket. Simple example problems are solved in detail to highlight the effects of the assumptions. We start with simple nonspinning, two-dimensional problems and gradually proceed to the full three-dimensional spinning case. Analytical solutions are used wherever possible in order to produce the clearest picture of the interaction between the several parameters that characterize the problem. These include motor size, spin rate, mass flow rate, chamber thermodynamic conditions, burn rate, and so on.

The analytical results offer us the opportunity to understand in detail the origin of the jet damping torque. This is somewhat obscured by the classical analysis which is based on simple angular momentum arguments. We will show that the jet damping torque is the resultant of the surface pressure forces within the motor chamber due to the reaction of the gas flow as it is forced to conform to the moving chamber walls. As the analysis proceeds, we will make it clear why jet damping theory fails when applied to large spinning motor cavities. The size effects will be shown to be represented by an important scaling parameter, the Rossby number that controls the nature of the chamber response. Earlier rocket systems were characterized by a relatively large Rossby number. We will show that in this case the classical theory of jet damping is adequate. However, as motor size increases, the Rossby number decreases, and when it approaches a critical value of about unity, the nature of the flow field changes dramatically. Vorticity waves are formed and may grow to significant amplitude. These modify the pressure distribution importantly and because the disturbances have wavelike characteristics they may interact in a resonant manner with the vehicle dynamics. Energy may be stored in the oscillating gas flow and significant destabilizing moments can appear under

certain conditions that we will explore in detail.

A central theme throughout this section will be the exact mechanism by which interaction torques are produced. In this we will depart from most earlier analyses including those used over the years to deduce jet damping effects. These earlier analyses have mostly taken advantage of the inherent simplicity and elegance represented by the momentum and angular momentum balances in control volume form. This gives a direct way to assess interaction forces and moments without detailed consideration of the actual process by which they are applied within the system. This is analogous to use of the usual momentum balance to deduce the thrust force produced by a propulsion system. One does not worry about the internal distribution of pressure forces that actually produce the thrust forces. It is only necessary to determine the momentum flux through the boundary of the control volume (the nozzle) and the usual formula showing thrust is equal to the mass flow rate times the average exhaust speed. We believe that much of the confusion regarding jet damping and the nutation instability problem, in general, is the result of not understanding how the forces are communicated internally between the gas and the motor chamber boundaries. In the following analyses we will carefully develop a more complete picture by closely examining the details of the internal flow with special attention to the nonuniform pressure distributions that actually account for the interaction forces and torques.

As we include more realistic fluid mechanics and geometry, our ability to deal with the problem using simple analytical techniques finally fails. If effects of compressibility, viscosity and realistic motor geometries, and boundary conditions are incorporated, the resulting mathematical problem can no longer be handled without recourse to numerical techniques. We choose to approach this problem with the most powerful tool available, the high-speed digital computer and a full compressible Navier-Stokes computational tool. A major effort was made to develop the necessary software so that realistic spinning rocket internal ballistics problems may be addressed. This program task was intended to be an exploratory effort only. However, because of its great importance, we decided to develop it to the extent possible within the contract period. A detailed discussion of our computational program completes this section of the report. We demonstrate its application in the study of spinning rocket fluid dynamics. Further, we use it to check many important findings that previously had to be based on simple analyses without any independent verification.

An important finding of the analytical study which is verified by the numerical solutions is the central role played by vorticity in the spinning rocket internal ballistics problem. The vorticity in the gas flow has not been properly dealt with in earlier models of flow interactions with vehicle dynamics, and the significance of its presence has not been appreciated. This is glaringly obvious in the case of jet damping and in some earlier attempts to analyze possible flow-induced nutation mechanisms. Effects of vorticity are important not only in the unsteady flow resulting from inertial body forces due to spin and nutation but in the steady flow itself. This results not only from spin effects but also from the type of boundary conditions that characterize gas flow produced in a chamber by combustion at a propellant surface. We will demonstrate all of these effects by means of simple examples as we work toward a complete determination of the flow in a spinning motor system.

As in previous sections, all details of the analytic developments are presented in order that the findings are available to persons not having extensive experience in fluid dynamics. It is expected that most readers will be in this category. Those needing only physical descriptions and discussions of the experimental findings should find the material in the executive summary sufficient. Again, the attempt is made in what follows to show all details of the transition from

fundamentals to their application to the several classes of problems that must be solved. These include the details of the gas motions in the chamber and the effects of these motions on the force system acting on the vehicle. All assumptions are justified as thoroughly as it is possible to do in the available space. Obviously, some subjective judgement is necessary in any analytical procedure. Whenever possible, the successful application of analogous assumptions in other fields is cited as evidence of the validity of the judgement.

Formulation of Flow Equations for a Spinning, Nutating Rocket Chamber

In this subsection, we will show how the governing equations for the unsteady flow of combustion gases through a spinning, nutating rocket motor are derived from the fundamentals of fluid dynamics. Two types of formulations will be used. In the first case, we will attempt to reduce the equations to a form appropriate for the generation of analytical solutions. In the second, we will set the problem up for numerical solution. The latter is obviously the preferred approach to the problem because, in principle, it allows direct treatment of all the features that make the problem complicated. The problems associated with difficult geometrical features such as a complex propellant burning surface and chamber shape with a submerged nozzle are fairly easily handled in a finite-difference numerical approach. Similarly, the need to handle a flow field comprised of several types of flow regimes from inviscid to highly viscous and from incompressible to compressible can be addressed without difficulty only by numerical means.

However, to rely entirely on numerical techniques would be a mistake at the present stage of understanding of the nutation instability problem. Development of reliable numerical solutions is a very difficult undertaking fraught with pitfalls analogous to those we face in developing experimental approaches to the problem. It is important that we deduce, insofar as possible, the nature of the flow from the simplest possible analyses. This brings into focus the interactions between the parameters of the problem. This information provides guidance for both the numerical and experimental study of spinning motor flows.

As more is learned of the phenomenon, it will undoubtedly be possible to reduce the main findings to simple analyses and design tools that are adequate for engineering calculations. An entire section of the report is devoted to reduction of the findings of the research to this form. The result is a set of interim scaling rules that can be applied immediately in attacking nutation instability control system sizing problems and in interpretation of experimental data. These rules will be improved as more experimental information becomes available, and as experience accrues in their application in actual system studies.

A basic assumption to be used is that the combustion gases behave as a compressible Newtonian fluid. We will include the effects of the two-phase flow of particulate matter within the gas stream produced in the combustion of the metallic additives in the propellant. These are the source of the aluminum oxide slag that is blamed for nutation instability in other studies. This will be done in a simple way by adjusting the gas properties to reflect the influence of the particulates. The basic hypothesis used here is that it is the gas dynamics that controls the slag motion. That is, slag does not form liquid pools that oscillate independently of the gases. Questions related to the effects of slag require a great deal more study than could be devoted in this one-year program, but first steps are taken in the formulation process. Some possible implications of the influence of the Al_2O_3 particles on the nutation problem from the gasdynamic standpoint will be discussed in later subsections.

Governing Equations and Dimensionless Variables

The set of equations that describe time-dependent motion of a compressible, viscous flow of combustion gases consists of continuity, momentum, energy, and state equations shown in Table 1. The flow is assumed to be Newtonian. The equations shown are in dimensional form, but it is advantageous to render them dimensionless in order that dependence on the parameters of the problem can be emphasized. The value of this approach need not be justified further here.

Definitions for the dimensionless variables are not unique. However, the choices for scaling parameters are fairly obvious in the coning problem. The motor chamber size provides the appropriate length scale. Either chamber length or radius can be used since they are proportional for a given motor. The latter seems more convenient and it is used here. Several characteristic velocities are available, but one that makes the most sense is one that represents a measure of the flow speed through the chamber. We select the speed of gas particles emerging from the burning zone of the propellant as the most appropriate velocity scale. This velocity is readily estimated from knowledge of the propellant characteristics and the motor chamber pressure using the standard exponential burning rate law

$$v_b = \left(\frac{\rho_p}{\rho} \right) r = \left(\frac{\rho_p}{\rho} \right) a \left(\frac{P}{P_{ref}} \right)^n \quad (56)$$

where ρ is the gas density and ρ_p is the density of the solid propellant. v_b is very nearly constant at any point in the chamber. The coefficient a and exponent n characterize a particular propellant.

Table 1. Governing Equations for Chamber Flow

Equations in Dimensional Form:	
$\frac{\partial \rho^*}{\partial t^*} + \nabla \cdot (\rho^* \mathbf{u}^*) = 0$	(57)
$\frac{\partial \mathbf{u}^*}{\partial t^*} + \mathbf{u}^* \cdot \nabla \mathbf{u}^* = -\frac{\nabla P^*}{\rho^*} - \boldsymbol{\omega}^* \times \boldsymbol{\omega}^* \times \mathbf{r}^* - 2\boldsymbol{\omega}^* \times \mathbf{u}^* - \frac{\partial \boldsymbol{\omega}^*}{\partial t^*} \times \mathbf{r}^* - \mathbf{a}_o^* + \nu \nabla^2 \mathbf{u}^*$	(58)
$c_p \left(\frac{\partial T^*}{\partial t^*} + \mathbf{u}^* \cdot \nabla T^* \right) = \frac{1}{\rho^*} \left(\frac{\partial P^*}{\partial t^*} + \mathbf{u}^* \cdot \nabla P^* \right) + \frac{\partial Q^*}{\partial t^*} + \Phi + \frac{\kappa}{\rho^*} \nabla^2 T^*$	(59)
$P^* = \rho^* R T^*$	(60)

There are several choices for a time scale. For instance, the period of nutation oscillations would be an appropriate choice. However, the nutation frequency is proportional to the rate of spin of the vehicle about its axis of symmetry. Thus a convenient time scale is the inverse of the spin rate Ω . If we use the mean gas density in the chamber as a measure of the mass distribution, we can characterize all physical parameters that appear in the problem. Table 2 summarizes the set of dimensionless variables constructed in this way. At this point in the analysis we must include continuity, momentum, energy and state equations in order that a

complete description of the gas motion is available. In starting the numerical treatment of the problem, these are the equations to be addressed. In a later section we will describe further rearrangements necessary to allow efficient numerical solution of this set.

When we use analytical methods in treating the flow within the chamber we will take advantage of the fact that the Mach number is very small except in the vicinity of the nozzle entrance. Thus the flow is essentially incompressible everywhere but in the nozzle. This is verified numerically using geometry and parameters for typical space motors.

Table 2. Dimensionless Variables

Length:	$r = \frac{r^*}{R}$	Pressure:	$P = \frac{P^*}{\rho_o R \Omega v_b}$
Time:	$t = \Omega t^*$	Force:	$F = \frac{F^*}{\rho_o R^3 \Omega v_b}$
Velocity:	$u = \frac{u^*}{v_b}$	Moment:	$M = \frac{M^*}{\rho_o R^4 \Omega v_b}$
Acceleration:	$a = \frac{a^*}{\Omega v_b}$	Star * denotes dimensional quantity	
Angular Velocity:	$\omega = \frac{\omega^*}{\Omega}$		

Similarity Parameters

Table 3 defines the several similarity parameters that appear naturally in writing the equations in dimensionless form. If the speed of sound were to be used as the reference speed (a choice that would be appropriate in regions dominated by compressibility) then the Mach number appears instead of the Rossby number. Also, in that case, a Reynolds number takes the place of the Ekman number that appears with our choice of governing variables. Mach number and Reynolds number represent concepts familiar to all; Rossby number and Ekman number are less familiar, and it is appropriate that we carefully define their physical interpretation.

Table 3. Similarity Parameters

Mach Number:	$M_b = \frac{v_b}{a_o}$	Relative Importance of Compressibility
Ekman Number:	$E = \frac{\mu}{\rho_o R^2 \Omega} = \frac{\nu}{R^2 \Omega}$	Relative Importance of Viscosity
Rossby Number:	$Ro = \frac{v_b}{R \Omega}$	Relative Importance of Coriolis Acceleration (Small Rossby number indicates important Coriolis Effects)

This is of great importance as we plan the strategy needed for developing analytical solutions. For instance, solutions for "small Ekman number" imply the same set of assumptions one would invoke for a "large Reynolds number (inviscid)" solution. A small Rossby number solution is somewhat analogous to a small Mach number solution although quite different physical effects are being addressed.

The Rossby number is a very important parameter because it governs the relative effects of gas motion due to convection and to motion of the chamber. It can be interpreted in a variety of ways. The standard definition is that it is a measure of the importance of Coriolis forces in the flow field as compared to convective forces. A very large Rossby number indicates that Coriolis forces play a minor role. Small values imply that inertial forces are a major influence on the gas motion. A few simple examples are useful in developing a feel for the significance of the Rossby number.

In our definition of the Rossby number, it is the ratio of the mean flow velocity through the chamber to the product of the characteristic length, the radius[†], and the spin rate:

$$Ro = \frac{vb}{R\Omega} \quad (61)$$

It is easy to see that the product in the denominator is a measure of the azimuthal speed (in absolute coordinates) of a fluid particle due to rotation about the motor axis, so the Rossby number measures the relative speeds. Clearly as the motor spin rate or size increased, the Rossby number decreases indicating that spin effects are relatively more important. It is of great significance that the major difference between earlier space vehicles that did not cone and later ones of similar design that did is that the motor chamber size increased. That is, the trend has been to lower Rossby numbers. We take great pains to show that this means that the departure from a simple flow interaction as in classical jet damping to the complex unsteady flow in large motors is related to the decrease in Rossby number.

This parameter plays a central role in choosing mathematical strategies for approaching the nutation instability problem. Notice that for large stay-times implying a large modification of the internal flow by Coriolis forces, the Rossby number is small. The reason the simple theories of jet damping worked in smaller rockets was that the Rossby number was very large, and the assumption of a uniform gas stream unaffected by the vehicle wobbles was justified. This is equivalent to the statement that the Coriolis forces in the flow relative to the chamber are balanced by the pressure forces acting on its boundaries. The integrated pressure force is the jet damping resistance.

Flow Regimes

In formulating an analytical approach to the formidable problem of flow in a rotating rocket chamber, it is a great help to take advantage of certain characteristics of the field in several distinct regions of the chamber. This is a standard procedure that has been used (for example in aeronautics) to make it possible to deal with complex flow problems. In effect the problem is reduced to a series of simpler ones each corresponding to one of the flow regions. These are linked across boundaries between the regions and may be used to formulate boundary conditions as one moves from one region to another. A good example is the

[†]The radius used in the definition of the Rossby number is the instantaneous radius of the combustion chamber. Since the chamber shape can be irregular, we take this to be the radius of the "best-fit" right circular cylinder.

treatment of boundary layer flows in which viscous motion dominates in a thin region next to the surface of a body and the flow outside this region that may be represented as an inviscid fluid.

There are several flow regimes of potential importance in the present problem. Several boundary flows may be required. Examples are those gas layers near the burning propellant surface and the Ekman layers at inert chamber surfaces. We will assume that such regions are so thin that they may be treated separately from the main chamber in a standard boundary layer approach. Results from their analysis provide boundary conditions on the main chamber flow.

Notice that the main chamber volume may be represented by an incompressible flow since the Mach number is very small everywhere except within the gas entering the nozzle at which point compressibility dominates the flow. The small Mach number is the result of the elevated gas temperature and resulting high speed of sound and the low mean flow speeds resulting from low burn rates used in most space motor designs.

Flow in the Main Chamber

Let us now write the equations that will be of central importance in the analysis. These govern the motion within the major volume of the combustion chamber and strongly control the behavior of the interactions with the nutating vehicle. In addition to the simplifications resulting from relegation of viscous effects to boundary layers and to taking wholesale advantage of the incompressible nature of the flow, we will find it a great benefit to further break the flow into steady and unsteady parts. This allows us to break the effects of rotation into two parts. The first represents the effect of the main chamber spin on the gas motion. This is a steady effect since changes in the spin rate take place very slowly compared to the nutation oscillations. The latter control the time-dependent motion. In this regard we can also take advantage of the smallness of the lateral angular velocity amplitude compared to the main spin and develop a perturbation approach that effectively linearizes the problem. The angular velocity perturbations representing the nutation wobble are directly responsible for exciting unsteady gas motions within the chamber. We will see that these are nonuniform and may give rise to unbalanced torques acting on the vehicle system. Since the wobble angular velocity is small, it is appropriate to treat the time-dependent gas oscillations also as small perturbations.

In the main chamber, the flow is governed by

$$\left\{ \begin{array}{l} \nabla \cdot \mathbf{u} = 0 \end{array} \right. \quad (62)$$

$$\left\{ \begin{array}{l} \frac{\partial \mathbf{u}}{\partial t} + Ro \mathbf{u} \cdot \nabla \mathbf{u} = - \left[\nabla P + \frac{1}{Ro} \boldsymbol{\omega} \times \boldsymbol{\omega} \times \mathbf{r} \right] - 2\boldsymbol{\omega} \times \mathbf{u} - \frac{1}{Ro} \frac{\partial \boldsymbol{\omega}}{\partial t} \times \mathbf{r} - \mathbf{a}_o + E \nabla^2 \mathbf{u} \\ \quad = - \nabla p - 2\boldsymbol{\omega} \times \mathbf{u} - \frac{1}{Ro} \frac{\partial \boldsymbol{\omega}}{\partial t} \times \mathbf{r} - \mathbf{a}_o + E \left[\frac{4}{3} \nabla (\nabla \cdot \mathbf{u}) - \nabla \times \nabla \times \mathbf{u} \right] \end{array} \right. \quad (63)$$

where the energy and state equations are no longer needed since the flow is incompressible. The centripetal acceleration is combined with the pressure since it can be written in gradient form. We define the reduced pressure as

$$p = P - \frac{1}{2Ro} (\boldsymbol{\omega} \times \mathbf{r})^2 = \text{Reduced Pressure} \quad (64)$$

We break the flow into steady and unsteady parts by writing

$$\mathbf{u} = \mathbf{U} + \mathbf{u}' \quad (65)$$

$$p = P_0 + p' \quad (66)$$

where \mathbf{U} and P_0 represent the steady flow and \mathbf{u}' and p' represent the unsteady corrections. It is very important to understand that the unsteady terms are very small compared to the mean flow effects. One expects only a small response in gas motion to the chamber wobbling. This requires numerical verification, but will be assumed to be true at this point.

Equations in Vorticity Transport Form

As already brought out in emphatic terms, it is crucial in dealing with motor flows in spinning wobble motion to consider the generation and propagation of vorticity. Therefore, we devote this subsection to a brief review of the associated fluid mechanics and to the steps needed to rewrite the momentum equation in vorticity form. That is, as an equation with the vorticity vector as the main variable.

The vorticity is defined as

$$\boldsymbol{\zeta} = \nabla \times \mathbf{u} \quad (67)$$

and represents a vector with twice the instantaneous angular velocity of the fluid particle located at its point of evaluation. The vector points along the instantaneous axis of spin of the particle. In an inviscid flow, there is no decay of particle spin so any vorticity present must have its origin in body forces of certain types or in effects influencing the flow before it enters the region of interest. To put the momentum equation in vorticity form one takes the curl of both sides with the result

$$\frac{\partial \boldsymbol{\zeta}}{\partial t} - Ro \nabla \times (\mathbf{u} \times \boldsymbol{\zeta}) = -2 \nabla \times (\boldsymbol{\omega} \times \mathbf{u}) - \frac{1}{Ro} \nabla \times \left(\frac{\partial \boldsymbol{\omega}}{\partial t} \times \mathbf{r} \right) - E (\nabla \times \nabla \times \boldsymbol{\zeta}) \quad (68)$$

where viscous terms have been retained. The vorticity must also satisfy the "vorticity continuity" relationship

$$\nabla \cdot \boldsymbol{\zeta} = 0 \quad (69)$$

since by a well-known vector identity,

$$\nabla \cdot \nabla \times \mathbf{u} = 0 \quad (70)$$

Thus in any given situation, the vorticity must satisfy this pair of equations.

Several properties of vorticity are worth reviewing. First of all, vorticity is a property of the fluid that stays attached and propagates with fluid particles. If one identifies a particular particle at a given instant and position, its spin, or vorticity would stay constant as it moves with the stream unless acted upon by body or viscous forces. Descriptions of such fluid motion is contained in the famous Helmholtz vorticity laws. These provide incredible physical insight that we will use continually throughout the analysis. Readers not familiar with these ideas are directed to several excellent discussions (see refs. 31 and 32) that are easily accessed even by those without extensive fluid dynamics training. Concepts such as vortex stretching, vortex tubes, and so on will be of great value in interpreting the complex flow in a spinning motor.

It is very useful to carefully rewrite the momentum equation in a form that can be interpreted in the usual fluid mechanics fashion. That is, we wish to put the left-hand side in the form of the total (or substantial) rate of change of the vorticity. This is analogous to the momentum equation in velocity form. To put the vorticity equation in similar form we expand the cross product term on the left side. After applying standard vector identities we find

$$\begin{aligned} \frac{\partial \zeta}{\partial t} + Ro \mathbf{u} \cdot \nabla \zeta = & Ro(\zeta \cdot \nabla) \mathbf{u} - Ro \zeta \nabla \cdot \mathbf{u} - 2(\boldsymbol{\omega} \nabla \cdot \mathbf{u} - \boldsymbol{\omega} \cdot \nabla \mathbf{u}) - \\ & - \frac{1}{Ro}(\boldsymbol{\alpha} \nabla \cdot \mathbf{r} - \boldsymbol{\alpha} \cdot \nabla \mathbf{r}) - E(\nabla \times \nabla \times \zeta) \end{aligned} \quad (71)$$

where additional simplifications have been performed on the right-hand terms. The various terms have clear physical interpretations. Identifying each term we find

$$\begin{aligned} \frac{D\zeta}{Dt} = \underbrace{\frac{\partial \zeta}{\partial t} + Ro \mathbf{u} \cdot \nabla \zeta}_{\text{Total Vorticity Rate of Change}} = & \underbrace{Ro(\zeta \cdot \nabla) \mathbf{u} - Ro \zeta \nabla \cdot \mathbf{u}}_{\text{Vortex Stretching and Divergence Effect}} + \underbrace{2(-\boldsymbol{\omega} \nabla \cdot \mathbf{u} + \boldsymbol{\omega} \cdot \nabla \mathbf{u})}_{\text{Coriolis Effect}} + \\ & + \underbrace{\frac{1}{Ro}(-\boldsymbol{\alpha} \nabla \cdot \mathbf{r} + \boldsymbol{\alpha} \cdot \nabla \mathbf{r})}_{\text{Angular Acceleration Effect}} - \underbrace{E(\nabla \times \nabla \times \zeta)}_{\text{Viscous Shear Effect}} \end{aligned} \quad (72)$$

which shows that vorticity changes are affected by several influences that act in spinning motor problems.

The first term on the right of equation 72 represents modification of vorticity by "stretching," that is, by lengthening of vortex tubes. This effect is important as gases move into the constriction represented by the nozzle throat. Vortex lines must be lengthened enormously with a resultant increase in particle spin. This is closely related to conservation of angular momentum. For instance, the axial vortex formed in the mean flow spins faster as it is stretched through the nozzle. We will demonstrate this and similar effects as we develop the necessary chamber flow solutions.

The second term represents the effect of the Coriolis body force. This will be a key item in later parts of the analysis where we will find that the Coriolis force is directly responsible for the jet damping. Its presence in the vorticity transport equation is significant. We will need to see how production of vorticity is affected by this important body force.

The third term is analogous to the Coriolis effect. It represents the fact that the angular velocity environment may be changing with time. That is, we must account for the angular acceleration body forces. These are also sometimes included in the jet damping definitions as we shall see.

The fourth and last term reflects the presence of viscosity. Normally, viscous forces will only be important in highly sheared regions of the flow wherein the velocity changes rapidly in a short distance. Such regions are represented by the boundary layers at solid surfaces and in the core of rapidly spinning vortices.

We will continually refer to the definitions and observations made in this subsection as we pursue an understanding of the internal flow in a spinning motor. Again, readers that are seriously concerned with interpretation of the results presented later should make sure that the concepts discussed here are understood completely. Again, the stigma of "dirty fluid mechanics" must be dealt with. One must accept that fluid flows, especially rotational ones, are exceedingly complex and involve a rich variety of physical phenomena. To describe them requires that we adopt a more broad view of nature than needed in simple particle dynamics or rigid body dynamics usually associated with spacecraft dynamic problems.

The equations presented in this subsection are completely general except for a few easily justified simplifying assumptions. The assumption of a Newtonian gas is the most far reaching. We have yet to deal with assumptions regarding time-dependence, compressibility, and viscous forces. In the following sections we will process and simplify the equations further to tailor them to specific applications. This will be done first in regard to the jet damping effect. It is vitally important to gain a full understanding of this part of the problem because it represents the "jumping off point" from accepted flow interaction effects into a new area of rocket motor analysis. We will then deal with the important problem of the mean or steady part of the flow field in a spinning rocket. This is an important step in treating the unsteady cases that we need in understanding nutation instability flow interactions.

Simple Flow Interactions: Jet Damping

The jet damping calculation is based on an extremely crude model of the dynamics of the system and must be subjected to careful scrutiny. Unfortunately, the "classical" jet damping model has been used for such an extended period of time that its validity is seldom questioned. It has not previously been subjected to either a searching analysis or a detailed experimental verification. The classical model apparently has a range of validity that adequately covers earlier applications, such as in small artillery rockets, but its validity in the case of large spinning systems has not been established. The purpose of this section is to subject jet damping to a searching examination in terms of its applicability in modern space motor applications.

It is very important that one fully understands the jet damping mechanism, the set of assumptions on which it is based, and the corrections that must be made in order that it can be applied with confidence to the case of large spin-stabilized rocket systems. Armed with the detailed formulation of the fluid mechanics of a spinning rocket developed earlier, we are now in a position to ask the right questions regarding the validity of the accepted jet damping model.

In this subsection, we will carefully investigate the origins of the jet damping concept along with the assumptions and observations on which it is based. We will then proceed to test these underlying assumptions to determine the range of validity of the accepted jet damping algorithm. Effects of motor size, combustion chamber and nozzle geometry, and axial spin

will be carefully examined.

The close correspondence of both the magnitude and time history of the theoretical jet damping torque to the apparent disturbing torque determined from PAM-D and DII flight data has been emphasized in earlier sections. This leads to several significant observations:

- The interaction between spacecraft motion and the motor gas flow leads to a force system with magnitudes comparable to those producing the coning.
- The correspondence in amplitude and time history is too close to be purely coincidental.
- Jet damping predictions are based on simplistic models of the combustion chamber gas flow that do not account for potentially important interactions that can affect both magnitude and direction of the force system acting on the vehicle.

It is also interesting to observe, that if interaction forces determined using jet damping concepts were applied to the vehicle *with reversed sense*, then the resulting motion would closely resemble the observed coning instability.

Origins of Classical Jet Damping Concepts

It is useful to trace the origins of jet damping or "thrust damping" as it is sometimes called in order to expose the underlying assumptions about motor operation on which it is based. The first formal mention of jet damping was in the text on theory of rocket flight by Newton, Rosser, and Gross.³ This publication was based on a secret wartime study performed during 1944 and 1945 at the Allegheny Ballistic Laboratory by the same authors. The origins of the concept are not known precisely, but postwar questioning of German rocket experts makes it clear that jet damping was known to them and accounted for in their missile programs.

Many authors have contributed to the gradual development of the accepted theory. Several improvements were introduced in the text by Davis, Follin, and Blitzer⁴ and by Kolk.⁵ A clear presentation of the simple theory both with and without spin is given by Thomson.⁶ Thomson also demonstrated that the theory closely fit experimental data from the Explorer 6 spinning orbital injection stage.⁷ There were indications of nutation divergence near the end of the (short) motor burn, but these were small and were perhaps the result of a nonuniform pressure distribution within the motor as the propellant surface burned to the chamber wall.

With such impressive experimental verification, it may appear to the reader that we are barking up the wrong tree. However, we will show conclusively that jet damping theory was a reasonable model for flow interactions until more recent flight operations in which motor size exceeded a critical limit.

A more recent work by Rott and Pottsepp⁸ includes a somewhat more careful assessment of the effects of the details of the internal flow field. However, the authors yield to the temptation of oversimplification, and finally state that it is appropriate to make the "... apparently radical simplifying assumption ..." that the gas flow is everywhere parallel to the motor axis of symmetry regardless of the lateral angular disturbances represented by the nutation wobble. We will demonstrate that this picture of the flow is inappropriate in a large spinning rocket. It precludes the possibility that the flow streamlines are perturbed by the external motion of the vehicle.

Despite the significant attention devoted to jet damping over the years the model used at present in making important system design decisions is nearly indistinguishable from that used in 1947. This is largely the result of the failure to assess the effects of the internal ballistics in a realistic way. Also, as we shall show, axial spin greatly affects the jet damping behavior. This is contrary to the results of simplified jet damping theory which indicates that the interaction forces are not affected by spin. As pointed out by Rosser, et al., in 1947, no careful experimentation has been made to verify it and they state that "... in fact the whole question of jet damping has received little attention... We are thus compelled to leave the reader with jet damping in an unsettled status." Unfortunately, the same observations hold forty years later; little improvement has been made in the theory and no detailed experimentation has been carried out to verify it. The reasons for this are that in most circumstances it represents a fairly minor influence on the vehicle motion and usually a beneficial one at that. Thus, until the discovery of the PAM-D nutation phenomenon, there has simply been no motivation for research on this seemingly simple and well-understood phenomenon.

The Classical Jet Damping Effect: Angular Momentum Approach

By the "classical jet damping" effect, we mean the accepted model that is based on a simple angular momentum balance for a dynamic system of variable mass. In starting a detailed analysis, it is essential to understand that simple jet damping does not depend on the presence of axial spin. It is simply the response of the system to changes in direction of the gas stream emanating from the vehicle. If the rocket rotates around an axis normal to the nominal direction of motion, forces between the gas flow and chamber boundaries must arise in the accommodation of the gas to the changing geometry. That is, the gas must accelerate since a direction change is required.

We start the analysis by reviewing the simplest case without spin. We will determine what changes result, if any, when axial spin is introduced. The approach to be used in this section is from the point of view of the fluid mechanics of the problem; this is an aspect given scant attention in the classical analysis or in subsequent analyses. First, however, we will carefully review the classical analysis in order to identify all of the assumptions used and to guide us in later, more complete, calculations.

In the early analyses given in the literature (Refs.3-7) the problem is attacked from the point of view of Lagrangian dynamics. The gas flow is treated as a simple stream of particles produced at an indefinite point within the system. It is often assumed that the particles emanate from the center of mass. Since no attention is paid to the particle trajectories and interaction forces within the motor chamber, a simple momentum balance is used to estimate the effect on lateral motion of the vehicle. The analysis given here is identical to that in reference 3, which was followed later, with minor variations, and evolved into the form used presently.

At the outset, it is important to notice that no attempt is made to account for axial spin. Later analysts included spin, but made the strong assumption that this has no effect on the characteristics of the internal flow. We will examine this situation in detail.

The vehicle is assumed to be yawing about its center of mass in a plane at instantaneous rate, $\dot{\phi}$. The moment of inertia about the yaw axis is

$$I = mk^2 \quad (73)$$

where k is the radius of gyration and m is the instantaneous mass. If no consideration is given to the motion of combustion gases within the vehicle and the flow is uniform across the nozzle

exit, then a gas particle of mass dm leaving the system has a sidewise velocity component of

$$L_{cg} \dot{\phi} \quad (74)$$

where L_{cg} is the distance from the mass center to the nozzle exit plane. Therefore the same particle carries angular momentum of

$$m L_{cg}^2 \dot{\phi} \quad (75)$$

with respect to the mass center. The flux of angular momentum for the entire gas stream is therefore

$$\frac{d}{dt}(mk^2 \dot{\phi}) + m L_{cg}^2 \dot{\phi} = \text{Externally Applied Torques} \quad (76)$$

again assuming uniform gas motion relative to the vehicle. If one now considers the angular momentum balance for the entire system, assuming that no external moments are present, then

$$\frac{d}{dt}(mk^2 \dot{\phi}) = -m L_{cg}^2 \dot{\phi} \quad (77)$$

which states that the rate of change of system angular momentum equals the rate of flux of lateral angular momentum. We will have cause in the next section of the report to more carefully derive a more general form of this expression. Note that in the form given, the angular momentum flux can be interpreted as an "interaction torque," which modifies the angular motion of the system. We will usually refer to this as the jet damping torque, but in the classical analysis, the vehicle angular momentum is differentiated to give

$$mk^2 \ddot{\phi} = -m(L_{cg}^2 - k^2)\dot{\phi} - 2mk \frac{dk}{dt} \dot{\phi} \quad (78)$$

and the jet damping torque is taken as the combination shown when all but the term involving the product of the lateral moment of inertia times the angular acceleration are moved to the right hand side. The term involving the rate of change of the radius of gyration is small and is usually neglected. Therefore, the classical definition of the apparent jet damping moment is

$$M_j = -m(L_{cg}^2 - k^2)\dot{\phi} \quad (79)$$

Notice that the damping is negative (that is, lateral oscillations are reduced) when the length L_{cg} is larger than the radius of gyration. This is normally the case for typical slender vehicles of conventional layout with the nozzle at the rear-most position. The second term in the expression represents the effect of flow of mass from the system on the lateral inertia. It could be interpreted as a "driving" effect because it is always negative. The net jet damping is a balance of the speeding up of the lateral rate, due to loss of system mass against the slowing down because the gas particles must be accelerated within the system in order that they exit the system with the same lateral speed as a point on the nozzle exit plane. The original analysts were somewhat concerned about the simplifications leading to this result as expressed in the following excerpt from their writeup:

"We call attention to one tacit assumption made in deriving the formula for jet damping. When we gave the sidewise component of velocity of the gas issuing from the nozzle as we were assuming that the gas was going "straight" through the nozzle. Actually, this has not been proved so far as we know... it needs to be shown that the

main stream of gas going through the nozzle shares this sidewise motion. One can make a rough argument as follows: Until the gas reaches the throat of the nozzle, it is moving more slowly than the speed of sound. Hence disturbances, such as the yawing motion of the rocket can be propagated into the gas stream faster than they are swept downstream by the gas flow. Consequently, *we may expect the gas stream as a whole to participate in the yawing motion of the rocket until it reaches the throat of the nozzle.* Thereafter, the gas is going faster than the speed of sound and *probably leaves the nozzle without acquiring any additional sidewise motion.* Thus the sidewise motion of the gas is probably where L_t is the distance from the center of gravity of the rocket to the throat of the nozzle. This is multiplied by $\dot{\theta} L_t$ and so we conclude that probably L_{cg}^2 should be replaced by $L_t L_{cg}$ in equation 79." †

This is the first discussion in the literature indicating suspicion that the fluid dynamics of the situation is more complicated than assumed. Suggestions for possible experimental means for checking the validity of the jet damping term then followed. Such experiments have apparently never been conducted until those carried out in the present program.

The reader should notice that the interaction torque was estimated by a process that bypassed the need to understand the manner in which the torque is actually applied to the vehicle. Clearly this must be through an unsymmetrical pressure distribution by analogy with the origin of momentum thrust. As with the latter force, a good estimate can be made without recourse to actually determining the pressure distribution or any other details of the internal flow and the momentum changes that produce the forces. Unfortunately, this procedure is fraught with danger because it is a great temptation to oversimplify the fluid mechanics. In the thrust calculation such simplifications, such as one-dimensional uniform flow have little effect, but when subtle changes in angular momentum balance are involved it would appear that more care is warranted. In the next section we begin our detailed study of jet damping by examining the details of the pressure distributions that actually produce the damping torque.

The Classical Jet Damping Effect: Fluid Dynamics Approach

In this subsection, we will reexamine origins of the jet damping effect from the point of view of the flow of gas particles. In order to set the stage for our complete calculations to be presented in later sections, we will base the analysis on standard Eulerian fluid mechanics. This requires a more involved mathematical formulation than needed in the Lagrangian approach. The governing equations will be carefully analyzed after being put in appropriate nondimensional form to bring out the important scaling and similarity parameters. All calculations will be discussed in rather complete detail for the benefit of readers not familiar with the Eulerian point of view. Those with fluid dynamics backgrounds will be able to skim to the end of each subsection in order to concentrate on the results of each calculation. We will review all assumptions needed to extract the classical jet damping effect from the field equations describing the gas flow.

In the classical theory, one simply assumes that there is nothing interesting going on inside the motor chamber. Combustion gas is produced at the burning surface and then commences to travel in straight lines through the chamber and out the nozzle despite any lateral oscillations

† Italics were added by the writer for emphasis. Equation numbers and notation have been modified to correspond to those in the present report.

of the chamber. Let us see what the fluid dynamics equations tell us about this assumption. If we assume the gas is incompressible and steady, the flow is governed by

$$R\omega \cdot \nabla \mathbf{u} = -\nabla p - 2\omega \times \mathbf{u} - \frac{1}{Ro} \frac{\partial \omega}{\partial t} \times \mathbf{r} \quad (80)$$

Now, if we further assume the flow is uniform, that is, there is no variation in speed or direction of the gas particles as they flow through the chamber then the pressure gradient is given by

$$\nabla p = -2\omega \times \mathbf{u} - \frac{1}{Ro} \frac{\partial \omega}{\partial t} \times \mathbf{r} \quad (81)$$

which shows that the pressure forces are balanced by a combination of the Coriolis force and the effect of angular acceleration. Remember that centripetal effects are integrated within the "reduced pressure" p because they can be written as the gradient of a potential. Now, if we assume that the angular velocity perturbation follows the simple pattern we established in the last chapter for a spinning, nutating body, it is easy to determine the pressure distribution produced in the chamber when it is wobbling. This angular velocity vector

$$\omega' = \omega_0 \exp(i\lambda t) = \omega[1 + i\mathbf{j}] \exp(i\lambda t) = \omega[\mathbf{e}_r + i\mathbf{e}_\theta] e^{i\theta} \exp(i\lambda t) \quad (82)$$

closely simulates the conditions present in a nutating PAM-D. Please note that this is the perturbation angular velocity introduced in equation 1. It follows the form suggested earlier (see development leading to equation 51) in carrying out simple solutions for the spacecraft motion. The use of complex notation simplifies the bookkeeping involved in keeping track of the relative angular position or phase angle of the angular velocity perturbation and any resulting flow phenomena with respect to the body-fixed coordinates. Also, the conversion to polar coordinates is shown to make evaluation of the equations easier for axisymmetric chamber geometries.

Since we require the flow to remain uniform with respect to the wobbling chamber, then it is clear that the pressure must vary in time in the same manner as the angular velocity in order that the momentum equation is satisfied. The time dependence is accounted for by putting

$$p' = \phi \exp(i\lambda t) \quad (83)$$

where λ is the precession frequency as discussed earlier, and ϕ is the spatial part of the pressure distribution.

For simplicity, let us assume that the chamber is a straight cylinder with an end-burning propellant grain at the head end. As in classical theory, we assume a uniform flow

$$\mathbf{U} = -k \quad (84)$$

The position vector for the coordinate system described earlier (body-fixed with the origin at the mass center) is

$$\mathbf{r} = r\mathbf{e}_r + (z' - L_t)\mathbf{k} \quad (85)$$

and we can easily evaluate the pressure gradient. Resolving the gradient into its polar components, we find

$$\nabla\phi = \frac{\partial\phi}{\partial r} \mathbf{e}_r + \frac{1}{r} \frac{\partial\phi}{\partial\theta} \mathbf{e}_\theta + \frac{\partial\phi}{\partial z} \mathbf{k} = \varpi \exp(i\theta) \begin{cases} \mathbf{e}_r \left[2i + \frac{\lambda}{Ro} (z' - L_t) \right] \\ \mathbf{e}_\theta \left[-2 + i \frac{\lambda}{Ro} (z' - L_t) \right] \\ \mathbf{k} \left(-\frac{\lambda}{Ro} r \right) \end{cases} \quad (86)$$

These are readily integrated to yield a simple expression for the pressure distribution throughout the chamber volume. The result is†

$$\phi = \varpi \exp(i\theta) \left[\frac{\lambda}{Ro} r (z' - L_t) + i(2r) \right] \quad (87)$$

and therefore the real part of the pressure perturbation is (using expression 83)

$$p' = \varpi \left[\frac{\lambda}{Ro} r (z' - L_t) \cos(\lambda t + \theta) - 2r \sin(\lambda t + \theta) \right] \quad (88)$$

The two remaining terms represent the effect of Coriolis and angular acceleration effects. The Coriolis term (the second term in the brackets) is the one responsible for most of the features of classical jet damping.

† For the benefit of readers not familiar with complex notation, the details of this derivation follow:

Note that $\exp(i\lambda t) = (\cos \lambda t + i \sin \lambda t)$ and $\exp(i\theta) = (\cos \theta + i \sin \theta)$ so their product is

$$\begin{aligned} \exp(i\lambda t) \exp(i\theta) &= (\cos \lambda t + i \sin \lambda t)(\cos \theta + i \sin \theta) = \\ &= (\cos \lambda t \cos \theta - \sin \lambda t \sin \theta) + i(\cos \lambda t \sin \theta - \sin \lambda t \cos \theta) = \\ &= \cos(\lambda t + \theta) + i \sin(\lambda t + \theta) \end{aligned}$$

where standard trigonometric identities have been employed. If this combination is multiplied by any complex number, say $(a + ib)$ as in the square brackets in equation 87, we find for the real part of the product,

$$\begin{aligned} \Re\{\exp(i\theta) \exp(i\lambda t) (a + ib)\} &= \\ &= \Re\{ [\cos(\lambda t + \theta) + i \sin(\lambda t + \theta)](a + ib)\} = \\ &= \Re\{ [a \cos(\lambda t + \theta) - b \sin(\lambda t + \theta)] + i[a \sin(\lambda t + \theta) + b \cos(\lambda t + \theta)] \} \\ &= a \cos(\lambda t + \theta) - b \sin(\lambda t + \theta) \end{aligned}$$

Notice that in the pressure function ϕ , the Coriolis term is positive and imaginary while the angular acceleration term is real. We will show that a positive imaginary part always implies a damping influence since the torque on the chamber from the integrated pressure distribution will be opposite to the perturbation angular velocity vector. For later use, we note that *in order for a pressure distribution to be destabilizing the imaginary part must be negative*. It is also worth remembering that any torque component normal to ω' has the effect of modifying the precession frequency. Therefore, in the present case the Coriolis yields a damping influence, the jet damping, and the angular acceleration term produces a shift of wobbling frequency. Also notice that the Coriolis term does not vary with axial position; the angular acceleration term is directly proportional to axial position in the chamber.

Figure 31 shows the pressure distribution in the chamber at a particular location in terms of isobars. These are straight lines in the simple jet damping case. The isobars are inclined to the direction of the angular velocity perturbation because of the effect of the angular acceleration.

In order to determine the effect of the pressure perturbation on the vehicle motion, we must integrate the pressure forces over the chamber surfaces. This has already been set up for the appropriate control volume in equation 43. Because of our assumption of a uniform flow with no time-dependent correction, the flow interaction torque is

$$M_{flow} = M_J = - \int_S \mathbf{r} \times (p' \mathbf{n}) dS \quad (89)$$

This result can be found directly from one of the standard representations of the Jet Damping in integral form. For example, in Reference 1, the jet damping integral is defined as

$$M_J = - \int_V \mathbf{r} \times (2\omega \times \mathbf{u}) dV \quad (90)$$

In some definitions, the angular acceleration term is included too, as we have done in determining the pressure distribution of equation 88. Let us concentrate on the Coriolis term since it is responsible for the nutation damping. Using the momentum equation, and assuming the Coriolis force is balanced by pressure,

$$2\omega \times \mathbf{u} = -\nabla p' \quad (91)$$

The reader is reminded that we are now working with equations in dimensionless form, so that in equation 90, the density does not appear because it is assumed constant and was incorporated into the dimensionless variable (see Table 2). Replacing the Coriolis term by the equivalent pressure gradient, the jet damping moment becomes

$$M_J = \int_V \mathbf{r} \times \nabla p' dV \quad (92)$$

A simple application of Green's theorem shows that this is equivalent to the result shown in pressure surface integral of equation 89. To prove this, note that by simple rearrangement,

$$\mathbf{r} \times \mathbf{n} p' = -\mathbf{n} \times (p' \mathbf{r}) \quad (93)$$

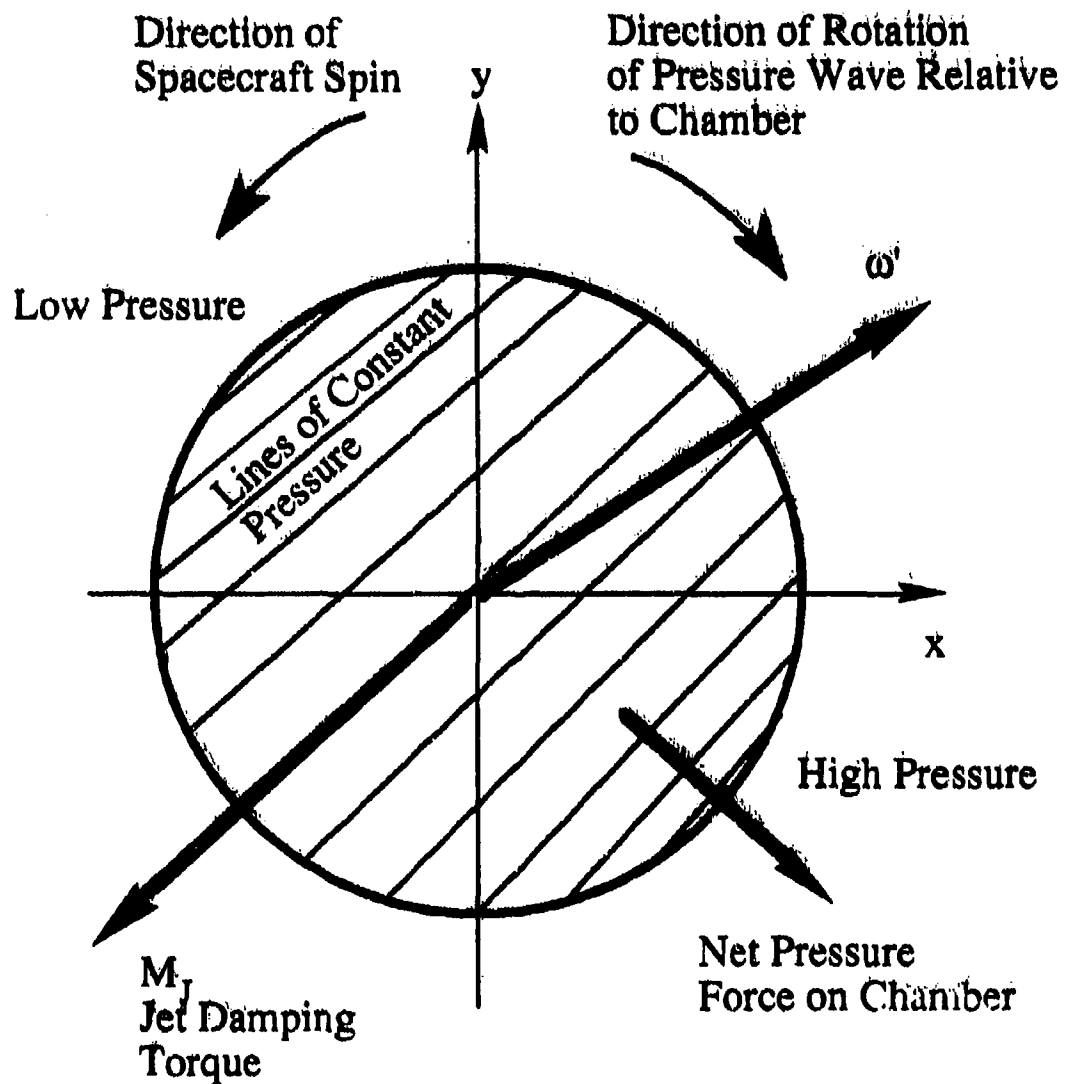


Figure 31. Nonuniform Pressure Distribution Induced by Wobbling Jet Damping Case (Uniform Steady Mean Flow)

Thus

$$\int_S \mathbf{r} \times \mathbf{n} p' dS = - \int_S \mathbf{n} \times (p' \mathbf{r}) dS = - \int_V \nabla \times (p' \mathbf{r}) dV$$

but $\nabla \times (p' \mathbf{r}) = p' \nabla \times \mathbf{r} + \nabla p' \times \mathbf{r}$ and $\nabla \times \mathbf{r} = 0$. Therefore

$$\int_S \mathbf{r} \times \mathbf{n} p' dS = - \int_V \nabla p' \times \mathbf{r} dV = \int_V \mathbf{r} \times \nabla p' dV \quad (94)$$

Finally, it is clear that

$$\boxed{M_{\text{flow}} = M_J = - \int_V \mathbf{r} \times (2\boldsymbol{\omega} \times \mathbf{u}) dV = - \int_S \mathbf{r} \times (p' \mathbf{n}) dS} \quad (95)$$

So we have proved directly that the Coriolis body force on the gas is equivalent to a nonuniform pressure distribution acting on the internal surfaces of the chamber. This greatly clarifies the jet damping mechanism by showing how the interaction torques are produced.

Careful interpretation of the results is of considerable benefit in guiding us to a more complete representation of the chamber flow. We have just shown that the wobbling of the spacecraft induces a nonuniform pressure pattern (illustrated in Figure 31) that rotates relative to the chamber. This pattern can be described as a pressure wave. It has all the wavelike attributes that we will study in the next subsection as part a more complete model of the chamber flow.

It is a consequence of the assumptions (mainly the uniform flow assumption) that have been made that this jet damping pressure pattern always represents a damping effect on the vehicle angular motion. That is, the high pressure part of the pressure wave leads the wobble angular velocity perturbation by 90° and thus produces a damping torque. It is very important to understand that this is not damping in the sense of frictional dissipation of energy. Some investigators have misconstrued the meaning of the word damping as used here. This then introduces a conceptual difficulty in accepting the fact that the pressure pattern may not have the orientation shown in Figure 31. That is, *driving instead of damping might occur.*

To summarize, we have shown that wobbling induces a traveling wavelike pressure pattern. In the case of the classical jet damping assumption of a uniform, steady flow that always adjusts to the chamber motion without dynamic interaction forces, the pressure balances the Coriolis forces and a damping torque results. We must now determine whether this assumption is appropriate in the case of combustion gas flow in a large spinning rocket chamber.

Effects of Spin on Flow Interactions

In this subsection we will carefully analyze the motion of spinning vehicles with interacting internal motion of a contained fluid or gas. This is a familiar problem to spacecraft dynamicists who have had to deal with sloshing liquid stores in spin stabilized satellites. However, the version of the problem that we must solve involves additional complications resulting from expulsion of mass, linear and angular momentum, and energy from the system with the combustion gas flow from the motor.

The problem we must solve will be shown to be an extension of the jet damping analysis. As we demonstrated in the previous section, jet damping represents an approximate way to account for the interaction between the spacecraft motion and the flow of combustion gases through the system. Several features that we identified provide the starting point for an improved model:

- Jet damping is not a dissipative mechanism. It is the reaction torque due to changing the direction of the gas particles flow through the motor chamber.
- Analyses based on an angular momentum balance using a control volume containing the chamber flow gives an approximate result for the reaction torque that may be valid in some cases but obscures the details of the processes that create the torque.
- The jet damping force is produced by a traveling pressure wave induced by the wobbling of the chamber. The unsymmetrical pressure pattern balances the Coriolis force on the gas particles.
- The gas particles traverse the chamber in such a way that the streamline pattern relative to the chamber behaves as though no wobble is present.

It now becomes necessary to determine if this picture of the gas flow interactions is adequate. Our working hypothesis is that it is not a correct picture for large spinning chambers. It seems quite unreasonable to expect the gas motions to be unaffected by the angular motion of the chamber walls. We must determine the range of validity of the jet damping formulation and more importantly, we must deduce corrections for cases where it is not valid. It should be completely obvious to the careful reader that, if the gas velocity takes part in the response to the spacecraft motion, then *the pressure distribution predicted by jet damping theory is wrong.*

We have found many important hints that will guide our thinking. Of great importance is the knowledge that the jet damping torque is caused by a traveling pressure pattern induced by the wobbling chamber boundaries. As viewed from the body-fixed coordinates, this disturbance has all the attributes of a pressure wave. We are therefore led to expect wave motion within the chamber. It will be necessary to show that the wave behavior includes velocity perturbations as well as a pressure disturbance. Again, for emphasis, the simple jet damping flow field is the result of the assumption that the gas velocity field remains uniform and steady relative to the chamber. The pressure gradient balances all inertial forces, particularly the Coriolis force, due to nutation wobbling. We will show that *this model does not represent a correct solution when the chamber is spinning and when the characteristic size of the chamber exceeds a critical value.*

Simplifying Assumptions

Since we are now confronted with a much more difficult fluid mechanics problem than jet damping theory addresses, we will need to use every available tool to make it tractable. Ultimately we will need to rely on numerical techniques to make accurate solutions possible. That is, the problem involves a complex mixture of flow regimes and geometry. The complex burning surface/combustion chamber geometry cannot be handled by analytical methods. Regions dominated by viscosity and compressibility border other zones that behave as an incompressible, inviscid medium. However, to jump directly into the problem with an off-the-shelf numerical code would be a terrible mistake.

The approach to full numerical solutions must be made with as much physical understanding of the problem as we can gather by analysis. This is perhaps the most difficult part of the problem for the reader because it involves myriad assumptions and mathematical developments. However, our experience with our earlier attempts to explain the gas dynamic nutation mechanism¹ has led us to conclude that it is necessary to show every step in the mathematical developments. This is necessary because many of the concepts needed are foreign to readers with typical engineering backgrounds. We therefore will undertake to lead the interested reader through each step of every important phase of the analysis.

The first step is to simplify the motor geometry in order that analytical solutions are possible. Our approach is to model the combustion chamber as a cylinder as depicted in Figure 32. Also defined are several of the geometrical parameters and lengths. Notice that there are two axial coordinates, z (measured forward from the mass center) and z' , measured from the aft surface of the cylinder. The placement of the burning surface is adjustable. The simplest choice is to place all gas production on the forward surface in end-burner fashion. This is a close approximation to the typical modern space motor such as the STAR 48 with its head-end web. Other motors have a more nearly cylindrical geometry with burning on the vertical sidewalls of the chamber. Either of these configurations or combinations can be accommodated.

We will pay careful attention to the nozzle because there has been much controversy over the role it might play in the coning problem. The quote from Newton, et al.³ in the last section makes clear that this is not a new concern. In fact, their analysis of the nozzle effect in a yawing motor is far superior (in the opinion of the author) than in any of the more recent treatments of jet damping. Their insight that the compressible nature of the nozzle flow strongly controls the interactions between gas and the nozzle boundaries is evidence of much deeper understanding than others have displayed. For the time being, the nozzle will be relegated to a section of the cylinder surface through which the gas leaves the motor volume. A more detailed representation will be discussed later.

As discussed earlier, we choose to make wholesale use of the incompressible nature of the flow within the motor burning port. The largest Mach number expected in the motor is of the order of 10^{-2} . This is valid to within very close proximity of the nozzle entrance as our numerical solutions verify. Therefore, an incompressible gas model is an accurate representation of the flow.

Effects of viscosity are also not expected to dominate the flow by direct action. Our problem is characterized by a very small Ekman number of the order of 10^{-8} . That is not to say that we are ignoring rotational flow effects. In fact, as the jet damping solution of the last section demonstrates, it is the rotational nature of the flow field that controls the interactions with the spacecraft motion. The presence of the Coriolis and other inertial effects force vorticity into the chamber gas flow. The jet damping pressure wave represents a kind of

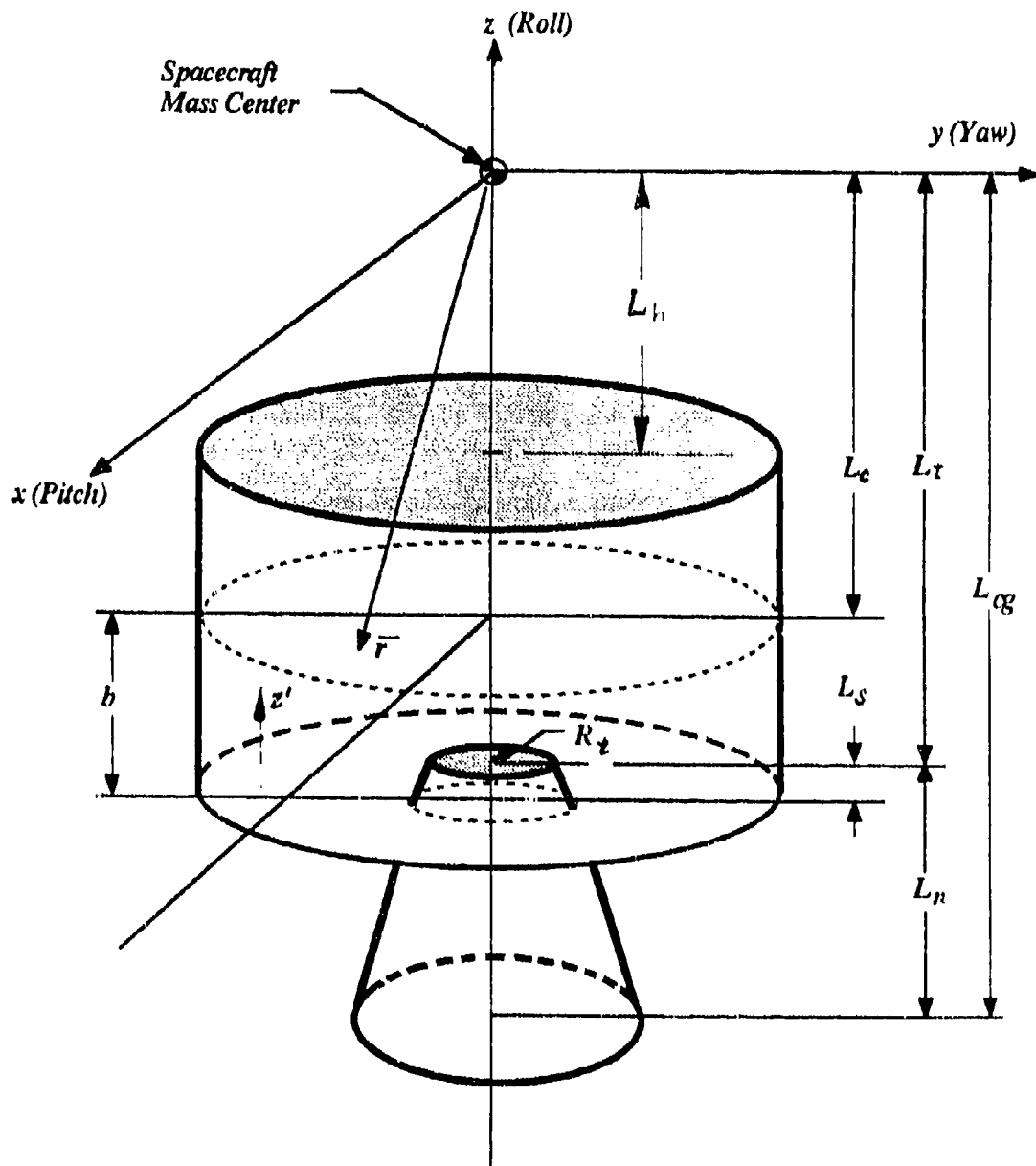


Figure 32. Simplified Motor Geometry for Analytical Solutions

vortical wave. Its identification gives us much guidance in our development of a more complete solution.

In order to determine the flow interaction effects, we must use an accurate description of the vehicle dynamics. We will use the model discussed in the last section, which is based on an axisymmetric rigid spacecraft. This yields a very simple but accurate picture of the angular velocity and angular acceleration environment within the motor chamber. This information, in turn, provides us with a direct link between the gas response and the inertial effects that control it.

The assumptions we have just listed leave us with a simple but completely adequate model for the PAM-D geometry. They allow us to use straightforward mathematical procedures to deduce approximate solutions for the unsteady gas flow. One might object that the problem has been "assumed out of existence," but such is not the case. We will demonstrate that the solutions finally arrived at are an amazingly good representation for what is actually observed in the system dynamic behavior.

Mean Flow Analysis

In order to carry out useful solutions of the unsteady flow field, one must first obtain an adequate representation for the steady part of the flow. We choose to use the simplest possible representation that contains the necessary physics and matches the boundary constraints. We will, in fact, use several models to emphasize the role played by several features of the mean flow. The simplest model (corresponding to an end-burning configuration) will be a uniform one-dimensional flow of the same type used in the jet damping model. However, we will not place any restrictions on the unsteady part of the flow superimposed on this mean flow. This is our main departure from the jet damping approach.

A flow feature often neglected in modeling the mean flow in a spinning rocket is the nearly potential vortex flow induced because of the radially inward flow into the nozzle entrance. If the flow does not contain a strong radial component, then the circumferential flow takes the form of a solid body rotation in the direction of chamber spin. In body-fixed coordinates it is not necessary to superimpose an additional circumferential velocity component.

Perhaps too much attention was focused on the vortex flow in earlier work on gas dynamic nutation interactions.¹ However, the vortex provides a useful way to describe the nonuniform undulating flow field induced by the inertial accelerations. In other words, it represents a useful flow visualization device.

The circumferential velocity component plays a significant role in the inertial force configuration as we will demonstrate shortly. This affects the orientation of the induced pressure wave and therefore the direction of the interaction torque.

All features of the mean flow we employ in the analysis will be verified directly by means of full Navier-Stokes numerical solutions to be described later.

Perturbation Analysis

The equations of motion for the gas flow were derived in a previous subsection. The version we need for our analysis is represented by the continuity and momentum equations 46 and 47, respectively. We also now drop the viscous terms on the basis that the Ekman number is very small. Any viscous effects are assumed to be confined to thin layers near the solid boundaries. We will assume that our chamber boundaries are just outside the boundary layers (Ekman layers) in the manner of low-speed aerodynamics. Thus, the analysis requires solution

of the set

$$\begin{cases} \nabla \cdot \mathbf{u} = 0 \end{cases} \quad (96)$$

$$\begin{cases} \frac{\partial \mathbf{u}}{\partial t} + R\omega \cdot \nabla \mathbf{u} = -\nabla p - 2\omega \times \mathbf{u} - \frac{1}{Ro} \frac{\partial \omega}{\partial t} \times \mathbf{r} \end{cases} \quad (97)$$

and corresponding boundary conditions. We will devote an entire later subsection to the boundary condition question. In writing equations 96 and 97, we have also dropped the axial acceleration term. This is based on the axisymmetric mass distribution of the chamber gases. Since the flow is incompressible, there are no shifts of center of mass that would result in a net torque on the fluid from this source. That is, this part of the acceleration field is completely symmetrical and cannot produce nonuniformities of the sort generated by Coriolis acceleration. We will show that the latter effect is the main source of the flow interaction as strongly suggested by the jet damping results.

In order to make the problem solvable, we must take advantage of the smallness of the flow perturbations. We can quantify this assumption of smallness by using the jet damping results. The jet damping part of the pressure disturbance is from equation 88,

$$p' = -2\omega r \sin(\lambda t + \theta) \quad (98)$$

in dimensionless form. To estimate the actual pressure amplitude in a typical nutating rocket, we convert to dimensional form using the definitions in Table 2. The maximum pressure amplitude occurs at the chamber wall where $r = 1$. Thus, the pressure at a given circumferential location and time is, in dimensional form

$$p^* = (\rho_0 R \Omega v_b) p' = -2(\Omega \omega) R \rho_0 v_b \sin(\lambda^* t^* + \theta) \quad (99)$$

If we insert typical values for the various parameters based on a PAM-D near motor burnout ($R = 2.0$ ft., $\rho_0 = 0.0088$ slug/ft³, $v_b = 15$ ft/sec), we find

$$p_{\max}^* \approx 0.5 \text{ lbf / ft}^2 = 3.2 \cdot 10^{-3} \text{ psi} \quad (100)$$

which corresponds to a typical maximum nutation amplitude of 50 degrees/sec (dimensional)

$$\omega^* \equiv \Omega \omega = \frac{50}{57.3} \text{ rad / sec} \quad (101)$$

This is a very small pressure disturbance. The jet damping torque corresponding to the integrated effect of this pressure over the chamber surfaces is

$$|M_j| \approx 40 \text{ ft} \cdot \text{lbf} \quad (102)$$

This demonstrates that a small pressure amplitude is sufficient to generate a torque of the same order of magnitude as that which produces the observed coning. If velocity perturbations accompanied this pressure field they would also, obviously, be small.

The amplitude of the angular velocity perturbation is similarly a very small parameter. Its amplitude is about 5 deg/sec near the point of maximum coning growth at midburn. Thus

$$\omega = \frac{1}{\Omega} \frac{5}{57.3} = 1.6 \cdot 10^{-2} \quad (103)$$

in dimensionless form. Recall that in scaling angular velocities we are comparing them to the spacecraft spin rate Ω (typical value about 50 rpm or 5.3 rad/sec). So the angular perturbations remain small throughout coning growth.

We now take advantage of the smallness of these key parameters to linearize the problem. Put

$$\begin{cases} p = P_0 + p' \\ u = U + u' \\ \omega = \Omega_0 k + \omega' \end{cases} \quad (104)$$

where primes will always denote small quantities. Here, Ω_0 is the dimensionless axial spin rate and since all angular velocities are normalized to the spin rate, its value is one. These expansions also, in effect, separate the steady and unsteady parts of the problem. The steady flow field can be determined independently for later use in solving the unsteady problem. If we neglect terms involving products of the small quantities, we arrive at the working equations we need. That is, combinations of the form

$$(p')^2, u' \cdot u', \omega' \cdot \omega', p'u', \text{etc.} \quad (105)$$

are very small and can be safely neglected. The working equations for the unsteady flow become

$$\nabla \cdot u' = 0 \quad (106)$$

$$\frac{\partial u'}{\partial t} + Ro(u' \cdot \nabla U + U \cdot \nabla u') = -\nabla p - 2\omega \times u - \frac{1}{Ro} \frac{\partial \omega}{\partial t} \times r \quad (107)$$

This is the standard perturbation approach and is fully justified on the basis of the smallness of the unsteady terms. There are no singular perturbation characteristics present, so a clean, regular perturbation problem results.

Unsteady Flow Computations

Before attempting to solve the equations in complete form, it is advantageous to discuss certain properties in the light of work in the field of rotating fluids. Before doing so, please note that equations 106 and 107 describe a gas motion forced by several inertial terms including the potent Coriolis term. These can be taken as known forces because we are specifying the angular velocity environment by using results from the dynamics analysis of the previous chapter.

The job ahead of us is to determine the gas response to the forces created by the spin and wobble of the vehicle. We will not, as in jet damping theory, assume that these are balanced only by pressure. We will solve the complete problem by letting the velocity field be determined by the equations of motion instead of by assumption. We remind the reader that in the jet damping approach, one sets the perturbation velocity equal to zero:

$$u' = 0 \quad (\text{JET DAMPING ASSUMPTION})$$

A very strong (and very wrong) assumption.

Before attacking the problem of forced motion of the gas, it is beneficial to study a simpler case describing the free-motion of the system. We anticipate oscillatory gas behavior, and as in all vibration problems it is a benefit to use the free solutions (the natural modes) in

representing the forced ones. This will aid in our recognition of the wave nature of the flow interactions. The first order of business is to demonstrate that the jet damping pressure wave should not have come as a surprise. Rotating flows support waves.

Pressure Waves in Spinning Flows

We now demonstrate by direct solution of the governing equations without the forcing terms, that the spinning gas in the combustion chamber can support oscillations in pressure and velocity. These are, in effect, waves of vorticity and come about because of the Coriolis effect from the axial spin.

The Coriolis effect provides a restoring force that is completely analogous to the presence of elastic spring forces, compressibility forces, or free surface effects so that wave-like solutions are expected. We will present a very careful analysis to show this. Such waves are known in the literature of meteorology as "inertial waves" or "elastoid inertia waves." They have been subjected to intense study in a number of disciplines but are not known to many persons in the engineering community. Inertial waves arise in spinning gases or liquids and are not dependent on the compressibility of the medium. For a given chamber geometry, there are, as in most systems capable of oscillatory behavior, an infinite number of possible modes and corresponding frequencies. However, as we shall prove in the case of inertial waves, the mode frequencies are confined to the range

$$0 \leq \lambda \leq 2\Omega \quad (108)$$

where Ω is the spin rate (rad/sec). It is important to compare this frequency range to the natural wobbling frequency of the spacecraft given in equation 52. We rewrite this here for emphasis. The nutation wobbling frequency is, in dimensional form,

$$\lambda_s = \Omega \left(1 - \frac{I_2}{I_1} \right) \quad (109)$$

The wave frequency range coincides with the nutation frequency range, and the possibility for resonant interactions in the forced motion case clearly exists.

Unperturbed Inertial Waves: The Poincare' Problem

To highlight the properties of the chamber natural modes of oscillation, we will use the same approach applied in the classical treatment of this problem. We will assume that the chamber is closed and that there is no mean flow. We will later treat the mean flow as an additional forcing effect. Since, for the moment, the system is not forced by nutation wobbling, the equations for the velocity fluctuations become

$$\begin{cases} \nabla \cdot \mathbf{u}' = 0 \\ \frac{\partial \mathbf{u}'}{\partial t} = -\nabla p - 2\mathbf{k} \times \mathbf{u}' \end{cases} \quad (110)$$

$$(111)$$

These represent the flow in a chamber spinning about its longitudinal axis at rate Ω . The Ω does not appear explicitly in the Coriolis term because angular velocities have been normalized to this value. The \mathbf{k} in equation 111 is the axial unit vector and therefore the dimensionless spin vector.

Since we are interested in oscillatory solutions, let us assume that they exist by putting

$$p = \phi \exp(i\lambda t) \quad (112)$$

$$\mathbf{u}' = \mathbf{Q} \exp(i\lambda t) \quad (113)$$

where λ is a frequency to be determined. Amplitudes of the pressure and velocity perturbations are denoted by ϕ and \mathbf{Q} . These are functions of position also to be determined. The problem becomes

$$\begin{cases} \nabla \cdot \mathbf{Q} = 0 \\ i\lambda \mathbf{Q} + 2\mathbf{k} \times \mathbf{Q} = -\nabla \phi \end{cases} \quad (114)$$

$$i\lambda \mathbf{Q} + 2\mathbf{k} \times \mathbf{Q} = -\nabla \phi \quad (115)$$

A decision must be made at this point regarding which variable to eliminate from the equations. Poincaré^{14, 15} chose to write the equation for pressure, and we will follow his procedure. This has the usual advantage of allowing us to work with a scalar variable. The corresponding velocity vector solution can then be found using relationships between pressure and velocity to be deduced from the momentum equation. The algebraic steps are difficult to find in the literature, so we will present them in detail. First, take the divergence of the momentum equation 115:

$$\nabla \cdot (i\lambda \mathbf{Q} + 2\mathbf{k} \times \mathbf{Q}) = -\nabla^2 \phi \quad (116)$$

and then apply the continuity equation

$$\nabla \cdot \mathbf{Q} = 0$$

to yield

$$\nabla \cdot (2\mathbf{k} \times \mathbf{Q}) = -\nabla^2 \phi \quad (117)$$

Now expand the term on the left involving the Coriolis acceleration by means of standard vector identities with the result

$$\nabla \cdot (2\mathbf{k} \times \mathbf{Q}) = 2\mathbf{Q} \cdot \nabla \times \mathbf{k} - 2\mathbf{k} \cdot \nabla \times \mathbf{Q} \quad (118)$$

Noting that

$$\nabla \times \mathbf{k} = 0$$

one finds

$$\nabla \cdot (2\mathbf{k} \times \mathbf{Q}) = -2\mathbf{k} \cdot \nabla \times \mathbf{Q} \quad (119)$$

Taking the curl of the momentum equation eliminates the pressure gradient

$$i\lambda \nabla \times \mathbf{Q} = -2\nabla \times (\mathbf{k} \times \mathbf{Q}) \quad (120)$$

since

$$\nabla \times \nabla \phi = 0$$

Solving for the vorticity vector amplitude

$$\nabla \times \mathbf{Q} = \frac{2i}{\lambda} \nabla \times (\mathbf{k} \times \mathbf{Q}) \quad (121)$$

where the right-hand side can be expanded to

$$\nabla \times (\mathbf{k} \times \mathbf{Q}) = [\mathbf{Q} \cdot \nabla \mathbf{k} - \mathbf{k} \cdot \nabla \mathbf{Q} + \mathbf{k} \nabla \cdot \mathbf{Q} - \mathbf{Q} \nabla \cdot \mathbf{k}] = -\mathbf{k} \cdot \nabla \mathbf{Q} \quad (122)$$

The differentiations involving the axial unit vector \mathbf{k} all yield zero so that

$$\nabla \times \mathbf{Q} = -\frac{2i}{\lambda} \mathbf{k} \cdot \nabla \mathbf{Q} \quad (123)$$

Therefore, equation 117 becomes

$$\nabla^2 \phi = -\frac{4i}{\lambda} \mathbf{k} \cdot (\mathbf{k} \cdot \nabla \mathbf{Q}) \quad (124)$$

Consider the term $\mathbf{k} \cdot \nabla \mathbf{Q}$, which represents the rate of change of \mathbf{Q} in the axial direction.

$$\mathbf{k} \cdot \nabla \mathbf{Q} = \frac{i}{\lambda} \mathbf{k} \cdot \nabla [2\mathbf{k} \times \mathbf{Q} + \nabla \phi] = \frac{i}{\lambda} \left[\frac{\partial}{\partial z} (-2Q_y \mathbf{i} + 2Q_x \mathbf{j}) + \frac{\partial}{\partial z} \left(\frac{\partial \phi}{\partial x} \mathbf{i} + \frac{\partial \phi}{\partial y} \mathbf{j} + \frac{\partial \phi}{\partial z} \mathbf{k} \right) \right]$$

Hence the right-hand side of 124 becomes

$$\mathbf{k} \cdot (\mathbf{k} \cdot \nabla \mathbf{Q}) = \frac{i}{\lambda} \frac{\partial^2 \phi}{\partial z^2} \quad (125)$$

Inserting this result into equation 124 eliminates the velocity amplitude. Therefore,

$$\nabla^2 \phi - \frac{4i}{\lambda} \left(\frac{i}{\lambda} \frac{\partial^2 \phi}{\partial z^2} \right)$$

Rearranging yields

$$\nabla^2 \phi - \frac{4}{\lambda^2} \frac{\partial^2 \phi}{\partial z^2} = 0$$

or

$$\left[\nabla^2 \phi - \frac{4}{\lambda^2} (\mathbf{k} \cdot \nabla)^2 \phi = 0 \right] \quad (126)$$

as it is often written in the literature. This is the famous Poincare' inertial wave equation. We will carefully examine its solutions with the object of learning how wave motions can arise in a spinning gas. In particular, we need to determine the mode shapes and frequencies of these waves.

Before attempting to solve the wave equation, it is necessary to deduce the proper form for the boundary conditions. The basic condition is that the normal velocity component is zero at the surface. However, since we chose the pressure as the main variable, we will need a way to relate the pressure and velocity perturbations. This relationship is also needed later to determine the corresponding velocity waveforms.

From the momentum equation 115 it is clear that

$$\mathbf{Q} = \frac{i}{\lambda} [2\mathbf{k} \times \mathbf{Q} + \nabla \phi] \quad (127)$$

Now, examining the Coriolis term we find

$$\mathbf{k} \times \mathbf{Q} = \frac{i}{\lambda} [2\mathbf{k} \times (\mathbf{k} \times \mathbf{Q}) + \mathbf{k} \times \nabla \phi] \quad (128)$$

but

$$\mathbf{k} \times (\mathbf{k} \times \mathbf{Q}) = (\mathbf{k} \cdot \mathbf{Q})\mathbf{k} - (\mathbf{k} \cdot \mathbf{k})\mathbf{Q} \quad (129)$$

Therefore, equation 128 becomes

$$\mathbf{k} \times \mathbf{Q} = \frac{i}{\lambda} [2(\mathbf{k} \cdot \mathbf{Q})\mathbf{k} - 2\mathbf{Q} + \mathbf{k} \times \nabla \phi]$$

Consider the term

$$2(\mathbf{k} \cdot \mathbf{Q})\mathbf{k} - 2\mathbf{Q} = 2\mathbf{k} \left(\frac{i}{\lambda} \mathbf{k} \cdot \nabla \phi \right) - 2 \frac{i}{\lambda} [2\mathbf{k} \times \mathbf{Q} + \nabla \phi]$$

Also,

$$\mathbf{k} \times \mathbf{Q} = \frac{i}{\lambda} \left[2\mathbf{k} \left(\frac{i}{\lambda} \mathbf{k} \cdot \nabla \phi \right) - 2 \frac{i}{\lambda} [2\mathbf{k} \times \mathbf{Q} + \nabla \phi] + \mathbf{k} \times \nabla \phi \right]$$

Rearranging,

$$\mathbf{k} \times \mathbf{Q} \left(1 - \frac{4}{\lambda^2} \right) = -\frac{2}{\lambda^2} (\mathbf{k} \cdot \nabla \phi) \mathbf{k} + \frac{2}{\lambda^2} \nabla \phi + \frac{i}{\lambda} \mathbf{k} \times \nabla \phi$$

Thus,

$$\mathbf{k} \times \mathbf{Q} = \left(\frac{1}{4 - \lambda^2} \right) [2(\mathbf{k} \cdot \nabla \phi) \mathbf{k} - 2\nabla \phi - i\lambda \mathbf{k} \times \nabla \phi] \quad (130)$$

Inserting this result into equation 127 gives the required expression for \mathbf{Q} in terms of ϕ :

$$\mathbf{Q} = \frac{i}{\lambda} [2\mathbf{k} \times \mathbf{Q} + \nabla \phi] = \frac{i}{\lambda} \nabla \phi + 2 \frac{i}{\lambda} \left(\frac{1}{4 - \lambda^2} \right) [2(\mathbf{k} \cdot \nabla \phi) \mathbf{k} - 2\nabla \phi - i\lambda \mathbf{k} \times \nabla \phi]$$

or

$$\mathbf{Q} = \left(\frac{1}{4 - \lambda^2} \right) \left[2\mathbf{k} \times \nabla \phi - i\lambda \nabla \phi + \frac{4i}{\lambda} (\mathbf{k} \cdot \nabla \phi) \mathbf{k} \right] \quad (131)$$

which shows the velocity amplitude in terms of the pressure amplitude. We will find several applications for this result. For example, we can now write the pressure boundary condition. In order that the velocity is zero at the surface

$$\mathbf{n} \cdot \mathbf{Q} = 0 \quad \text{on } S \quad (132)$$

and we find

$$\mathbf{n} \cdot \left[2\mathbf{k} \times \nabla \phi - i\lambda \nabla \phi + \frac{4i}{\lambda} (\mathbf{k} \cdot \nabla \phi) \mathbf{k} \right] = 0$$

Therefore, at any point on the surface, the normal component of the pressure gradient is

$$\boxed{\mathbf{n} \cdot \nabla \phi = -\frac{2i}{\lambda} \mathbf{n} \cdot \mathbf{k} \times \nabla \phi + \frac{4}{\lambda^2} \mathbf{n} \cdot \mathbf{k} (\mathbf{k} \cdot \nabla \phi) \quad \text{on } S} \quad (133)$$

Readers familiar with acoustics will notice that the pressure boundary conditions is far more complex than in the case of waves of compressibility. In the acoustics case the normal component of the pressure gradient vanishes at the wall.

Solution of the Poincare' Equation

The pressure fluctuations in a closed chamber without mean flow are governed by the Poincare' wave equation 126 and the corresponding boundary condition equation 133. We must solve the set

$$\left\{ \begin{array}{l} \nabla^2 \phi - \frac{4}{\lambda^2} (\mathbf{k} \cdot \nabla)^2 \phi = 0 \end{array} \right. \quad (134)$$

$$\left\{ \begin{array}{l} \mathbf{n} \cdot \nabla \phi = -\frac{2i}{\lambda} \mathbf{n} \cdot \mathbf{k} \times \nabla \phi + \frac{4}{\lambda^2} \mathbf{n} \cdot \mathbf{k} (\mathbf{k} \cdot \nabla \phi) \quad \text{on } S \end{array} \right. \quad (135)$$

Once solutions have been determined for a particular chamber configuration, we can find the velocity field from equation 131.

Solutions are known only for simple chamber shapes. Greenspan¹¹ states his belief that solutions for other than cylindrical, spherical, or oblate spheroidal chambers is virtually impossible in analytical form. We have chosen to represent the rocket chamber by a cylinder. This is a good approximation for the geometry and allows use of relatively simple expressions to represent the wave motions. For this shape, the equations become (in cylindrical polar coordinates)

$$\left\{ \begin{array}{l} \frac{\partial^2 \phi}{\partial r^2} + \frac{1}{r} \frac{\partial \phi}{\partial r} + \frac{1}{r^2} \frac{\partial^2 \phi}{\partial \theta^2} + \left(1 - \frac{4}{\lambda^2}\right) \frac{\partial^2 \phi}{\partial z^2} = 0 \end{array} \right. \quad (136)$$

$$\left\{ \begin{array}{l} r \frac{\partial \phi}{\partial r} - \frac{2i}{\lambda} \frac{\partial \phi}{\partial \theta} = 0 \quad \text{on } r = 1 \end{array} \right. \quad (137)$$

$$\left\{ \begin{array}{l} \frac{\partial \phi}{\partial z} = 0 \quad \text{on } z = 0, z = 2b \end{array} \right. \quad (138)$$

where b is the length to diameter ratio (dimensionless chamber half-length). This is a simple linear partial differential equation that is readily solved by separation of variables with the result

$$\phi = J_k(\xi r) \exp(ik\theta) \cos\left(\frac{n\pi z}{2b}\right) \quad (139)$$

The frequency eigenvalue, ξ , must satisfy

$$\xi \frac{dJ_k(\xi)}{d\xi} + k \sqrt{1 + \frac{1}{2} \left(\frac{2\xi b}{n\pi} \right)^2} J_k(\xi) = 0 \quad (140)$$

and the eigenvalues are given by

$$\lambda_{kmn} = \frac{2}{\sqrt{1 + \left(\frac{2\xi b}{n\pi} \right)^2}} \quad (141)$$

Figure 33 shows the variation of the frequencies with slenderness ratio for several low-order modes. Notice that there are an infinite number of modes in the range (dimensionless because spin rate was used to define the characteristic time) and that they are a function only of the chamber shape. That is, they do not depend on the size of the chamber. We will find later that many resonant interactions with vehicle wobbling are possible.

Finally, we can write the expressions for the pressure and velocity distributions. We find

$$p' = \phi \exp(i\lambda t) = J_k(\xi r) \cos\left(\frac{n\pi z}{2b}\right) \exp[i(\lambda t + k\theta)] \quad (142)$$

$$u' = Q \exp(i\lambda t) = [if_1 e_r + f_2 e_\theta + if_3 k] \exp[i(\lambda t + k\theta)] \quad (143)$$

where functions f_1, f_2 , and f_3 are

$$f_1 = -\frac{1}{(4-\lambda^2)} \left[\frac{2k}{r} J_k(\xi r) + \lambda \xi J'_k(\xi r) \right] \cos\left(\frac{n\pi z}{2b}\right) \quad (144)$$

$$f_2 = \frac{1}{(4-\lambda^2)} \left[\frac{\lambda k}{r} J_k(\xi r) + 2\xi J'_k(\xi r) \right] \cos\left(\frac{n\pi z}{2b}\right) \quad (145)$$

$$f_3 = -\left(\frac{n\pi}{2\lambda b}\right) J_k(\xi r) \sin\left(\frac{n\pi z}{2b}\right) \quad (146)$$

The set of integers (k, m, n) define a given mode. Mode integer k sets the number of azimuthal nodal lines. Integers m and n set the number of radial and axial nodes. As in any wave system, the larger the mode integer the more complex the mode geometry. Thus, in nature, the low order modes are more readily excited because they require less energy input.

The gas motion consists of a traveling wave of pressure and velocity. Unlike the simple wave solutions in the jet damping case, these exhibit complex three-dimensional motion. Study of Figures 6 and 7 in the Summary will aid the reader in visualizing the type of gas motion involved. The latter figures describe numerical solutions of a similar physical problem that is forced by nutation. We will generate similar solutions later.

It is also worth showing that the waves can be interpreted as waves of vorticity. The vorticity is generated by the nonuniform Coriolis body force. The vorticity fluctuation is given by

$$\zeta = \nabla \times u' = \xi \exp(i\lambda t) = \nabla \times Q \exp(i\lambda t) \quad (147)$$

where vorticity amplitude is

$$\xi = \nabla \times Q = [g_1 e_r + ig_2 e_\theta + g_3 k] \exp(ik\theta) \quad (148)$$

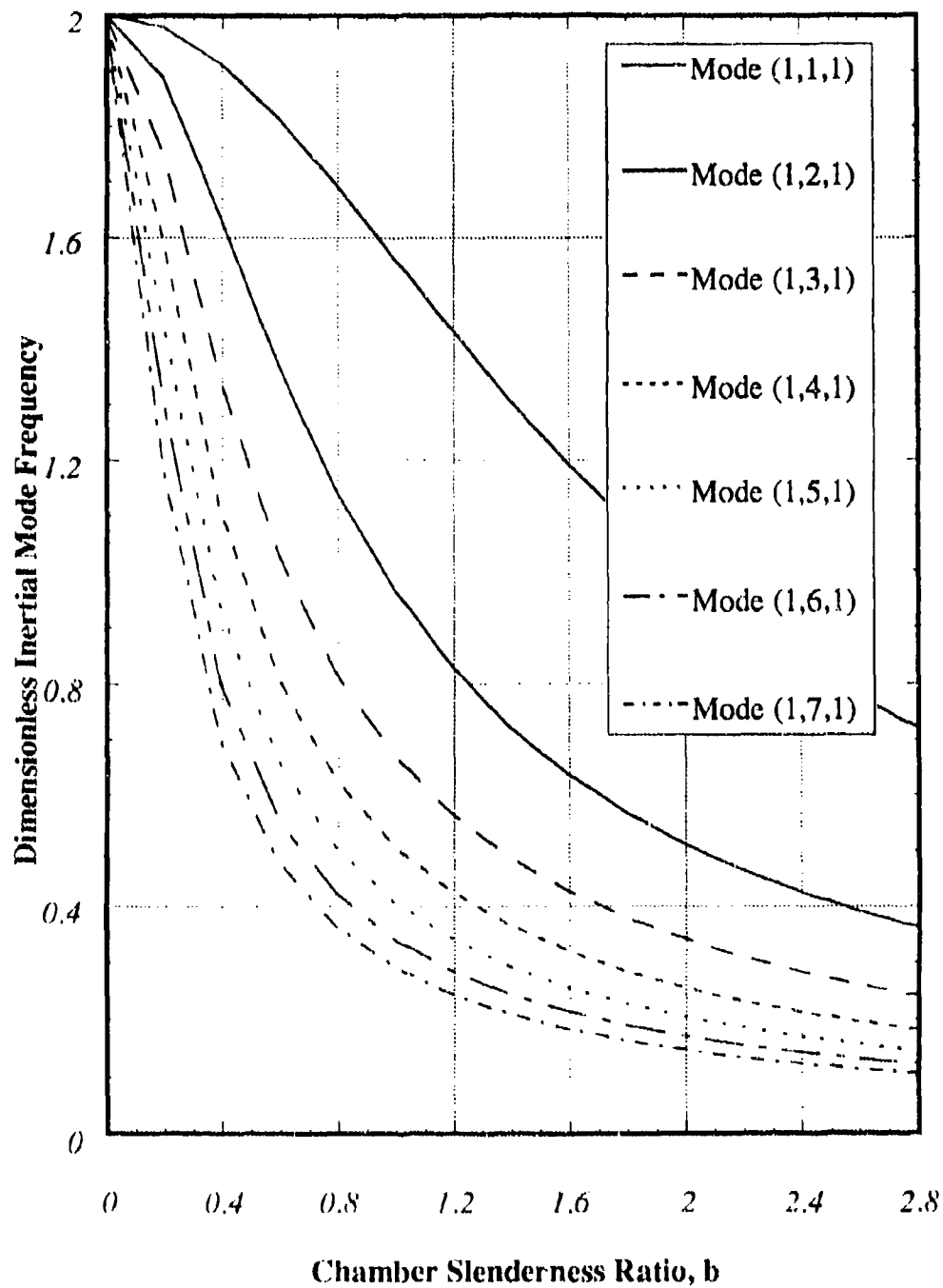


Figure 33. Variation of Inertial Wave Frequencies with Chamber Slenderness Ratio, b

Functions g_1 , g_2 , and g_3 are

$$\begin{cases} g_1 = \left(\frac{n\pi}{2b} \right) \left\{ \frac{J_k(\xi r)}{\lambda r} + \frac{1}{(4-\lambda^2)} \left[\frac{k\lambda}{r} J_k(\xi r) + 2\xi J'_k(\xi r) \right] \right\} \sin\left(\frac{n\pi}{2b} z \right) \\ g_2 = \left(\frac{n\pi}{2b} \right) \left\{ \frac{\xi}{\lambda} J'_k(\xi r) + \frac{1}{(4-\lambda^2)} \left[\frac{2k}{r} J_k(\xi r) + \lambda\xi J'_k(\xi r) \right] \right\} \sin\left(\frac{n\pi}{2b} z \right) \\ g_3 = \frac{1}{(4-\lambda^2)} \left\{ -\frac{2k}{r^2} J_k(\xi r) + \frac{\xi}{r} [\lambda(k-1) + 2] J'_k(\xi r) + 2\xi^2 J''_k(\xi r) \right\} \cos\left(\frac{n\pi}{2b} z \right) \end{cases} \quad (149)$$

Again, it is important that the reader associates inertial wave motion with production of vorticity. This is the time-dependent analog of the generation of the axial vortex flow by spin in the steady part of the problem.

Summary

The significance of a wave-like response to vehicle nutation in the chamber gas flow has escaped many investigators of nutation instability. The most widely held notion is that the only important gas response is jet damping. The influence of the internal ballistics coning problem is viewed as a mild damping effect that is overcome by another interaction such as the sloshing of slag.

What we have shown in this subsection is that jet damping itself is related to a wave-like response that produces a traveling pressure pattern exactly balancing the Coriolis acceleration due to wobbling. We have used this as a hint to look more carefully at the fluid dynamics. We have demonstrated that because of the spin, the chamber gas can support waves of vorticity that are analogous to the jet damping pressure wave. In fact, as we shall demonstrate in following sections, they are the correct solution to the "jet damping" problem when the chamber is spinning. The assumption that the gas velocity is unaffected by nutation in jet damping theory is incorrect. The Coriolis acceleration is balanced by both pressure and velocity perturbations as the conservation equations require.

These waves are waves of vorticity sometimes called inertial waves because they are associated with the inertial body forces arising from the combined spinning and nutation coupled with the relative motion of combustion gas particles through the chamber.

We have concluded this subsection with a detailed derivation of the classical inertial wave solution for a cylindrical geometry. We emphasize this solution because we can use it to approximate the waves in a motor. Furthermore, we have shown that the natural frequencies of the waves are in precisely the same range as the spacecraft nutation frequency. The possibility of resonant interaction cannot be denied. Such resonance is, in fact, the very essence of all nutation mechanisms including those related to sloshing of slag or of liquid stores carried in partially filled tanks.

Nozzle Effects

There can be no doubt that the nozzle flow pattern plays a role in producing flow interactions of importance in the PAM-D coning problem. We have already shown how the internal flow is rendered unsymmetrical by the driving effect produced by the wobbling chamber. It is clear that gases do not enter the nozzle in an axisymmetric pattern. Side forces and resulting lateral moments are thus created. The direction and magnitude of the force system produced within the nozzle by the nonuniform flow entering from the chamber is crucial in determining whether the spacecraft system is nutationally stable.

We will treat the nozzle as a separate element in handling the combustion gas flow and its interaction with the vehicle dynamics. Up to this point, most emphasis in our treatment of the flow effects has been on the internal flow field sufficiently far from the nozzle that high-speed motion and compressibility were not of crucial importance. As gas particles approach the nozzle, these effects begin to dominate, and one must deal with an entirely separate flow regime as they pass through the throat region into the expansion cone.

It is necessary to formulate appropriate boundary conditions for the interface between the internal gas flow that is dominated by slow, nearly incompressible rotational effects, and the nozzle flow that is dominated by high-speed compressible flow and a transition to supersonic conditions in the expansion cone.

Two nozzle interactions with the coning effects will be evaluated in this subsection. The first involves establishment of the boundary condition between the nozzle entrance zone and the contained slow rotational flow within the chamber as we have just described it. The second is an assessment of the nonsymmetric forces produced by the nozzle flow and their influence on the net nutation disturbing torque environment.

Lateral Torques and Side Forces Produced in the Nozzle Flow

Concern for nonsymmetric flow interactions with nozzles has existed for many years. Darwell and Trubridge carried out a detailed study in 1968.³⁸ A very elaborate investigation based on conventional analytical methods was published by Walters³⁹ in 1972. This research also included an experimental verification program involving direct sideforce measurements and flight testing employing solid rocket motors. Later work has focused on numerical simulations of the off-axis nozzle flow effects. A study by Hoffman,⁴⁰ a well-known numerical analyst, is of direct applicability because the nozzle geometries represented are quite similar to those used in the STAR motor series of central interest in the coning problem.

A recent cold flow experimental study⁴¹ was carried out to determine the effects of nozzle entrance flow asymmetry in producing lateral torques. The authors concluded that if the asymmetry is characterized by the angle of the flow entering the nozzle entrance plane, or plenum, as they describe it (as opposed to the throat plane), the side force produced was much smaller than expected on the basis of the theoretical results. They indicate their belief that, if the nozzle and throat entrance zones are axisymmetric, then the effect of flow misalignment at the entrance plane on the force system is small. They attribute this to the compressible (but subsonic) straightening of the flow in the entrance zone.

The Nozzle Boundary Condition

In order to properly carry out the time dependent solutions of the chamber flow, it is necessary to treat it as a separate flow regime separated from the nozzle by the arbitrarily chosen nozzle entrance plane or surface. Obviously there does not exist a sharp demarcation between the zones of flow. However, the nature of the field changes so rapidly as the gas

particles enter the nozzle that it is a useful artifice to define a surface of demarcation. At this surface, we must match the motions of the gas particles so that continuity and other physical and geometrical requirements are met.

The problem we are addressing was anticipated by the early investigators of jet damping. Careful perusal of their analysis is very helpful in guiding us in the direction we must go. Consider this quotation from Newton, Rosser and Gross³:

"We call attention to one tacit assumption made in deriving the formula for jet damping. When we gave the sidewise component of velocity of the gas issuing from the nozzle as ref, we were assuming that the gas was going 'straight' through the nozzle. Actually, this has not been proved so far as we know. The rocket walls have a sidewise motion of ref, but it needs to be shown that the main stream of gas going through the nozzle shares this sidewise motion. One can make a rough argument as follows: Until the gas reaches the throat of the nozzle, it is moving more slowly than the speed of sound. Hence disturbances, such as the yawing motion of the rocket, can be propagated into the gas stream faster than they are swept downstream by the gas flow. Consequently, we may expect the gas stream as a whole to participate in the yawing motion of the rocket until it reaches the throat of the nozzle. Thereafter, the gas is going faster than the speed of sound and probably leaves the nozzle without acquiring any additional sidewise motion."

The authors then propose a modification to the jet damping that seems to have been lost to later analysts who have paid scant attention to the physical realities of the nozzle effects. They also discussed experiments that would verify the jet damping analysis, but laboratory scale measurements have not been attempted until those described later were carried out in the present study.

The approach used here to define the conditions at the boundary plane follows one successfully used for many years in an analogous problem involving acoustic waves in the chamber flow. Except for the frequencies involved, the waves of compressibility behave much like the waves of vorticity that we have described earlier in the report. In fact, in the rocket combustion instability problem, the two types of waves are inextricably linked.^{41, 42} When conditions are such that acoustic waves can be amplified, vorticity waves also appear because rotational flow is generated at the chamber boundaries. This is completely analogous to the problem of interest here. However in our case the vorticity is introduced because of the angular motion of the chamber boundaries as already described in detail.

In the combustion instability problem, one must analyze the growth and decay of a wave system superposed on a mean flow just as we must do in the nutation instability problem. It is also necessary to treat boundary conditions at the nozzle entrance plane in an analogous fashion. Here we can draw from much experience in the part of the rocket community that has dealt with instability problems.

The method that has evolved is based on the notion that the deviations from the mean flow are quite small and a perturbation is completely justified. One is then enabled to treat the boundary condition by a transfer or "admittance" function. Since the inertial wave problem is completely similar, it is clear that a nozzle admittance function is a useful way to approach this important boundary condition. What we must do is define a relationship between the velocity and pressure fluctuations at the nozzle entrance surface that properly represents the response of the compressibility-dominated downstream flow to the fluctuations

at the entrance plane.

The admittance function, in effect, represents the local influence of a complex train of physical events within the nozzle that act in response to the flow oscillations at the entrance. One must carefully account for the important physical effects. It is clear that oscillations excite a compressible response in the nozzle. That is, the inertial pressure fluctuations at the boundary plane produces a train of acoustic waves in the nozzle. The effects of rotation are negligible compared to the effects of compressibility in the nozzle. The disturbances propagate at the sonic speed rather than at the local flow speed as they did inside the combustion chamber.

Account must be taken of the behavior near the throat. At this point, yet another regime of flow is entered because of the critical conditions at the throat. The sonic plane at the throat does not allow passage of small disturbances existing downstream to be propagated upstream because the flow speed exceeds the sonic velocity. Disturbances generated by wobbling within the nozzle cannot affect similar oscillatory gas motions within the motor chamber. This is a problem familiar to combustion instability analysts and we may directly utilize their results if care is taken to properly define matching conditions at the nozzle entrance plane. Since there exists an extensive literature on this problem, we will not repeat it here. Instead we will simply state the results we need and direct interested readers to the source of the information. There have been very elaborate analyses designed to account for interacting wave systems of exceeding complexity. For our purposes we need only the following information:

- Relationship between velocity fluctuations parallel to the surface and the local pressure fluctuations
- Relationship between velocity fluctuations normal to the surface and the local pressure fluctuations

Keep in mind that the inertial waves consist of velocity fluctuations with axial, radial and circumferential motions. We must account for velocity fluctuations both parallel and normal to the entrance plane. The former are readily accommodated by noting that any gas motions across the nozzle entrance are quickly dissipated without important reflection within the compressible region. This observation may seem conveniently simple, but it is in fact the result of extraordinarily complex analyses carried out by several investigators.⁴³⁻⁴⁵ We may also utilize a similarly simple result for the axial motions. In this case, it is known both analytically and experimentally that a simple transfer function applies in the majority of cases. Again, an elaborate analysis has been carried out, but the simple theory of Crocco and Cheng⁴⁵ applies in our case. It was originally deduced by applying an assumption of quasi-steady flow. That is, it was assumed that the oscillations are fairly slow. In our case this assumption is entirely adequate; the inertial frequencies are much lower than the acoustic frequencies characterizing the combustion chamber. From the nozzle entrance gasdynamics, one finds the following relationship between small pressure and velocity fluctuations at the entrance plane:

$$\mathbf{u}' \cdot \mathbf{n} = A_N p' \quad (150)$$

The factor of proportionality

$$A_N = \left(\frac{R\Omega}{a_0} \right) \frac{\gamma - 1}{2} M_N \quad (151)$$

is the nozzle admittance function that we need to complete our treatment of the chamber boundary conditions. The value for A_N has been corrected for the set of nondimensional parameters appropriate to the study of spinning rockets. The factor in parentheses in equation 151 corrects the acoustic admittance value for use in the present situation. Notice that this factor is the ratio of the gas velocity due to spin to the sound speed: a very small number. This shows that the inertial pressure fluctuations, induced by chamber wobbling, do not strongly interact with the nozzle. The assumption:

$$\mathbf{u}' \cdot \mathbf{n} = 0 \quad (152)$$

is valid across the nozzle entrance. The flow through the nozzle is dominated by compressibility effects, and it thus appears that the nozzle flow does not play an important role in the nutation instability problem.

Forced Motion of the Combustion Chamber Gas Flow

Overview

We have demonstrated, in the last subsections, that the gas contained in a spinning chamber can support inertial waves in the same frequency range as the coning frequency of the spacecraft. It is now necessary to determine if such waves can be driven by the nutation. The objective is to see how such waves interact in terms of reaction torques acting on the vehicle. We expect that these torques will not be the same as those arising in the classical jet damping analysis because of assumptions that preclude the possibility of relative motion of gas particles in response to nutation.

To explore these matters further, we must study a more complete representation of the chamber gas flow. The following elements must be included:

- Inertial forces such as angular acceleration and Coriolis
- Convective fluid accelerations
- Nozzle flow
- Combustion
- Compressibility
- Viscous shear stresses
- Combustion chamber and nozzle geometry
- Resonant interaction with nutation

To accommodate all of these influences requires a numerical solution. We fully understand the need for this approach and we will discuss our progress in implementing it in the next section. We also emphasize, however, that analytical solutions must be pursued simultaneously: both as a guide to the numerical work and to provide better physical understanding of the flow.

We will use the inertial wave model as a starting point in developing an analytical solution. A cylindrical geometry and several simple mean flow models that simulate the real system sufficiently well will be utilized. The main objective is to see how the gases react dynamically to the chamber motion. We will incorporate, to the greatest extent possible, the influences we have listed in simple analytical form.

Forced Oscillations

Earlier studies¹ attempted to show that gas motions are dominated by vorticity wave effects. This was done in terms of the velocity disturbance directly. It is instructive to extend our discussion of the closed chamber case in a previous subsection, which focused on the pressure perturbations. We will set up the machinery needed to include nozzle and combustion effects. We will find that the latter are of no consequence.

Since the vehicle nutation drives the gas motions, it is appropriate to assume that the system response is a harmonic oscillation at the nutation frequency. Thus, we put

$$\begin{aligned}\omega' &= \omega_0 \exp(i\lambda_s t) \\ u' &= Q \exp(i\lambda_s t) \\ p' &= \phi \exp(i\lambda_s t)\end{aligned}\tag{153}$$

where λ is the spacecraft frequency. Using these expressions to simplify equations 106 and 107 we find

$$\begin{cases} \nabla \cdot \mathbf{Q} = 0 \\ i\lambda \mathbf{Q} + 2\mathbf{k} \times \mathbf{Q} + \nabla \phi = \mathbf{F} \end{cases} \quad (154)$$

$$\quad (155)$$

where \mathbf{F} is the forcing function

$$\mathbf{F} = -Ro(\mathbf{Q} \cdot \nabla \mathbf{U} + \mathbf{U} \cdot \nabla \mathbf{Q}) - 2\boldsymbol{\omega}_o \times \mathbf{U} - \frac{i\lambda}{Ro} \boldsymbol{\omega}_o \times \mathbf{r} \quad (156)$$

consisting of the inertial and convective accelerations. Notice that the latter terms are proportional to the Rossby number. In large rockets the Rossby number is small. Indeed, as we will emphasize in the next chapter, it is because of the low Rossby number that flow-induced nutation was not observed in earlier rockets.

Using Rossby Number as a Small Parameter

In the classical solution of rotating fluid problems, the smallness of the Rossby number often leads to simplified solutions. We will also be able to take advantage of this smallness in our problem. One can do this in a formal manner by introducing perturbation expansions of the form

$$\mathbf{u}' = \mathbf{u}^{(0)} + Ro\mathbf{u}^{(1)} + Ro^2\mathbf{u}^{(2)} + O(Ro^3) \quad (157)$$

This breaks a complex problem into a series of simpler linearized ones. In our case, the linearization has already been accomplished by using the smallness of the nutation-induced flow disturbances. Further algebraic simplification results if we use expansions using the Rossby number as the perturbation parameter.

The inertial forcing function, \mathbf{F} , in equation 156 can be expanded using this approach. One can write

$$\mathbf{F} = \mathbf{F}_0 + Ro\mathbf{F}_1 + O(Ro^2) \quad (158)$$

where

$$\begin{cases} \mathbf{F}_0 = -2\boldsymbol{\omega}_o \times \mathbf{U} - \frac{i\lambda}{Ro} \boldsymbol{\omega}_o \times \mathbf{r} \\ \mathbf{F}_1 = -(\mathbf{Q}_0 \cdot \nabla \mathbf{U} + \mathbf{U} \cdot \nabla \mathbf{Q}_0) \\ \mathbf{F}_2 = -(\mathbf{Q}_1 \cdot \nabla \mathbf{U} + \mathbf{U} \cdot \nabla \mathbf{Q}_1) \\ \text{etc.} \end{cases} \quad (159)$$

This gives us a method for improving the solution by a simple iterative procedure. In the limit as Rossby number approaches zero, the first term in the expansion becomes an increasingly better approximation to the solution.

Derivation of the Forced Wave Equation for the Pressure

A procedure similar in all respects to that used in deriving the Poincare' equation must be followed to find the forced wave equation and boundary conditions for the pressure. The terms on the right of 155 have the form of harmonically oscillating forces. We wish to determine how the chamber pressure field responds to these forces. Eliminating the velocity in favor of pressure just as we did in the previous subsection, we find the boundary value problem

$$\left\{ \begin{aligned} \nabla^2 \phi - \frac{4}{\lambda^2} (\mathbf{k} \cdot \nabla)^2 \phi &= G \end{aligned} \right. \quad (160)$$

$$\left\{ \begin{aligned} \mathbf{n} \cdot \nabla \phi + \frac{2i}{\lambda} \mathbf{n} \cdot \mathbf{k} \times \nabla \phi - \frac{4}{\lambda^2} \mathbf{n} \cdot \mathbf{k} (\mathbf{k} \cdot \nabla \phi) &= H \quad \text{on } S \end{aligned} \right. \quad (161)$$

where functions G and H are given by

$$\left\{ \begin{aligned} G &= \nabla \cdot \mathbf{F} - \frac{4}{\lambda^2} \frac{\partial}{\partial z} \mathbf{k} \cdot \mathbf{F} - \frac{2i}{\lambda} \mathbf{k} \cdot \nabla \times \mathbf{F} \end{aligned} \right. \quad (162)$$

$$\left\{ \begin{aligned} H &= \mathbf{n} \cdot \mathbf{F} - \frac{4}{\lambda^2} (\mathbf{n} \cdot \mathbf{k}) \mathbf{k} \cdot \mathbf{F} + \frac{2i}{\lambda} \mathbf{n} \cdot \mathbf{k} \times \mathbf{F} \end{aligned} \right. \quad (163)$$

This is an inhomogeneous wave equation that must satisfy an inhomogeneous boundary condition. It is completely appropriate to construct solutions for this set by using superposition of solutions of the unperturbed problem. This is such a basic approach that it should require no lengthy discussing here. The authors have been chagrined to find that readers of our previous work¹ that used a similar approach could not understand the benefits of this method. We have been criticized for associating inertial waves with the gas motion in a spinning rocket. After very carefully reexamining the problem we insist that this is the proper way to describe the time-dependent gas motions. The response is basically a forced oscillation of a spinning fluid. It is perfectly correct to describe this an inertial wave response.

We will therefore attempt to find solutions by superimposing the simple solutions for the closed chamber by writing

$$\phi = \sum_m A_m \Phi_m \quad (164)$$

where the inertial eigenfunctions for a particular mode $m = n$ (remember that m is a set of three integers that specify the mode)

$$\Phi_n = J_k(\xi r) \exp(ik\theta) \cos\left(\frac{n\pi z'}{2b}\right) \quad (165)$$

represents the pressure wave. After some algebraic manipulation, an equation for the coefficients in the Fourier expansion can be derived. One must solve

$$\frac{4(\lambda - \lambda_n)}{\lambda^2} \left[D_n A_n - \frac{i}{2} \sum_{m \neq n} A_m \left\{ \frac{(\lambda - \lambda_n)}{(\lambda_m + \lambda_n)} \int_S \mathbf{n} \cdot \mathbf{k} \times \Phi_n^* \nabla \Phi_m dS \right\} \right] = \int_V \Phi_n^* G dV + \int_S \Phi_n^* H dS \quad (166)$$

where

$$D_n = \frac{\lambda}{\lambda_n} \left[\left(\frac{1}{\lambda_n} + \frac{1}{\lambda} \right) \int_V |\mathbf{k} \cdot \nabla \Phi_n|^2 dV - \frac{i}{2} \int_S \mathbf{n} \cdot \mathbf{k} \times \Phi_n^* \nabla \Phi_n dS \right] \quad (167)$$

for the coefficients. The * denotes the complex conjugate. The method described was developed by Kudlick^{11,12}. Notice that this is a set of simultaneous algebraic equations. Solutions can in principle be found for any forcing functions as represented by functions G and H. To simplify notation we are using the index n to represent any given mode. Remember that three mode integers are required to specify a given three-dimensional inertial mode so that each n represents a set of three integers. A simple numerical procedure can be used to solve the resulting set of equations since they are a linear set.

Since a cylindrical geometry is assumed, the various terms in equations 166 and 167 are readily evaluated. For example

$$\mathbf{k} \cdot \nabla \Phi_n = \frac{\partial \Phi_n}{\partial z} = -\left(\frac{n\pi}{2b} \right) J_k(\xi r) \exp(ik\theta) \sin\left(\frac{n\pi z'}{2b} \right) \quad (168)$$

and

$$\int_S \mathbf{n} \cdot \mathbf{k} \times \Phi_n^* \nabla \Phi_n dS = -i(2\pi b) J_1^2(\xi) \quad (169)$$

The volume integral is

$$\begin{aligned} \int_V |\mathbf{k} \cdot \nabla \Phi_n|^2 dV &= \left(\frac{n\pi}{2b} \right)^2 \int_0^1 \int_0^{2\pi} \int_0^{2b} r J_1^2(\xi r) \sin^2\left(\frac{n\pi z'}{2b} \right) dr d\theta dz' = \\ &= \left(\frac{n\pi}{2b} \right)^2 \int_0^1 r J_1^2(\xi r) dr \int_0^{2\pi} d\theta \int_0^{2b} \sin^2\left(\frac{n\pi z'}{2b} \right) dz' = \\ &= \pi b \left(\frac{n\pi}{2b} \right)^2 \left[J_1^2(\xi) + \left(1 - \frac{1}{\xi^2} \right) J_1^2(\xi) \right] \end{aligned} \quad (170)$$

Thus coefficient Dn becomes

$$D_n = \frac{\lambda}{\lambda_n} \left[\left(\frac{1}{\lambda_n} + \frac{1}{\lambda} \right) \pi b \left(\frac{n\pi}{2b} \right)^2 \left[J_1^2(\xi) + \left(1 - \frac{1}{\xi^2} \right) J_1^2(\xi) \right] - (\pi b) J_1^2(\xi) \right] \quad (171)$$

In dealing with the right-hand forcing terms, we must specify the mean flow field and the chamber geometry as well as the assumed vehicle angular motion. We will assume a small Rossby number as already discussed and write

$$\begin{cases} G_o = \nabla \cdot \mathbf{F}_0 - \frac{4}{\lambda^2} \frac{\partial}{\partial z} \mathbf{k} \cdot \mathbf{F}_0 - \frac{2i}{\lambda} \mathbf{k} \cdot \nabla \times \mathbf{F}_0 \\ H_o = \mathbf{n} \cdot \mathbf{F}_0 - \frac{4}{\lambda^2} (\mathbf{n} \cdot \mathbf{k}) \mathbf{k} \cdot \mathbf{F}_0 + \frac{2i}{\lambda} \mathbf{n} \cdot \mathbf{k} \times \mathbf{F}_0 \quad \text{on } S \end{cases} \quad (172)$$

where

$$\begin{aligned}
 F_0 &= -2\varpi e^{i\theta} [iU_z \mathbf{e}_r - U_z \mathbf{e}_\theta + (U_\theta - iU_r) \mathbf{e}_z] - \frac{i\lambda}{Ro} \varpi e^{i\theta} [i(z' - L_1) \mathbf{e}_r - (z' - L_1) \mathbf{e}_\theta - ir \mathbf{e}_z] \\
 &= \varpi e^{i\theta} \left\{ \left[\frac{\lambda}{Ro} (z' - L_1) - i(2U_z) \right] \mathbf{e}_r + \left[(2U_z) + i \frac{\lambda}{Ro} (z' - L_1) \right] \mathbf{e}_\theta + \right. \\
 &\quad \left. + \left[-\left(2U_\theta + \frac{\lambda}{Ro} r \right) + i(2U_r) \right] \mathbf{e}_z \right\} \quad (173)
 \end{aligned}$$

These results must now be inserted in equation 166, which can first be simplified by using equation 169. Thus equation 166, giving the coefficients becomes

$$\frac{4(\lambda - \lambda_n)}{\lambda^2} \left[D_n B_n + \sum_{m \neq n} B_m \left\{ \frac{(\lambda - \lambda_n)}{(\lambda_m + \lambda_n)} (\pi b) J_1^2(\xi) \right\} \right] = \int_V \Phi_n^* G dV + \int_S \Phi_n^* H dS \quad (174)$$

The position vector (origin at the vehicle mass center) and other quantities needed in the evaluations are:

$$\omega_o = \varpi(1 + ij) = \varpi(\mathbf{e}_r + i\mathbf{e}_\theta) e^{i\theta}$$

$$\mathbf{U} = U_r \mathbf{e}_r + U_\theta \mathbf{e}_\theta + U_z \mathbf{e}_z$$

$$\mathbf{r} = r \mathbf{e}_r + (z' - L_1) \mathbf{k}$$

where L_1 locates the aft end of the chamber (see Figure 32). We will insert specific functions for the mean flow velocity components later. After some algebra, we find for a cylindrical chamber:

$$G_0 = -2\varpi e^{i\theta} \left\{ \left(1 - \frac{4}{\lambda^2} \right) \left(\frac{\partial U_\theta}{\partial z} - i \frac{\partial U_r}{\partial z} \right) + i \left(1 + \frac{2}{\lambda} \right) \frac{\partial U_z}{\partial r} \right\} \quad (175)$$

and

$$H_0 = \begin{cases} \pm \varpi e^{i\theta} \left(1 - \frac{4}{\lambda^2} \right) \left[-\left(2U_\theta + \frac{\lambda}{Ro} r \right) + i(2U_r) \right] & \text{on endwalls} \end{cases} \quad (176)$$

$$\begin{cases} \varpi e^{i\theta} \left(1 + \frac{2}{\lambda} \right) \left[\frac{\lambda}{Ro} (z' - L_1) - i(2U_z) \right] & \text{on sidewalls} \end{cases} \quad (177)$$

The integral on the right of the coefficient equation can now be evaluated. One finds

$$\int_V \Phi_n^* G dV = -4\pi\varpi \int_0^1 \int_0^{2b} r J_1(\xi r) \cos\left(\frac{n\pi z}{2b}\right) \left[\left(1 - \frac{4}{\lambda^2} \right) \left(\frac{\partial U_\theta}{\partial z} - i \frac{\partial U_r}{\partial z} \right) + i \left(1 + \frac{2}{\lambda} \right) \frac{\partial U_z}{\partial r} \right] \quad (178)$$

$$\int_S \Phi_n^* H dS = 2\pi\omega \left\{ \left(1 - \frac{4}{\lambda^2}\right) \cos(n\pi) \int_0^1 r J_1(\xi r) \left[-\left(2U_\theta + \frac{\lambda}{Ro} r\right) + i(2U_r) \right]_{z'=2b} dr \right. \\ \left. - \left(1 - \frac{4}{\lambda^2}\right) \int_0^1 r J_1(\xi r) \left[-\left(2U_\theta + \frac{\lambda}{Ro} r\right) + i(2U_r) \right]_{z'=0} dr \right. \\ \left. + \left(1 + \frac{2}{\lambda}\right) J_1(\xi) \int_0^{2b} \cos\left(\frac{n\pi z'}{2b}\right) \left[\frac{\lambda}{Ro} (z' - L_1) - i(2U_z) \right] dz' \right\} \quad (179)$$

Now all that is needed is specification of the mean flow field and final evaluation of the integrals in order to find the forced solution.

We have investigated several cases using progressively more realistic models for the mean flow. This was done to determine the sensitivity of the solutions to the actual chamber mean flow. This mean flow was taken to be the flow field that would be present in the spinning rocket in the absence of nutation disturbances.

Case 1 was defined to be the flow field assumed in jet damping theory and in other gas interaction studies by other groups.³⁴⁻³⁷ This consists of a uniform flow such as would be generated at a head-end web. The chamber contains a solid-body vortex because of the axial spin, but account is taken of the free vortex component introduced by radial flow into the nozzle. Table 4 shows this model and the corresponding results for the forcing integrals.

Case 2 again assumes a uniform flow. However, a more realistic azimuthal flow is included. A potential vortex is assumed in place of the solid body vortex. Table 5 summarizes the results for this case.

Case 3 represents a simple, but far more realistic, model for the mean flow. It includes the potential vortex and a representation for the radial flow component required to account for the nozzle. This solution has been discussed in detail by Or.³⁶⁻³⁷ Table 6 shows the velocity components and resulting force integrals

We have also studied more general approximate solutions for the mean flow that account for the nozzle flow in more detail. However, numerical results for the coefficient in the Fourier series were not strongly affected. Therefore, no detailed discussion is given here. When a truly realistic mean flow is needed, recourse must be made to a full finite-difference numerical treatment of the type discussed in the next section.

Table 4. Forcing Functions for Case 1

Case 1: UNIFORM FLOW, SOLID BODY VORTEX

$$U_r = 0, \quad U_\theta = 0, \quad U_z = -1$$

$$\int_V \Phi_n^* G dV = 0$$

$$\begin{aligned} \int_S \Phi_n^* H dS &= 2\pi\omega \frac{\lambda}{Ro} \left\{ \left(1 + \frac{2}{\lambda}\right) J_1(\xi) \int_0^{2b} z' \cos\left(\frac{n\pi z'}{2b}\right) dz' - \right. \\ &\quad \left. - \left(1 - \frac{4}{\lambda^2}\right) [1 - \cos(n\pi)] \int_0^1 r^2 J_1(\xi r) dr \right\} \\ &= 2\pi\omega \frac{\lambda}{Ro} [\cos(n\pi) - 1] \left[\left(\frac{2b}{n\pi}\right)^2 \left(1 + \frac{2}{\lambda}\right) J_1(\xi) - \right. \\ &\quad \left. - \left(1 - \frac{4}{\lambda^2}\right) \left(\frac{2J_1(\xi)}{\xi^2} - \frac{J_0(\xi)}{\xi}\right) \right] \end{aligned}$$

Table 5. Forcing Functions for Case 2

Case 2: UNIFORM FLOW, POTENTIAL VORTEX

$$U_r = 0, \quad U_\theta = \frac{1}{Ro} \left(\frac{1}{r} - r \right), \quad U_z = -1$$

$$\int_V \Phi_n^* G dV = 0$$

$$\int_S \Phi_n^* H dS = 2\pi\omega [\cos(n\pi) - 1] \left\{ \frac{\lambda}{Ro} \left(\frac{2b}{n\pi}\right)^2 \left(1 + \frac{2}{\lambda}\right) J_1(\xi) - \right. \\ \left. - \frac{1}{Ro} \left(1 - \frac{4}{\lambda^2}\right) \left[\frac{\lambda - 2}{\xi^2} (2J_1(\xi) - \xi J_0(\xi)) + \frac{2}{\xi} (1 - J_0(\xi)) \right] \right\}$$

Table 6. Forcing Functions for Case 3

Case 3: SIMPLE ROCKET FLOW, POTENTIAL VORTEX

$$Ur = -r, \quad U_\theta = \frac{1}{Ro} \left(\frac{1}{r} - r \right), \quad U_z = 2z' - (4b+1), \quad \frac{\partial U_\theta}{\partial r} = 0, \quad \frac{\partial U_z}{\partial r} = 0, \quad \frac{\partial U_r}{\partial z} = 0$$

$$\int_V \Phi_n^* G dV = 0$$

$$\int_S \Phi_n^* H dS = 2\pi\omega [\cos(n\pi) - 1] \left\{ \begin{aligned} & \frac{\lambda}{Ro} \left(\frac{2b}{n\pi} \right)^2 \left(1 + \frac{2}{\lambda} \right) J_1(\xi) \\ & - \frac{1}{Ro} \left(1 - \frac{4}{\lambda^2} \right) \left[\frac{\lambda - 2}{\xi^2} (2J_1(\xi) - \xi J_0(\xi)) + \frac{2}{\xi} (1 - J_0(\xi)) \right] \\ & + i \left\{ -2 \left(1 - \frac{4}{\lambda^2} \right) \frac{1}{\xi^2} [2J_1(\xi) - \xi J_0(\xi)] - 4 \left(\frac{2b}{n\pi} \right)^2 \left(1 + \frac{2}{\lambda} \right) J_1(\xi) \right\} \end{aligned} \right\}$$

$$\int_S \Phi_n^* H dS = 2\pi\omega [\cos(n\pi) - 1] \left\{ \begin{aligned} & \underbrace{\frac{\lambda}{Ro} \left(\frac{2b}{n\pi} \right)^2 \left(1 + \frac{2}{\lambda} \right) J_1(\xi)}_{\text{Sidewall Effect}} \\ & - \frac{1}{Ro} \left(1 - \frac{4}{\lambda^2} \right) \left[\frac{\lambda - 2}{\xi^2} (2J_1(\xi) - \xi J_0(\xi)) + \frac{2}{\xi} (1 - J_0(\xi)) \right] \\ & \quad \underbrace{\hspace{10em}}_{\text{Vortex and Endwall Effect}} \\ & + i \left\{ -2 \left(1 - \frac{4}{\lambda^2} \right) \frac{1}{\xi^2} [2J_1(\xi) - \xi J_0(\xi)] - 4 \left(\frac{2b}{n\pi} \right)^2 \left(1 + \frac{2}{\lambda} \right) J_1(\xi) \right\} \\ & \quad \underbrace{\hspace{10em}}_{\text{Radial Flow and z-Dependent Axial Flow}} \end{aligned} \right\}$$

Solution for the Pressure Wave

In order to determine the system stability, we will employ the alternate control volume shown in Figure 30. Equation 43 is used to calculate the interaction moment. This approach is deliberately used so that we can bypass the conceptual difficulties experienced in the method used in Reference 1. In that case, attention was focused on the velocity perturbations. Interaction torques were determined by estimating the angular momentum flux passing across a control volume encompassing the entire vehicle, including the motor and contained gas flow.

In order to use the alternative approach in which the control volume boundary separates the gases from the solid parts of the system, it is necessary to determine the pressure distribution within the chamber in order to calculate the reaction torque. A computer program was written for this purpose. It is designed to solve for the coefficients of the Fourier-Bessel series. These results are then used to determine the reaction torque coefficient, R_{gain} , for the system. Appendix A is the source code for this program. It is arranged in a modular way so that changes in spacecraft parameters and motor geometry can be readily incorporated. The case shown represents a typical PAM-D using the Case 3 model for the gas flow. All program modules are given including Bessel function routines and the routine for solving the simultaneous equations. This program will be referred to later in terms of determination of the disturbing torques. This, of course, is the aim of the entire calculation.

In carrying out solutions for the Case 1 mean flow condition, the departure from jet damping theory was immediately apparent. What this solution represents is a relaxation of the restrictive assumptions that resulted in classical jet damping. We have now allowed the gas particles to play a role in the response to the chamber motion. The result is a greatly modified pressure pattern. In particular, the pressure is no longer 180° out of phase with the angular velocity as in jet damping. This is a major difference. In fact, even for this simple mean flow there is a jet driving effect of the order of what was before a damping influence. This is a very significant finding. It shows that jet damping is inappropriate when the Rossby number is small. That is, the jet damping assumptions do not apply when the chamber is large and spinning rapidly.

Similar results were found for the other cases. The presence of the strong circumferential vortex flow, induced in the nozzle by chamber spin, produced a significant modification and further increased the reaction torque. As the more realistic flow models (such as Case 3) were used, in which appropriate estimates of the radial mean flow velocity are introduced, the main effect was the swinging of the reaction torque vector more nearly into line with the nutation angular velocity vector.

The major difference between the vorticity wave solutions and the jet damping pressure solution is the introduction of an axial variation in pressure perturbation amplitude and phase. Notice in the jet damping case (see equation 98) the Coriolis term does not have any axial dependence. The pressure pattern rotates uniformly with respect to the chamber wall. In the more realistic case, the pressure distribution along the wall follows more nearly a cosine distribution. The pressure maxima are on opposite sides at the front and rear of the chamber; a greatly enhanced nutation interaction moment results.

Solution for the Unsteady Velocity Field

In order to evaluate the interaction moment, we must estimate the momentum flux carried out of the control volume through the propellant surfaces. That is, we must also evaluate the second term in equation 96,

$$\overline{M}_{flow} = - \int_S \mathbf{r} \times \phi \mathbf{n} \, dS - \int_S \mathbf{r} \times \mathbf{Q} (\mathbf{U} \cdot \mathbf{n}) \, dS \quad (180)$$

To do this, it is necessary to calculate the velocity perturbation. This is most easily accomplished directly by writing the velocity wave equation. Starting again with equations 154 and 155,

$$\begin{cases} i\lambda \mathbf{Q} + 2\mathbf{k} \times \mathbf{Q} + \nabla \phi = \mathbf{F} \\ \mathbf{n} \cdot \mathbf{Q} = G \quad \text{on } S \end{cases} \quad (181)$$

where we are accounting for combustion and nozzle effects as discussed in the last subsection by means of response functions. As we did with the pressure field calculations it is useful to use the inertial eigenfunctions to produce a Fourier-Bessel series for the velocity distribution. Thus, we write

$$\mathbf{Q} = \sum_m B_m \mathbf{Q}_m \quad (182)$$

In order to find the coefficients, it is helpful to use the orthogonality properties of the eigenfunctions. Two useful expressions are

$$\int_V \mathbf{Q}_m \cdot \mathbf{Q}_n^* dV = \begin{cases} 0 & (m \neq n) \\ E_m^2 & (m = n) \end{cases} \quad (183)$$

$$\int_V \mathbf{k} \cdot \mathbf{Q}_m \cdot \mathbf{Q}_n^* dV = \begin{cases} 0 & (m \neq n) \\ -\frac{i\lambda_m}{2} E_m^2 & (m = n) \end{cases} \quad (184)$$

these are easily derived using the unperturbed momentum equation developed in the Poincaré solution (see equation 115). The * denotes the complex conjugate.

As before, we expand the forcing function using the Rossby number as a small parameter. Retaining first order terms, we find

$$\mathbf{F} = \mathbf{F}^{(0)} + Ro \mathbf{F}^{(1)} + Ro^2 \mathbf{F}^{(2)} + \dots = -2\omega_o \times \mathbf{U} - \frac{i\lambda}{Ro} \omega_o \times \mathbf{r} + O(Ro) \quad (185)$$

and the expression for the Fourier coefficients is easily found using the orthogonality results. Thus,

$$B_m = \frac{-i}{(\lambda - \lambda_m) E_m^2} \int_V \mathbf{Q}_m^* \cdot \mathbf{F} dV \quad (186)$$

where we have neglected the response function terms because they are very small for cases of interest.

The same mean flow cases were studied in determining the velocity perturbations. Tables 7 and 8 summarize the results. Unlike the pressure solutions, it is not necessary to solve for the coefficients by solving simultaneous equations. For the low Rossby number case, equation

186 gives them directly. The final results are shown in the tables. The velocity distributions are quite similar to those shown in the numerical solutions for the closed chamber by Vaughn²⁶ (see Figures 6 and 7) and by Flandro.¹

Table 7. Solution for Fourier Coefficients for Case 1

CASE 1: Small Rossby Number, Uniform Flow, Constant Amplitude

$$U_r = U_\theta = 0, \quad U_z = -1$$

$$\begin{aligned} \int_V \mathbf{Q}_m^* \cdot \mathbf{F} dV &= -\omega \int_V \left\{ \left[2U_z(f_1 - f_2) - 2(U_r - iU_\theta)f_3 \right] \right. \\ &\quad \left. + \frac{i\lambda}{Ro} [(z' - L_t)(f_1 - f_2) - rf_3] \right\} dV \\ &= -2\pi\omega \int_0^1 \int_0^{2b} r \left\{ (f_1 - f_2) \left(-2 + \frac{i\lambda}{Ro} (z' - L_t) \right) - \frac{i\lambda}{Ro} rf_3 \right\} dr dz \end{aligned}$$

$$\begin{aligned} \int_V \mathbf{Q}_m^* \cdot \mathbf{F} dV &= -2\pi\omega \frac{i\lambda}{Ro} (\cos n\pi - 1) \int_0^1 r \left\{ \frac{1}{(\lambda_m - 2)} \left[\frac{1}{r} J_1(\xi r) + \xi J_1'(\xi r) \right] \left(\frac{2b}{n\pi} \right)^2 \right. \\ &\quad \left. + \frac{r}{\lambda_m} J_1(\xi r) \right\} dr \\ &= -2\pi\omega \frac{i\lambda}{Ro} (\cos n\pi - 1) \left\{ \left(\frac{2b}{n\pi} \right)^2 \frac{J_1(\xi)}{(\lambda_m - 2)} + \frac{1}{\xi^2 \lambda_m} [2J_1(\xi) - \xi J_0(\xi)] \right\} \end{aligned}$$

$$B_m = -2\pi\omega \frac{\lambda}{Ro(\lambda - \lambda_m)E_m^2} (\cos n\pi - 1) \left\{ \left(\frac{2b}{n\pi} \right)^2 \frac{J_1(\xi)}{(\lambda_m - 2)} + \frac{1}{\xi^2 \lambda_m} [2J_1(\xi) - \xi J_0(\xi)] \right\}$$

Table 8. Solution for Fourier Coefficients for Case 3

CASE 3: Simple Rocket Flow with Vortex:

$$Ur = -r, \quad U_\theta = \frac{1}{Ro} \left(\frac{1}{r} - r \right), \quad U_z = 2z' - (4b + 1), \quad \frac{\partial U_\theta}{\partial r} = 0, \quad \frac{\partial U_z}{\partial r} = 0, \quad \frac{\partial U_r}{\partial z} = 0$$

$$B_m = \frac{-i}{(\lambda - \lambda_m) E_m^2} \int_V \mathbf{Q}_m^* \cdot \mathbf{F} dV$$

$$\int_V \mathbf{Q}_m^* \cdot \mathbf{F} dV = -2\pi\omega(\cos n\pi - 1) \left\{ \begin{aligned} & \frac{4}{(\lambda_m - 2)} \left(\frac{2b}{n\pi} \right)^2 J_1(\xi) - \\ & - \left(\frac{2}{\lambda_m \xi^2} \right) [2J_1(\xi) - \xi J_0(\xi)] \\ & + \frac{i}{Ro} \left\{ \begin{aligned} & \frac{\lambda}{(\lambda_m - 2)} \left(\frac{2b}{n\pi} \right)^2 J_1(\xi) - \\ & - \frac{1}{\lambda_m} \left[\frac{2}{\xi} [1 - J_0(\xi)] - \frac{(2 + \lambda)}{\xi^2} [2J_1(\xi) - \xi J_0(\xi)] \right] \end{aligned} \right\} \end{aligned} \right\}$$

$$B_m = -\frac{4\pi\omega}{(\lambda - \lambda_m) E_m^2} \left\{ \begin{aligned} & i \left\{ \begin{aligned} & \frac{4}{(\lambda_m - 2)} \left(\frac{2b}{n\pi} \right)^2 J_1(\xi) - \\ & - \left(\frac{2}{\lambda_m \xi^2} \right) [2J_1(\xi) - \xi J_0(\xi)] \end{aligned} \right\} \\ & - \frac{1}{Ro} \left\{ \begin{aligned} & \frac{\lambda}{(\lambda_m - 2)} \left(\frac{2b}{n\pi} \right)^2 J_1(\xi) - \\ & - \frac{1}{\lambda_m} \left[\frac{2}{\xi} [1 - J_0(\xi)] - \frac{(2 + \lambda)}{\xi^2} [2J_1(\xi) - \xi J_0(\xi)] \right] \end{aligned} \right\} \end{aligned} \right\} \quad n \text{ odd}$$

Calculation of Nutation Interaction Torques

The object of the detailed computation of the unsteady flow field is the estimation of the interaction torques produced during nutation. As already shown, the pressure field is drastically altered from the pattern determined when jet damping assumptions are made. The additional degrees of freedom resulting from properly allowing the gas particles to move freely greatly affects the response.

All required elements are now assembled for estimating the torque gain factors and associated stability characteristics for a motor/spacecraft system. We will apply the results to typical system configurations to determine what features are important in promoting nutation instability.

To determine the impact of a realistic unsteady nutation-induced flow on the interaction torques, we use the solutions for pressure and velocity distributions just discussed with the equation

$$\mathbf{M}_{flow} = - \int_S \mathbf{r} \times p \mathbf{n} \, dS - \int_S \mathbf{r} \times \mathbf{u} (\mathbf{u} \cdot \mathbf{n}) \, dS \quad (187)$$

as derived for the alternate control volume in Section 3. As with the other variables, the moment can be written in complex form as an amplitude times the assumed sinusoidal time dependence, so that

$$\mathbf{M}_{flow} = \bar{\mathbf{M}} \exp(i\lambda t) \quad (188)$$

where

$$\bar{\mathbf{M}}_{flow} = - \int_S \mathbf{r} \times \phi \mathbf{n} \, dS - \int_S \mathbf{r} \times \mathbf{Q} (\mathbf{U} \cdot \mathbf{n}) \, dS \quad (189)$$

The expressions for ϕ and \mathbf{Q} can then be inserted and the indicated integration carried out to determine the flow interaction torque acting on the spacecraft. The two components are discussed separately in the following subsections.

Pressure Torque

In computing the pressure contribution to the moment it is necessary to account for both endwall and sidewall pressure distributions. Since the pressure function, ϕ , is in complex form as well as the Fourier coefficients, it is necessary to obtain the real part before carrying out the integrations. Therefore, we put

$$\phi = \varpi \sum_m A_m \phi_m = \varpi \sum_m \left(A_m^{(r)} + i A_m^{(i)} \right) J_1(\xi r) \exp(i\theta) \cos\left(\frac{n\pi}{2b} z'\right) \quad (190)$$

and the real part of the complex function is

$$\phi = \varpi \sum_m \left(A_m^{(r)} \cos \theta - A_m^{(i)} \sin \theta \right) J_1(\xi r) \cos\left(\frac{n\pi}{2b} z'\right) \quad (191)$$

Thus, in terms of the Fourier coefficients, the sidewall torque can be written

$$\begin{cases} \bar{M}_{s_x} = \omega \sum_m \int_0^{2\pi} \int_0^{2b} \left[-A_m^{(r)} \sin \theta \cos \theta + A_m^{(i)} \sin^2 \theta \right] J_1(\xi) \cos\left(\frac{n\pi}{2b} z'\right) (z' - L_{cg}) d\theta dz' \\ \bar{M}_{s_y} = \omega \sum_m \int_0^{2\pi} \int_0^{2b} \left[A_m^{(r)} \cos^2 \theta - A_m^{(i)} \sin \theta \cos \theta \right] J_1(\xi) \cos\left(\frac{n\pi}{2b} z'\right) (z' - L_{cg}) d\theta dz' \end{cases} \quad (192)$$

The integrations are readily accomplished (Appendix B gives several important Bessel function integrals required in the evaluations). The result is

$$\begin{cases} \bar{M}_{s_x} = -2\pi\omega \sum_m \left(\frac{2b}{n\pi}\right)^2 A_m^{(i)} J_1(\xi) \\ \bar{M}_{s_y} = -2\pi\omega \sum_m \left(\frac{2b}{n\pi}\right)^2 A_m^{(r)} J_1(\xi) \end{cases} \quad (193)$$

Similarly the endwall contribution is

$$\begin{cases} \bar{M}_{e_x} = -2\omega \sum_m \int_0^1 \int_0^{2\pi} \left[-A_m^{(r)} \sin \theta \cos \theta + A_m^{(i)} \sin^2 \theta \right] r^2 J_1(\xi r) dr d\theta \\ \bar{M}_{e_y} = -2\omega \sum_m \int_0^1 \int_0^{2\pi} \left[A_m^{(r)} \cos^2 \theta - A_m^{(i)} \sin \theta \cos \theta \right] r^2 J_1(\xi r) dr d\theta \end{cases} \quad (194)$$

The integrals are again easily carried out analytically for the cylindrical geometry and expressions for the torque components can be written in series form as

$$\begin{cases} \bar{M}_{e_x} = -2\pi\omega \sum_m A_m^{(i)} \int_0^1 r^2 J_1(\xi r) dr = -\pi\omega \sum_m A_m^{(i)} \left[J_1'^2(\xi) + \left(1 - \frac{1}{\xi^2}\right) J_1^2(\xi) \right] \\ \bar{M}_{e_y} = -2\pi\omega \sum_m A_m^{(r)} \int_0^1 r^2 J_1(\xi r) dr = -\pi\omega \sum_m A_m^{(r)} \left[J_1'^2(\xi) + \left(1 - \frac{1}{\xi^2}\right) J_1^2(\xi) \right] \end{cases} \quad (195)$$

Since the coefficients are determined in the computer algorithm, it is a simple matter to generate the torque results simultaneously. The program source code listing included in Appendix A implements this calculation.

The total pressure torque is

$$\begin{cases} \bar{M}_x = -\varpi \pi \sum_m \left\{ A_m^{(i)} \left[2 \left(\frac{2b}{n\pi} \right)^2 J_1(\xi) + J_1'^2(\xi) + \left(1 - \frac{1}{\xi^2} \right) J_1^2(\xi) \right] \right\} \\ \bar{M}_y = -\varpi \pi \sum_m \left\{ A_m^{(r)} \left[2 \left(\frac{2b}{n\pi} \right)^2 J_1(\xi) + J_1'^2(\xi) + \left(1 - \frac{1}{\xi^2} \right) J_1^2(\xi) \right] \right\} \end{cases} \quad (196)$$

Notice that the form taken by the analytical results is exactly that expected on the basis of the experimental data. The pitch and yaw moment components are proportional to the amplitude of the nutation wobble, ϖ .

Momentum Torque

The second term in equation 189 represents the flux of angular momentum caused at the burning surface. The gas particles must, in effect, pick up angular momentum due to the chamber motion. The momentum is convected into the chamber with the combustion flow, and must be balanced by a torque acting on the chamber. We must evaluate

$$\bar{M}_{\text{Momentum}} = - \int_S \mathbf{r} \times \mathbf{Q} (\mathbf{U} \cdot \mathbf{n}) dS \quad (197)$$

To set up the calculation, recall that

$$\mathbf{Q} = \varpi \sum_m B_m \mathbf{Q}_m = \varpi \sum_m (B_m^{(r)} + i B_m^{(i)}) (i f_1 \mathbf{e}_r + f_2 \mathbf{e}_\theta + i f_3 \mathbf{k}) e^{i\theta} \quad (198)$$

or

$$\begin{aligned} \mathbf{Q} = \varpi (Q_r^{(r)} \cos \theta - Q_r^{(i)} \sin \theta) \mathbf{e}_r + \varpi (Q_\theta^{(r)} \cos \theta - Q_\theta^{(i)} \sin \theta) \mathbf{e}_\theta + \\ + \varpi (Q_z^{(r)} \cos \theta - Q_z^{(i)} \sin \theta) \mathbf{k} \end{aligned} \quad (199)$$

where the components are

$$\begin{cases} Q_r^{(r)} = \sum_m -B_m^{(i)} f_1 & Q_r^{(i)} = \sum_m B_m^{(r)} f_1 \\ Q_\theta^{(r)} = \sum_m B_m^{(r)} f_2 & Q_\theta^{(i)} = \sum_m B_m^{(i)} f_2 \\ Q_z^{(r)} = \sum_m -B_m^{(i)} f_3 & Q_z^{(i)} = \sum_m B_m^{(r)} f_3 \end{cases} \quad (200)$$

Functions f_1 , f_2 , and f_3 are given by equations 144-146.

Inserting these results in equation 197 yields the momentum torque. The pitch and yaw components are

$$\begin{cases} \bar{M}_x = \omega L_h \int_0^1 \int_0^{2\pi} r \left[(Q_\theta^{(r)} \cos^2 \theta - Q_\theta^{(i)} \sin \theta \cos \theta) + (Q_r^{(r)} \sin \theta \cos \theta - Q_r^{(i)} \sin^2 \theta) \right] dr d\theta \\ \bar{M}_y = \omega L_h \int_0^1 \int_0^{2\pi} r \left[(Q_\theta^{(r)} \sin \theta \cos \theta - Q_\theta^{(i)} \sin^2 \theta) - (Q_r^{(r)} \cos^2 \theta - Q_r^{(i)} \sin \theta \cos \theta) \right] dr d\theta \end{cases} \quad (201)$$

where L_h locates the chamber forward end relative to the vehicle center of mass. Carrying out the integrations, we find

$$\begin{cases} \bar{M}_x = -\omega \pi L_h \sum_m B_m^{(r)} \int_0^1 r (f_1 - f_2) dr \\ \bar{M}_y = \omega \pi L_h \sum_m B_m^{(i)} \int_0^1 r (f_1 - f_2) dr \end{cases} \quad (202)$$

where

$$f_1 - f_2 = \frac{1}{(2 - \lambda_m)} \left[\frac{1}{r} J_1(\xi r) + \xi J_1(\xi r) \right] \quad \text{at } z = 2b \quad (203)$$

Finally, the pitch and yaw momentum torque components are found to be

$$\begin{cases} \bar{M}_x = -\omega \pi L_h \sum_m \frac{1}{(2 - \lambda_m)} B_m^{(r)} J_1(\xi) \\ \bar{M}_y = \omega \pi L_h \sum_m \frac{1}{(2 - \lambda_m)} B_m^{(i)} J_1(\xi) \end{cases} \quad (204)$$

As in the case of the pressure torque, the torque components are easily determined in the computer program because all the necessary coefficients are available.

Torque Gain Factors

The form of the moment results exactly matches our expectations based on the experimental data. As written, the torque components correspond to the configuration at some arbitrary reference time with the perturbation angular velocity pointing parallel to the positive pitch (x-axis) direction. This makes identification of the parallel and normal (to the nutation angular velocity vector) components of the interaction torque a simple matter. Remember that the moment component parallel to the perturbation angular velocity vector ω' controls the growth or decay of the nutation; the normal component determines the nutation frequency shift.

We will denote the proportionality factors between the moment and the magnitude of the perturbation velocity, $\omega = |\omega'|$ as the Rgain and Sgain factors, respectively.

The total interaction torque is the combination of equations 196 and 204:

$$\left\{ \begin{aligned} \bar{M}_x &= -\omega \pi \sum_m \left\{ A_m^{(i)} \left[2 \left(\frac{2b}{n\pi} \right)^2 J_1(\xi) + J_1'^2(\xi) + \left(1 - \frac{1}{\xi^2} \right) J_1^2(\xi) \right] + \right. \\ &\quad \left. + \frac{L_h}{(2 - \lambda_m)} B_m^{(r)} J_1(\xi) \right\} \\ \bar{M}_y &= -\omega \pi \sum_m \left\{ A_m^{(r)} \left[2 \left(\frac{2b}{n\pi} \right)^2 J_1(\xi) + J_1'^2(\xi) + \left(1 - \frac{1}{\xi^2} \right) J_1^2(\xi) \right] - \right. \\ &\quad \left. - \frac{L_h}{(2 - \lambda_m)} B_m^{(i)} J_1(\xi) \right\} \end{aligned} \right\} \quad (205)$$

and the gain factors are easily identified as:

$$\left\{ \begin{aligned} Rgain &= -\pi \sum_m \left\{ A_m^{(i)} \left[2 \left(\frac{2b}{n\pi} \right)^2 J_1(\xi) + J_1'^2(\xi) + \left(1 - \frac{1}{\xi^2} \right) J_1^2(\xi) \right] + \right. \\ &\quad \left. + \frac{L_h}{(2 - \lambda_m)} B_m^{(r)} J_1(\xi) \right\} \\ Sgain &= -\pi \sum_m \left\{ A_m^{(r)} \left[2 \left(\frac{2b}{n\pi} \right)^2 J_1(\xi) + J_1'^2(\xi) + \left(1 - \frac{1}{\xi^2} \right) J_1^2(\xi) \right] - \right. \\ &\quad \left. - \frac{L_h}{(2 - \lambda_m)} B_m^{(i)} J_1(\xi) \right\} \end{aligned} \right\} \quad (206)$$

These expressions are evaluated in the computer program listed in Appendix A. The results correspond to the low Rossby number limit and are increasingly valid as the end of the motor run in a typical PAM-D orbit raising maneuver is approached. They can be used for stability calculations by inserting values of the spacecraft parameters at times of interest. Notice that there is a strong dependence on motor geometry, as represented by the chamber slenderness ratio, b , and on vehicle geometry, as represented by the position of the motor relative to the center of mass. The chamber geometry also has a powerful effect because of the resonance effect when a particular mode frequency is close to the spacecraft frequency at a particular time.

Sample Stability Computations

Overview

One can determine the spacecraft system nutation characteristics by examining the gain factors as functions of time. Equations 206 and 207 provide all of the necessary information. They can be used to compute instantaneous growth rate (or time constant) if desired. However, it is perhaps just as useful to examine the Rgain behavior directly in assessing the tendency for nutation growth. It is important to realize that the actual cone angle reached at a given time is a strong function of the initial conditions at the beginning of the motor run. Thus, vehicles that started with a larger than normal tipoff disturbance will reach correspondingly larger final cone angles. The dependence on initial nutation amplitude has been found to be approximately linear.¹

Determination of Rgain for Actual Vehicle Configurations

Let us now apply the results of the last subsection to actual motor/spacecraft combinations. This will provide us with a measure of the validity of the analysis and its associated set of assumptions. The sample version of the computer program in Appendix A shows application of the theory to the WESTAR-V, a typical PAM-D, STAR 48 spacecraft. Rgain data and other measured system behavior are summarized in the second chapter. We will refer to several of the figures in that material in assessing the validity of the theoretical calculations.

Figure 34 is a plot of Rgain vs. time for WESTAR-V. This is similar to plots developed in earlier studies.¹ Differences are attributed to major improvements in the analysis resulting from direct calculation of the pressure distributions rather than reliance on estimates of angular momentum flux through the control volume. This yields a considerably sharper model for the nutation interactions. Of greatest importance is the evidence of resonant response at several times. The peaks correspond to points in time where there is resonant coincidence between the vehicle nutation frequency and low-order inertial modes. Higher-order modes produce little effect because they require much larger energy input for excitation. Comparison of the theoretical results in Figure 34 with the experimental data of Figure 24 will show a remarkable degree of correlation. The two major Rgain peaks are reproduced. Event times are not in exact agreement, and should not be expected to be because the wave frequencies are sensitive to actual chamber shape. The early peaks are exaggerated because the effects of damping of the wave motions due to chamber boundary irregularities present in the early stages of the burn are not represented in the solutions.

To understand the timing of the peaks in the Rgain curve, it is necessary to examine the wave spectra for the system. Figure 35 shows the frequency variations with time for a number of low order vorticity wave modes. Superimposed on this plot is the spacecraft nutation frequency as computed from equation 2. The reasons for the peaks in the Rgain plot are now clearly evident. Strong resonant interactions occur precisely at the points where the mode curves cross the spacecraft frequency trace.

It is significant that, because of the motor design, the inertial mode frequencies increase slowly with time because the slenderness ratio decreases. The spacecraft frequency on the other hand slowly decreases with time. Thus, chances of resonant interaction are increased.

The predicted Rgain magnitudes are in reasonable agreement with the measured values. In making stability assessments, it is not necessary to obtain exact values for the torque gain factor. One can make decisions on stability on the basis of the presence of large Rgain peaks and on the timing of those peaks.

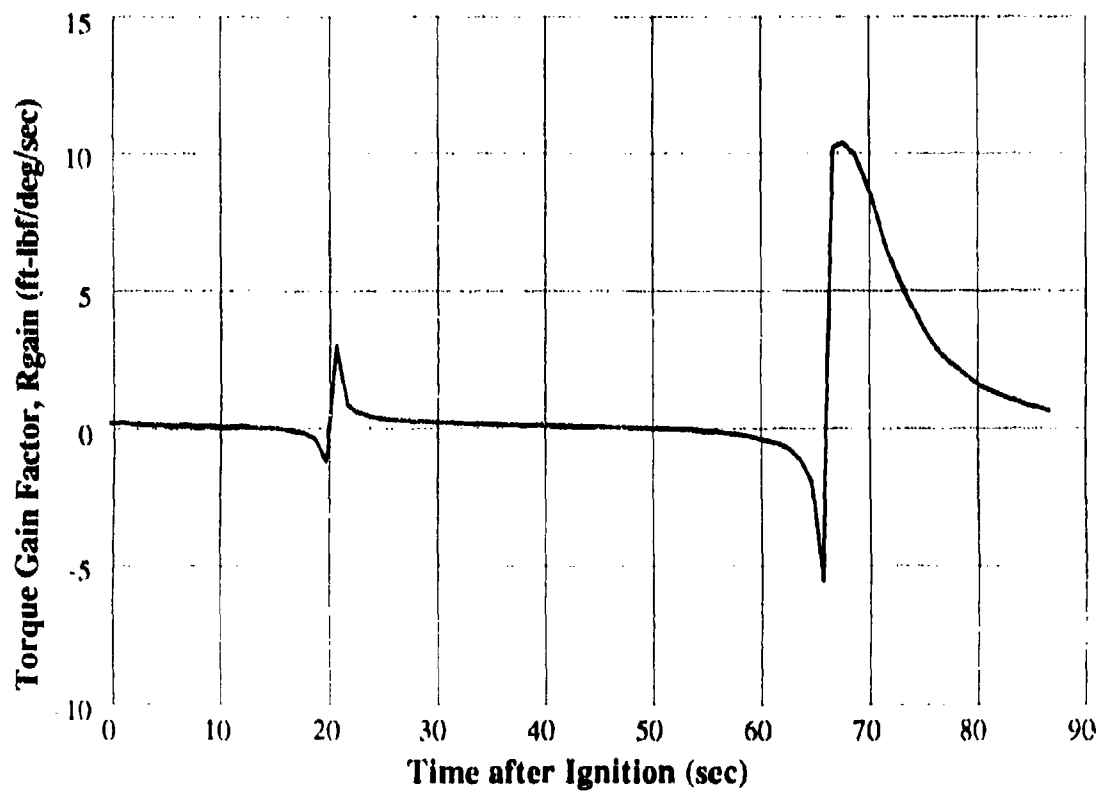


Figure 34. Predicted Torque Gain Factor, Rgain vs Time (WESTAR-V)

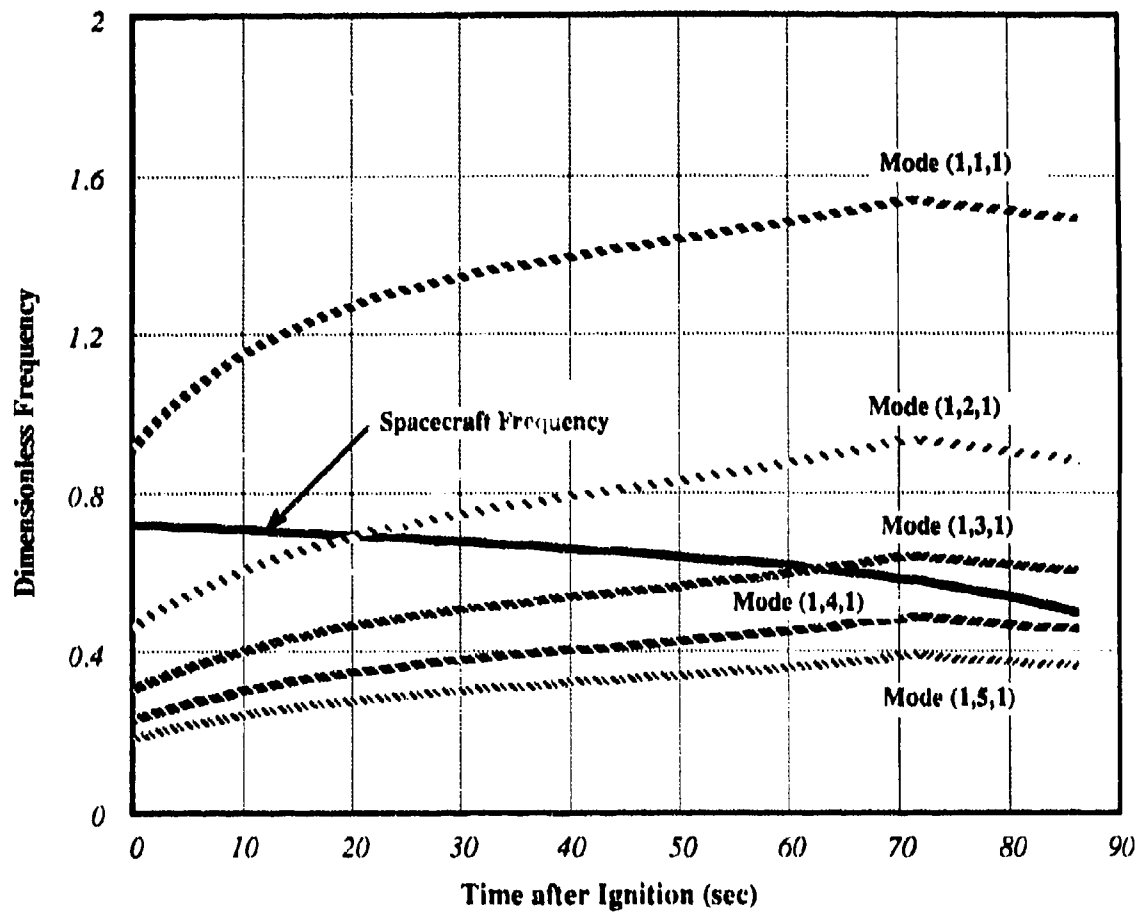


Figure 35. Resonant Coincidence of Spacecraft and Wave Frequencies

It should also be clear that the results described give us a means for devising system changes that can reduce the nutation growth. For example, modifications in motor placement or grain configuration can be used to shift the point of mode coincidence as a means for controlling resonance. Notice also for the STAR 48 motor that there is a distinct kink in the mode frequencies that coincides with the time the sidewall propellant web reaches the chamber boundary. The length continues to increase as the headend web burns causing the frequency to decrease during the last 15 seconds of burn. This may be one of the features of the grain design that enhances coning growth because it causes the mode (1,3,1) frequency to remain in the vicinity of the spacecraft coning frequency during the final seconds of the burn when sustained coning growth is most dangerous. The final part of the burn is critical because the moments of inertia are then low and the system becomes more susceptible to nutation growth.

NAVIER-STOKES SOLUTIONS OF SPINNING ROCKET FLOW

Overview

As we have mentioned several times, in order that predictive nutation instability calculations can properly represent all physical and geometrical effects present in a spinning, nutating rocket, it is necessary to utilize the great potential of finite-difference numerical procedures. A task was included in this program was intended only to explore possible techniques for generating such solutions. We realized, however, the great potential importance of such tools in the nutation problem and have undertaken a much more complete development.

We describe in this section the development and testing of a full three-dimensional, time-dependent Navier-Stokes solution of the spinning rocket flow problem. Included is full treatment of viscous and compressibility effects as well as the effects of the inertial forces that drive wave motions in the combustion chamber. The fine numerical studies and program development were carried out by Dr. Robert L. Roach at Georgia Tech, School of Aerospace Engineering.

Since we are concerned about nozzle effects as well as gas motions in the chamber, the solutions are carried through the entire system from the burning surface to the nozzle exit. This provides a unique opportunity for exploring the entire flow field in a completely general way. This amounts to computational experimentation with no limitations on the amount of detailed information available at any point in the motor or at any time during the motor run. The tool we have devised will have a much broader application than the one that motivated its development.

Numerical Procedure

Several numerical solution procedures for the Navier-Stokes equations have been written over the past several years in the School of Aerospace Engineering at Georgia Tech.⁴⁷⁻⁵⁰ In this case a new code was written⁵⁰ based on the hybrid Approximate Factorization (AF) scheme of Sankar et. al..⁴⁹ In this method, the solution is generated on one circumferential plane at a time. Derivatives in the circumferential direction use the latest values available and are then temporally biased in one direction. The procedure calls first for a solution of all the planes rotating in one direction around the axis. On the next iteration, the direction of rotation is reversed. Sankar has shown this to be not only a stable procedure but also time accurate if sufficient numbers of time steps to resolve the time scale of the phenomenon are used.

For axisymmetric problems, the solution is found on the center of three meridional planes. After each time iteration, the solution on the adjacent planes is updated based on the new values of the center plane. During the solution, the full three-dimensional equations are used. Thus, the axisymmetry is introduced through the metrics in the meridional derivatives. As fewer planes are required, there is considerable computational savings for axisymmetric cases. The results presented here are for two cases of axisymmetric spin which take advantage of this savings.

The unsteady, 3-dimensional Navier-Stokes equations can be written in vector form for Cartesian coordinates as:

$$q_t + (F - F_v)_x + (G - G_v)_y + (H - H_v)_z = K \quad (208)$$

where:

$$q = \begin{bmatrix} \rho \\ \rho u \\ \rho v \\ \rho w \\ e \end{bmatrix} \quad F = \begin{bmatrix} \rho u \\ \rho u^2 + p \\ \rho uv \\ \rho uw \\ u(e + p) \end{bmatrix} \quad G = \begin{bmatrix} \rho v \\ \rho uv \\ \rho v^2 + p \\ \rho vw \\ v(e + p) \end{bmatrix} \quad H = \begin{bmatrix} \rho w \\ \rho uw \\ \rho vw \\ \rho w^2 + p \\ w(e + p) \end{bmatrix}$$

$$P = (\gamma - 1) \left[e - \frac{\rho}{2} (u^2 + v^2 + w^2) \right]$$

$$F_v = \begin{bmatrix} 0 \\ \tau_{xx} \\ \tau_{xy} \\ \tau_{xz} \\ \delta_x \end{bmatrix} \quad G_v = \begin{bmatrix} 0 \\ \tau_{xy} \\ \tau_{yy} \\ \tau_{yz} \\ \delta_y \end{bmatrix} \quad H_v = \begin{bmatrix} 0 \\ \tau_{xz} \\ \tau_{yz} \\ \tau_{zz} \\ \delta_z \end{bmatrix}$$

(209)

$$\begin{cases} \tau_{xx} = 2\mu \frac{\partial u}{\partial x} + \lambda \nabla \cdot \mathbf{V} \\ \tau_{yy} = 2\mu \frac{\partial v}{\partial y} + \lambda \nabla \cdot \mathbf{V} \\ \tau_{zz} = 2\mu \frac{\partial w}{\partial z} + \lambda \nabla \cdot \mathbf{V} \end{cases} \quad \begin{cases} \tau_{xy} = \mu \left(\frac{\partial u}{\partial y} + \frac{\partial v}{\partial x} \right) \\ \tau_{xz} = \mu \left(\frac{\partial w}{\partial x} + \frac{\partial u}{\partial z} \right) \\ \tau_{yz} = \mu \left(\frac{\partial v}{\partial z} + \frac{\partial w}{\partial y} \right) \end{cases}$$

$$\begin{cases} \delta_x = \frac{\gamma\mu}{Pr} \frac{\partial e}{\partial x} + u\tau_{xx} + v\tau_{xy} + w\tau_{xz} \\ \delta_y = \frac{\gamma\mu}{Pr} \frac{\partial e}{\partial y} + u\tau_{yx} + v\tau_{yy} + w\tau_{yz} \\ \delta_z = \frac{\gamma\mu}{Pr} \frac{\partial e}{\partial z} + u\tau_{zx} + v\tau_{zy} + w\tau_{zz} \end{cases}$$

and the noninertial terms are:

$$K = \begin{bmatrix} 0 \\ -\rho \left[\frac{\partial \Omega}{\partial t} \times r + 2\Omega \times V + \Omega \times \Omega \times r \right] \cdot i \\ -\rho \left[\frac{\partial \Omega}{\partial t} \times r + 2\Omega \times V + \Omega \times \Omega \times r \right] \cdot j \\ -\rho \left[\frac{\partial \Omega}{\partial t} \times r + 2\Omega \times V + \Omega \times \Omega \times r \right] \cdot k \\ -\rho V \cdot \left[\frac{\partial \Omega}{\partial t} \times r + 2\Omega \times V + \Omega \times \Omega \times r \right] \end{bmatrix} \quad (210)$$

When transformed to a curvilinear coordinate system, then the system becomes:

$$\hat{q}_\tau + \hat{F}_\xi^{n+1} + \hat{G}_\eta^{n+1} + \hat{H}_\zeta^{n+1} = (\hat{F}_v)_\xi^n + (\hat{G}_v)_\eta^n + (\hat{H}_v)_\zeta^n + \hat{K} \quad (211)$$

where

$$\begin{cases} \hat{F} = \frac{1}{J} (\xi_t q + \xi_x F + \xi_y G + \xi_z H) \\ \hat{G} = \frac{1}{J} (\eta_t q + \eta_x F + \eta_y G + \eta_z H) \\ \hat{H} = \frac{1}{J} (\zeta_t q + \zeta_x F + \zeta_y G + \zeta_z H) \end{cases}, \quad \hat{q} = \frac{1}{J} \begin{bmatrix} \rho \\ \rho u \\ \rho v \\ \rho w \\ e \end{bmatrix}, \quad \hat{K} = \frac{K}{J} \quad (212)$$

Note that with a moving coordinate system the unsteady metrics are nonzero and must be carried along. These are used in burnback simulation. The derivatives are replaced by standard finite difference operators and the unsteady term uses the two-point backward difference:

$$\hat{q}_\tau = \left(\frac{\hat{q}^{n+1} - \hat{q}^n}{\Delta t} \right) = \frac{\Delta \hat{q}}{\Delta t} \quad (213)$$

In the the hybrid scheme⁴⁹, the convection terms in two of the coordinate directions are treated as implicit while everything else is evaluated explicitly. The "delta" form is obtained by subtracting from both sides the nth level convection terms. The equation is linearized by a Taylor series expansion around the known time level.

$$\hat{F}^{n+1} = \hat{F}^n + \left\{ \frac{D\hat{F}}{D\hat{q}} \right\}^n (\hat{q}^{n+1} - \hat{q}^n) \quad (214)$$

Finally, the implicit finite difference operator is approximately factored into one-dimensional operators in each direction to get:

$$\left[I + \Delta t \delta_{\xi} \left\{ \frac{D\hat{F}}{D\hat{Q}} \right\}^n \right] \left[I + \Delta t \delta_{\eta} \left\{ \frac{D\hat{G}}{D\hat{Q}} \right\}^n \right] \Delta\hat{Q} = \text{RHS} \quad (215)$$

This formulation allows for relatively efficient block triadiagonal matrices to be solved in each direction. Thus the two step procedure is to solve the following two systems:

$$\begin{cases} \left[I + \Delta t \delta_{\xi} \left\{ \frac{D\hat{F}}{D\hat{Q}} \right\}^n \right] \Delta\hat{Q}^* = \text{RHS} \\ \left[I + \Delta t \delta_{\eta} \left\{ \frac{D\hat{G}}{D\hat{Q}} \right\}^n \right] \Delta\hat{Q} = \Delta\hat{Q}^* \end{cases} \quad (216)$$

As central difference operators are used for the convection differences, some extra terms must be added to smooth out the odd/even decoupling that occurs after a few steps into the solution. These terms are also known to damp out the high frequency errors that may occur in the vicinity of steep gradients. As suggested by Pulliam and Steger (Ref. 51), to the explicit right-hand side is added:

$$- \Delta t \epsilon_E J^{-1} \left[\epsilon_x \delta_{\xi\xi\xi\xi} + \epsilon_y \delta_{\eta\eta\eta\eta} + \epsilon_z \delta_{\zeta\zeta\zeta\zeta} \right] J \hat{Q}^n \quad (217)$$

To the implicit left-hand side is added:

$$- \Delta t \epsilon_I J^{-1} \left[\delta_{\xi\xi} + \delta_{\eta\eta} \right] J \quad (218)$$

where the constants are user input and typically vary between 1 and 3.

To complete the formulation, initial conditions must be specified to start the solution procedure and boundary conditions must be imposed during the solution. Here, explicit boundary conditions are used wherein the interior flow is computed using boundary information lagged by a single time step. This is a standard procedure and has not been found to provide any numerical difficulties other than to somewhat reduce the maximum time step size. The alternative is to solve for the boundary values along with the interior. However, this results in a computer code that can only run a few restricted classes of problems without major modification. A description of the initial and boundary conditions for the two axisymmetric spin cases follows.

Initial Conditions

In order to permit a rapid solution for the steady state case, an initial condition was generated using one-dimensional relations based on an area ratio with the nozzle throat. This provides an initial solution close to the converged steady solution.

Boundary Conditions

As mentioned, dependent variables along the boundaries are computed after the values have been computed on the interior.

Inflow Boundary:

The inflow boundary in this problem is the propellant surface, which we have modelled in a "cold-flow" fashion. The thermodynamic variables, density and pressure, are specified from given stagnation conditions and held fixed throughout the computation. Surface velocities are computed from a one-dimensional Mach number/area relationship with the nozzle throat area and the stagnation conditions specified. That is, initially, the burning surface area divided by the geometric throat area specifies the surface Mach number. The cartesian velocity components are resolved from the resulting total velocity vector, which is oriented normal to the burning surface.

To account for the mass flux reduction through the nozzle throat, due to boundary layer growth on the nozzle walls, the burning surface velocity magnitude is presently adjusted at various times during the computation. The net mass flux through the throat is computed after every iteration. The surface velocities are adjusted by a simple ratio every tenth iteration. The remaining dependent variables on the inflow are held fixed. This procedure produces a very stable solution. No large pressure oscillations or other transients were noticed prior to convergence with this method.

An alternative procedure for updating the surface mass flux is to use the empirical relationship between the chamber pressure and the burnback velocity. This has not yet been tried but will be implemented in future versions of the code for purposes of verification.

Solid Wall Boundaries:

No-slip walls are imposed by maintaining all velocity components to zero on the nonburning solid surfaces. In addition, adiabatic walls are assumed which requires a zero-normal temperature gradient. The surface pressure is found by assuming a zero normal gradient. An alternative is to compute the normal pressure gradient from the normal momentum equation evaluated at the surface. As the terms remaining in the equation are usually rather negligible, the normal pressure gradient is typically negligible as well.

Since both pressure and temperature have zero normal gradients, the state equation requires a zero-density gradient as well. Hence, all thermodynamic variables at the no-slip solid surface are determined from second order, one-sided differencing.

Centerline Boundary:

Zero gradients are imposed on the thermodynamic variables and the tangential velocity component along the centerline boundary. Again, second order, one-sided differencing is used. The velocity components normal to the centerline are held fixed at zero.

Outflow Boundary:

The outflow boundary is the most sensitive boundary from a stability standpoint. It consists primarily of a core of supersonic flow from the expansion nozzle. In this region, all variables are determined either by linear extrapolation along the (roughly) streamwise coordinate or by a simple wave procedure. The simple wave condition is more stable and is used in the initial stages of the calculation. This boundary condition results from the fact that

properties are constant along characteristic lines. Hence, characteristic lines from the nozzle wall are computed at the outflow and are used to determine the direction of extrapolation. In reality, there are also characteristic lines of a second family emanating from the centerline. To include these would require a relatively complex iterative procedure and was deemed not worth the effort. Ignoring the centerline characteristics explains the "kink" in the various quantities at the exit plane.

The kink can be eliminated by using a linear extrapolation. However, this method is less stable and is susceptible to divergence if too large a time step is used. Hence, this method is used only near convergence of the solution. This means that unsteady runs will likely require the simple wave procedure.

In addition, near the nozzle wall is a thin boundary layer which includes a subsonic region. Here, it is not proper to extrapolate all flow variables. In this portion, density and the velocity components are extrapolated and the total energy is computed from these values and the back pressure. The back pressure is considered to be the pressure computed at the first supersonic point above the boundary layer.

Another possibility is to solve the governing equations along the entire exit plane. This would automatically capture the full characteristics nature of the flow in the supersonic region and account for the pressure in the subsonic region. But due to the added stability and accuracy, the entire boundary would have to be solved together as the equations would be coupled.

Computational Grid

Finite difference solutions to differential equations require the domain to be divided into small computational regions. These regions are described either by points or by small cells. The pattern of these cells or points resembles a net and is called a computational grid. Specification of the locations of these regions usually requires some care and is the subject of much research. The interested reader is referred to excellent summaries on the subject (Ref. 52, 53 for example).

Here it is only necessary to briefly describe some of the features of the grids used. The grids used in the examples done here are presented in Figures 36-37. Only a single meridional plane is presented as representative. For axisymmetric calculations, three of these planes are used. For full three-dimensional problems, this plane is rotated around the motor axis to generate the remainder of the points.

A sheared cartesian grid was used for the SRB-like motor shown in Fig. 36. The outer boundary is described by piecewise algebraic relations as shown in Fig. 36(a). The various geometric parameters are user selectable. The resulting shape and interior grid are given in Fig. 36(b). The interior grid was generated by equally spacing points in the axial direction and using a hyperbolic tangent distribution in the radial direction. The radial direction spacing allows for point clustering near the walls and near the centerline. For most of the upstream portion of the grid, the geometry is simply cylindrical. At the diffuser and nozzle locations, however, the radial coordinate of the outer boundary changes. Here, the interior grid is stretched over the radial distance using the same relative spacing as upstream. This is called "shearing" and produces a smooth change in the radial spacing. In this example, 84 points were used in the axial direction and 21 in the radial direction.

The PAM-type motors present a far more complex geometry for purposes of grid generation. Again, piecewise algebraic relations were used to produce the outer boundary (Fig. 37(a)) with user selectable parameters. The parameters chosen here are those that closely

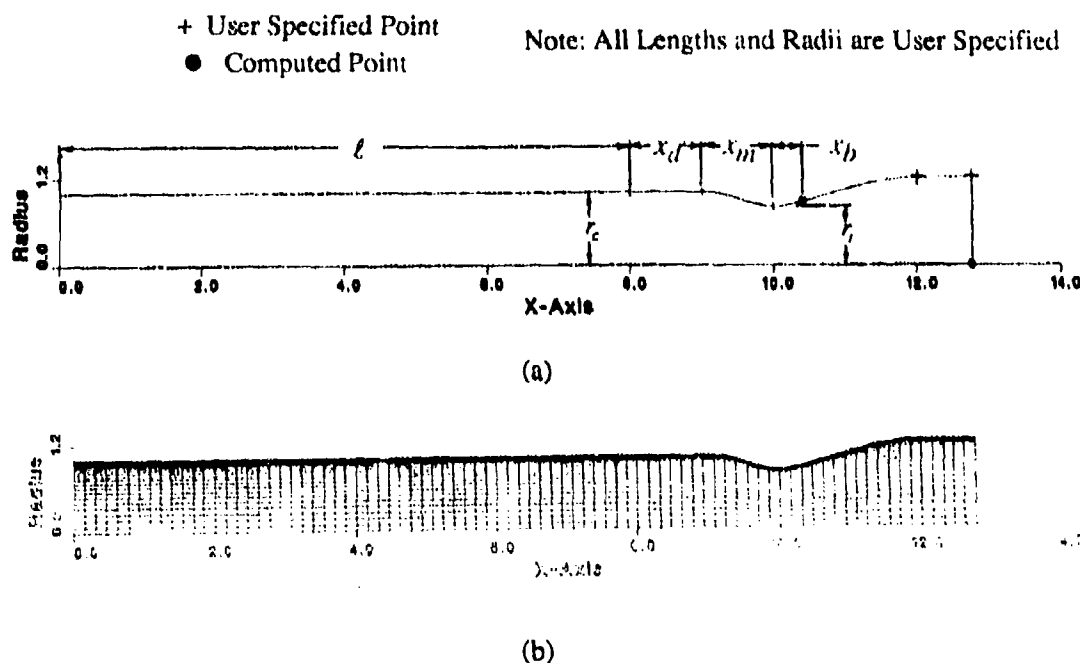


Figure 36. Finite Difference Grid for Generic Rocket Motor

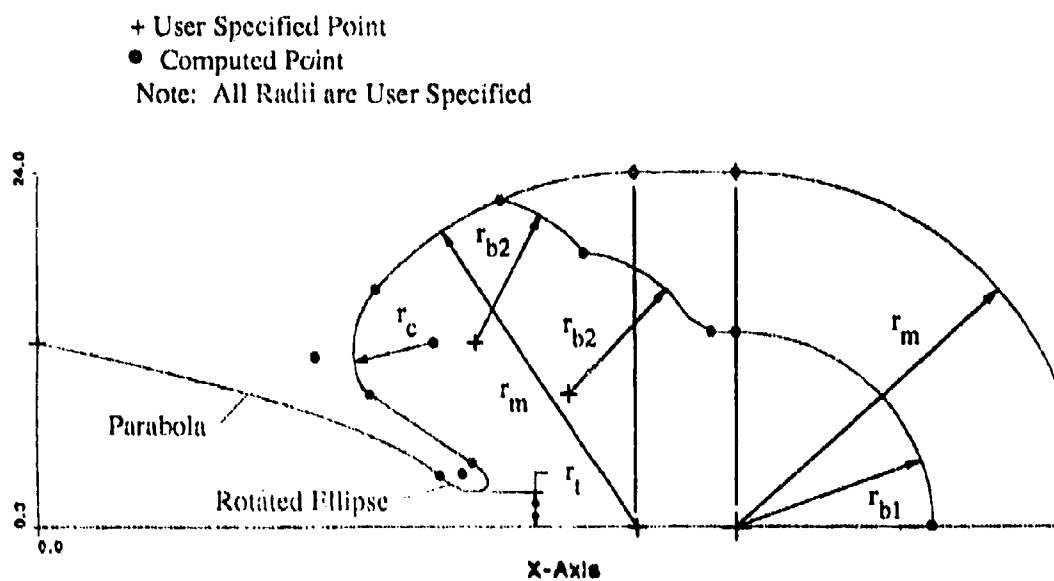
resemble the STAR-48 motor. The outer boundary here refers to the centerline, exit plane, nozzle/combustion chamber walls, and the propellant surface.

The motor outer geometry is specified so that the intersection of the propellant and combustion chamber can be found. This is necessary since an additional feature of the grid generation package is the ability to simulate burnback. Hence, the user must also specify the time into the burn. The burnback profiles are shown in Fig. 38. In the results presented here, the grid was generated at roughly 39 seconds into the burn. This time was chosen as being about the time that some interesting flow features begin to arise in the motor.

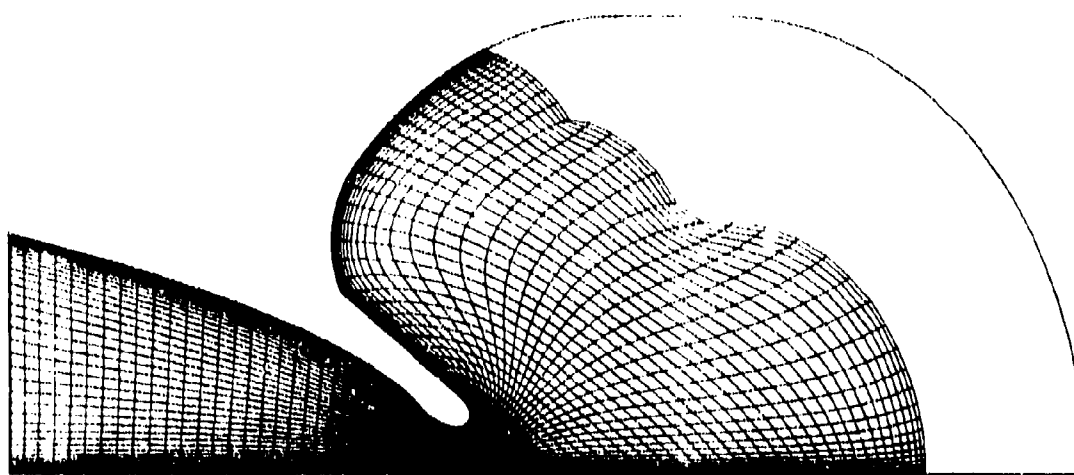
Once the outer boundary is specified, the interior grid is generated using Poisson-type partial differential equations.⁵³ As can be seen in Fig. 37(b) one set of curvilinear coordinates coincides fairly closely with the expected flow direction. Forcing functions used by the program require the grid to retain the relative spacing specified at the outflow and along the centerline.

Again, a hyperbolic tangent distribution of points was used in the radial direction to cluster points near the solid wall and near the centerline. In the axial direction, clustering is used near the nozzle throat and at the propellant surface. The grid has 81 points in the axial direction and 47 in the radial.

Since the numerical procedure used the time dependent form of the Navier-Stokes equations, each solution can be seen as a time-dependent calculation. Steady-state solutions are obtained by starting with an initial guess and calculating for sufficient time steps to insure some convergence criteria.



(a)



(b)

Figure 37. Finite Difference Grid for STAR-48 Motor Type

While the program is written for a full three-dimensional flow calculation, the problems solved thus far are axisymmetric. The three-dimensional equations are solved on three meridional planes with a common intersection at the symmetry axis. Computation of the metrics thus produce the effects of the axisymmetric geometry.

The flow is solved only on the middle of the three planes. The dependent variables on the other two planes are resolved from the center plane after each time iteration. This produces the axisymmetric solution.

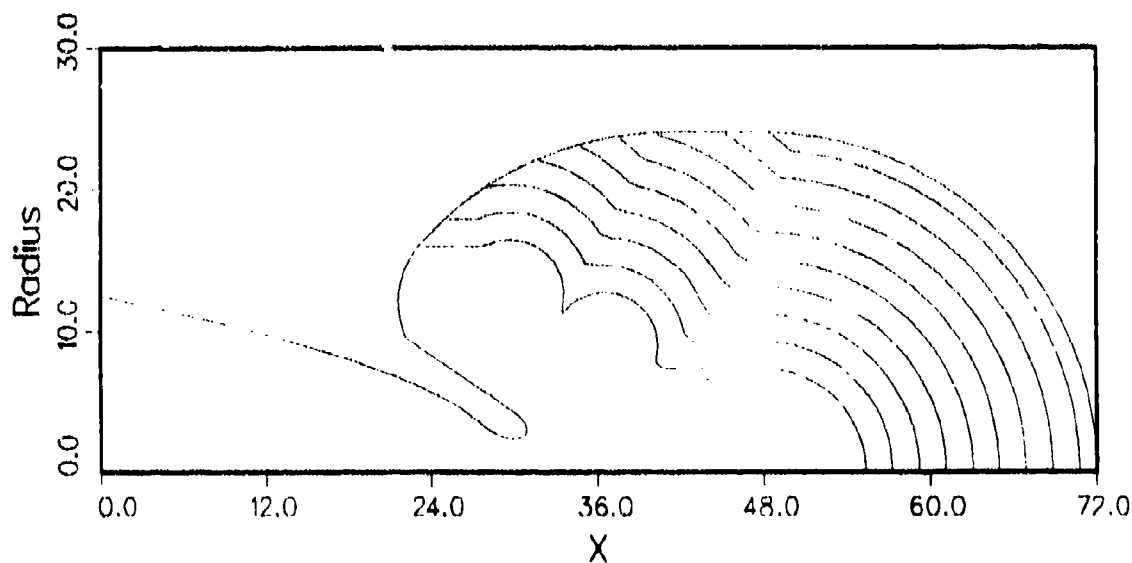


Figure 38. Burnback Profiles for STAR-48 Motor Type

Results

Results are presented for two different motor geometries, an SRB-type and a submerged nozzle type modelled after the STAR-48 motor. In each a calculation was performed for both spin and nonspin. Spin rates were fixed to give a Rossby number less than unity as corresponds to the cases of interest here. In all cases the flow was axisymmetric requiring only three grids for the three-dimensional flow solver. The solutions were begun from an initial condition described previously and marched in time to a steady state solution. Steady state was deemed to have been reached when the maximum residual of the x-momentum equation was reduced by at least three orders of magnitude.

SRB Motor Results

Figures 39-43 show the calculated flow for the SRB motor. Figures 39 and 40 compare the axial and radial velocities at $x/D = 1.8$ with Culick's analytical solution⁵⁰ and with the experimental data of Dunlap, et al.⁵⁵ The results are in rather close agreement even though the geometries were slightly different. The experimental data is from a chamber with an L/D of 9.5, whereas here the ratio is 10.

Aerodynamic flow features are more evident in the contour plots of Fig. 41(a-d). The Mach number contours of Fig. 41(a), for example, show a smooth axial acceleration which is greatest in the throat as expected. The boundary layer can be seen in the diffuser, throat, and nozzle walls. At the outflow, the nozzle has become a straight duct so that the growth of the boundary layer constricts the flow causing a series of supersonic compression waves which traverse the exit plane.

Similar features are seen in the pressure and density contours of Figures 41(b) and 41(c). The chamber is seen to have a relatively constant pressure. As the flow approaches the diffuser, the pressure begins to drop as the accumulated mass flux causes an acceleration. The pressure remains constant in the short, straight-duct section just prior to the diffuser, where no more mass flux has been introduced, and then rapidly drops through the diffuser and nozzle. Nearly constant pressure through the boundary layer, as expected, is seen by the lack of contours in that region. However, the density changes greatly in response to the temperature rise appropriate for an adiabatic wall. A small disturbance near the upper head-end in the density is likely caused by a slight incompatibility in the boundary conditions at the corner. The effects do not persist in the domain and later computer runs are expected to have corrected the incompatibility.

Figure 41(d) shows the rather interesting behavior of the radial velocity component. In the combustion chamber, the flow turns quickly axial and has little variation until it reaches the diffuser. Here it is directed, at first, toward the centerline and then parallel again in the nozzle throat. The resulting series of contours, resembling the crest of a hill, indicate a maximum about halfway through the diffuser and close to the wall. The effects diminish away from the wall. The reverse process occurs downstream in the nozzle. The compression waves at the exit plane are also seen.

The next calculation added a spin rate of 606 RPM to the motor to give a Rossby number of 0.8. The main aerodynamic features of the flow were not affected greatly except to now include a core vortex. Figures 42(a) and 42(b) present particle traces of the gas flow for the spin case. In Fig. 42(a), particles were released at seven different meridional stations at the propellant surface near the head end. As the axial velocity is lowest here, the spin is most evident. As the flow accelerates out the nozzle throat, the rate of rotation decreases. In Fig. 42(b), the view is more from the head end and particles were released from only three

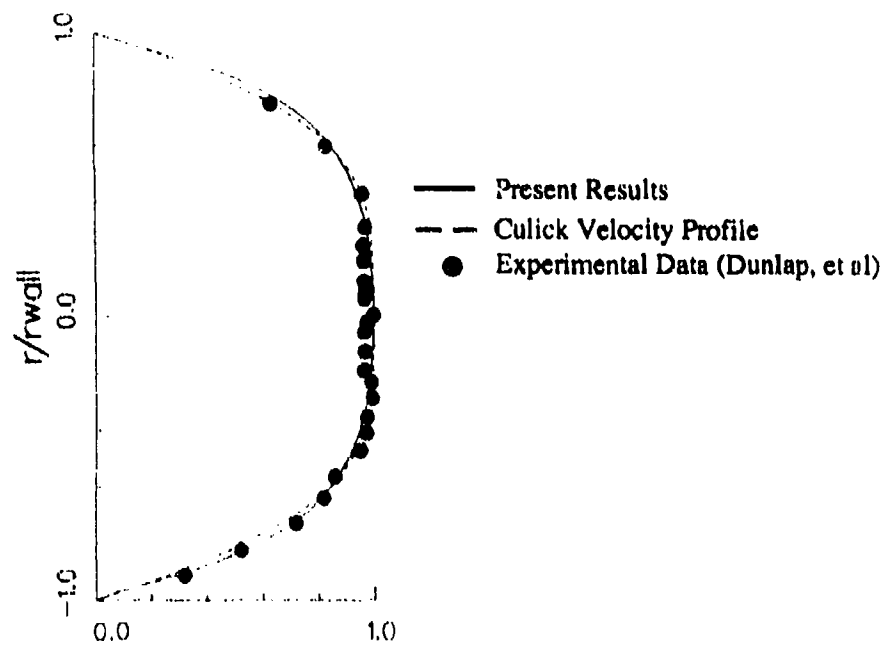


Figure 39. Comparison of Experimental and Computed Axial Velocity Profiles

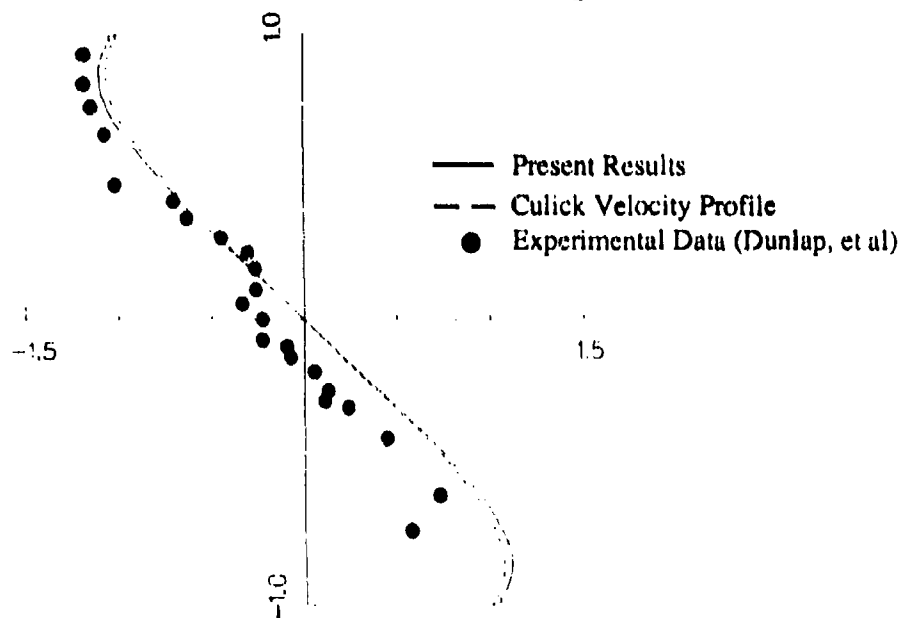
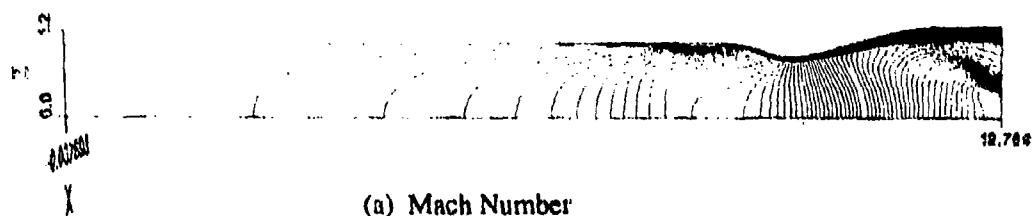
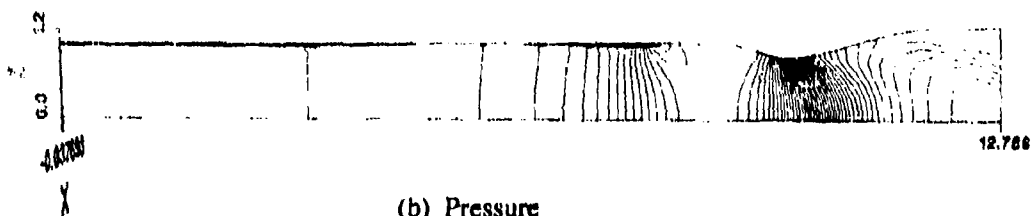


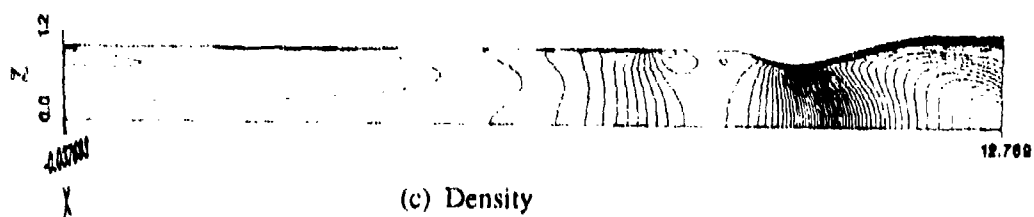
Figure 40. Comparison of Experimental and Computed Radial Velocity Profiles



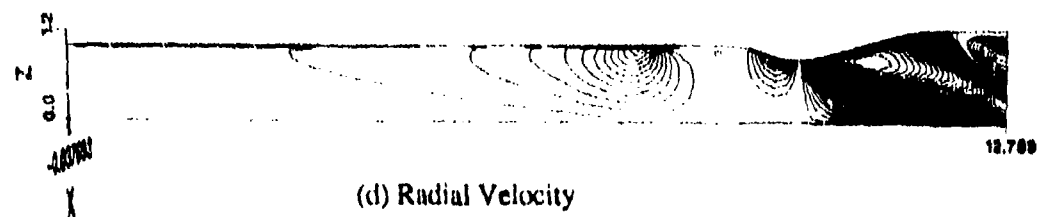
(a) Mach Number



(b) Pressure



(c) Density



(d) Radial Velocity

Figure 41. Contours of Dependent Variables for Generic Motor

meridional locations, but the vortical paths taken by the particles are more clearly seen.

Another spin case was run at 250 RPM in which the time history of the circumferential velocity was tracked. As in the previous case, the nonspin flow was used as the initial condition and the spin impulsively imposed. Figures 43(a-f) show a region in the combustion chamber and diffuser where the circumferential velocity in the direction of the spin grows. In addition, a starting vortical region of spin in the opposite direction in the nozzle diminishes as it is convected out of the domain. The final result shows the expected result of the greatest velocity at the throat as angular momentum from the larger radius regions is conserved.

STAR 48/PAM-D Results

Rotating and non-rotating cases were run for the PAM motor as well. Aerodynamic features analogous to those in the SRB were observed, though the change in variables was more severe due to larger area ratios. The particle paths of the nonspin case were already seen in Fig. 9 and show the expected behavior. Those for the spin case are shown in Fig. 44. The view is from an angle near the top of the motor looking aft so that the azimuthal motions are more evident as in the SRB case.

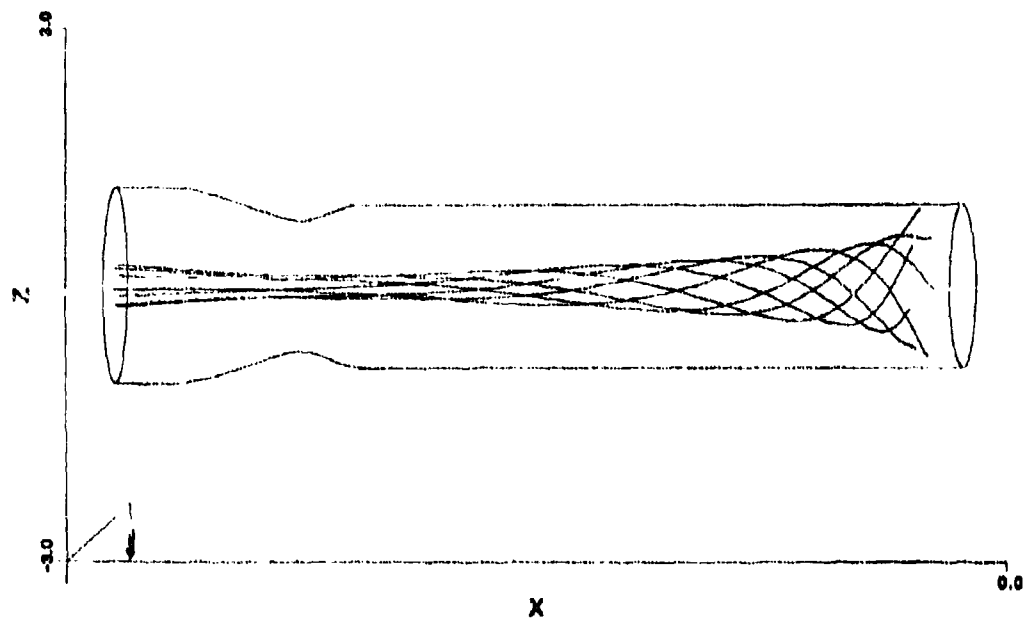
Figures 45-46 show Mach number and circumferential velocity contours. In these figures the outer motor case was not drawn, so that the leftmost boundary is the propellant surface. The large accelerations near the throat cause contour lines to be rather bunched in that vicinity, so a subset of the range of the variables were used.

The Mach number contours in Fig. 45 range from a value of .025 to 2.0. The expected acceleration of the mean flow gas and the boundary layer growth are seen in the diffuser and nozzle. In Fig. 46 the circumferential velocity component has the expected peak near the throat at about 17% of the throat radius.

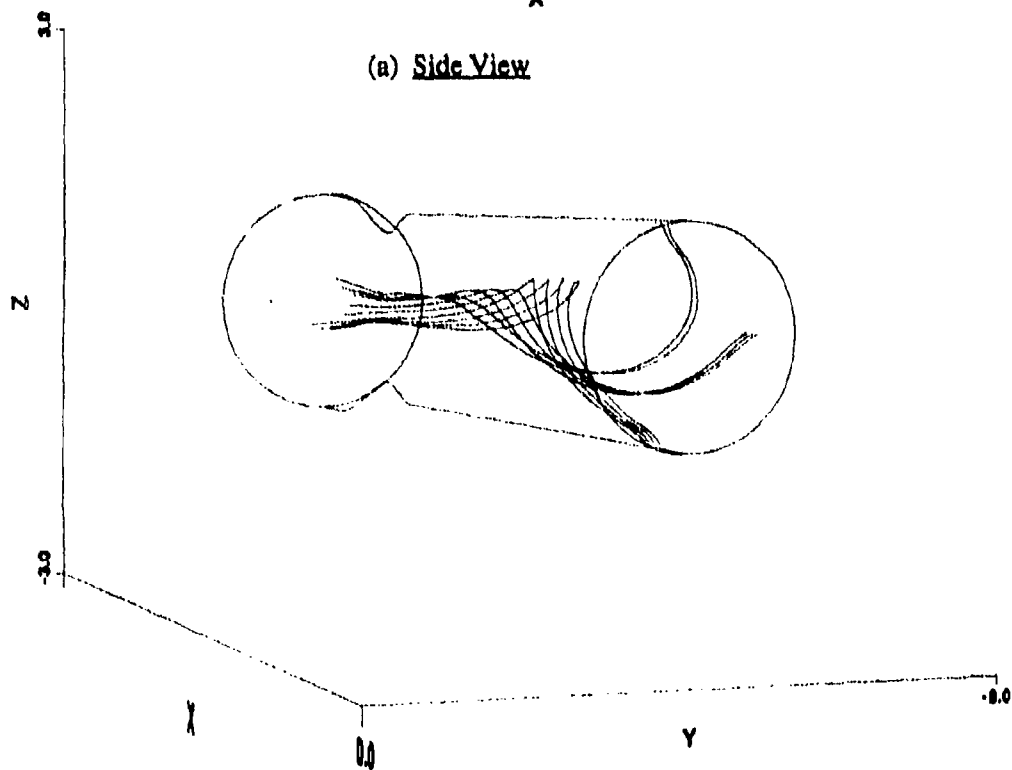
Future Work

The results presented above represent the preliminary efforts of the three-dimensional Navier-Stokes solution procedure applied to the case of spinning rockets. So far only the axisymmetric spin has been performed. The computations were performed on the Georgia Tech CYBER 990. Runs of 400 iterations were typical and consumed approximately 1280 CPU seconds for the STAR-48 configuration. Since the grid consists of about 3800 points, the speed performance of the code was thus about 0.00084 CPU seconds per time step per grid point (about 10% to 20% of the rate that would be attainable on a CRAY-class machine). Converged solutions require about one to two hours of computation time. Since the nutating case will require using many more circumferential planes, the run time would begin to become prohibitive. As a consequence, the first task will be to vectorize the code. This has already been anticipated and a vector version is now in the debug phase. It should be ready sometime in the Fall of 1989 and should result in a speed-up of about five on the 990 based on experience with other computer codes. In addition, access to a CRAY-class machine has been made available at the Pittsburgh Supercomputing Institute on a limited basis and more time is being applied for.

The next computational task will be to compute the spinning case with nutation. Initial conditions will be an axisymmetric spin result with spin about an additional axis added. This will require much more run time as at least three cycles of vortex undulation need to be captured. Time histories of the aerodynamic forces and moments are to be tracked to assess the phase relationship between the dynamics and spin rates. In addition, the inclusion of burnback



(a) Side View



(b) Oblique View Near Head-End

Figure 42. Particle Trace Diagrams for Spinning Generic Rocket

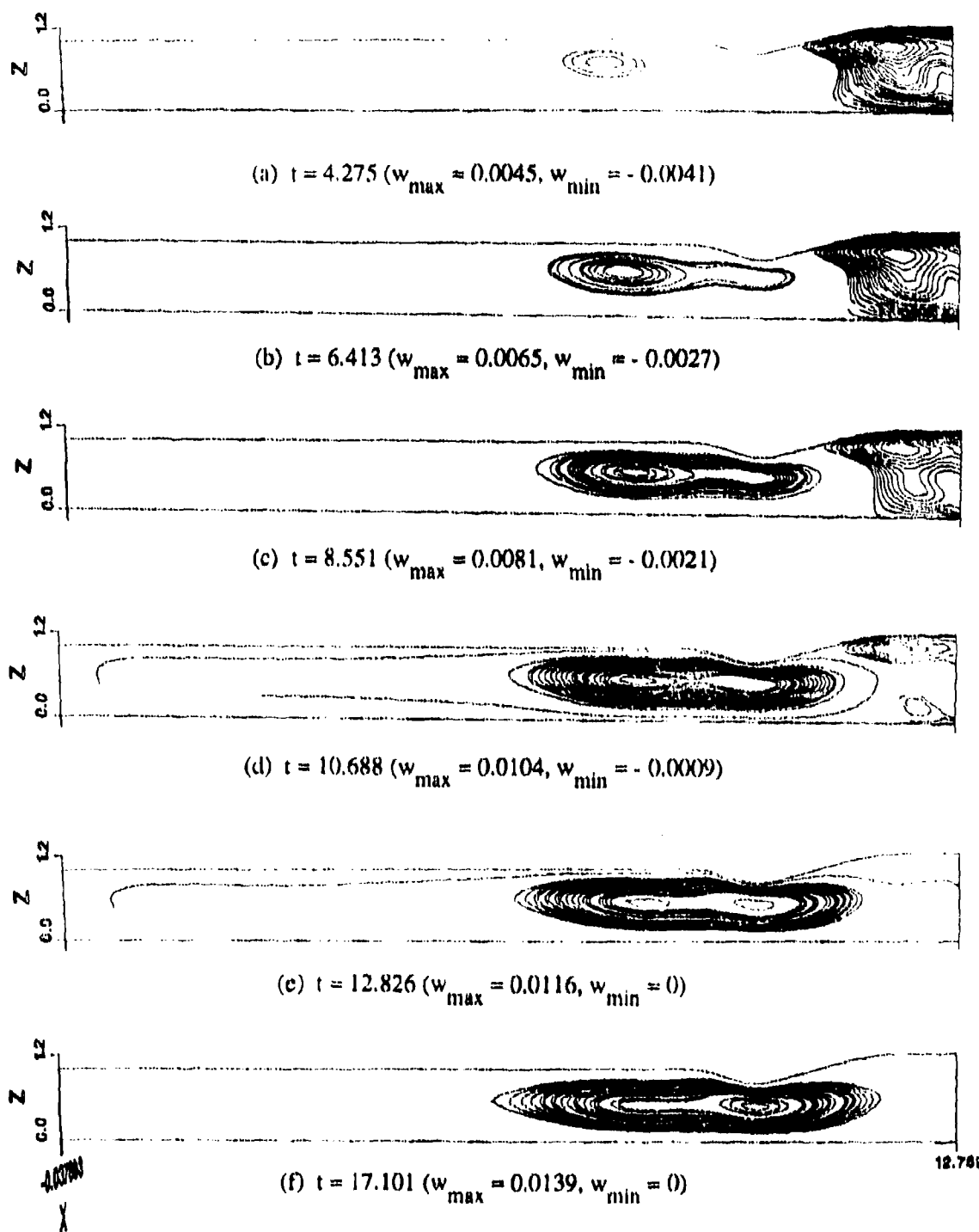


Figure 43. Development of Circumferential Velocity

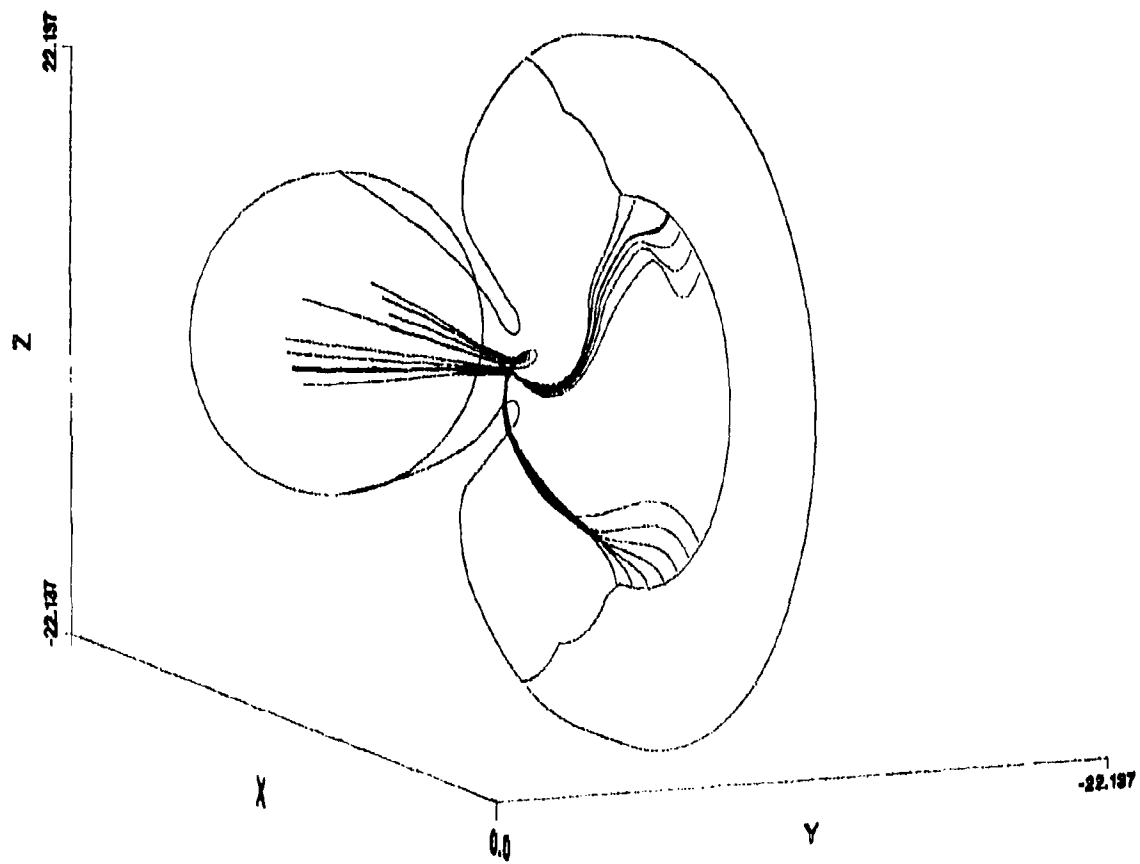


Figure 44. Oblique View of Particle Trace for the STAR 48 Type Motor

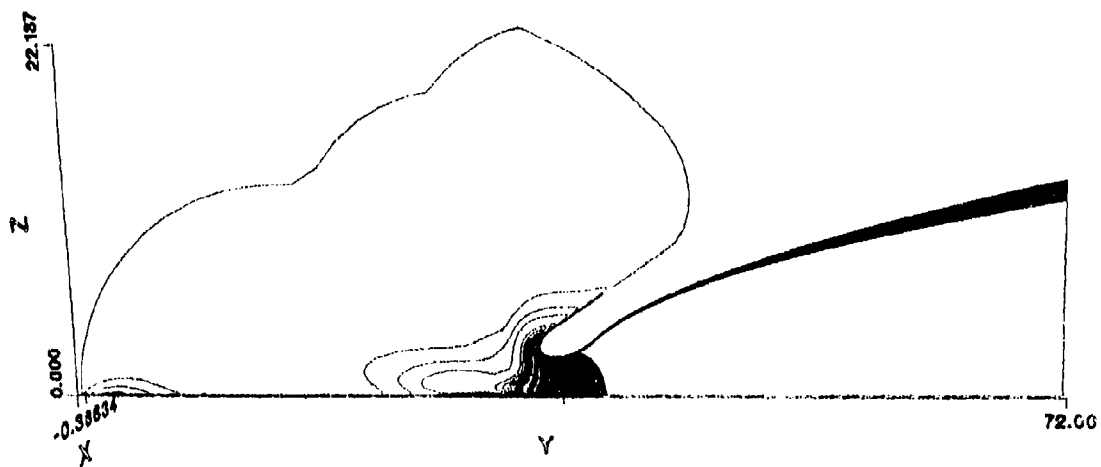


Figure 45. Mach Number Contours for STAR 48 Type Motor

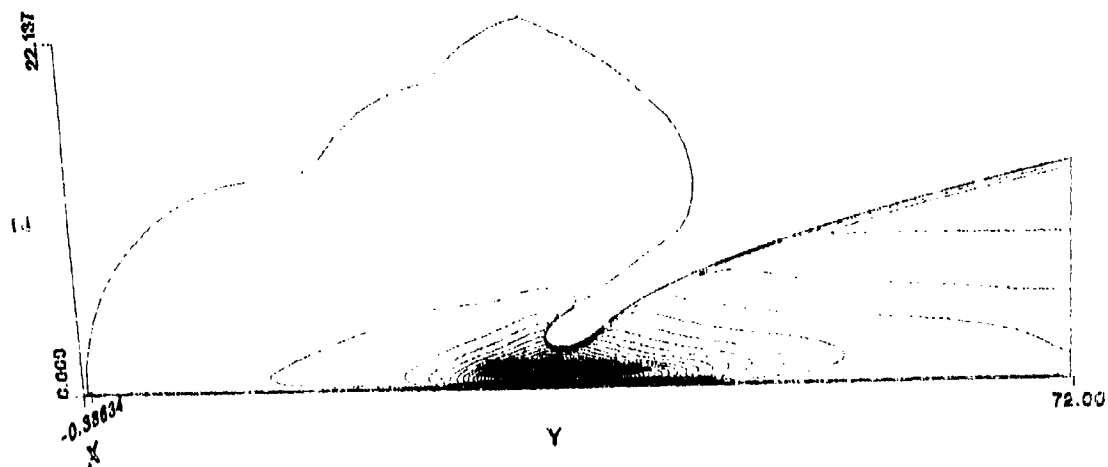


Figure 46. Circumferential Velocity Contours for STAR 48 Type Motor

is to be examined. As mentioned, the grid generation package already has the ability to model the burnback, and the numerical procedure has included unsteady grid transformation metrics.

The remaining computational tasks include the addition of a dynamics package to examine the effects of spin and nutation on the net forces and moments, and to allow these to be fed into the forces and moments applied to the Navier-Stokes equations.

EXPERIMENTAL METHODS IN FLOW-DRIVEN NUTATION INSTABILITY

Overview

In this section, we describe the procedures needed to secure experimental information regarding behavior of the gas flow and interaction force and torque effects in a spinning rocket chamber. The experiments described are based on a set of scaling rules that were deduced by using available flight data from the PAM-D series in concert with a careful dimensional analysis of the problem. These scaling rules are essential in determining the correct values for test parameters in small scale-tests in order that data can be extrapolated to full-scale motors. The scaling rules are also of great utility in estimating nutation effects in new motor/spacecraft configurations.

Two types of experimental methods were developed. In the first, we seek to understand the flow field generated in a spinning, nutating chamber by observing the actual flow pattern generated by the inertial forces. Methods were devised to produce an angular velocity environment identical to that experienced by gas particles inside an actual motor. The simplest device was a spinning chamber with lateral fluid motions driven by an oscillating piston. This produced inertial waves of the sort predicted by the theory. A second method that more nearly simulates a coning rocket utilizes two spin tables. The secondary spin axis carrying the simulated motor chamber is tilted with respect to the primary table, and the combined angular velocities exactly simulate the effects of nutation and spin. Observation of the fluid motion induced in the chamber gives information concerning the flow response. All of these experiments confirmed that vorticity waves (inertial waves) are produced in the environment of a spinning, wobbling rocket. The waves include both pressure and velocity fluctuations and correspond in all respects to the flows predicted by the theory.

Since it is highly likely that there will be future studies of nutation instability that require full-scale motor data, considerable effort was devoted to design of techniques that could be scaled to full size. These are intended to make it possible to measure important motor interaction information in a direct manner. What is needed is a technique for determining the Rgain (torque gain factor) in an actual motor in a ground test environment.

We developed two approaches to this problem. They were implemented for laboratory scale rockets using 2" diameter propellant grains. The scaling rules predict rather small interaction forces for such small motors. Spin rates must be high to simulate full-scale conditions. Thus, the tests were not expected to yield comprehensive nutation data, but rather to explore the approaches required for larger motor sizes.

We did observe nutation driving in some of these small scale tests, but the effects involved are quite small. We do not claim to have verified any particular model of nutation instability. Modifications of the test techniques we have devised may make it possible to measure interaction torques fairly precisely in both small-scale and full-size systems. Suggestions for continued effort in this direction are discussed.

Scaling Laws for Propulsion-Induced Nutation

In order to carry out useful experimentation in the study of nutation instability it is essential to construct appropriate scaling laws so that effects of size and dynamical factors can be properly accounted for. Rational scaling laws are also a much needed interim tool for avoiding instability problems. Such information is required in the design of attitude control systems to limit coning growth. The problem can be handled in a practical way while the search for the origin of the disturbing mechanism continues. The purpose of this subsection is to establish appropriate scaling laws by application of similarity and dimensional analysis to a set of system parameters suggested by the jet gain theory of flow-induced nutation instability. The results are tested by application to available experimental data. They are then applied, in later subsections, in the layout of appropriate small-scale experiments.

The analysis indicates that the main scaling parameters are the motor size and mass flow rate, and a characteristic spacecraft dimension. The scaling rules are readily verified, since data from at least three distinct motor/spacecraft combinations are available. The results fit either of the two viable physical models (namely the slag sloshing and the gasdynamic or jet gain mechanisms) although we develop them here for the jet gain model.

The scaling rules show that laboratory-scale experiments might yield useful direct information regarding the mechanism if it is related to motor gas flow. The interaction forces produced are small but appear to be in a measurable range. However, such tests do not simulate the conditions necessary to activate the slag mechanism. Even experiments with full-scale motors conducted in spinning ground tests do not address several crucial features of the flight environment essential in the slag accumulation theory. Instrumented full-scale flight tests may be required to successfully discriminate between potential disturbing mechanisms.

Features of the Jet Gain Nutation Instability Theory

The basic concepts of the jet gain driving mechanism are now briefly described as a model for constructing nutation instability scaling laws. Its basic physical premises are reviewed in light of scaling effects. The reader is directed to earlier chapters for a full description of the theory.

A useful starting point is to review the familiar jet damping effect, since it represents an established description of an important interaction between the vehicle angular motion and the combustion chamber gas flow. Except for the fact that jet damping torques usually act to reduce lateral angular velocities (both with and without axial spin), their magnitudes and time dependence closely resemble the disturbing torques measured in flight. The basic hypothesis that led to investigation of gasdynamic driving effects is that it is related to the jet damping phenomenon, hence the name *jet gain*. The gasdynamic coning mechanism represents the influence of powerful spin effects on jet damping. Figure 47 shows the difference between effects predicted by jet damping theory and those observed in flight.

There is much to support the idea that disturbing effects arise in a natural way in the combustion flow field. Jet damping produces a stabilizing torque of the same order of magnitude as that giving rise to the nutation growth itself. This demonstrates that the combustion gas flow is capable of exerting forces of the correct magnitude. The word *damping* as used here does not mean that the jet damping is a *dissipative mechanism*. It does not represent a frictional loss causing decay of the rotational energy of the system. It is a *reaction force* between the gas flow and the combustion chamber and nozzle surfaces. These forces result from an unsymmetrical pressure distribution that reflects the resistance of the internal flowing gas particles to changes in direction.

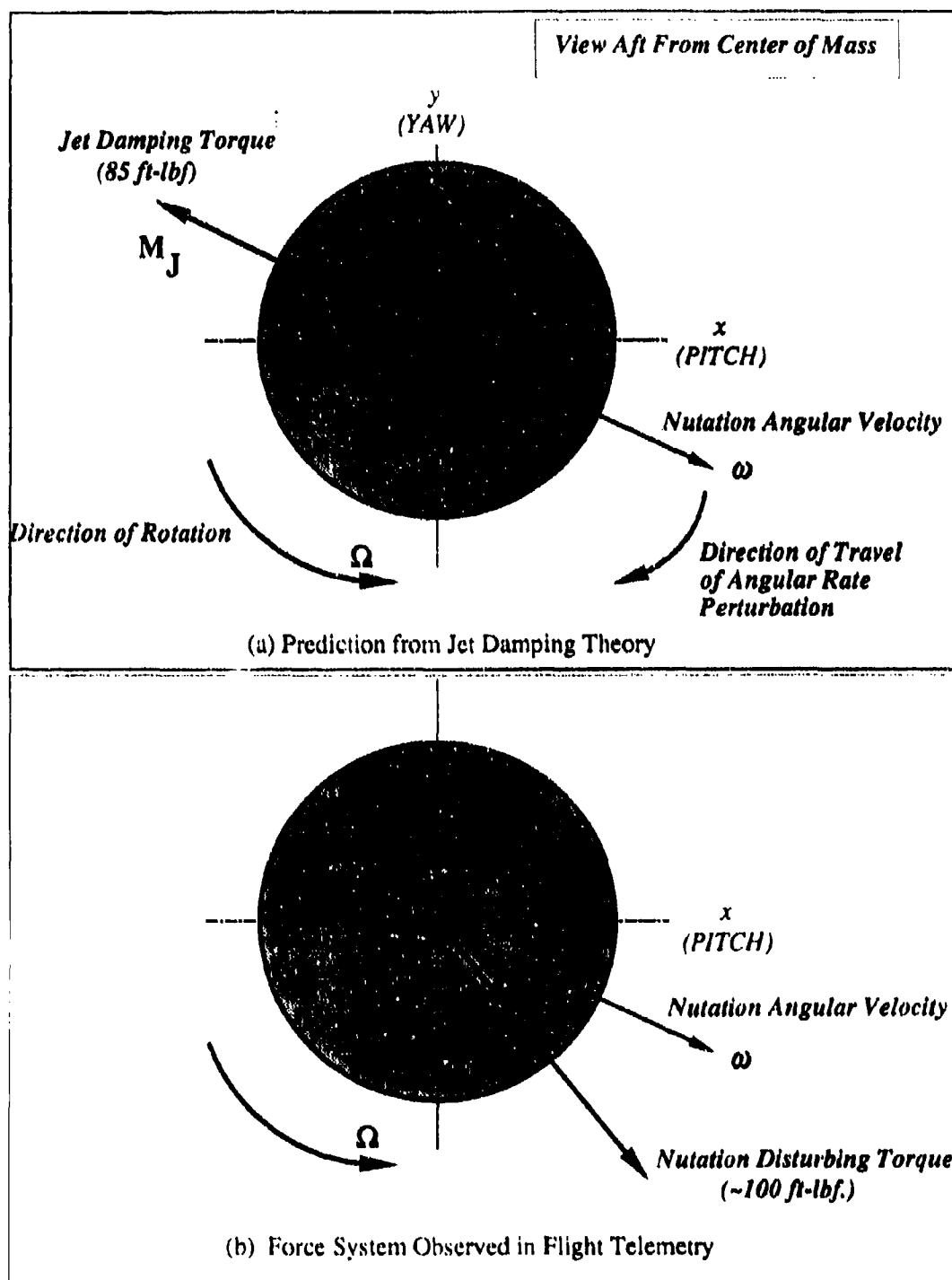


Figure 47. Comparison of Predicted and Actual Interaction Moments

Before the PAM-D coning effect was first encountered, it was assumed that jet damping theory, as it had been successfully applied to many smaller systems, was the only motor-related interaction of any importance. The spin rates for a given system are selected on the basis of an algorithm intended to minimize nutation growth from a variety of sources such as sloshing liquid stores and structural flexibility. During the early part of the motor burn in the STAR 48 (PAM-D) operations, the standard jet damping estimates account for the observed motion fairly well. However, as burning proceeds, there is a gradual transition from damping into driving, as if the the damping force mysteriously switches *direction*. The *magnitude* of the apparent torque remains in a range typical of jet damping.

The situation is displayed conceptually in Figure 47. The lateral force configuration expected on the basis of classical jet damping (Fig. 47(a)) is similar in all respects but one to the actual system shown in Figure 47(b). The latter is the force system deduced from flight telemetry near the peak of the coning instability. The lateral force now has a component parallel to and in the same direction as the instantaneous later angular velocity vector. This component leads to increasing lateral angular velocity. The component normal to the angular velocity vector causes the nutation frequency to shift. The force and angular velocity vectors traverse the system in the retrograde direction relative to the rotation of the spacecraft.

Jet damping calculations are based on an exceedingly simplified model of the gas flow in the motor. An incompressible one-dimensional flow is usually assumed. Models now in widespread use are only slightly better than the those deduced in the classical literature.³⁻¹⁰ These work acceptably well for small chambers with large length to diameter ratios such as in the tactical rockets for which they first used. Figure 48 describes two ways of describing the jet damping mechanism. Both have been used in developing the standard theory. In the first, the gas flow is represented by an incompressible fluid with axial streamlines produced at an end-burning propellant surface. The inertial forces on the gas are balanced by an unsymmetrical pressure distribution as illustrated. This simple model works whether or not the system is spinning. For the arguments to follow, the second view is more enlightening. Now instead of representing the forces acting at the walls of the chamber we examine the equivalent reaction force to the volume force distribution on the gas particles themselves. In body-fixed coordinates, this force is the familiar Coriolis force as shown. Again, notice that the model takes no account whatsoever to the fact that the gas is a deformable medium. If there is a force acting on the gas particle portrayed in Figure 48, this must cause its velocity and path direction to change. This is a weakness of classical jet damping analyses that doesn't matter for small, slender motor chambers. If the gas particles move quickly through the system then the deviation in the streamlines caused by Coriolis acceleration is negligible and the old view is still acceptable. In a large rocket with large lateral dimensions, the path lengths to the nozzle are significantly longer owing to the nearly spherical shape associated with space motors. Thus, gas particles remain longer within the system, implying an extended opportunity for exchanges of angular momentum between the gas flow and the vehicle and thus an alteration of the net reaction torques. A useful estimate of the residence time of a gas particle is the time required for a particle to traverse the chamber radius

$$t^* = \frac{R}{v_b} \quad (219)$$

where v_b represents the typical gas speed in the chamber. For convenience, we will take this to be the speed of gas particles leaving the burning surface. R is the average chamber radius at a given burn time. In large motors, this parameter is typically two orders of magnitude larger

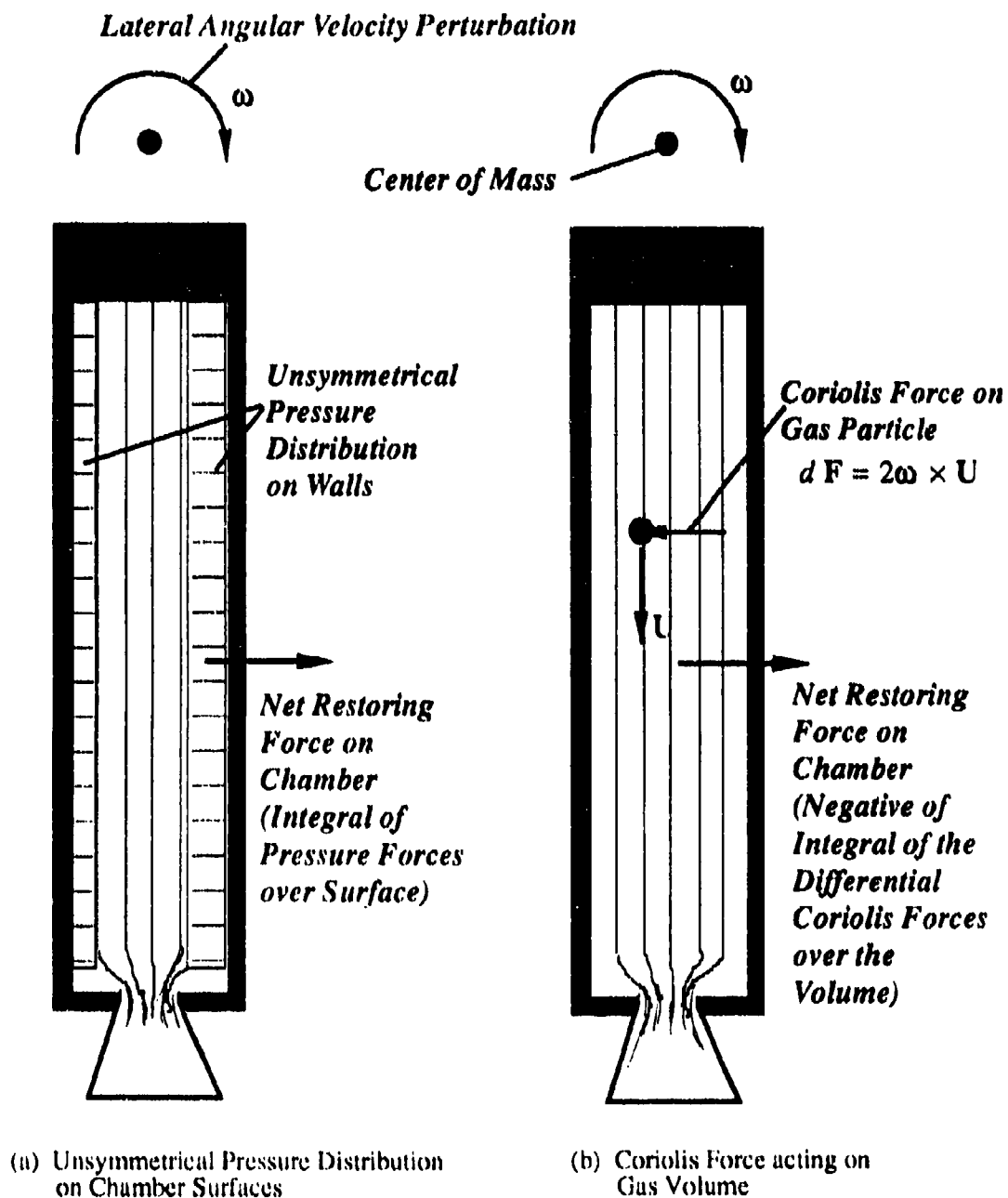


Figure 48. Two Views of the Origin of Jet Damping

than in tactical rockets. Clearly one must be concerned about the actual gas dynamic effects when the flow field does not consist of simple axial streamlines with constant particle velocity.

Another flow feature entirely neglected in jet damping theory is the presence of an azimuthal flow component, a vortex flow, induced by the spin. Gas particles leaving the burning surface carry the angular velocity of the solid body. As they move toward the nozzle, their spin is enormously amplified due to angular momentum conservation. The pressure distribution (or the equivalent forces acting on the body of the fluid) must clearly be affected by this complex flow field. The central idea of the gasdynamic nutation theory is that the pressure distribution, especially in the vicinity of a submerged nozzle entrance is modified by the inertial forces acting on the gases as they traverse the chamber. The longer the residence time, τ , the larger these effects should be. The motor size is then obviously a key parameter. One must account for the effect of the unbalanced Coriolis force on the particle motion, and hence the related pressure fields. Calculations described in earlier sections of this report are aimed at quantifying this complicated situation.

Since we have identified one key parameter in the jet damping problem, it is useful at this point to select others that will be needed in carrying out dimensional analyses of the jet gain effect in the next section. Characteristic parameters in spinning rocket internal flow problems are easily chosen. A convenient set easily quantified for a given motor design is

$$\begin{cases} \text{Characteristic Length:} & R \\ \text{Characteristic Speed:} & v_b \\ \text{Characteristic Time:} & \Omega^{-1} \end{cases} \quad (220)$$

where Ω is the spin rate of the vehicle (rad/sec). If the gas particle residence time is made dimensionless by dividing by the characteristic time, one finds

$$T = \frac{\tau}{\Omega^{-1}} = \frac{R \Omega}{v_b} \quad (221)$$

This is just the inverse of the Rossby number familiar to investigators in rotating fluid theory.¹¹ That is,

$$Ro = \frac{v_b}{R\Omega} \quad (222)$$

This parameter plays a central role in choosing mathematical strategies for approaching the nutation instability problem. Notice that for large stay-times implying a large modification of the internal flow by Coriolis forces, the Rossby number is small. The reason the simple theories of jet damping worked in smaller rockets was that the Rossby number was very large, and the assumption of a uniform gas stream unaffected by the vehicle wobbles was justified. This is equivalent to the statement that the Coriolis forces in the flow relative to the chamber are balanced by the pressure forces acting on its boundaries. The integrated pressure force is the jet damping resistance.

To reiterate, in large spinning rockets such as the STAR 48 and especially in even larger motors now being developed for orbit raising missions, the residence time of gas particles is much increased from earlier rockets. Significant induced currents in the internal flow and associated asymmetrical pressure distributions must be accounted for. To make further progress, one must determine the nature of the internal flow perturbations and their influence on the force balance on the vehicle.

Unfortunately, as we have found in our theoretical studies described in earlier sections, the fluid mechanics problem thus posed is very complex so it is difficult to present simple physical descriptions of the resulting time-dependent, three-dimensional flow field. We are looking for unsymmetrical pressure fields caused by the gas flow perturbations. Unless the gas is a rigid body, we must account for its relative motion and related impact on the system dynamics. This is not done in jet damping theory. Correction of this situation is the fundamental basis of the jet gain mechanism. The flow field is modified by the Coriolis forces, and the net result is that a lateral velocity perturbation is induced in the flow entering the nozzle. This results in an asymmetrical pressure distribution. The integrated pressure force on the chamber boundaries rotates relative to the chamber in the retrograde direction (for a prolate spacecraft mass distribution). The torque produced by this force can be as large (or larger) than the predicted jet damping torque, and more importantly, it can act in the opposite direction thus driving nutation instead of damping it.

Scaling Laws for the Jet Gain Model

The characteristics of the PAM nutation instability are sufficiently well represented by the experimental data set¹ that appropriate scaling rules can be established and tested. In order to apply the familiar methods of similarity and dimensional analysis, it is necessary to select a set of parameters expected to affect the underlying physical mechanism. The choice of scaling variables is imposed once the physics of the model have been decided upon. One can then test the mechanism in a semi-quantitative manner by comparing its predictions to available experimental data. Although the gasdynamic model will be used here, it will be demonstrated that the resulting scaling laws are also valid for the slag sloshing mechanism in an overall sense.

Dimensional Analysis of the Jet Gain Coning Mechanism

The primary scaling variables that naturally arise in the internal flow problem were discussed in the previous section. Additional variables are added to the list, since the experimental data suggest that they affect the flow-driven instabilities. We propose to write a functional expression for the disturbing torque based on the following system variables:

\dot{m}	Motor Mass Flow Rate (kg / sec [slug / sec])	
R	Combustion Chamber Radius (m [ft])	
Ω	Axial Spin Rate (rad / sec)	
ω	Nutation Angular Velocity Perturbation (rad / sec)	(223)
L_{cg}	Location of Center of Mass Relative to Motor (m [ft])	
v_b	Gas Speed at the Burning Surface (m / sec [ft / sec])	
ρ_o	Average Density of Combustion Gas (kg / m ³ [slug / ft ³])	

The spacecraft moments of inertia are not included in the set of variables for the disturbing torque. They will, of course, enter the problem strongly when the torques are used to estimate the dynamic response of the spacecraft. Applying the Buckingham PI Theorem in the usual fashion, and using mass flow rate, center of mass position, and the lateral angular velocity perturbation as the running variables, we find for the disturbing moment

$$M_{\text{flow}} = R \text{gain } \omega = \left\{ \dot{m} L_{cg}^2 C_T \right\} \omega \quad (224)$$

where the interaction torque coefficient C_T is a function of several dimensionless parameters, must be determined experimentally. The torque is proportional to the nutation angular velocity; this is one of the features of the phenomenon that is clearly indicated in the experimental data described in Section 2.

From the dimensional analysis we find

$$C_T = \text{Flow Interaction Torque Coefficient} = C_T \left(Ro, \frac{R}{L_{cg}}, \frac{\omega}{\Omega} \right) \quad (225)$$

Notice that the moment scaling coefficient, C_T , depends on several dimensionless groups that reflect mainly the motor characteristics. The Rossby number, the ratio of the disturbance angular velocity to the spin rate, and the size of the combustion chamber relative to spacecraft size (as represented by the center of mass distance L_{cg}) are the main similarity parameters. To summarize, on a strictly dimensional basis, we find that the nutation torque gain factor depends on the physical parameters of the nutating spacecraft and motor according to:

$$R_{\text{gain}} = m L_{cg}^2 C_T \left(Ro, \frac{R}{L_{cg}}, \frac{\omega}{\Omega} \right) \quad (226)$$

To properly simulate coning behavior in laboratory experiments or in small scale laboratory tests, it is necessary that the Rossby number, relative size of the angular disturbance, and relative chamber size be equal to the values corresponding to the flight data. Some physical reasons for the importance of the Rossby number were established earlier. Examination of the available flight data shows that only spacecraft systems with a relatively small Rossby number have experienced coning instability related to motor operation. The decrease in the Rossby number with time (as R becomes larger as propellant is consumed) explains why the disturbance is most important at the end of the motor run. Other contributing factors are the decreasing moments of inertia as propellant is consumed, and the increase in lever arm length between the motor and the center of mass.

Since spin rates and internal gas flow speeds are similar in most orbit raising vehicles, it is clearly the size of the chamber that represents the most important difference between various systems. Perhaps this is the main reason that the nutation phenomenon was not apparent in earlier spinning vehicle operations. As payloads requirements have grown larger, so have the required propulsion system impulse and, hence, the motor size. It appears from the data that only if the Rossby number approaches the order of unity or smaller does the coning problem become important. Effects of vehicle oscillations on the gas motion are more important for small Rossby numbers as discussed already.

Motor burn time is indirectly involved in the net impact of the coning disturbance on the spacecraft motion, since the larger motors have thicker propellant webs and hence a longer action time. Small disturbances arising in the gas flow are likely to be more important if they act for longer periods of time.

Application of Nutation Scaling Rules

The main result is the simple expression given in equation 224. It can be used to estimate nutation torques needed in designing nutation attitude control systems. It is interesting to note that the disturbing torque model could also have been written in the form shown in 224 even if slag sloshing were the actual physical mechanism. Slag models are usually written in terms of

the vehicle acceleration. This parameter clearly depends on the thrust, which in turn depends on motor mass flow rate. A very similar dependence on parameters results, and 224 could be rewritten to emphasize some of the variables that are important in the slag mechanism.

However, unlike the jet gain model, the slag model requires knowledge of several parameters that cannot be readily determined. For instance, C_T would be expected to depend on the amount of slag accumulated at a given time, the physical properties of the hypothesized liquid material, and any spring constants or pendulum lengths needed to represent the dynamics of the liquid pool.

To use equation 224 in a quantitative sense, it is necessary to estimate the magnitude of the dimensionless torque coefficient C_T . This factor can be determined with acceptable accuracy from flight telemetry data for the PAM-D flights. Examination of this data shows that C_T is approximately

$$C_T \approx 2 \quad (227)$$

during the last seconds of burn when growth of nutation is greatest. The corresponding values of the three similarity parameters corresponding to the jet gain model are

$$\left\{ \begin{array}{l} Ro = 0.82 \\ \frac{R}{L_{cg}} = 0.21 \\ \frac{\omega}{\Omega} = 0.08 \end{array} \right. \quad (228)$$

In a situation involving similar values, the stated value of C_T should provide a reasonable estimate of the average torque gain factor. However, great care should be taken in using such estimates. Examination of the flight data shows that large peaks in torque occur (indicating transient resonant response) and these have an important impact on the actual coning growth. For instance, in all PAM-D and SGS-II data there is a large midburn peak that is responsible for triggering the wobble that grows in a sustained way during the last 10-15 seconds of motor burn.

To test the scaling rules one must determine if equation 224 fits available data. Fortunately, all flight data is for motors with similar parameters, so they are also approximately dynamically similar to the PAM-D configuration. For example, in the case of the four SGS vehicles, the experimentally determined Rgain near the end of the first stage burn peaks at about the value

$$R_{gain} = 7.5 \frac{\text{ft} \cdot \text{lbf}}{\text{deg} / \text{sec}} \quad (\text{from SGS - II first - stage telemetry data}) \quad (229)$$

The corresponding mass flow rate and center of mass position are approximately

$$\dot{m} \approx 1.6 \frac{\text{slug}}{\text{sec}}, \quad L_{cg} \approx 11.3 \text{ ft} \quad (230)$$

Using equation 224 and assuming $C_T = 2$ yields a predicted Rgain of

$$R_{gain} \approx 1.6 * 11.3^2 * 2 = 408.6 \frac{\text{ft} \cdot \text{lbf}}{\text{rad} / \text{sec}} \approx 7.1 \frac{\text{ft} \cdot \text{lbf}}{\text{deg} / \text{sec}} \quad (\text{predicted value}) \quad (231)$$

This compares favorably with the flight measurement. The small discrepancy (less than 5% difference) could be the result of the fact that the systems are not completely similar. The spin rate of the SGS-II's was approximately 1.5 times the PAM-D angular rates, and the length ratio was also larger by a similar factor. It worth noting that had the slag mechanism been used, then the effect of the much lower acceleration (about a third the PAM-D axial acceleration) of the SGS-II would need to be accounted for. Considerably less slag accumulation would be expected under these acceleration conditions. Also, the driving torque should be lessened considerably. This is strong evidence in favor of the gasdynamic mechanism.

Application to Design of Nutation Experiments

As a final example of the application of the scaling laws, consider the problem of measuring Rgain in a laboratory scale device. Several proposals for tests using cold flow or small rocket motors have been studied. Three of these were tested as part of the work described in the following subsections.

To make routine testing economical, one would like to employ readily available motors of the order of, say, two inches outside diameter and five inch length. For dynamic similarity, it is necessary that a spin rate of about 200 rad/sec (~2000 rpm) is needed to match the flight Rossby number. Mass flow rate would be approximately 0.01 slug/sec. The resulting torque gain factor is about

$$R_{\text{gain}} = 5 \cdot 10^{-3} \frac{\text{ft} \cdot \text{lbf}}{\text{rad} / \text{sec}}$$

Under these conditions, a maximum reaction torque of about 0.2 ft-lb would be generated depending on the coning angle relative to the spin axis used during a test. In order to enhance the torque it is necessary that the angular velocity perturbation also be sufficiently large. This is a very small but, perhaps, measurable torque.

Such a test is appropriate for simulation of the jet gain effects, but is not useful if slag motion is the source of nutation growth. Axial acceleration is an important factor in the latter mechanism. Some slag mechanism simulations using small, free-flight rockets is presently underway in a program sponsored by the Hughes Aircraft Company. The results of these interesting experiments have not yet been published. There have also been several captive "cold-flow" simulations, aimed at establishing the possibility of resonant response of a trapped pool of slag. These have not been successful in demonstrating resonant conditions.⁵⁶

In the next subsection we discuss experimental findings for the jet gain mechanism that utilize the scaling rules developed here.

Summary

Finally, application of the method of dynamic similarity yields a simple and useful scaling law for nutation instability experienced during spinning upper stage propulsion maneuvers. The form of the scaling law is appropriate to either of two viable disturbing mechanisms. The derivation was carried out using the parameter set corresponding to the *jet gain* gasdynamic interaction mechanism. The scaling system described enables data from the PAM-D flight series to be extended in estimating nutation characteristics of new spacecraft configurations. Thus it can be used in determining required attitude control capacity in systems using geometrical arrangements similar to those previously experiencing coning instability. It should also prove valuable in the preliminary design of experimental procedures for simulating the gasdynamic coning mechanism in laboratory-scale tests.

Experimental Techniques

Since the propulsion-driven PAM-D nutation instability problem is known only from telemetry data from about 20 flight vehicles, it is highly desirable to determine methods for study of the basic mechanisms in a laboratory environment. Also, it is quite likely that ground tests of full-scale motors will be needed in the future to determine the nutation interaction characteristics before risking them in flight. Since extensive qualification testing is done on new motors for spin-stabilized systems in large spin test facilities, it makes considerable sense to investigate possible modifications to the test procedures that could yield nutation data in addition to the other performance data that are presently collected.

This subsection consists of three parts. In the first one, we discuss a method for simulating the angular velocity environment experienced in a spinning, nutating vehicle. This method was applied in two laboratory-scale experiments described in the last two sections. One experiment was aimed at flow visualization of the complex wave patterns we expect in a nutating rocket chamber. The last set of experiments was aimed at developing test methods for simulating coning behavior in ground tests of small spinning rockets that could be scaled up for use with full-scale space motor hardware.

The Two-Spin Axis Nutation Simulation Technique

In order to simulate the gas flow behavior in ground testing, it is necessary to reproduce the angular velocity environment experienced in flight by a spinning nutating rocket motor. It happens that this can be accomplished by means of a relatively simple mechanical arrangement that requires only two rotational degrees of freedom. No translational motion is necessary.

Consider the wobbling motion as it appears in flight (see Figure 1) in body-fixed coordinates. The angular velocity environment consists of the axial spin with superposed lateral oscillations:

$$\omega = \Omega k + (\omega_x i + \omega_y j) \quad (231)$$

One can readily show, by means of the standard Euler angle transformations, that this environment is identical to that produced by a body spinning simultaneously about two axes inclined to one another as shown in Figure 49. In terms of the Euler angles, the body-fixed angular velocity components are

$$\begin{cases} \omega_x = \sin \theta \sin \phi \dot{\psi} + \cos \phi \dot{\theta} \\ \omega_y = \sin \theta \cos \phi \dot{\psi} - \sin \phi \dot{\theta} \\ \Omega = \cos \theta \dot{\psi} + \dot{\phi} \end{cases} \quad (232)$$

To simulate a specific nutation amplitude in which the perturbation velocity is fixed, one can assume that angle θ is constant so that

$$\theta = \text{Constant} = \theta_0 \quad (233)$$

Also, for any practical experiment the spin rates in laboratory coordinates must be constant so the primary spin

$$\dot{\psi} = \text{Constant} = \dot{\psi}_0 \quad (234)$$

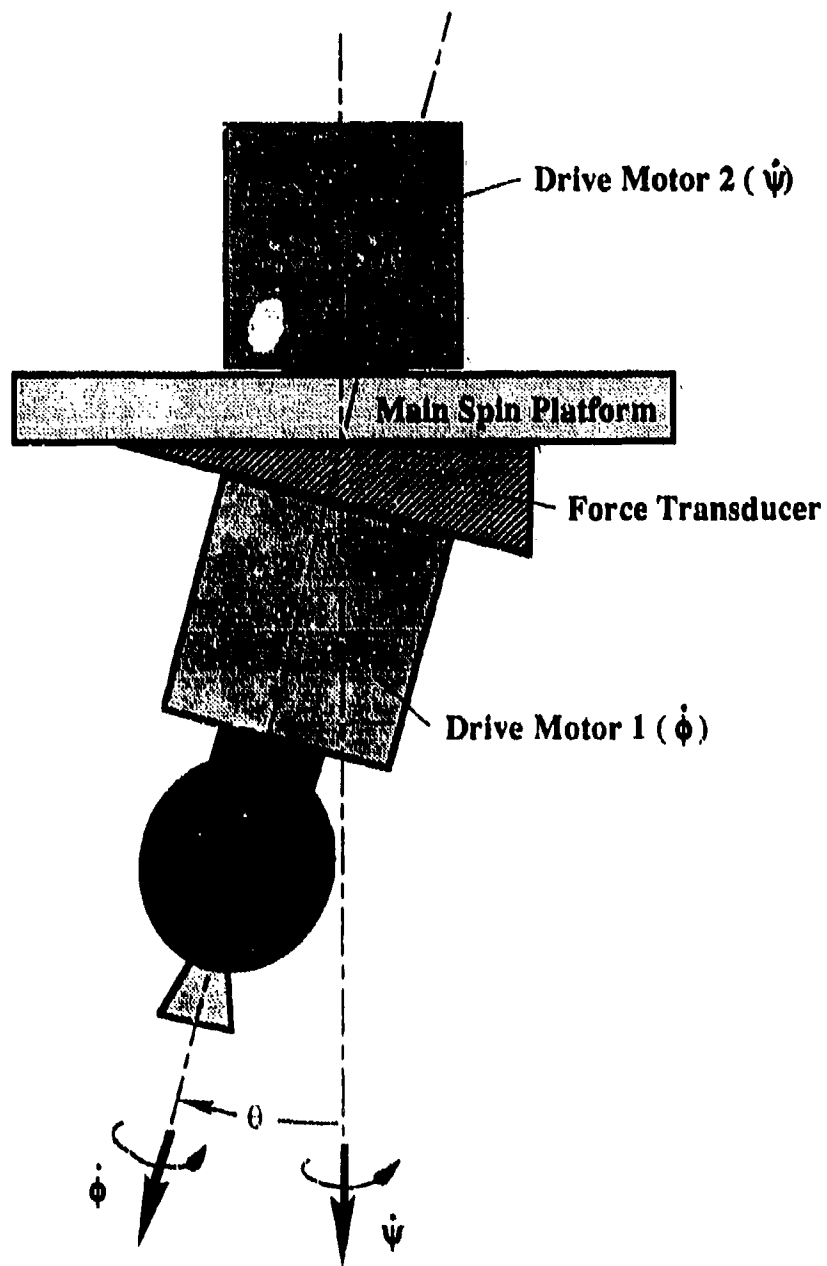


Figure 49. Simulation of Nutation Angular Velocities by Two-Axis Spin Method

is taken to be fixed. Then the following relationships must be satisfied:

$$\begin{cases} \omega_x = \omega_o \sin \lambda_s t = \sin \theta_o \sin \phi \dot{\psi}_o \\ \omega_y = \omega_o \cos \lambda_s t = \sin \theta_o \cos \phi \dot{\psi}_o \\ \Omega = \cos \theta_o \dot{\psi}_o + \dot{\phi} \end{cases} \quad (235)$$

Thus the nutation wobble amplitude is related to the primary spin rate and the nutation angle θ_o through the first two equations as

$$\omega_o = \dot{\psi}_o \sin \theta_o \quad (236)$$

Thus, in order that the wobble rate is represented, the secondary spin must be

$$\dot{\phi} = \lambda_s \quad (237)$$

Finally, the following relationships are found

$$\begin{cases} \theta = \tan^{-1} \left(\frac{\omega_o}{\Omega - \lambda_s} \right) \\ \dot{\phi} = \lambda_s = \Omega \left(1 - \frac{I_2}{I_1} \right) \\ \dot{\psi}_o = \sqrt{(\omega_o)^2 + (\Omega - \lambda_s)^2} \end{cases} \quad (238)$$

Picking an appropriate combination of the two spin rates and the offset angle allows simulation of any angular velocity environment experienced in flight. For example, in a typical situation one might expect

$$\begin{aligned} \omega_o &= 20 \text{ degree / sec} \\ \Omega &= 50 \text{ rpm} = 5.24 \text{ rad / sec} \\ \lambda_s &= 0.6 * \Omega = 3.14 \text{ rad / sec} \end{aligned}$$

which leads to the following test conditions

$$\begin{aligned} \theta &= 9.4 \text{ degrees} \\ \dot{\phi} &= 3.14 \text{ rad / sec} = 29.98 \text{ rpm} \\ \dot{\psi}_o &= 2.13 \text{ rad / sec} = 20.33 \text{ rpm} \end{aligned}$$

The angular rates and the offset angle are fixed throughout a motor burn at values that simulate behavior that is reached only near the end of the burn when instability grows to the chosen condition. Response of the system to realistic perturbations can therefore be assessed throughout the motor burn and it is not necessary to allow incipient growth of the disturbance as in other proposed test methods. Thus, in a full-scale test, one can apply two modest angular rates with a reasonable offset angle. These are within the ranges of equipment already in place. However, modification of full-scale test hardware is an extremely costly venture and may never be undertaken. Therefore, we will explore methods for applying the suggested technique in laboratory-scale experiments.

Design of a Laboratory-Scale Test Techniques

Two approaches have been developed in this program. Although beyond the scope of the original work statement, they have both been brought to the hardware stage. Additional funding was made available at the end of the program that allowed testing of the most promising of these methods. The first approach is a small-scale implementation of the two-spin axis arrangement already discussed. Figure 50 shows the test hardware as assembled by Dr. R. S. Brown at United Technologies Chemical Systems Division using the concepts developed in this program. Figure 51 is a schematic of the layout. The goal of this experiment is to directly determine the reaction moment of the system to the imposed nutation motion. This is most conveniently done by means of a multi-axis load cell fixed in laboratory coordinates on which the spin apparatus is mounted. This allows direct measurement of the interaction moment. The results then yield information on the gain factors produced during the test. Since a small rocket motor is used (two inch outer diameter) short burn times would not allow natural development of significant nutation from initially small wobbling as in the full scale flight instability.

The second method utilizes the Froude pendulum concept. This consists of a small rocket motor attached to a physical pendulum free to swing in any direction about a universal joint or gimbal. The pendulum shaft is mounted in bearings so that the motor can be spun by an electric motor mounted at the opposite end of the shaft. In the design shown, the pendulum swings freely in a stable circular arc at the moment of motor ignition. The angular velocity environment the rocket chamber is identical to that experienced in flight. The same interaction torques are generated. The effect of these torques can be determined in principle by observing the effect on the pendulum motion.

We have implemented the Froude pendulum technique as shown in Figures 52 and 53 showing the gimbal arrangement and drive motor and the rocket motor firing during a typical test. The rocket is of conventional design and utilizes two-inch outside diameter propellant grains with 1/2-inch web thickness. Three grain lengths, 2.3, 3, and 3.5 inches were used in the tests to allow determination of the effects of chamber slenderness ratio. The motor is equipped with a readily replaceable submerged nozzle with a graphite nozzle entrance section. The grains are inhibited at each end so they produce a moderately progressive pressure trace. Throat size was determined to give an average mean pressure similar to the flight conditions in a STAR 48 motor (approximately 800 psi). The motors employed the same propellant used in actual STAR 48 flight hardware. Figures 54 and 55 show views of the motor hardware. The motor is equipped with a spring loaded closure system to allow fail safe operation. Chamber sealing was accomplished with O-rings as shown in the figures.

Motors were ignited with 1 gram BKNO_3 "baggie" ignitors and an electric match. Power for the ignitor passed through a slip-ring assembly that can be seen in Figure 56. Slip-rings for transmission of Kistler transducer data were also mounted in this assembly as shown.

Tests were conducted, as described, with the pendulum motion simulating a 30° cone angle instability at the beginning of the motor run. Motor burn time was about two seconds. Motion of the pendulum was tracked by means of a mechanical linkage moving an encoding device. The signals were sampled at 1/60 second intervals and simultaneously analyzed and stored on a hard disk. Additionally, provision was made to measure chamber pressure near the motor head end by means of Kistler transducers.

There was evidence of slag deposition, but we noticed that even though the motor was nutating with large amplitude during the tests the slag was nearly uniformly distributed



Figure 50. Two-Axis Spin Lab-Scale Motor Test Device

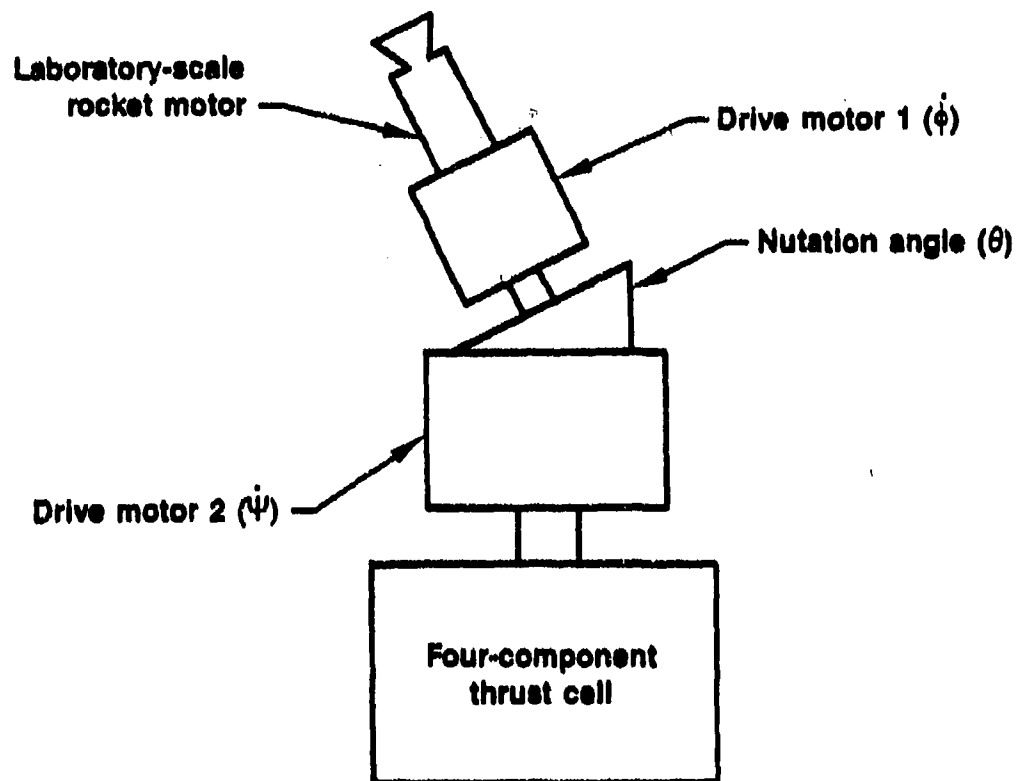


Figure 51. Schematic of Laboratory Scale Nutation Experiment

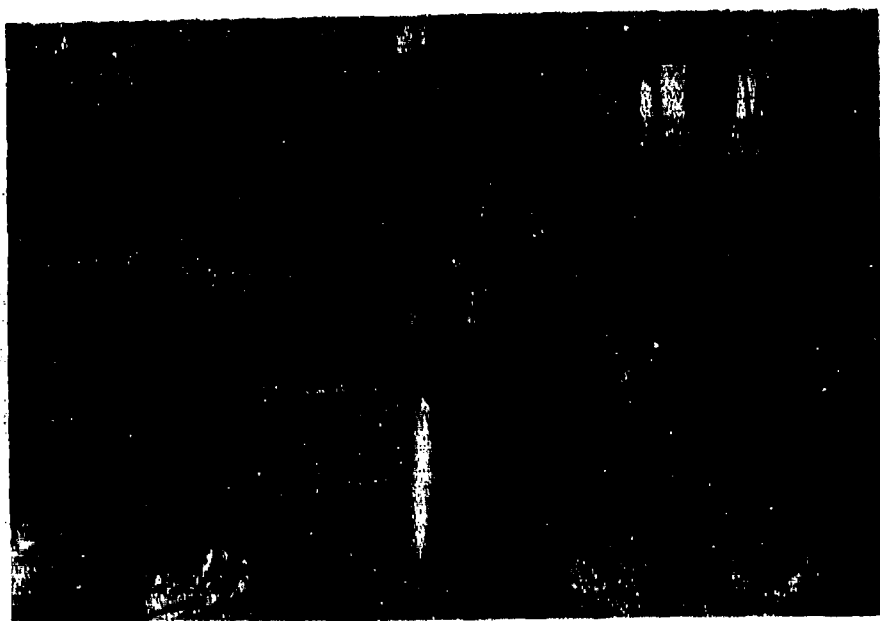


Figure 52. Two-Inch Leloudis Rocket Firing During Froude Pendulum Nutation Test



Figure 53. Drive Motor and Gimbal Arrangement in Froude Pendulum Test

around the periphery. Figure 57 shows a grain fired without spin and an identical one fired with 1700 rpm spin. The nozzle pointed downward in these firings so that any liquid slag should have moved to the area surrounding the submerged nozzle as has been expected in flight. There was no evidence of such "pooling" of the slag in these tests.

Results

The availability of two inch propellant grains set the size of the experimental apparatus. Motors of this size are commonly used in laboratory testing of propellant formulations. As the scaling laws show, the flow interaction torques produced in such small motors are very small. As the last subsection indicates, torques less than 0.2 ft-lbf are expected if full dynamic similarity to the full-scale motors is achieved. The test conditions chosen resulted in a Rossby number of about 1, which is similar to that experienced in a full-scale STAR-48 at midburn. Thus, conditions for similarity were achieved, and an Rgain factor of about 0.005 ft-lbf/rad/sec would be present as predicted by the theory.

In the free precession testing, the effective amplitude of the angular velocity perturbation is set by the natural frequency of the pendulum swing (see equation 236). The natural frequency was lower than desired because of the large mass of the large electric motor required to spin the motor assembly at 1700 rpm. The pendulum frequency was approximately 0.6 cycles/sec, corresponding to a wobble amplitude (with a pendulum swing angle of 30°) to about 1.9 rad/sec. Thus, the actual interaction torque present was about 0.01 ft-lbf, which was not large enough to detect by means of changes in the free motion.

The test results seemed to show evidence of nutation growth during the second half of the motor burn. These data are not conclusive, and we do not offer them in support of any particular model of nutation instability. Also, due to the small size of the disturbing torques, the reproducibility of the tests was not acceptable, and no conclusions can be reached on the basis of the present results.

However, we have demonstrated a new experimental technique for study of nutation characteristics of a spinning rocket motor for the first time. The experimental systems performed properly and motor operations were generally normal. Ignition difficulties appeared in one firing, but these were apparently due to a debonded propellant grain.

Our main goal of developing practical nutation test methods was met. The conclusions at this stage of the research is that the two-axis method shows promise as a practical method for determining the nutation interaction torques in a spinning motor.

Modifications of the experimental procedure can be used to increase the interaction torque. If small motors of the type used in the present experiments are to be employed, it will be necessary to greatly increase the primary spin rate. Thus, the pendulum method must be abandoned since the effective spin rate is dependent on the pendulum frequency. If is increased to, say, the same rate as the axial spin, 1700 rpm, by driving as in the two-axis method (see Fig. 49), the interaction torque in a two inch motor would be increased to approximately 1 ft-lbf. It should be possible to accurately measure such a torque if the apparatus is dynamically balanced so that vibration effects do not affect the torque measurements. In order to produce torques that can be measured with adequate resolution, it will be necessary to use larger test rocket motors. It appears that use of motors of the order of six inches in diameter will be large enough to produce nutation gain data in laboratory-scale testing.

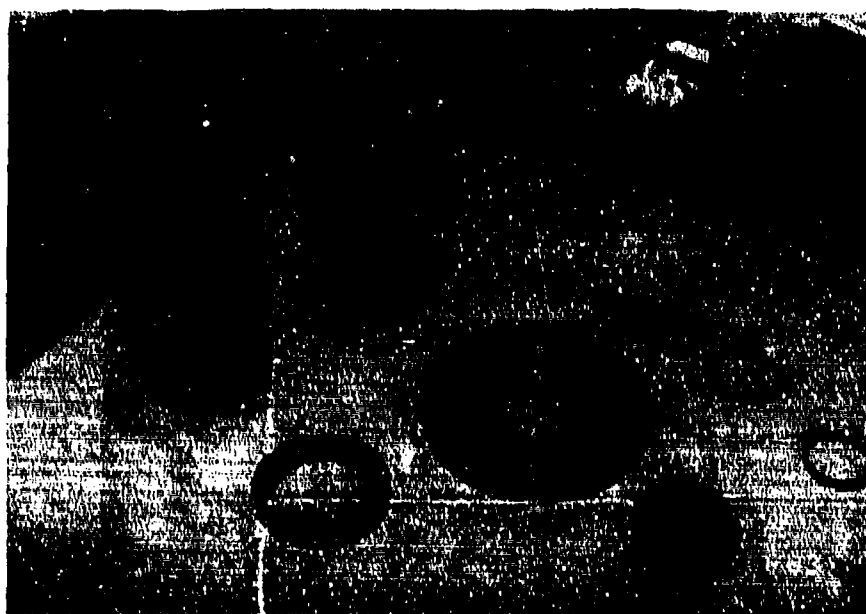


Figure 54. Motor Components Showing Typical Grain and Aft Closure

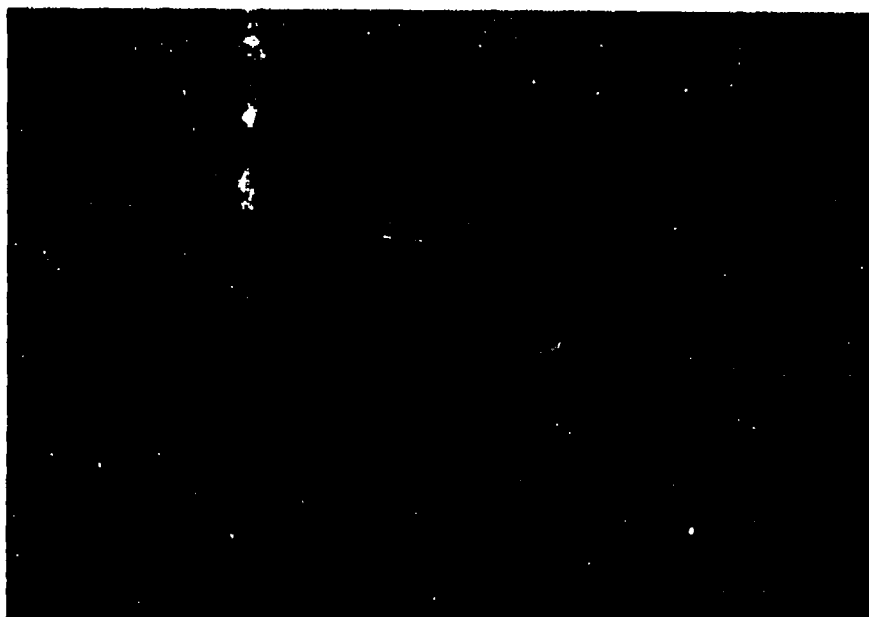


Figure 55. Assembled Motor Showing Pressure Relief System



Figure 56. Slip Ring Assembly in Froude Pendulum Test Device

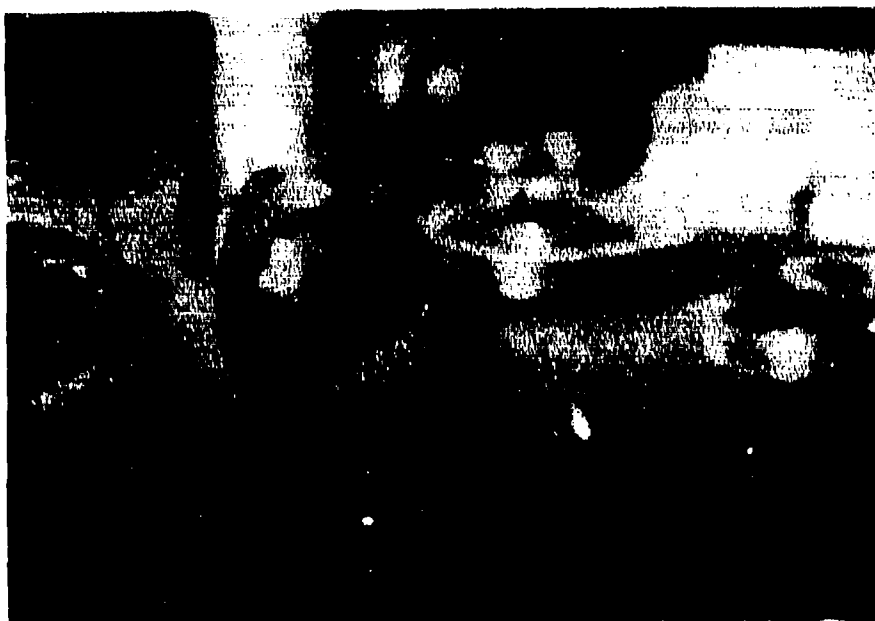


Figure 57. Slag Deposition (Motor on Left Was Fired Without Spin)



Figure 58. Cold Flow Test Arrangement

Cold Flow Nutation Simulations

The experimental setup is shown in Fig. 58. The main spin platform is a Genisco C-180 rate of turn table with mechanical feedback. The rotation rate is stable to less than 0.1 degree/sec. The rotation range is 0.01 to 1200 degrees per second, for loads up to 50 pounds. The main platform is equipped with sixteen slip-ring assemblies. The secondary spin table was designed to rotate in the range 0-360 degrees/second, and is equipped with fourteen slip rings. The secondary platform was modified to operate at a tilt angle up to 30°. There was a slight centrifugal drag generated by the outer table which tended to slow the inner table compared to its nominal operating characteristics. To compensate for this, the secondary spin table was driven at a higher voltage to maintain a given rotation rate. It was expected that the first inertial mode would be excited when the ratio of the main spin rate to the secondary spin rate was 2.2. The test cell was illuminated with an 18-watt fluorescent light. Five video tapes were made with a Canon E70 Camcorder. Voice recording was made on the video tapes describing the test conditions used in each run.

All tests were run in the clockwise direction as viewed from above. Distilled water and oil (Cargille Immersion Fluid) were used in the test cell. Photo-Flow 200 solution was used with the distilled water. The particles used to render the flow visible to the recording camera were 0.03 mm, 0.3 mm, and 1.0 mm alpha-alumina powder, 30 mm aluminum powder and crescule violet dye diluted with distilled water.

A Breul and Kjaer hydrophone was mounted near the sidewall of the forward face of the chamber to record pressure variations. However, the wave amplitudes were so low that no conclusive data was produced during these tests. Earlier tests using the piston-driving technique showed definite pressure wave effects when resonant inertial modes were excited.

Results

The flow visualization experiments confirm that the angular velocity environment in a spinning, nutating chamber produces a traveling wave motion in the contained fluid. The results confirm earlier measurements in which the waves were driven by an oscillating piston mounted off-axis as described in Reference 1. The recordings verify that the fluid particle oscillations are in the form of a retrograde three-dimensional traveling wave. They also confirm that there is a 180 degree phase shift between lateral particle motions and associated pressure patterns between the forward and aft end of the test chamber. This is one of the key features of the unsteady flow in a nutating chamber predicted by the analyses presented earlier.

Tests conducted with the simulated submerged nozzle did not differ substantially from those using a flush nozzle. Thus the nozzle apparently has little effect on the overall flow pattern except in its immediate vicinity.

Recordings from the cold flow tests are included in the video tape summarizing the program findings. These clearly demonstrate the wave behavior of the flow in a spinning, nutating chamber.

CONCLUSIONS

This study was motivated by a need to understand, in detail, the mechanics of interactions of an internal flow in a spinning rocket with the dynamics of the vehicle. Proposed mechanisms for the PAM-D instability have not been successful either in predicting coning effects in new vehicles or in suggesting corrective procedures. The problem is currently handled by guesswork using strap-on nutation control devices that cannot be properly matched to the system because the characterization of the disturbing torque has been incomplete. It is clear that the exact nature of the coning mechanism must be determined along with its physical characteristics and its dependence on vehicle parameters.

We have found that a strong disturbing mechanism is present in the internal flow field. In large motors (such as the PAM-D, STAR 48), the gas motions are dramatically affected by vehicle nutation. The jet damping concept, found to be a reasonable model for gas flow interactions in earlier, smaller spinning vehicles, does not apply in large motors. The assumption that the gas immediately accommodates to the motion of the chamber boundaries so that the flow remains uniform is incorrect in a large motor.

Jet damping has been demonstrated in the report to be a consequence of a traveling pressure wave induced by Coriolis forces in the gas. By assumption, the Coriolis acceleration is balanced by a nonuniform pressure field in the classical jet damping model. The force produced by the action of this traveling pressure wave on the walls of the combustion chamber produces the damping torque. This representation of the flow interactions is not correct in a large spinning system.

In large spinning rockets, the flow field is significantly perturbed by nutation wobbling. The velocity field in the combustion gases is modified and complex three-dimensional waves are produced. The corresponding pressure pattern is dramatically altered compared to the one predicted by jet damping theory. In particular, the point of maximum pressure is rotated relative to the chamber and a driving force instead of a damping effect is produced.

As a check on earlier work based on this model, we have computed the interaction forces directly by determining the details of the internal pressure distribution and their effect on the motor force system. In earlier studies, the interactions were computed indirectly by estimating the unsteady flow field and resultant nonuniform angular momentum flux from the system. This was described as an undulating vortex flow in an attempt to produce a easily visualized physical model. The fact that the flow leaves the system unsymmetrically is a demonstration of the presence of unbalanced forces within the chamber. These nonuniform pressure disturbances have been directly determined in this report.

We find that resonance of the gas oscillations with the vehicle nutation motion is an important feature of the instability. Greatest growth of the nutation takes place when there is resonant coincidence between one of the low-order vortical wave modes of the chamber and the nutation frequency of the spacecraft.

Experimental methods were developed to allow verification of the features of the proposed jet gain mechanism. The cold flow experiments verify, in detail, the flow disturbances predicted by the theory. Methods for carrying out nutation tests with small spinning motors were developed. However, the magnitudes of the disturbing torques are very small, and no conclusive data could be provided within the time constraints of the study. The equipment is being improved and new motor grains have been acquired so that testing can continue. Modifications are being made to increase the spin rate about the primary axis by several orders

of magnitude to improve the resolution of the torque measurements. The free pendulum method was used in the initial tests because it offered a simple means for both measuring the nutation disturbance and demonstrating its effects. However, the natural frequency of the pendulum is greatly reduced because of the mass of the large spin motor needed to rotate the rocket motor chamber. Therefore the effective amplitude of the simulated nutation disturbance is greatly diminished. Additional instrumentation has also been installed making it possible to directly measure the interaction torques. Both aluminized and nonaluminized motors will be tested in subsequent experiments. The data will be released in the form of a technical paper during the summer of 1990.

Summary of Program Results

- There are strong resonant, wavelike interactions between the flow of combustion gases in the motor chamber and the angular motion of a wobbling spacecraft.
- These interactions have been previously accounted for by a simple theory, the classical jet damping model, that is based on an overly simplified description of the internal flow, namely that the relative motion of gases passing through the motor chamber and nozzle are unaffected by the wobbling of the vehicle.
- The magnitude of the jet damping torque predicted by the classical theory follows a time-history and exhibits similar magnitude to the torque that drives the coning instability. The direction of the torque vector predicted by this model is always such that it decreases the amplitude of nutation wobbles.
- If proper account is taken of the details of the time-dependent internal flow effects, then the flow interaction torque vector changes direction. Nutation growth may then occur.
- Jet damping theory applies only in small rocket systems. In large spinning space motors (such as those in used in the PAM-D and DII series), jet damping results are no longer applicable.
- Although it is possible that slag accumulation mechanisms could affect nutation characteristics, the gas dynamic effects alone are sufficient to explain the nutation instability.
- All effects predicted in detailed theoretical treatments of the problem are borne out in simple cold flow experiments. The basic wavelike nature of the internal flow response to vehicle wobbling is clearly present in flow-visualization experiments.
- Unsymmetrical pressure forces within the combustion chamber produce the major part of the nutation torque. Unbalanced forces in the nozzle appear to play a less important role than expected on the basis of earlier studies.

- It is possible to simulate the nutation effects in small-scale rocket motor firings. However, in order that measureable interaction torques are produced, it is necessary to spin the motor at very high angular rates. Also, the torque varies approximately as the fourth power of the average diameter of the combustion chamber, so motors of the order of six inches in diameter may be needed to make laboratory scale experiments useful. Tests run with two-inch motors in this program were inconclusive.
- Scaling rules have been devised that show that the nutation torque generated by the gas flow is proportional to the mass flow rate of combustion products and to the square of the distance from the motor chamber to the vehicle center of mass. The torque depends on several similarity parameters, the most important of which is the Rossby number.
- The theoretical results show that changes in internal configuration of the motor chamber, placement of the motor relative to the vehicle mass center, and axial spin rate can be used to control the tendency for nutation growth in a given system.

Methods for accurately representing the time-dependent by means of numerical solutions of the full Navier-Stokes equations for the chamber gas flow were developed. This part of the program progressed considerably beyond what was originally expected. It is strongly recommended that this part of the effort be carried out to completion. It offers the capability to determine, in detail, all of the flow features and interaction forces and torques in a spinning, nutating rocket chamber. The computer algorithms developed for this purpose are completely realistic in terms of flow velocity distributions, Mach number ranges, Reynolds number values, and chamber and nozzle geometry. This code development has obvious applications beyond the one for which it was intended in this research program.

(Blank Page)

APPENDIX A

Analytical Solution for Nutation Gain Factor

This program implements the solutions described in the flow field analyses described in this report. The unsteady pressure and velocity distributions are represented in Fourier-Bessel series form. A best-fit cylinder is used to represent the combustion chamber. Results are valid for small a Rossby number of the order of values appearing near the end of a PAM-D burn.

Changes in chamber size, slenderness ratio, thermodynamic properties, mean flow speed, vehicle moments of inertia, and mass center position are computed in the program. Using this data, torque gain factors are computed at selected time points.

The sample program listing includes data representing a typical PAM-D spacecraft configuration. The complete program includes provision for simulating the spacecraft motion corresponding to the predicted flow interaction gain factors. It also provides options for generating unsteady pressure and velocity distributions in the rocket chamber.

A users manual and complete source code listing for this program is available as a separate document.

program Nutation; (NUTATION INSTABILITY IN SPINNING
 PROPULSION MANEUVER)
 G. A. Flandro, WASATCH RESEARCH, Inc., September 1989
 SIMPLE ROCKET MEAN FLOW WESTAR-V PARAMETERS

```
const ndims = 40;
type matrix = array[1..ndims,1..ndims] of extended;
vector = array[1..ndims] of extended;
jmat = array[0..10] of extended;
var
  psi,x,lambda,b,c,I0,I1,Lcg,Lnozz,Ls,Lt,Lh,Rn,Rt,Omega,Scfreq,t,p1,p2      :extended;
  Rho,Nuo,Vb,Mdot,Mdot1,Rosby,Ekman,Delta,Rgain,Sgain                     :extended;
  psirt,Rhop,ro,r1,r2,Lo,r,z,Arg,p,Xir,Vbent                             :extended;
  Mo,R3,L3,ao,Po,g,det,k0,k1,k2,k3,k4,k5,k6,k7,k8,k9,k10                 :extended;
  f1,f2,f3,f4,f5,f6,f7,f8,f9                                             :extended;
  j                                                                           :jmat;
  Er,Ei,Fr,Fi,E,Br,Bi,Lam,Xi,J0,J01,J1,J11                             :vector;
  A                                                                           :matrix;
  found                                                                      :boolean;
  n,m,i,k,n1,m1,order                                                       :integer;
```

procedure spacecraft; (compute variable spacecraft parameters WESTAR-V)
 begin

```
{MASS PROPERTIES;}
I1 := 2124.097 - t*(12.932835+0.048777056*t);      ! Moments of Inertia (slug ft^2)
I0 := 586.776 - t*(0.6186363636 +0.027954545454*t);
```

```
{LENGTHS;}
r1 := (7.46294+t*(0.77687+t*(-0.015888+t*(1.41725e-4))))/12.0;
r2 := (7.46294 +0.1896295*t)/12.0;
ro := (r1 + 3*r2)/4.0;      ! Chamber Radius (ft)
if ro > 1.9 then ro := 1.9;
Lo := (32.8432 +t*(0.2384 + t*(5.612e-4)))/12.0;      ! Chamber Length (ft)
b := Lo/(2*ro);      ! Chamber Slenderness Ratio
Lcg := (6.3025731+t*(0.02190887+
  t*(-7.55762e-5+t*2.678833e-6)))/ro;      ! CM position
Lnozz := 29.0/(12.0*ro);      ! Nozzle length (dimensionless)
Rn := 14.73/(12.0*ro);      ! Nozzle exit radius ( " )
Rt := 1.8116 + 0.00456*t;      ! Nozzle throat radius
if t < 40 then Rt:=1.9947;
Rt := Rt/(12.0*ro);      ! Dimensionless throat radius
Ls := 6.9/(12.0*ro);      ! " nozzle submergence depth
Lt := Lcg - Lnozz;      ! Nozzle Entrance Position
Lh:=Lcg-(Lnozz-Ls)-2*b;
```

```
{GAS PROPERTIES;}
g:=1.18;      ! Ratio of specific heats
Rhop := 3.36;      ! Propellant density (slug/ft^3)
Mdot1:= (1.349651+0.003086*t);      ! Mass flow rate (slug/sec)
```



```

Po:= Mdot1/(1.9492136346E-4*pi*(ro*Rt)**2);      ! Chamber pressure
ao:= 3592.397;                                   ! Speed of sound (ft/sec^2)
Rho := g*Po/(ao*ao);                             ! Gas density
Vb := 0.000663062*(Po**(0.3))*Rhop/Rho;          ! Gas speed at burn surface (ft/sec)
Vbent:=Mdot1/(Rho*Pi*ro**2);                     ! Gas speed at nozzle Entrance(ft/sec)
Mdot:=Mdot1/(Rho*Vb*ro*ro);                       ! Dimensionless mass flow rate
Omega := (5.375+t*(-8.23529411765e-4) +          ! Spin Rate (rad/sec)
          t**3.87543252595e-5);
Rossby := Vb/(ro*Omega);                          ! Rossby number
Scfreq := (1.0-I0/I1);                            ! Dimensionless nutation frequency
Delta := Rho*ro**4*Vb/(I1*Omega);                 ! Scaling parameter
end;

-----Bessel Functions and Derivatives-----
procedure Bess (order :integer; x :extended; var j : jmat );
var f,h,h1,h2,t,theta :extended;
var k1,v :integer;
begin
  v:= order;
  f:=0.5;
  h:=0.5;
  k1:=0;

  If (x<=(7.5+0.3*v) )Then Begin
    If v = 0 then begin
      v:=-v;
      f:=(-1)**v/2;
      h:=f;
    end;
  repeat
    k1:=k1+1;
    f:=f+h;
    h:=-h*x*x/(4*k1*(k1+v));
    f:=f+h;

    until abs(f/h)>2e7;
    If v = 0 then begin
      j[0]:=f;
      Exit(bess);
    end;
  repeat
    v:=v+1;
    f:=2*f*v/x;
    until v>3;
    h:=(1+2.0*(2.0/(3.0*v*v)-1)/(7.0*v*v))/(30.0*v*v*v);
    h1:=x/(2*v);
    h2:=ln(h1);
    h:=(h-1)/(12.0*v)+v*(1+h2);
    f:=f*exp(h)/sqrt(2*pi*v);
    j[0]:=f;
  End;

  If x>(7.5+0.3*v) Then Begin;
    t:=sqrt(2/(pi*x));

```

```

theta :=(pi/2)*(v+h-t*t*x*x);
f:=0.0;
repeat
  f:=f+t*cos(theta);
  t:=t*(h*h-v*v)/((2*h+1)*x);
  theta := theta +pi/2;
  h:=h+1;
until (h*h>((2*h+1)*x+v*v));
End;
j[0]:=f;
end;
)
procedure Bessfunc (order,nder :integer; psi :extended; var j : jmat );
begin
  If nder = 0 then begin;
    Bess(order,psi,j);
    j[0]:=j[0];
  end;
  If nder = 1 then begin;
    If order =0 then begin;
      Bess(1,psi,j);
      j[1]:=-j[0];
      Bess(0,psi,j);
      j[0]:=j[0];
    end;
    If order =1 then begin;
      Bess(0,psi,j);
      j[1]:=j[0];
      Bess(1,psi,j);
      j[1]:=j[1]-j[0]/psi;
      j[0]:=j[0];
    end;
  end;
End;
end;
)
Root Finder
)
procedure Findrootn ( function f(x:extended) :extended; lowx, highx, del :extended; nroot :
integer; var found :boolean; var root : extended);
( This procedure finds the nth root (root nroot) in the interval lowx < x < highx )
var x, flowx,delx,flast,fx,fprime : extended; i : integer;
begin
  if nroot < 1 then nroot :=1;
  x:= lowx; found:= true;
  for i:=1 to nroot do begin
    flowx:= f(x);
    repeat x:= x + del until (f(x)*flowx < 0) or (x > highx);
    if x > highx then begin found := false; exit (findrootn) end;
  end;
  delx:= 0.005; flast := inf; x:= x - del/2;
  for i:=1 to 100 do begin
    fx:=f(x); fprime:= (f(x+delx) - fx)/delx; x:= x - fx/fprime;
    if abs(fx) >= abs(flast) then begin root:=x; exit(findrootn) end;
    flast:=fx;
  end;
  if abs(fx) > 0.01 then found:= false;
end;
end;

```

```
(----- Mode Frequencies -----)
procedure FindLambda( n,m :integer; b :extended; var psi,lambda :extended; var found :boolean
);
```

```
  var start,c:extended;
  function f( x :extended ) :extended;
  var j : jmat;
  begin
    Besfunc(1,1,x,j);
    f:=x*j[1] +sqrt(1 + x*x*c)*j[0];
  end;

  begin
    start:= 0.2; c:= 1/sqr(n*pi/b);
    findrootn( f, start, 40, 0.2, m, found, psi);
    if found then lambda:=2/sqrt(1+psi*psi*c);
  end;
```

```
(----- Coefficients -----)
Procedure System(ndims: integer; var A:matrix;var F,E :vector; var det :extended);
```

```
  var i,k,m:integer;
  k9: extended;
  begin
    det:=1.0;
    for m := 1 to ndims-1 do begin
      det:= det*A[m,m];
      for i:= m+1 to ndims do begin
        k9:=A[i,m]/A[m,m];
        for k:= m+1 to ndims do A[i,k] := A[i,k] - k9*A[m,k];
        F[i]:=F[i] - k9*F[m];
      end;
    end;
    det:=det*A[ndims,ndims];
    for m:=ndims downto 1 do begin
      E[m] := F[m]/A[m,m];
      for i:= 1 to m-1 do F[i]:=F[i] - E[m]*A[i,m];
    end;
  end;
```

```
(----- MAIN PROGRAM -----)
begin
```

```
  m1:=10; {Number of m indices}
  n1:= 7;  {Number of n indices}
```

```
  t := 0.0;
```

```
repeat
```

```
  spacecraft; {Get Spacecraft and Motor Data at time t}
  {writeln('R =' ,ro:9:5,' ','Rossby No.=',Rossby:9:5,' ','b =' ,b:9:5,' ','Vb =' ,Vb:9:5,'
  ','Lambda =' ,Scfreq:9:5);}
```

(----- Calculate E,J, Lambda, Xi -----)

```

n := 1;
repeat
  m:= 1;
  repeat
    FindLambda( n,m,b, psi,lambda,found);
    i :=m+(m1*(n-1)) DIV (2);
    Lam[i]:=Lambda;
    Xi[i]:=psi;
    Besfunc(1,1,psi,j);
    J1[i] :=j[0];
    J11[i] := j[1];
    Besfunc(0,1,psi,j);
    J0[i] := j[0];
    J01[i] := j[1];
    E[i]:=(4+Lam[i]**2)*((psi**2/2)*(J0[i]*J0[i]+J01[i]*J01[i])-
      J1[i]*J1[i])+4*Lam[i]*J1[i]*J1[i];
    E[i] := E[i]*(2*pi*b/(4-Lam[i]**2)**2);
    E[i] := E[i]+pi*b*((n*pi/(2*Lam[i]*b))**2)*(J11[i]*J11[i]+(1-1/psi)*J1[i]*J1[i]);
    {writeln( i:3,chr(9),m:3,chr(9),n:3,chr(9),Lam[i]:14:10 );}
    m:= m + 1
  until ( m > m1 ) ;
  n := n + 2;
until ( n > n1);

```

(----- Calculate A[i,j] -----)

```

i:=1;
repeat
  k:=1;
  repeat
    A[i,k]:=Pi*b*(J1[k]*J1[k])*(Scfreq-Lam[i])/(Lam[k]+Lam[i]);
    {writeln( i:3,chr(9),m:3,chr(9),n:3,chr(9),A[i,k]:14:10 );}
    k:=k+1;
  until (k>ndims);
  i:=i+1;
until (i>ndims);

```

(----- Calculate A[i,i], F[i] -----)

```

n := 1;
repeat
  m:= 1;
  repeat
    i :=m+(m1*(n-1)) DIV (2);
    k0:=(2*b)/(n*Pi);
    k1:=Pi*b*(Scfreq/Lam[i]);

```

```

k2:=(1/Lam[i]+1/Scfreq)/(k0*k0);
k3:=Scfreq*Scfreq/(4*(Scfreq-Lam[i]));
k4:=(Scfreq/Rosby)*k0*k0*(1+2/Scfreq)*J1[i];
k5:=- (1-4/(Scfreq*Scfreq))*((Scfreq-2)*(2*J1[i]/Xi[i]-J0[i]) +2*(1-J0[i]))/
(Ro*Xi[i]);
k6:=(1-4/(Scfreq*Scfreq))*(2*J1[i]/Xi[i]-J0[i])/Xi[i]+2*k0*k0*J1[i]*(1+2/
Scfreq);

k7:=4*Pi/(E[i]*(Scfreq-Lam[i]));
k8:=-4*k0*k0*J1[i]/(Lam[i]-2)+2*(2*J1[i]/Xi[i]-J0[i])/(Lam[i]*Xi[i]);
k9:=Scfreq*k0*k0*J1[i]/(Lam[i]-2);
k10:=- (2*(1-J0[i])/Xi[i]-(2+Scfreq)*(2*J1[i]/Xi[i]-J0[i])/Xi[i])/Lam[i];

A[i,i]:=k1*(k2*(J11[i]*J11[i]+(1-1/(Xi[i]*Xi[i]))*J1[i]*J1[i])-J1[i]*J1[i]);
Fr[i]:=-4*Pi*k3*(k4+k5);
Fi[i]:=8*Pi*k3*k6;

Br[i]:=k7*(k9+k10)/Rosby;
Bi[i]:=k7*k8;

m:=m+1;
until (m > m1);
n:=n+2;
until (n > n1);
(-----Solve System of Equations-----)

System( ndims, A, Fr, Er, det );
System( ndims, A, Fi, Ei, det );

(-----Print Coefficients-----)

(i:=1;
repeat
writeln( i:3,chr(9),Er[i]:14:10,chr(9),Ei[i]:14:10,Br[i]:14:10,chr(9),Bi[i]:14:10);
i:=i+1;
until (i > ndims);)

(-----COMPUTE TORQUE GAIN FACTORS-----)

Rgain:=0.0;
Sgain:=0.0;
n:=1;
repeat
m:=1;
repeat
i:=m+(m1*(n-1)) DIV (2);
f5:=Pi*(2*(2*b/(n*Pi)))**2*J1[i]+J11[i]**2+(1-1/Xi[i]**2)*J1[i]**2;
f6:=Pi*Lh*J1[i]/(2-Lam[i]);
Rgain:=Rgain-f5*Ei[i]-f6*Br[i];
Sgain:=Sgain-f5*Er[i]+f6*Bi[i];

```

```

        m:= m + 1
    until ( m > m1 ) ;
    n := n + 2;
until ( n > n1 ) ;

```

(Dimensional Values:)

```

Rgain:=Rho*ro**4*Vb*Rgain/(180.0/Pi);
Sgain:=Rho*ro**4*Vb*Sgain/(180.0/Pi);

```

```

writeln(t:10:2,chr(9),ro:14:10,chr(9),Scfreq:14:10,chr(9),Rgain:14:10,
chr(9),Sgain:14:10);

```

```

t := t + 1.0;

```

```

until ( t > 87.0 ) ;
end.

```

APPENDIX B

Integrals Used in Evaluation of Cylindrical Chamber Results

$$\int_0^1 J_1(\xi r) dr = \frac{1}{\xi} [1 - J_0(\xi)]$$

$$\int_0^1 r J_1(\xi r) dr = \frac{1}{\xi^2} \left[-\xi J_0(\xi) + 2 \sum_{n=1}^{\infty} J_{(2n-1)}(\xi) \right]$$

$$\int_0^1 r^2 J_1(\xi r) dr = \frac{1}{\xi^2} [2J_1(\xi) - \xi J_0(\xi)]$$

$$\int_0^1 r J_1'(\xi r) dr = \frac{1}{\xi^2} [\xi J_1(\xi) + (J_0(\xi) - 1)]$$

$$\int_0^1 r J_1^2(\xi r) dr = \frac{1}{2} \left[J_1^2(\xi) + \left(1 - \frac{1}{\xi^2}\right) J_1^2(\xi) \right]$$

$$\int_0^{2b} \sin\left(\frac{n\pi}{2b}\right) z dz = \left(\frac{2b}{n\pi}\right) (\cos n\pi - 1)$$

$$\int_0^{2b} \cos\left(\frac{n\pi}{2b}\right) z dz = 0$$

$$\int_0^{2b} \sin^2\left(\frac{n\pi}{2b}\right) z dz = b$$

$$\int_0^{2b} \cos^2\left(\frac{n\pi}{2b}\right) z dz = b$$

$$\int_0^{2b} z \cos\left(\frac{n\pi}{2b}\right) z dz = \left(\frac{2b}{n\pi}\right)^2 (\cos n\pi - 1)$$

REFERENCES

1. Flandro, G. A. and et. al. Fluid Mechanics of Spinning Rockets. AFRPL TR-86-072 1987.
2. Mingori, D. and Y. Yam. Nutational Instability of a Spinning Spacecraft with Internal Mass Motion and Axial Thrust. 1986 AIAA Astrodynamics Conference. 1986.
3. Rosser, J. B., R. R. Newton and G. L. Gross. "Mathematical Theory of Rocket Flight." 1947 McGraw-Hill Book Co. New York.
4. Davis, L. J., J. W. J. Follin and L. Blitzer. "Exterior Ballistics of Rockets." 1958 D. Van Nostrand Co. Princeton, New Jersey.
5. Thomson, W. T. and G. S. Reiter. Jet Damping of a Solid Rocket: Theory and Flight Results. AIAA J. 3(March 1965): 413-417, 1965.
6. Thomson, W. T. "Introduction to Space Dynamics." 1961 John Wiley and Sons. New York.
7. Kolk, W. R. "Modern Flight Dynamics." 1961 Prentice-Hall. Englewood Cliffs, New Jersey.
8. Rott, N. and L. Pottsepp. Simplified Calculation of the Jet Damping Effects. AIAA J. 2(April 1964): 764-766, 1964.
9. Pottsepp, L. PAM Coning Problem. McDonnell Douglas Astronautics Co., TM-82-101, 1982.
10. Finlayson, P. A. The Effect of Combustion Gas Flow on the Rotational Dynamics of a Spinning Solid Fuel Rocket. (to be published) 1989.
11. Greenspan, H. P. "The Theory of Rotating Fluids." 1980 Cambridge University Press. Cambridge.
12. Kudlick, M. D. On Transient Motions in a Contained Rotating Fluid. PhD Thesis, Dept. of Mathematics, Massachusetts Institute of Technology, 1966.
13. Thomson, W. (Lord Kelvin) On an Experimental Illustration of Minimum Energy. Nature 15: 297, 1877.
14. Poincare', H. Sur la Precession des Corps Deformables. Bull. Astronomique. 27: 321-356, 1910.
15. Cartan, E. Sur les Petites Oscillations d'une Masse Fluid. Bull.Sci.Math. 46: 317-369, 1922.
16. Fultz, D. A Note on Overstability and the Elastoid-Inertia Oscillations of Kelvin, Solberg, and Bjerknes. J. Meteorology. 16: 199-208, 1959.

17. Aldridge, K. D. Axisymmetric Inertial Oscillations in a Fluid in a Rotating Spherical Shell. *Mathematika*. 19: 163-168, 1972.
18. D'Amico, W. P. and M. C. Miller. Flight Instability Produced by Rapidly Spinning Highly Viscous Fluid. *J. Spacecraft and Rockets*. 16: 62-64, 1979.
19. Murphy, C. H. Angular Motion of a Spinning Projectile with a Viscous Liquid Payload. *Journal of Guidance, Control, and Dynamics*. 6(4): 280-286, 1983.
20. D'Amico, W. P., W. G. Beims and T. H. Rogers. Pressure Measurements of a Rotating Liquid for Impulsive Coning Motion. *AIAA Aerospace Sciences Meeting*. 1982.
21. Murphy, C. H. Influence of Moving Internal Parts on Angular Motion of Spinning Projectiles. *Journal of Guidance and Control*. 1(2): 117-122, 1978.
22. D'Amico, W. P. Comparison of Theory and Experiment for Moments Induced by Loose Internal Parts. *Journal of Guidance, Control, and Dynamics*. 10(1): 14-19, 1987.
23. Mermagen, W. H. Measurements of the Dynamical Behavior of Projectiles over Long Flight Paths. *J. Spacecraft and Rockets*. 8: 380-385, 1971.
24. Gans, R. F. Dynamics of a Near-Resonant Fluid-Filled Gyroscope. *AIAA J.* 22: 1465-1471, 1984.
25. Karpov, B. G., J. T. Frasier and W. P. D'Amico. Experimental Studies with a Liquid-Filled Gyroscope. *J. Spacecraft and Rockets*. 9: 220-222, 1972.
26. Vaughn, H. R., W. L. Oberkampf and W. P. Wolfe. Fluid Motion Inside a Spinning Nutating Cylinder. *J. Fluid Mech.* 150: 121-138, 1985.
27. Frederick, R. A. Design of Full-Scale Spin Motor Tests. Personal Communication, 1988.
28. Webster, E. A. Active Nutation Control for Spinning Solid Motor Upper Stages. *AIAA 21st Joint Propulsion Conference*. 1985.
29. Flandro, G. A. Scaling Laws for Propulsion-Induced Nutation Instability of Spin-Stabilized Spacecraft. *1989 JANNAF Propulsion Conference*. 1989.
30. Bolster, W. Delta/PAM Coning, Internal Memorandum (with attachment by J. F. McGarvey), NASA Goddard Spaceflight Center, Greenbelt, MD, 1982.
31. Lugt, H. J. "Vortex Flow in Nature and Technology." 1983 John Wiley & Sons. New York.
32. Currie, I. G. "Fundamental Mechanics of Fluids." 1974 McGraw-Hill Book Company. New York.
33. Flandro, G. A. Solid Propellant Acoustic Admittance Corrections. *J. Sound and Vibration*. 36(No. 3): 1974.

34. Meyer, R. X. Convective Instability in Solid Propellant Rocket Motors. AAS/AIAA Astrodynamics Specialist Conference. 1983.
35. Murdock, J. W. and R. X. Meyer. The Stability of a Precessing Vehicle with Outflow. Aerospace Corporation. 1988.
36. Or, A. C. The Non-adjustment of Gas Flow in a Coning Cylindrical Rocket-Motor Chamber without Nozzle. (unpublished manuscript). Hughes Aircraft Company: 1988.
37. Or, A. C. Nutational Instability of a Spin-stabilized Vehicle Driven by Thrust Misalignment produced by Non-adjustment of Gas Flow: A Scaling Analysis. (unpublished manuscript). Hughes Aircraft Company: 1988.
38. Darwell, H. M. and G. F. P. Trubridge. Design of Rocket Nozzles to Reduce Gas Misalignment. J. Spacecraft. 5(1): 36-41, 1968.
39. Walters, A. G. Non-symmetric Flow in Laval Type Nozzles. Roy.Soc.Phil.Trans.,A. 273: 185-235, 1972.
40. Hoffman, J. D. and A. R. Maykut. Gas Dynamic Gain of Supersonic Thrust Nozzles. AIAA J. 11(10): 697-704, 1974.
41. Varwig, R. L., J. S. Whittier, D. A. Durran, R. X. Meyer and E. K. Ruth. Aerodynamic Side-Force Induced by Nozzle Entrance Flow Asymmetry. TR-0088 (3470-02)-1 Aerospace Corporation. 1988.
42. Flandro, G. A. Solid Propellant Acoustic Admittance Corrections. J. Sound and Vibration. 36(No. 3): 1974.
43. Tsien, H. S. The Transfer Function of Rocket Nozzles. ARS J. 22: 139-143, 1952.
44. Culick, F. E. C. Stability of Three-Dimensional Motions in a Combustion Chamber. Combustion Science and Technology 10: 109-124, 1975.
45. Crocco, L. and S. I. Cheng. "Theory of Combustion Instability in Liquid-Propellant Rockets." AGARDograph No. 8. 1956 Butterworths Scientific Publications. London.
46. Culick, F. E. C. Acoustic Oscillations in Rocket Chambers. Astronautica Acta 12: 113-126, 1966.
47. Roach, R. L. An Implicit Finite Difference Procedure for the Laminar Supersonic Base Flow. PhD Thesis, Georgia Institute of Technology, School of Aerospace Engineering 1977.
48. Roach, R. L. and G. A. Flandro. Internal Ballistics of the Spinning, Nutating Solid Rocket Motor. Georgia Tech Internal Research Initiative. 1987.

49. Wake, B. E., L. N. Sankar, J. Wu and S. Y. Ruo. An Efficient Procedure for the Numerical Solution of Three-Dimensional Viscous Flows. AIAA 8th Computational Fluid Physics Conference. 1987.
50. Roach, R. L., Application of the Unsteady, 3-Dimensional Navier-Stokes Equations to the Sudden Pitch Change in the High Speed, High Angle of Attack Delta Wing, AFFDL TM (Progress Report, to be published) 1988.
51. Pulliam, T. H. and J. L. Steger. On Implicit Finite-Difference Simulations of Three-Dimensional Flow. AIAA J. 18: 159-167, 1980.
52. anon. Numerical Grid Generation. NASA CP-2166, NASA Langley Research Center, Hampton, VA, 1980.
53. Thompson, J. F., Z. U. A. Warsi and C. W. Mastin. "Numerical Grid Generation, Foundations and Applications." 1985 Elsevier Science Publishing Co. New York.
54. Culick, F. E. C. Rotational Axisymmetric Mean Flow and Damping of Acoustic Waves in a Solid Propellant Rocket. AIAA J. 4(8): 1462-1463, 1966.
55. Dunlap, R., G. A. Flandro, R. A. Beddini, R. S. Brown and H. McDonald. Internal Flow Field Study. AFRPL TR-85. 1985.
56. Reddall, W. F. Hydrostatic Slag Distribution in the PAM-D2 Motor Casing: Variation with Wobble Angle. Aerospace Corporation Report No. TOR-0089(4470-02)-1. 1989.